Tailoring Boron Doped Diamond Surface Properties for Sensing Applications

Samuel James Cobb

A thesis submitted in partial fulfilment of the requirements for the degree of Doctor of Philosophy in Chemistry

Department of Chemistry

June 2019

“I am no poet, but if you think for yourselves, as I proceed, the facts will form a poem in your minds.”

Michael Faraday

Table of Contents

List of Figures

List of Tables

Abbreviations

BDD	Boron Doped Diamond
C	Capacitance
Cdl	Double Layer Capacitance
CE	Counter Electrode
CV	Cyclic Voltammetry
CVD	Chemical Vapour Deposition
ET	Electron Transfer
HPHT	High Pressure High Temperature
IHP	Inner Helmholtz plane
IPE	Ideal polarisable Electrode
IR	Infrared
IS	Inner Sphere
LOD	Limit of Detection
LSV	Linear Sweep Voltammetry
MEA	Microelectrode Array
NEA	Negative Electron Affinity
NP	Nanoparticle
OHP	Outer Helmholtz Plane
ORR	Oxygen Reduction Reaction
OS	Outer Sphere
PSI	Phase Shifted Interferometry
R	Resistance
RE	Reference electrode
RMS	Root Mean Squared Roughness
R_s	Solution Resistance
R_u	Uncompensated Resistance
SCE	Saturated Calomel Electrode
SEM	Scanning Electron Microscopy
SW	Solvent Window
UNC	Ultrananocrystalline
UV	Ultraviolet

VSI	Vertical Scanning Interferometry
WE	Working Electrode
WLI	White Light Interferometry
XPS	X-Ray Photoelectron Spectroscopy

Glossary of symbols

a	Activity
A	Electrode area
AC	alternating current
C	Capacitance
C	concentration
C_{dl}	Double layer capacitance
D	Diffusion coefficient
DC	direct current
E	potential
E'	reduction potential
E^0	Formal potential
$E_{1/2}$	half wave potential
E_i	square wave increment
E_{pa}	anodic peak potential
E_{pc}	cathodic peak potential
E_{sw}	Square wave amplitude
eV	electron volts
F	Faradays Constant
f	frequency
i	current
i_f	Forward current sampling point
i_p	peak current
i_r	reverse current sampling point
j	flux
K	Kelvin
k	rate constant
k_0	intrinsic rate constant
n	number of electrons
Pa	Pascals
R	resistance
R	Molar Gas Constant

R_s	Solution resistance
R_u	Uncompensated resistance
s	seconds
t	time
T	Temperature
α	charge transfer coefficient
Γ	Surface coverage
δ	diffusion layer thickness
ΔE_p	peak to peak separation
ΔE_{step}	Potential step
Δi	differential current
ΔΨ	dimensionless peak height parameter (SWV)
η	Overpotential
ν	scan rate

Acknowledgments

Firstly, I would like to thank my supervisor Professor Julie Macpherson for her support and guidance throughout my PhD, in particular for providing an environment in which to conduct fantastic research and allowing me to pursue problems that interest me (even when I am proposing crazy ideas!). Thank you also to Professors Mark Newton and Pat Unwin for sharing their extensive knowledge and experience, along with the interesting discussions this has brought. I would also like to acknowledge Dstl and EPSRC for funding this PhD.

This thesis would not be anywhere near the quality it is without the assistance of the whole of Warwick Electrochemistry and Interfaces Group, the collaborative nature of research has made your assistance invaluable, not only with measurable contributions to papers and chapters, but also through the useful and stimulating discussions conducted within the group. Special thanks go to Dr Zoë Ayres and Dr Tania Read who I have published some pieces of work with, of which I am very proud. Also to Alex Borrill and James Teahan for tolerating my late night discussions about my latest idea/ theory/ crazy experiment and Dr Haytham Hussein for stimulating discussions and owing me a coffee. I would also like to thank (and apologise to) Josh Tully for having to take on my routine group jobs as I head towards graduation, as well as working with me on interesting research problems.

Finally thanks to Georgia for tolerating (however challenging that has been) and supporting me throughout, my brother Alex for distracting me from work by constantly talking about go-karting and of course my Mother and Father for always being there (and asking why I still haven't submitted yet).

Declaration

This thesis is submitted to the University of Warwick in support of my application for the degree of Doctor of Philosophy. It has been composed by myself and has not been submitted in any previous application for any degree.

The work presented (including data generated and data analysis) was carried out by the author except in the cases outlined below: The electrochemical data in Chapter 3 and Chapter 4 were collected in conjunction with Zoë Ayres. The electrochemical data in Chapter 5 was collected with Dr Tania Read.

Parts of this thesis have been published by the author:

Chapter 1:

Boron Doped Diamond: A Designer Electrode Material for the Twenty-First Century. Samuel J. Cobb, Zoë J. Ayres, Julie V. Macpherson. Annual Reviews of Analytical Chemistry, 2018, 11, 20 DOI: 10.1146/annurev-anchem-061417-010107

Chapter 3:

Quinone electrochemistry for the comparitive assessment of sp^2 surface content of boron doped diamond electrodes. Zoë J. Ayres,* Sam J. Cobb,* Mark E. Newton and Julie. V. Macpherson. Electrochemistry Communications 2016, 72, 59-63 DOI: 10.1016/j.elecom.2016.08.024

*Joint first author

Chapter 4:

Deconvoluting surface-bound quinone proton coupled electron transfer in unbuffered solutions: towards a universal voltammetric pH electrode. Samuel J. Cobb,* Zoe J. Ayres,* Mark E. Newton, and Julie V. Macpherson, Journal of the American Chemical Society, 2019, 141, 2, 1035-1044. DOI: 10.1021/jacs.8b11518

*Joint first author

Chapter 5:

An sp^2 Patterned Hybrid Boron Doped Diamond Electrode for the Simultaneous Detection of Dissolved Oxygen and pH. Tania L. Read, Samuel J. Cobb and Julie V. Macpherson. ACS Sensors, 2019, 4 (3), 756-763 DOI: 10.1021/acssensors.9b00137

Chapter 6:

Enhancing Square Wave Voltammetry Measurements via Electrochemical Analysis of the Non-Faradaic Potential Window. Samuel J. Cobb and Julie V. Macpherson. Analytical Chemistry, 2019, *Article ASAP*, DOI: 10.1021/acs.analchem.9b01857

Abstract

Boron doped diamond (BDD) has found numerous applications for electroanalysis in recent years. It's material properties set it apart from other electrode materials due to its oft quoted wide solvent window and low background capacitances. However, the electrochemical performance has been shown to be highly dependent on the quality of the material, in particular it's sp^2 carbon content. For some applications, such as pH sensing, it has been shown that the inclusion of sp^2 carbon impurities is advantageous. This can be achieved during diamond growth or by post-processing procedures, such as laser micromachining, as has been used in this thesis. Herein methods for electrochemically measuring *surface* sp^2 carbon have been developed, and the functional groups on the electrode surface used for pH sensing applications and the underlying sp^2 carbon component for dissolved oxygen sensing *via* the oxygen reduction reaction. To develop a pH sensor that works in unbuffered solutions laser micromachining, with control of the quinone surface coverage, was combined with pulsed voltammetric techniques to avoid perturbing the interfacial environment and control the local pH change. To further enhance pulsed voltammetric techniques, as used throughout this thesis, the raw current-time data was captured and post processed to extract information on the non-faradaic processes occurring, in addition to optimising the faradaic response. This work together advances the understanding of the effect of sp^2 carbon in BDD electrodes and its use for electrochemical applications that requires optimisation of the material properties and electrochemical methods.

Chapter 1: Introduction

1.1 Overview

Diamond has long been recognised as much more than just a gemstone due to its range of extraordinary chemical and physical properties. These include, but are not limited to, a broad wavelength transparency (from far infrared to deep ultraviolet and then again in the X-ray region); the hardest known material (~90 GPa); high thermal conductivity (2600 W m^{-1} K^{-1}) and extreme resistance to chemical corrosion.[1,2] It is through advancements in the artificial synthesis of diamond, particularly that of chemical vapour deposition (CVD),[3] that these favourable properties have been technologically exploited for a range of applications from e.g. radiation detectors [4,5] and high-power optical windows and lenses[6,7] to bionic eyes.[8,9] Furthermore, by controllably introducing impurities into diamond during chemical vapour deposition (CVD) growth, the characteristics of the material can be tailored for specific applications. For example, by incorporating boron into the lattice at concentrations in excess of 2-3 × 10^{20} B atom cm^{-3}, [10,11] the resulting boron doped diamond (BDD), achieves metal-like conductivity; albeit with a reduced number of available charge carriers compared to typical electrode metals such as Pt or Au. Incorporating boron also produces a visible colour change due to dopant-created energy levels absorbing visible light. Semi-conducting BDD exhibits a blue colour, whilst conducting BDD appears black.[12]

The virtuous electrochemical properties of BDD are often claimed to be: the widest solvent window (SW) of any electrode commonly in use (>> 3 V in 0.1 M KNO_3, using a ± 0.4 mA cm^{-2} threshold);[13] low background currents; very low electrocatalytic activity [14] and reduced fouling.[15,16] However, the extent to which these characteristics hold, depends very much on the material properties of the electrode itself, with the most important for consideration being:[14] (i) dopant concentration; has the material achieved metal-like conductivity, (ii) sp^2 content and (iii) surface termination. Understanding the relationship between the material properties and the electrode characteristics is essential in defining specifications for BDD growth; this is especially important as with advances in growth and post processing technology these properties can now be carefully controlled.

The work in this thesis focuses on the effects of sp^2 carbon content on the electrochemical properties of BDD. sp^2 carbon in BDD can be grown into the material in the CVD process,[17] or more recently has been shown to be controllably introducible using laser micromachining.[18,19] To assess the effects of sp^2 carbon on BDD a method for measuring the sp^2 content electrochemically was developed, this method has been applied throughout this thesis for assessing sp^2 content.[18] The knowledge gained in measuring and controlling sp^2 carbon content, and its surface functional groups, was applied to create a BDD pH sensor that worked in unbuffered solutions.[20] Finally study of square wave voltammetry (SWV) used in the development of a BDD pH sensor allowed for a novel way of measuring solution conductivity and electrode capacitance which could be used to infer on other electrode processes, in parallel with other analytical measurements using a high-quality BDD electrode.

1.2 Electrochemistry

Electrochemistry is an extremely powerful technique for understanding physical and chemical processes involving the movement of charge at an interface. In particular dynamic electrochemistry, *i.e.* driving the system away from equilibrium through the application of a potential or current, has been applied to a diverse range of problems from the calculation of fundamental kinetic properties of charge transfer reactions to the development of electroanalytical sensors.

The reactions occurring at an electrode interface can be divided into two classes: Faradaic, involving the transfer of electrons across the electrode interface, causing reduction and oxidation of molecules in solution to occur; and Non-Faradaic, where charge does not cross the interface but external currents may flow to compensate for changes at the electrode (such as a change in potential, electrode area or solution composition).[21]

1.2.1 Non-Faradaic processes

In the ideal case an electrode at which no charge transfer reactions can occur, regardless of applied potential, is referred to as an ideal polarizable electrode (IPE).[22] While such an electrode does not exist in reality, there are electrode materials, and solutions, where electrodes perform as such over a wide potential range, common examples being the mercury drop or a boron doped diamond (BDD) electrode in an inert salt such as KCl. BDD has been shown to exhibit this property over potential

ranges of up to 4 V in aqueous solutions.[14] The use of other electrolytes such as ionic liquids have also been shown to exhibit this property over wider ranges.[23] The range over which an electrode exhibits these properties is often referred to as its solvent window.[22]

In the case of the IPE, or an electrode which performs as such at the potentials applied, as charge cannot cross the electrode-solution interface, the system is analogous to a capacitor. Where the electrode surface is one plate, and the solution is the other, with the rearrangement of ions forming the electrical double layer (Figure 1.1) acting to compensate the charge on the electrode.

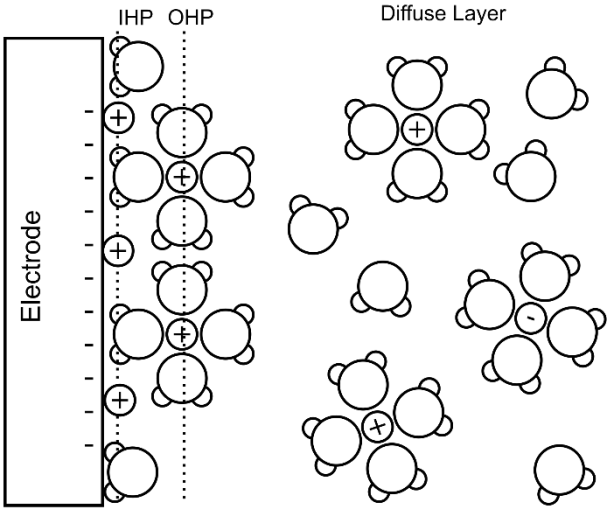

Figure 1.1: The electrical double layer.

The double layer consists of several regions to compensate the charge on the electrode. Closest to the electrode is the compact, or Helmholtz layer, consisting of species specifically adsorbed to the electrode surface, this can include solvent molecules and ions. The center of the adsorbed species is referred to as the inner Helmholtz plane (IHP). The outer Helmholtz place (OHP) is the distance of closest approach of solvated ions to the electrode surface and is governed by long distance electrostatic interactions. Beyond this distance is the diffuse layer which extends from the OHP into bulk solution, in this region molecules are disordered and only subject to non-specific interactions. There is an excess charge density across these regions which acts to compensate the charge on the electrode. The thickness of the double layer depends on the ionic strength of the solution, with a smaller double layer thickness in higher ionic

strength solutions, as the excess charge on the electrode can be compensated in a shorter distance.[22]

In the case of an IPE the cell can be represented by an equivalent circuit consisting of a capacitor and resistor (Figure 1.2). The capacitor represents the electrochemical double layer capacitance and the resistor represents the system resistance. Other components to this circuit can be considered such as the capacitance of the reference electrode. The system resistance can be subdivided into several series resistance, such as the solution resistance and potentiostat wire resistance. In a well-designed experiment the double layer capacitance and solution resistance can be considered to dominate the response and as such the equivalent circuit in Figure 1.2 can be used.

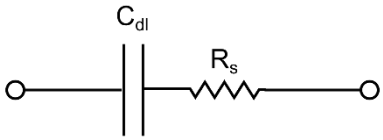

Figure 1.2: Equivalent circuit for an IPE.

Upon the application of a potential step (the basis of a staircase cyclic voltammogram and pulsed voltammetry techniques) the current-time (*i*-*t*) response of an IPE is an exponential decay, as described by Equation 1.1:

$$i = \frac{\Delta E_{step}}{R_u} e^{-\frac{t}{R_u C_{dl}}} \qquad [1.1]$$

Where *i* is the current, ΔE_{step} is the potential step, R_u is the uncompensated resistance, *t* is the time and C_{dl} is the double layer capacitance. The magnitude and duration of this current depends on the solution resistance (a key component of R_u) and C_{dl}, if R_u is low and C_{dl} is small, the non-faradaic currents are small and short lived. In typical voltammetric measurements the timescale and solution resistance are such that non-faradaic processes do not have an effect on the currents seen, and as such the currents can be assumed to be purely faradaic. This cannot always be considered to be the case for all solution and electrode conditions however.

1.2.2 Faradaic reactions

At its simplest a faradaic electrochemical reaction can be represented by Equation 1.2.

$$O + ne^- \rightleftharpoons R \qquad [1.2]$$

Where O and R represent the oxidized and reduced form of an electroactive species respectively. The position of the equilibrium is linked to the standard electrode potential, E^0, where all species are present at 298 K and unit activity. When not under standard conditions the Nernst equation (Equation 1.3) can be used to calculate the reduction potential.

$$E' = E^0 - \frac{RT}{nF} ln\left(\frac{a_{RHS}}{a_{LHS}}\right) \qquad [1.3]$$

Where *E'* is the reduction potential, E_0 is the formal potential, *R* is the gas constant, *T* is the temperature in K, n is the number of electrons, *F* is the Faraday constant, and a_{rhs} and a_{lhs} are the activities of the right (R) and left (O) sides of the reaction respectively.

The rate of electrode reaction is determined by the flux (*j*) and is a convolution of a number of factors including the mass transfer rate, electron transfer (ET) rate, chemical reactions and reactions with the electrode such as adsorption and desorption (Figure 1.3).

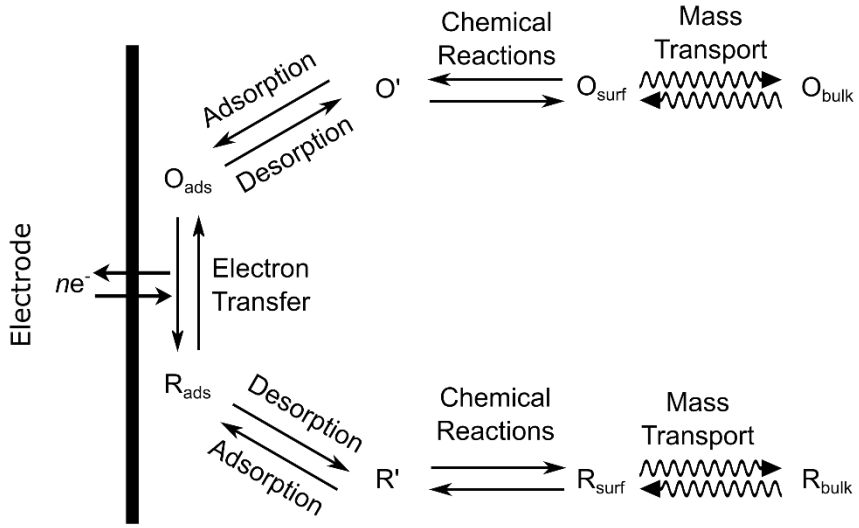

Figure 1.3: General scheme for a reaction at an electrode surface.

The flux at the electrode surface, in the absence of chemical and adsorption reactions, has a kinetic and a mass transport component, in this case mass transport is considered to be purely diffusional and the flux can be written as Equation 1.4:

$$-\frac{1}{j} = \underbrace{\frac{1}{nFk_{et}[O]_{\infty}}}_{Kinetics} + \underbrace{\frac{1}{nFk_{d,O}[O]_{\infty}}}_{Diffusion} \qquad [1.4]$$

Where k_{et} is the electron transfer rate constant, $k_{d,O}$ is the diffusion rate constant for the oxidised species and $[O]_{\infty}$ is the bulk concentration of the oxidised species.

This flux can be related to a current seen at a stationary planar electrode of area A using Equation 1.5 as the flux is constant across the electrode surface.

$$i = nAFj \qquad [1.5]$$

The kinetic rate constant in Equation 1.4 is potential dependent, and described by Equations 1.6 and 1.7 for the cathodic and anodic rate constants respectively. Increasing overpotential ($\eta = E\text{-}E^0$) causes an exponential increase in the rate.

$$k_c = k_0 e^{-\frac{\alpha_c nF\eta}{RT}} \qquad [1.6]$$

$$k_a = k_0 e^{\frac{\alpha_a nF\eta}{RT}} \qquad [1.7]$$

Where k_a is the anodic kinetic rate constants, k_o is the standard rate constant and α_c and α_a are the cathodic and anodic charge transfer coefficient, where α_a is often assumed to be $1\text{-}\alpha_c$. The kinetic flux can be described by Equation 1.8:

$$k = k_0 (e^{\frac{1-\alpha_c nF\eta}{RT}} - e^{-\frac{\alpha_c nF\eta}{RT}}) \qquad [1.8]$$

This is often known as the Butler-Volmer formulation of electrode kinetics.[22] In the case of a small overpotential, both the forward and backward rates must be considered, however once the overpotential becomes large the rate of the forward reaction far exceeds the back reaction and as such the back reaction can be considered to be negligible. This is the theoretical basis of the Tafel equation (Equation 1.9) that was first observed in 1905.[22]

$$\eta = a + b \log i \qquad [1.9]$$

Where $a = \frac{2.303RT}{\alpha nF} \log i_0$ [1.10] and $b = \frac{-2.303RT}{\alpha nF}$ [1.11]

The diffusional flux in Equation 1.12 is determined by the diffusion rate constant $k_{d,O}$, related to the diffusion coefficient (D) and diffusion layer thickness (δ) by:

$$k_d = \frac{D}{\delta} \qquad [1.12]$$

If $k_{et} >> k_d$ the flux is determined by the mass transport and the reaction is described as reversible, if $k_{et} << k_d$ the flux is determined by the reaction kinetics and the reaction can be considered irreversible.

1.2.3 The three electrode cell

For electrochemical experiments on the macro scale, the three electrode cell is used, consisting of a working electrode (WE), reference electrode (RE) and counter electrode (CE). A potentiostatic circuit is used to control the potential at the WE relative to the RE and measure the current flow between the WE and CE (Figure 1.4 1.4)

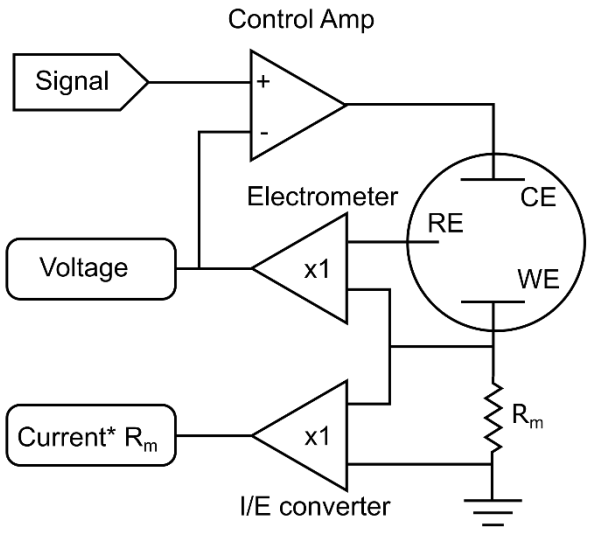

Figure 1.4: Potentiostatic circuit.

The potential is controlled between the WE and RE to be the input value (Signal) using the electrometer circuit and control amplifier as a negative feedback loop. The input potential can be held constant (chronoamperometry), swept linearly (cyclic and linear sweep voltammetry) or stepped (staircase and pulsed voltammetry). The same circuitry can also be used for AC techniques through the application of sine waves.

The electrometer is a unity-gain differential amplifier that outputs the potential difference between its two inputs (WE and RE), this potential is compared to the desired potential using the control amplifier. The electrometer output is fed into the negative terminal of the control amplifier to form a negative feedback loop, with the output driving current through the counter electrode to hold the cell voltage at the desired value. The current flowing through the cell is measured using the I/E converter, which outputs the difference in potential on either side of a known resistance (R_m), the magnitude of which depends on the expected currents flowing through the cell. Due to Ohms law this potential can be used to measure the current flowing through the cell, between the WE and CE.

1.2.4 Voltammetric techniques

Voltammetry is commonly used in analytical chemistry, where a potential waveform is applied and the current flowing through the cell measured using a potentiostat. This current represents a number of processes, both faradaic and non-faradaic depending on the experiment conditions.

1.2.4.1 Cyclic and linear sweep voltammetry

Potential sweep voltammetry is one of the most common potential waveforms, consisting of a potential continuously varying with time, scanning in one (linear sweep voltammetry, LSV) or both (Cyclic voltammetry, CV) directions (Figure 1.5a). The current response for a macroelectrode is plotted *vs* potential (Figure 1.5b).

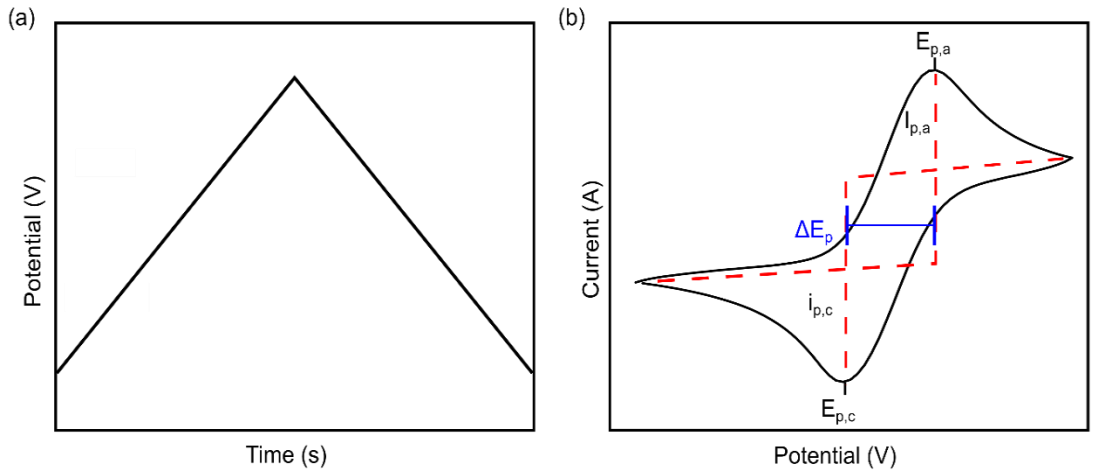

Figure 1.5:(a) The potential sweep for a CV experiment and (b) the voltammogram obtained.

For a species in solution in the reduced form the scan starts at a potential well negative of $E^{0'}$ and is scanned positive, in this region only non-faradaic currents flow. As the potential approaches $E^{0'}$, the oxidation starts to occur and the faradaic current starts to flow, depleting the species at the surface and causing an increase in flux and current. As the potential approaches and passes $E^{0'}$ the surface concentration approaches zero and the flux is at its highest, causing a peak in the current. Beyond this point the current decreases as depletion effects occur and the diffusion layer grows, causing a decrease in the flux until the system reaches a steady state. In the case of a CV the direction of the potential scan is then inverted and a reverse wave is seen, occurring due to the reduction of the oxidised species located close to the electrode from the forward scan.

In the case of a diffusion controlled reversible system the peak currents (i_p) can be modelled using the Randles-Sevcik equation(Equation 1.13):[22]

$$i_p = 0.4463nFAC(\frac{nF\nu D}{RT})^{0.5} \qquad [1.13]$$

Where A is the electrode area, C is the concentration of the redox species, ν is the scan rate and D is the diffusion coefficient. In the case of a reversible diffusion controlled system the peak separation between the forward and reverse peaks, ΔE_p is 59/n mV at 298 K.

1.2.4.2 Staircase CV

Digital potentiostats based on microprocessors mean that the application of analog 'true linear' sweep techniques have become less common, instead being replaced by staircase CV. In this method the potential sweep is approximated with a series of small (~1 mV) potential steps. This step causes a current decay that is a combination of faradaic and non-faradaic currents as discussed in more detail in Sections 1.2.1-2. To faithfully reproduce an analog linear sweep, the current at some point along the decay must be sampled. On some potentiostats this sampling point can be altered, but often the sampling position is set in the instrument by the manufacturer at a position that closely simulates the result of a true linear measurement[24] so analytical expressions such as the Randles-Sevcik equation can be used. This equivalence is usually based around a reversible species, and this sampling position may not be appropriate for more complex multistep reactions.

1.2.4.3 Pulse Voltammetry

Pulse voltammetry was made possible by the invention of the Kalousek commutator that allowed rapid switching between two potentials, so that pulse sequences could be applied.[25,26] A varied range of pulse sequences can and have been conceived, the most common being named normal pulse voltammetry, differential pulse voltammetry and square wave voltammetry. The work in this thesis focuses on square wave voltammetry, but similar approaches can be applied with other pulsed voltammetric techniques.

Square wave voltammetry has its origins in Barker's square wave polarography[27] (polarography refers to experiments on a mercury drop), where the application of a DC pulse in conjunction with a potential ramp could be used to increase sensitivity by increasing faradaic currents by pulsing and allowing charging currents to decay by sampling in the last portion of the scan. This allowed for good signals and fast scanning, meaning the measurement could be carried out in a single mercury drop.[27]

The method was developed further by superimposing a square wave onto a staircase voltammogram, as proposed by Ramaley and Krause[28,29], and sometimes referred to as Osteryoung SWV.[30] This involves the application of a series of potential pulses, formed from a staircase overlaid with a square wave pulse, with a forward and then reverse pulse occurring on each tread of the staircase.[31] The variables that can be changed include the pulse amplitude frequency and staircase increment (see Figure 1.6).

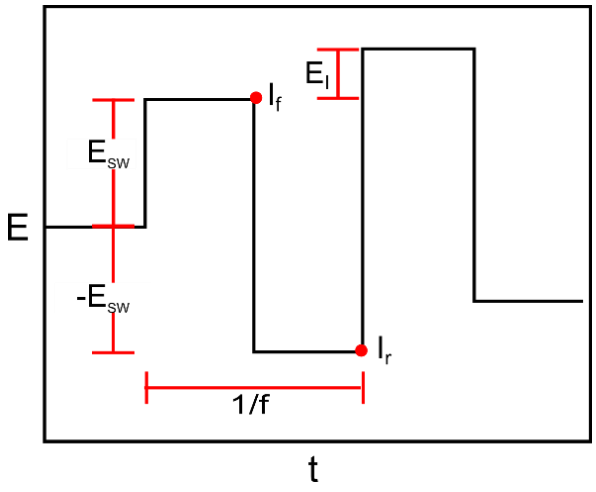

Figure 1.6: SWV potential pulse sequence, where E_{sw} is the amplitude, f is the frequency, E_I is the increment and I_f and I_r are the forward and reverse current sampling points respectively.

The raw data extracted is a series of current time (*i-t*) decays in the anodic and cathodic directions with the length of the decay determined by the frequency. These *i-t* decays are a combination of faradaic and non-faradaic components. As the faradaic components decay with $t^{-1/2}$ and the non-faradaic with e^{-t}, if the solution is sufficiently conductive the non-faradaic component will decay before the faradaic, therefore if the current is sampled at the end of the pulse the technique can discriminate the faradaic from the charging current. The sample current from the reverse pulse is subtracted from the forward current to give a net current (Equation 1.14), and is plotted against potential to obtain a voltammogram.

$$\Delta i = i_f - i_r \qquad [1.14]$$

Due to the diffusion layer not being renewed, in the case of a faradaic reaction each pulse cannot be treated in isolation, this makes the peak currents challenging to describe with a simple equation as can be done for a potential sweep experiment, with Equation 1.15 derived by Osteryoung:

$$i_p = nFAD^{0.5} f^{0.5} C \Delta\Psi \qquad [1.15]$$

Where *n* is the number of electrons, *F* is the faraday constant (96485 C mol^{-1}) *A* is the electrode area, *C* is the concentration of the redox species, *f* is the square wave frequency in Hz. $\Delta\psi$ is a dimensionless parameter, that relates the peak height in SWV to that in normal pulse voltammetry and depends on n, E_{SW} and E_I. While this value can be mathematically determined it is commonly tabulated.[32] It is the complexity of this equation that means the peak height in SWV is not often used to determine physical properties of the system such as the diffusion coefficient.

While the analytical solution determined by Osteryoung for SWV samples at the absolute end of the pulse, this is not always the case with real instruments, as to improve on noise the current can be averaged over some last percentage of the pulse (up to the last 50%).[33,34] The different currents of this altered sampling can be accounted for.[35] This further complicates the use of analytical expressions to describe the peak current in SWV.

1.3 Electrochemistry of Quinones

Quinones are a group of organic molecules characterised by having a fully conjugated cyclic dione structure, such as benzoquinones (Figure 1.7), derived from aromatic

compounds by the conversion of an even number of –CH= groups into –(C=O)- groups with the necessary rearrangement of double bonds.[36] Their structure and associated electrochemical properties has made quinones one of the most studied organic redox couples since the start of the 20th century.[37] Their study is important as quinone chemistry underpins a large number of biological processes such as mitochondrial ATP synthesis[38] and electron transfer[39] as well as being their involvement in cancer treatment.[40] Anthraquinone is also used to generate hydrogen peroxide on the tonne scale.[41] Electrochemically, quinones have found a diverse range of applications, including redox flow batteries[42] and catalysis of the oxygen reduction reaction (ORR)[43], however the most prevalent application is their use for pH sensing.[44]

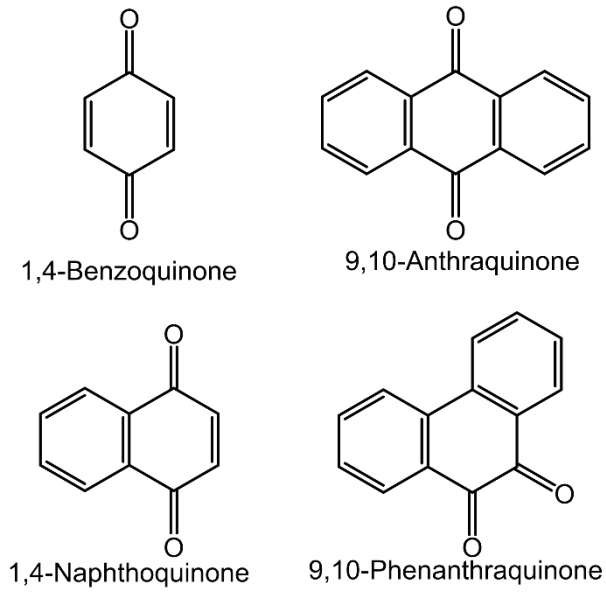

Figure 1.7: Example quinone species.

The electrochemistry of quinone groups is complex, with numerous pathways for the reaction to progress by. These are often described by the scheme of squares, originally proposed by Jacq (Figure 1.8),[45] with the theoretical treatment of these reactions at surfaces conducted by Laviron[46].

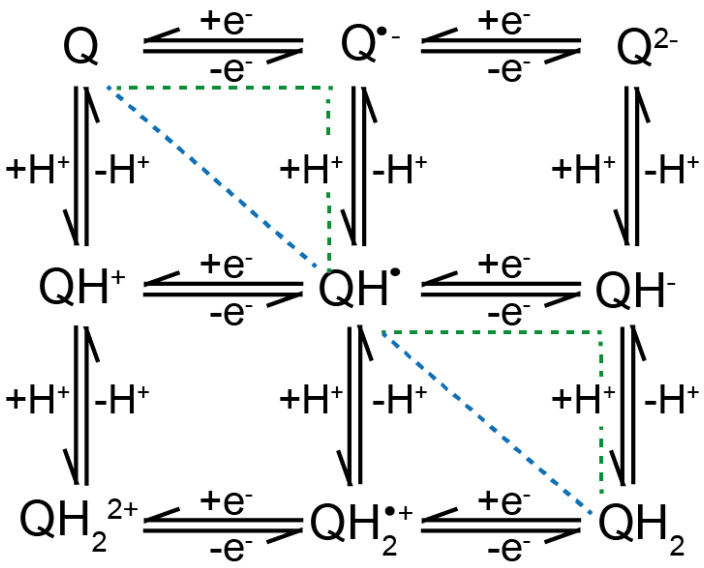

Figure 1.8: Quinone scheme of squares demonstrating the possible reaction pathways, as proposed by Jacq

From this scheme it is apparent that quinones (Q, Figure 1.8) can undergo a 1 or 2 electron reduction reaction, which may be accompanied by up to 2 proton transfer (PT) reactions. Where PT occurs these reactions can occur via a stepwise mechanism where each PT or ET step occurs separately. Or *via* a concerted mechanism, where a PT and ET step happen simultaneously. This is represented by the diagonal pathways on the scheme.

1.3.1 Quinones in aprotic solutions

In the absence of protons, such as in non-aqueous solutions e.g. acetonitrile, quinone groups undergo a $2e^-$ reduction to form a quinone dianion (Q^{2-}). This is often seen as two, distinct, $1e^-$ reduction waves, forming $Q^{-\cdot}$ as an intermediate that is subsequently reduced to the dianion. For the majority of quinones these reactions are reversible in nature.[47] The potentials of the two reaction steps are dependent on the nature of the solvent and supporting electrolyte, due to differing stabilisation of the products, intermediates and reactants. Upon the addition of weak proton donors and strong acids to aprotic solutions the reduction of quinones becomes much more complex,[48] with the nature of the proton donor having an effect on the mechanism. In addition to the scheme of squares, homogeneous ET (disproportionation reactions)[49] have been shown to occur under these conditions.[50]

1.3.2 Quinones in buffered solutions

In buffered solutions quinones at acidic and neutral pHs undergo a $2e^-/2H^+$ proton coupled electron transfer (PCET) reduction to form a hydroquinone.[51] A single wave is usually seen for this process, as the second ET step is energetically more favourable than the first and as such occurs simultaneously.[47] The pK_b of quinones (pK_a of the protonated Quinone, QH^+) is generally very low (Benzoquinone= -7)[46] and as such in aqueous solutions the quinone can generally be considered to be in its neutral, deprotonated, form at equilibrium. This simplifies the reaction routes available, as the lower left hand side of the scheme can be discounted and ET must occur before the first PT, as the quinone is above is pK_b. The first pK_a of the hydroquinone product is generally between 7 and 10 [51] and until the pH is higher than this, QH_2 is the favoured product. The reaction is generally proposed to proceed by an ECEC mechanism.[52] Due to the presence of protons in the rate determining step the $2e^-/2H^+$ reduction is pH dependent and *E*' of the reaction shifts as described by the Nernst equation, in this case at 59 mV per pH unit due to the equivalent number of protons and electrons transferred.

Above $pK_{a,1}$ of the hydroquinone, QH^- becomes the favoured product and the reaction proceeds from Q to QH^+ *via* a $2e^-/1H^+$ ECE process, giving a potential dependence of 29.5 mV per pH unit.[51,53] When the hydroquinone passes its second $pK_{a,}$ another shift in the mechanism is seen, and Q^{2-} becomes the most thermodynamically favourable product, with the mechanism proceeding by a $2e^-$ proton independent route. Despite initially appearing similar to the aprotic, non-aqueous case one wave only is still seen, which can either be attributed to potential inversion, with the second ET step being more favourable than the first or so close in potential that only one wave is observed.[54,55] This is often attributed to hydrogen bonding interactions between the $QH^{-\cdot}$ and water.[56]

1.3.3 Quinones in unbuffered solutions

The electrochemistry of quinones is generally studied in well buffered solutions, with a limited number of studies in unbuffered solutions[51,56,65,57–64]. This is often stated to be due to the complicated response under these conditions, where any changes in mechanism are further convoluted with local pH changes, due to consumption of protons.[51,57] The assumption has been made that in unbuffered solutions the reaction will still progress, at least in part, by a $2e^-/2H^+$ PCET mechanism (Figure 1.9a).

However, the peak shifts in response to the local pH change, which can be up to 5-6 pH units.[65] For this reason as far back as 1940 Muller recommended such experiments are conducted in well buffered solutions.[57]

In unbuffered solutions, when the proton concentration ($[H^+]$) is close to the quinone concentration ([Q]) two voltammetric waves are typically seen (Figure 1.9b), the first of which is always attributed to the $2e^-/2H^+$ PCET mechanism (Figure 1.9a).

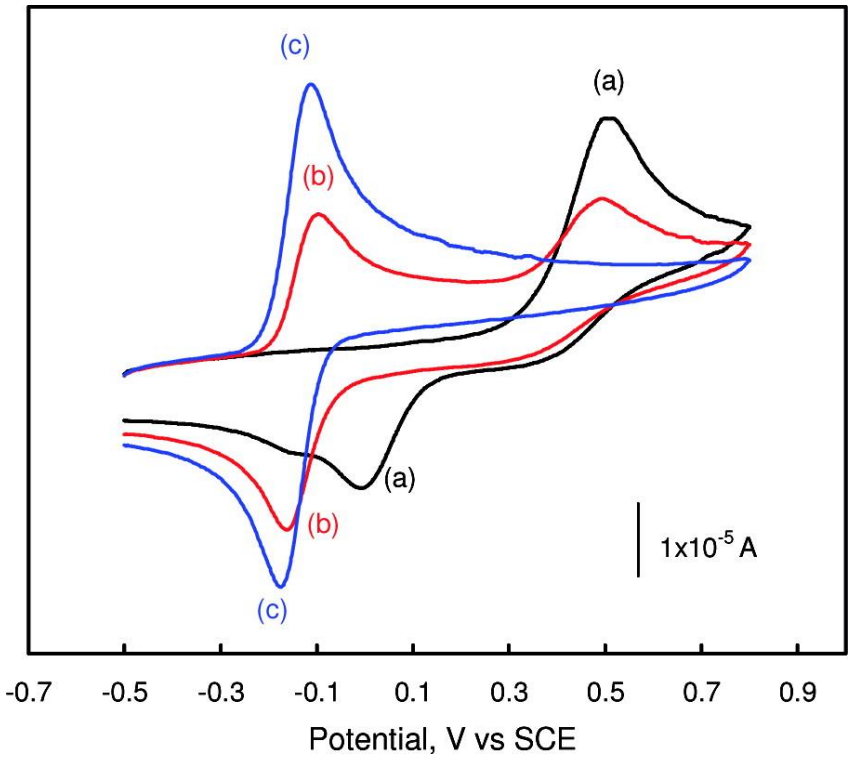

Figure 1.9:(a, black) CV of 1 mM Benzohydroquinone in unbuffered water. (b, red) CV after addition of 1 equiv of OH^- to the cell. (c, blue) CV after addition of a total of 2 equiv of OH- to the cell. 100 mV/s scan rate with a glassy carbon working electrode. From Quan et al.[56]

The interpretation of the second wave (Figure 1.9c) however is more varied, with some studies attributing this wave to the same $2e^-/2H^+$ reaction as the first wave, however with a different proton donor such as hydroquinone or water being responsible for its significant shift on the potential axis.[57–59,64] Alternatively the formation of 'some deprotonated form of the hydroquinone'[51](Q^- or Q^{2-}) is proposed, due to the lack of available protons. Some spectroscopic studies argue for the $1e^-$ reduction to form the radical anion, $Q^{-\cdot}$.[66,67] Others propose the formation of the quinone dianion by a $2e^-$ reduction, Q^{2-}.[61,62] Quan et al.[56] extended this description to include the role of hydrogen bonding, suggesting that Q undergoes a $2e^-$ reduction to form the strongly

hydrogen bonded Q^{2-} dianion, which due to its basicity will exist in an equilibrium mixture of Q^{2-}, QH^- and QH_2, the exact ratio of which is dependent on the particular hydroquinone pK_a and concentration.[56]

1.3.4 Quinone groups on electrode surfaces

Quinone groups have frequently been attached to electrode surfaces for fundamental studies and a number of applications, predominately pH sensing[44] and ORR.[43] It has been shown that the electrochemical response of surface bound molecules can differ significantly from their solution counterparts,[68–70] in particular due to an increase in the pK_a[62,71,72], from the change in the local environment. A variety of methods have been used, including but not limited to: self-assembled monolayers (SAM), covalent coupling chemistry, carbon paste electrodes and the use of quinone groups inherent in a materials surface termination.[44]

The simplest form of surface modification with quinone groups is physical adsorption, where quinones such as 9-10-phenanthraquinone[73], quinhydrone[74] and anthraquinone disulphonate[75] (for selected structures, see Figure 1.7) adsorb onto the surface during an electrochemical polarisation. However the stability of this modification is fairly low, with the quinone redox peaks decreasing with a first order dependence and a half-life of several hours when placed in pure supporting electrolyte solution, generally attributed to the detachment of molecules from the electrode surface.[73,75]

SAMs are one of the most common ways to incorporate a variety of quinone molecules onto electrode surfaces, through the use of a linker chain terminated by a thiol group that can spontaneously interact with the electrode surface by chemisorption. (Figure 1.10).

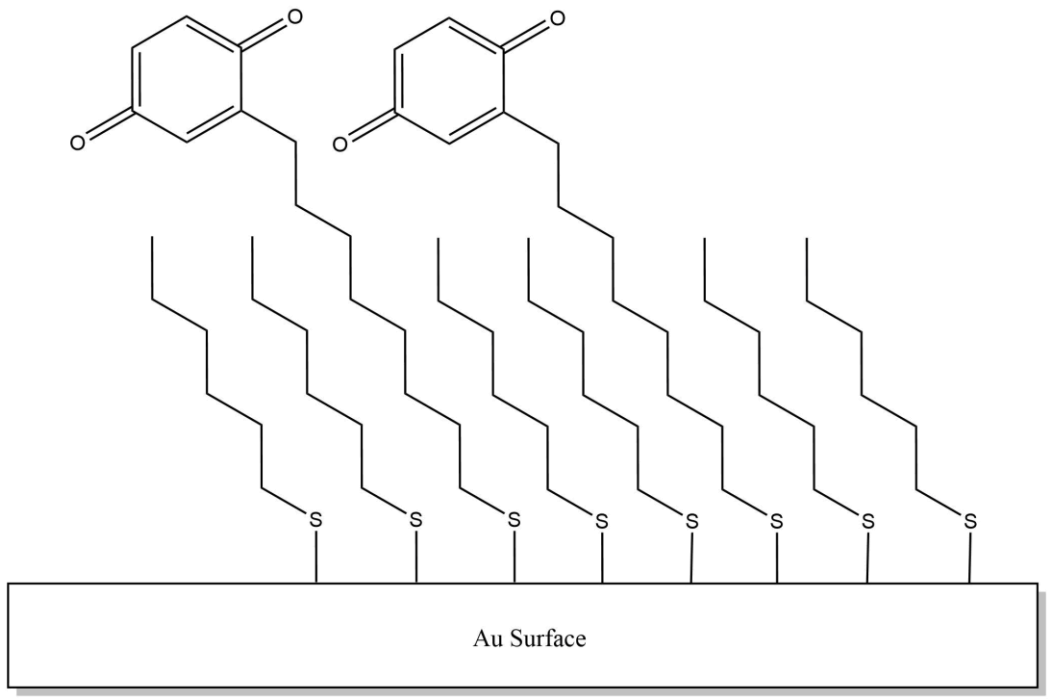

Figure 1.10: 2-(mercaptooctyl)hydroquinone with hexanethiol as a diluent to alter Γ. Adapted from Larsen et al.[76]

Most studies have used SAMs on Au,[60,76–82] although a limited number of studies have used Hg[62] as the base electrode material. The linker group has a significant effect on the ET rates,[77] as the shuttling of an electron from the electrode to the molecule can be rate limiting. The length of the linker chain affects the rate of ET, as the molecule is positioned further from the electrode surface. In the case of a non-conducting linker ET occurs via tunnelling from the electrode to the molecule or *vice versa* and the rate has an exponential dependence on distance.[81–83] This weak electronic coupling generally leads to rates of ET that are considerably slower than those in solution.[62,77] However, conjugated linkers can increase the rate of ET compared to unconjugated linkers, through increased tunnelling efficiency.[77]

The surface coverage (Γ) of quinone groups can also affect the electrochemical response,[76] with diluent molecules being used to change the Γ. This has been used to access a range of Γ, from 5.6×10^{-10} mol cm^{-2}(monolayer coverage) to 6×10^{-12} mol cm^{-2}(sub-monolayer coverage). [76] However, control of the Γ within this range was challenging, as the Γ does not trend linearly with diluent molecule concentration and several different diluent molecules were required to allow good control of Γ across this entire range.[76] This effect is attributed to hydrogen bonding interactions between

the quinone groups during monolayer formation, with different diluents screening this to different degrees.

In general, lower Γ (<<monolayer) exhibits better responses with smaller peak separations, full width half maximums and monolayer stabilities.[76] This has tentatively been attributed to electrostatic interactions between neighbouring groups at high Γ resulting in changes in the peak height and width.[84,85] While control of the Γ in SAMs is highly desirable, it can be challenging, especially at low Γ and other techniques, such as laser ablation, can offer better control. Another limitation of SAM is that this chemisorption is 'semi-covalent' in nature[86] and inherently weaker than a C-C covalent bond, and as such the long term stability of these monolayers can be poor.[76,87]

Covalent coupling chemistries, such as 'click' chemistry that can be electrochemically assisted offer increased stability for attaching redox molecules to electrode surfaces when compared to SAMs, due to the stronger C-C or C-N bond.[71,88] These reactions are generally conducted using oxide surface sites on carbon electrode materials and have been extensively reviewed,[89] with the reduction of diazonium salts being the most common.[90] This approach has been used to attach anthraquinone to diamond electrodes[91] and carbon powders[71,88,92,93] to give reversible voltammetric waves. However, this methodology requires complex synthetic procedures, and multilayer formation is common.

Carbon paste electrodes offer simpler electrode fabrication, as the redox species is merely mixed into a solution of graphite powder and oil or epoxy and allowed to set. A variety of quinone molecules, with different electrochemical properties have been included in these matrices[94,95] for pH sensing applications. However, the fabrication of the electrode is fairly ill defined, depending on the mixture used and how it is formed into an electrode.

Quinone groups also form part of the surface termination of sp^2 carbon electrode materials, such as edge plane pyrolytic graphite (EPPG)[96] and glassy carbon (GC)[97] and it has been shown that these groups can undergo a $2e^-/2H^+$ reduction to give a voltammetric wave that shifts at 59 mV pH^{-1}, up to pH values of 13. As such they have found application as a pH sensor, discussed in Section 1.5.2. However, as these groups are intrinsic to the electrode material the nature of the quinone species is not known and Γ is very difficult to control. To resolve the quinone wave on EPPG and GC the

solution had to be degassed, due to ORR on these materials obscuring the signal.[96,97] This is not practical for the measurement of pH in real world solutions. Recently laser ablation has been used as a route to introduce sp^2 carbon and therefore quinone groups into a BDD electrode, allowing for spatial and density control, well below monolayer.[19] The fabrication of these electrodes is discussed in more detail in chapter 4. By incorporating the quinone groups onto the electrode surface, the $pK_{a,1}$ of the hydroquinone form has been shown to be increase by several pH units.[98] In addition to changes in the order of the solvent molecules and effects from the hydrophobicity/philicity surface termination, it was shown that the electronic coupling to the electrode surface was partly responsible for this increase in pK_a, as when a linker molecule was used the effect was less significant.[98] Therefore, quinone groups on a BDD electrode should possess a high pK_a and operate *via* a $2e^-/2H^+$ PCET mechanism across a wide pH range.

1.4 Ion coupled electron transfer

Quinones are a common example of molecular systems that undergo PCET. The response of these molecules in solution has been described in Sections 1.3.1-3, as has the response when attached to a surface by a weak bond such as a SAM, Section 1.3.4. SAM based quinone systems have poor electronic coupling between the electrode surface and the appended group. It has been shown that ferrocene appended thiol SAMs display ET kinetics that are in line with outer sphere ET kinetics, including solvent reorganisation energies and electron tunnelling prefactors, suggesting there is a tunnelling barrier to ET in these systems.[99] However when a molecule is strongly electronically coupled to the electrode surface, for instance by a conjugated aromatic linkage as in Figure 1.11, it can be thought of more as an additional active site on a metal electrode, rather than as an independent molecule capable of undergoing ET.[100]

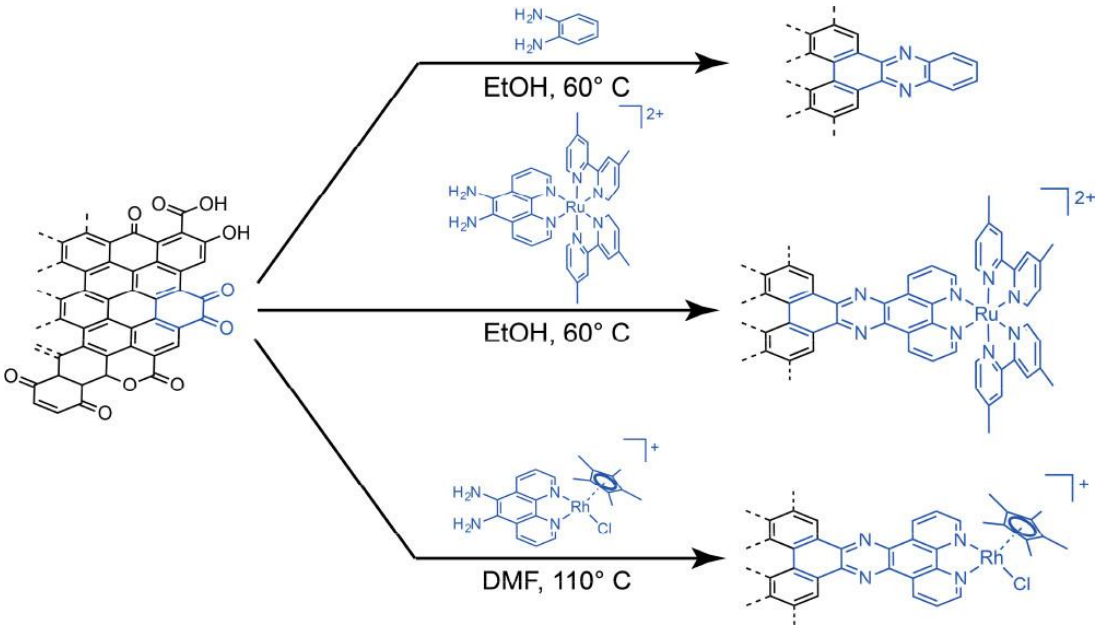

Figure 1.11: Synthesis of GCC-Phenazine (top) GCC-Ru (middle) and GCC-Rh (bottom). Reproduced from Jackson et al.[100]

To demonstrate this Jackson *et al*. coupled a variety of different molecules to a graphite surface *via* an aromatic pyrazine linkage and investigated their electrochemistry.[100] O-phenyldiamine was coupled to the electrode surface, (Figure 1.11, top) creating a phenazine like surface site with 2 nitrogen groups that can undergo PCET. In aqueous buffered solutions a single wave was seen across the entire pH range, shifting at 59 mV pH^{-1} as expected of a $2e^-/2H^+$ PCET reaction. In acetonitrile, in the absence of protons, no ET was witnessed. However, for the phenazine molecule *in solution* under the same conditions a wave corresponding to a reversible $1e^-$ ET reaction, was observed. It was only be adding 0.2 M tosylic acid that surface bound phenazine exhibited an electrochemical response, showing two distinct waves for the two $1e^-/1H^+$ waves reactions. The same was observed for phenazine in solution in the presence of acid.

Similarly, when a ruthenium complex that can undergo a reversible $1e^-$ reduction was incorporated onto the surface (Figure 1.11, middle) no ET was seen in aqueous solution, despite it readily undergoing ET when dissolved in solution. Finally, a rhodium complex (Figure 1.11, bottom) that can be reduced via a $2e^-$ process from Rh^{3+} to Rh^{1+} with accompanying dissociation of a bound chloride, was bound to the surface. In a similar manner to the phenazine in the absence of protons, no ET for the rhodium complex was seen in the absence of chloride in acetonitrile, however a $1e^-$

reversible ET was seen when surface bound in the presence of chloride. This wave was also shown to be dependent on the nature of the halide as when iodide and bromide were used as the anion, instead of chloride, the wave shifted by +40 and +60 mV respectively.

As the rhodium complex appeared to undergo a $1e^-$ reduction when surface bound, as opposed to the expected $2e^-$ reduction seen in solution, the surface bound redox wave is distinct from the solution phase process. X-Ray Absorption Near-Edge Spectroscopy was conducted, which can be used to analysed the oxidation state of the metal. From this it was determined that at all points during the voltammetric scan (i.e. when in its 'reduced' and 'oxidised' form) the Rh stays in the 3+ form and doesn't change its valency. This suggests the electron goes into the ligand, which in this case is the carbon electrode.

These observations together suggest ET is possible for strongly electronically bound species only in the presence of ion transfer. Due to this it can be inferred that the ion coupled electron transfer mechanism must be concerted, with ion and electron transfer happening simultaneously. From this the ET can be considered to be very different to in solution (Figure 1.12, top), where the ET occurs when the Fermi level of the electrode is increased above the reduction potential for the Rh species, leading to it being reduced from Rh^{III} to Rh^{I}, with the subsequent removal of a chloride. When the Rh is strongly electronically coupled to the electrode surface (Figure 1.12, bottom) the reduction potential is pinned to the electronic structure of the electrode and changes as the potential on the electrode is varied. As such the reduction potential is never reached. However when the potential reaches a point where the removal of a chloride from the surface is energetically favourable (Figure 1.12, green), the reaction occurs, and ET is witnessed to balance the charge. This work is analogous to the behaviour of quinone surface sites, in combination with protons, incorporated into the BDD surface.

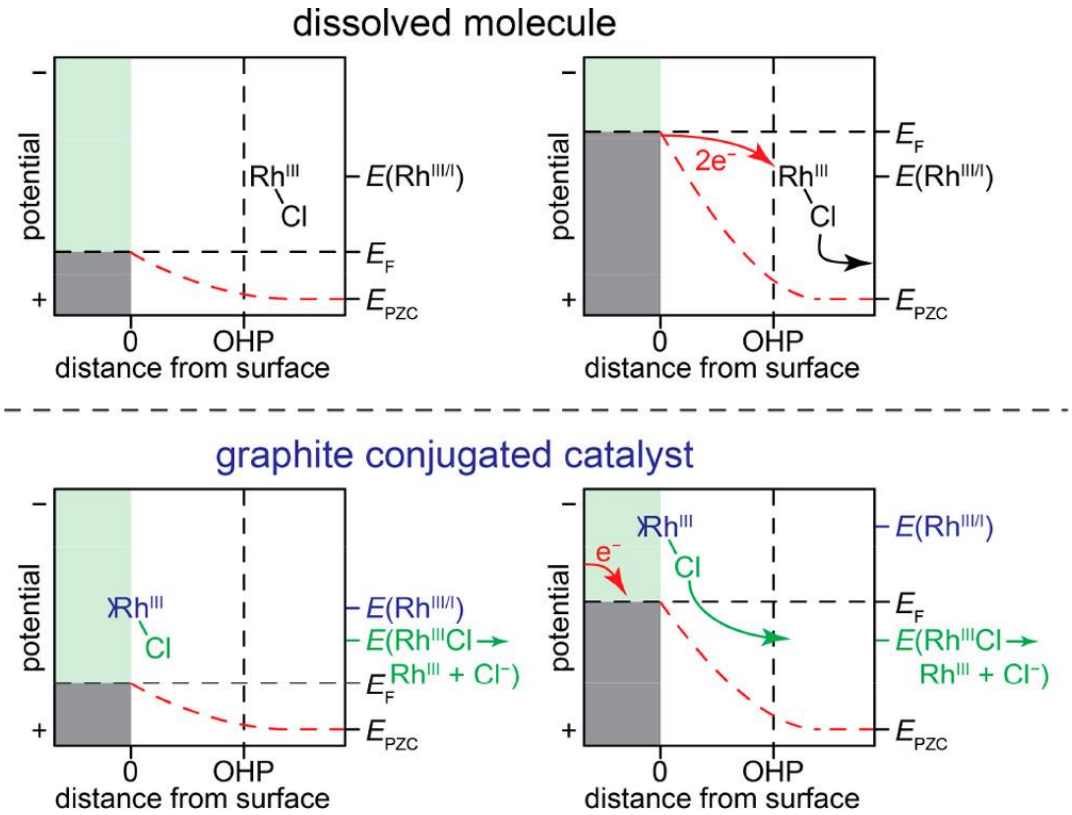

Figure 1.12: Energy level diagrams demonstrating the different mechanisms of ET in solution (top) and when strongly electronically coupled to the surface (bottom). Reproduced from Jackson et al.[100]

1.5 pH sensing

Solution pH is one of the most commonly measured solution properties. The pH scale was originally developed in 1909 by Danish chemist Søren Peder Lauritz Sørensen working at the Carlsberg laboratory in Copenhagen.[101] Sørensen defined pH as the negative logarithm of proton activity (aH^+, Equation 1.15)

$$pH = -\log(aH^+) \qquad [1.15]$$

1.5.1 The glass pH sensor

The most prevalent method of pH sensing is the glass pH probe, due to its wide dynamic range from pH 2-12, high sensitivity and acceptable response time.[102] The change in potential of a glass membrane when placed in solution of different pHs was first noted by Max Cremer in 1906,[103] even prior to the development of the pH scale. This sensor has since been subject to over 100 years of development.

The sensor is effectively a hydrogen ion selective electrode, comprised of two RE (typically Ag|AgCl RE) one of which sits in a constant, internal solution and the other in the solution of interest. The two RE are separated by a thin glass membrane (~0.1 mm thick) that consists of mainly amorphous silicon dioxide, with additional alkali metal ions embedded within its matrix. The Si-O groups in the glass can be protonated, with the degree of protonation dependent on the solution pH in which it resides. Protonation of the membrane creates a potential difference between the two sides of glass, dependent on their relative degree of protonation. As the internal solution is of a known, constant, pH the membrane potential is dependent only on the solution pH and changes in a manner that can be described by an adapted form of the Nernst equation. (equation 1.16)

$$E' = E^0 - \frac{2.303\ RT}{nF}\ pH \qquad [1.16]$$

Thus at T= 298 K a 59 mV pH^{-1} potential dependence is seen and the solution pH can be determined from the potential. The glass pH electrode is however subject to several issues. Firstly the glass is inherently fragile, limiting the environments in which it can be applied as it is not suitable for high-pressure or high temperature environments or in-situ measurements. It is also required to be stored hydrated and suffers from 'alkali' errors at high pH as similarly charged and sized ions such as Li , Na, K and Ca can interact with the membrane and result in erroneous pH measurements.[102,104]

1.5.2 Solid state pH sensing technologies

Solid state pH sensors have gone some of the ways to address the fragility issues of the glass pH electrode, and can also be stored dry. Ion sensitive Field Effect Transistors (ISFETs) operate in the normal manner of a field effect transistor, with the solution of interest acting as the gate and a pH sensitive material such as Si-O is used in the channel.[105] The pH of the solution changes the degree of protonation of the oxide, resulting in a concomitant change in current flow through the transistor. Therefore, the threshold voltage of the transistor is dependent on the solution pH. The ISFET has its own issues however, often being prone to drift and can become blocked when placed in real world solutions. Some corrosive solutions such as chlorine can also permanently damage the devices.

Proton sensitive metal oxide probes have also been developed that operate potentiometrically, such as ruthenium oxide, manganese oxide and tin oxide.[106] However these also suffer from redox interferences and drift issues. Due to its biocompatibility[107] and the fact it can be miniaturized[108] iridium oxide has been used extensively[109], however it must also stay hydrated to provide stable potentials.[110]

1.5.3 Optical pH measurements

Non-electrochemical methods such as optical pH measurements have also been developed, based on colorimetric reagents immobilized on a porous membrane and using absorbance, fluorescence and reflectance as a read out of the pH of the solution.[111] These sensors are low cost, easy to miniaturise and can offer high selectivity,[112] however they only operate over a limited pH range of approximately 1.5 units either side of the pK_a of the reagent.[111]

1.5.4 Quinone electrochemistry for pH sensing

Quinones have been used for pH sensing for almost as long as the glass electrode, with Biilmann first reporting the pH sensitivity of quinones in 1921.[113] This quinhydrone electrode consisted of an equimolar mixture of quinone and hydroquinone which forms a pH dependent redox couple, the potential of which can be measured against a RE. This electrode gave poor results above pH 8 as the hydroquinone reaches its pK_a. In recent years quinones have been employed as voltammetric pH sensors,[19,44,94,96,97] using the $2e^-/2H^+$ reduction mechanism as discussed *vide supra* to give a sensitivity of 59 mV pH^{-1}. This offers advantages in terms of selectivity and measurement time as the system stabilizes fast, however the measurement by its nature alters the local pH environment, and as such has been shown to struggle in unbuffered systems.

1.6 Boron Doped Diamond

Diamond's large bandgap of 5.5 eV makes it useful as an insulator (Figure 1.13a), however at times conducting diamond is desired. Diamond can be doped in a similar way to silicon, another group IV element, by introducing donors (group V elements) such as nitrogen or phosphorous to create n-type semiconductivity, or by adding acceptors (group III elements) such as boron to introduce p-type semiconductivity.[114]

N-type semiconductors such as nitrogen and phosphorous have not shown a great degree of success due to their ionisation energies being too large. Nitrogen has an activation energy of -1.7 eV, too large for a n-type dopant as no carriers will be

thermally activated. Phosphorous has a smaller but still significant activation energy of -0.55 eV[115] and also suffers from the issue that its relatively large atomic size means achieving high doping levels is challenging.

Boron readily incorporates into the diamond lattice, achieving dopant densities as high as ~10^{22} atoms cm^{-3}. Boron in diamond is a p-type dopant, creating an acceptor level in the diamond band gap (Figure 1.13b) and has an activation energy of 0.37 eV, which while still large compared to dopants in other semiconductors is small enough to be usable, as approximately 1% of carriers are active at room temperature. With dopant densities above ~10^{20} atoms cm^{-3} the material can become 'metallic' as the dopants are close enough together for their wavefunctions to overlap (Figure 1.13c).[10] This leads to hopping conduction and pinning the Fermi level in the dopant states. When doping levels increase beyond this point screening decreases the acceptor activation energy and the intrinsic bandgap will shrink (Figure 1.13d). Superconductivity at 4 K has been demonstrated in these extremely highly doped diamonds.[116]

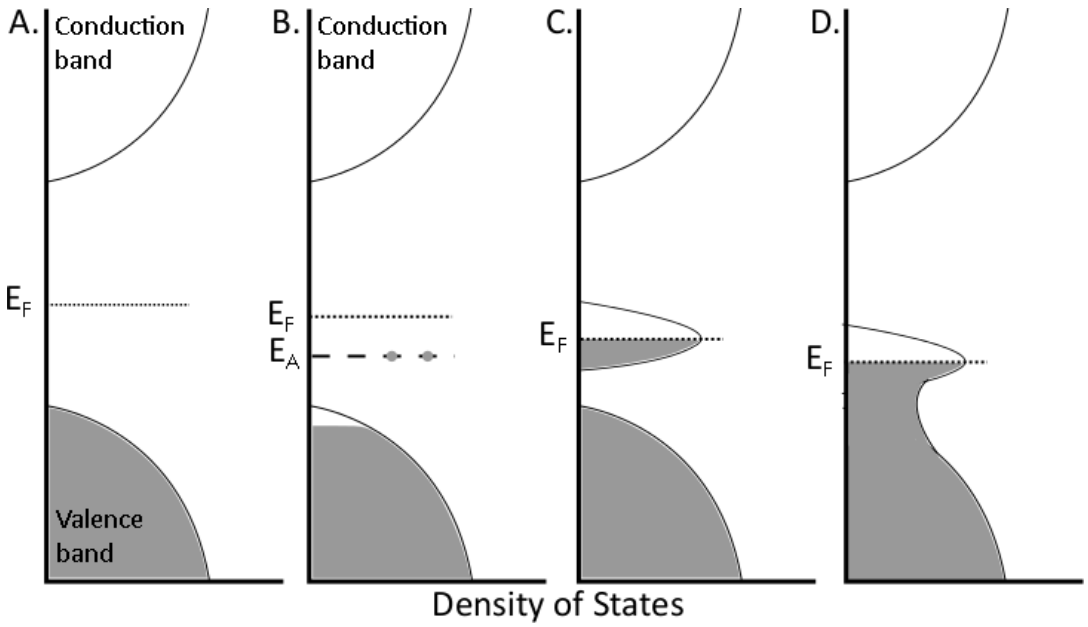

Figure 1.13:(a) In undoped diamond the Fermi level (E_F) lies between the valence band (VB) and conduction band (CB). (b) In lightly boron doped diamond the carrier concentration depends on the ionization energy of the dopant and the temperature. (c) When heavily doped (~10^{20} atoms cm^{-3}) the dopant wavefunctions overlap leading to delocalisation and metallic behaviour with E_F inside the dopant state. (d) In extremely heavily BDD, screening of impurities lowers the acceptor activation energy and the intrinsic bandgap will reduce. Adapted from Blase et al.[117]

1.6.1 Growth of BDD

The growth of diamond was first reported by General Electric in 1955 using a high pressure high temperature (HPHT) method.[118] In HPHT, a carbon source, usually graphite, is combined with a metal catalyst and heated to temperatures ≥1800 K under pressures of 3-5 GPa. The diamonds produced by this method are typically small (<10 mm) single crystals, heavily doped with nitrogen from the atmosphere. While heavily ($>10^{20}$) B-doped diamond has been produced by this method, the compensation of charge carriers by nitrogen limits conductivity.[119] HPHT has produced a limited number of BDD samples with metallic conductivity,[116] however their small size and complex synthesis has to date limited their application.

In contrast, CVD, has proven to be the more versatile technique for BDD growth. The technique deposits BDD, under plasma conditions, from a carbon containing gas mixture, such as methane, in the presence of hydrogen and a boron based gas e.g. diborane, onto a suitable growth substrate, seeded with diamond nanoparticles. Plasma temperatures around 2500 K, substrate temperatures of 1200 K and pressures of 25 mbar are typical, with plasmas generated using either microwaves or a hot filament. Hydrogen is a necessity as the plasma-generated hydrogen radicals not only suppress the growth of thermodynamically stable sp and sp^2 carbon, but also preferentially etch these species.[120] Through manipulating the gas mixture and reactor conditions, fine control over the material properties can be achieved. For example, an increased hydrogen concentration reduces sp^2 incorporation, but also slows growth rates; the use of a microwave plasma over hot filament generally enables hotter temperatures, leading to higher phase purity material and faster growth rates.[121]

Typical growth substrates, which can withstand the growth conditions, are niobium, tungsten, and silicon.[14] While most material is grown on a flat surface, the technique is amenable to almost any geometry substrate, allowing the creation of designer electrode geometries such as BDD microwires.[122] The transfer of BDD to flexible substrates such as polyimide and parylene C has also been reported,[9,123] enabling flexible electrode production. With the use of a diamond nanoparticle seed, polycrystalline BDD results. Using a single crystal diamond substrate[124] and no seeding layer, single crystal BDD can be produced.

The material growth conditions also influence the resulting material morphology. The vast majority of BDD electrodes in use are polycrystalline, due to the relative ease at which they can be produced, over a range of length scales.[14,121] The polycrystalline material grain size and surface roughness varies with growth time. In particular, longer growth times give rise to thicker substrates with larger grains and rougher growth surfaces, the latter attributed to the protruding crystallites.[14] Nanocrystalline BDD is typically sub-micron thickness, contains grains of sub-micron sized dimensions and has a surface roughness on the ~ nm scale. In contrast microcrystalline BDD is thicker, has an increased surface roughness and contains grains on the micron and larger scale. In general, nanocrystalline material tends to contains more sp^2 carbon due to the trapping of non-diamond impurities in grain boundaries.[125]

Thin film BDD is used still attached to the growth substrate, as the BDD is not robust enough to be removed. As BDD gets thicker (>10's of μm) it can be removed from the growth substrate to create freestanding material. However, the cost of growing freestanding BDD is higher than its thin film counterpart due to longer growth times. To significantly reduce surface roughness, the surface of freestanding BDD can be mechanically polished. However, poor polishing can cause sub-surface damage, creating defect sites that can trap charge carriers.[14] Polishing must therefore be carefully controlled in order to not adversely impact on the electrochemical properties of the BDD.[13] The difference in the types of BDD morphologies that can be produced is illustrated in Figure 1.14.[126]

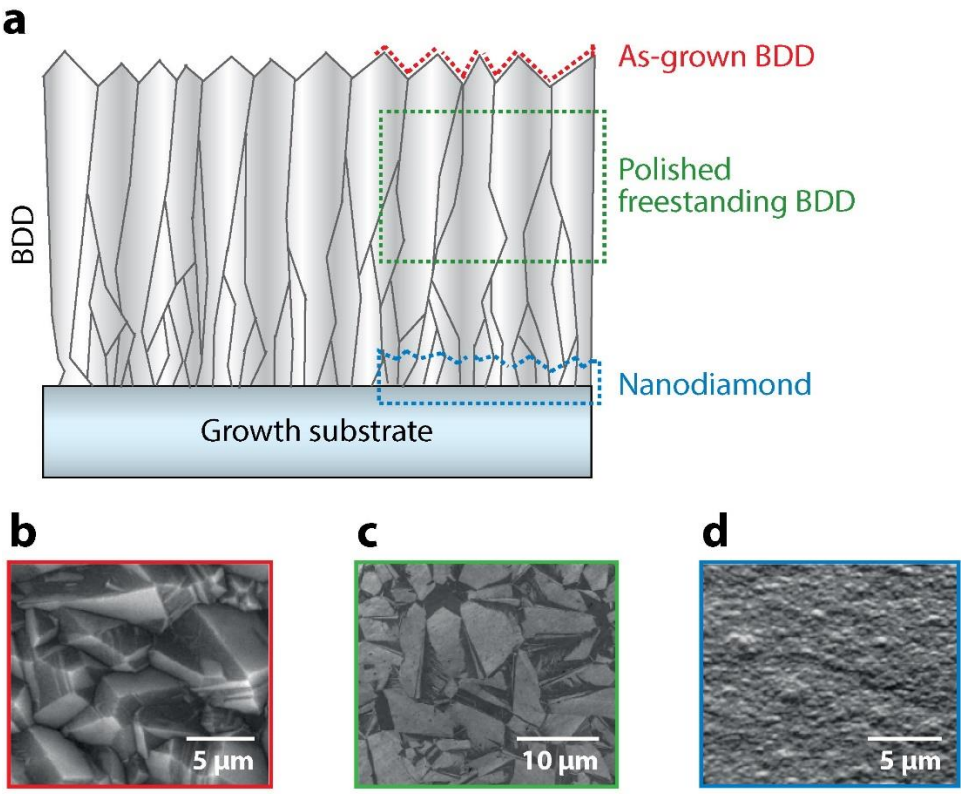

Figure 1.14:(a) Schematic of BDD grains grown on a substrate. Thick as-grown microcrystalline BDD (red, b) has a rough surface finish with different crystal faces exposed. This material can be polished (green, c) to give a smooth (sub-nm) surface roughness and be removed from the growth substrate. If short growth times are used, the material is nanocrystalline (blue,d) and cannot be removed from the growth substrate. SEM images adapted with permission from J. Phys. Chem. C, 2008,112,1232–1244.[127] Figure reproduced from Annu. Rev. Anal. Chem, 11:463-84.[126]

1.6.2 Electrochemical properties of BDD

Use of highly doped "black" BDD for electrochemical sensor applications is increasing in popularity due to the advantageous properties of BDD compared to other electrode materials including: a wide solvent window; resistance to chemical and mechanical wear; low background currents and low electrochemical fouling.[128–132] For this reason BDD has found many applications in electrochemistry.[131,133–139]

BDD has been shown to have a dopant dependence on the heterogeneous ET rates of outer sphere redox couples.[13] Note an outer sphere redox reaction only requires proximity of the analyte to the electrode surface for interactions to occur.[22] When doped to semiconducting levels the material exhibits lower capacitances and larger solvent windows, however due to the p-type nature of the doping the smaller number

of charge carriers at negative potentials results in sluggish electron transfer kinetics for redox couples in the bandgap (such as $Ru(NH_3)_6^{3+/2+}$). Even on metallically doped material the doping level affects the ET kinetics, due to the low local density of states in the material.[140] The density of states was measured to be on the order of 10^{20} cm^{-3} eV^{-1} in comparison to metals that are on the order of 10^{23} cm^{-3} eV^{-1}.[141] It is this low density of states that is responsible for some of BDDs unique electrochemical properties.

A pure sp^3 surface shows very little catalytic activity towards inner-sphere ET processes; i.e. where the analyte (or intermediate) must adsorb to the electrode surface in order for a redox event to occur.[22] For most inner sphere redox couples, ET is strongly retarded on BDD and occurs either significantly shifted compared to E^0 or doesn't occur at all within the solvent window e.g. as for the ORR on sp^2 free-BDD in aqueous solution.[142]. This is attributed to the lack of catalytically active sites on the surface for inner sphere electron transfer. This hinders water electrolysis due to a lack of binding sites to mediate electron transfer, and also pushes ORR to very negative potentials (very close to the reduction of water). This leads to the material's wide solvent window. The low density of states and lack of available catalytic surface sites lead to the observed rates of electron transfer and the chemical stability of the sp^3 diamond surface. Both are also responsible for the low capacitance values seen on BDD.

1.7 Surface termination of BDD

The electrochemistry of diamond is extremely dependant on the surface termination of the material, as it is at this interface that reactions occur. As such the nature of that surface is of the utmost importance. The bulk doping properties of diamond have a minimal effect on the diamond surface, as such studies on undoped material can provide useful information on the BDD surface. However, the conductive nature of the material opens up surface treatments that are not possible on undoped material.

1.7.1 Hydrogen termination

The as grown surface of CVD diamond has a hydrogen termination,[143] this is due to the large amounts of hydrogen present in the feed gases for diamond growth. However in air, the surface is slowly oxidised, leading to a degradation in the properties of the

surface, the same is also thought to be true if an oxidative potential is applied to the surface.

Hydrogen terminated surfaces exhibit a property known as negative electron affinity,[144–146] where the conduction band is located above the vacuum level. This property is of great interest as it has a large number of applications in thermionic emitters,[145,147,148] electrochemistry[149] and high power applications. This property of the surface can be measured using ultraviolet photoelectron spectroscopy. These surfaces also exhibit a surface conductivity in atmosphere through surface transfer doping.[150–152] The large surface dipole from the C-H bonds perpendicular to the surface leads to an electrostatic potential step, raising the energy levels at the surface and placing them at a mildly acidic chemical potential. This acidic chemical potential leads to the production of HCO_3^- and H_3O^+ from atmospheric H_2O and CO_2, which are physisorbed onto the surface.[151,152] The presence of these ions on the electrode surface gives rise to surface conductivity.

A hydrogen terminated surface can be generated by a number of methods including a hydrogen plasma,[153–157] cathodic treatment in acid[137,158–160] or high temperature annealing in the presence of hydrogen.[161,162] Hydrogen plasma treatment is generally considered to provide the best hydrogen terminated surface, with cathodic treatments being used widely due to the ease of application. However, there is debate as to the quality of the surface following these treatments in particular with respect to how closely it replicates the as grown hydrogen terminated surface from CVD.

Common cathodic treatments for hydrogen termination use ~-3 V vs Ag/AgCl in 0.5 M H_2SO_4[137,158,159] and are thought only to be successful due to an enhanced electrochemical response after treatment for particular analytes,[159] as would be expected of a hydrogen terminated surface. However, there is no direct comparison of these surfaces to plasma hydrogen terminated surfaces using techniques such as X-ray Photoelectron Spectroscopy (XPS). Hoffman *et al*. demonstrated that a harsher anodic treatment using -35 V vs Ag/AgCl could produce a hydrogen terminated surface that was similar to a hydrogen plasma treated surface, as demonstrated by XPS and contact angle measurements.[160]

Annealing at >800 ^oC in the presence of hydrogen can also be used to hydrogen terminate the diamond surface (Figure 1.15).[161] This has been shown to be a thermal

process with the removal of oxygen containing species forming part of the mechanism. There is some evidence that the mechanism progresses via hydroxyl groups as appropriate peaks were observed in the FTIR spectra of the sample when annealed at lower temperatures[161]

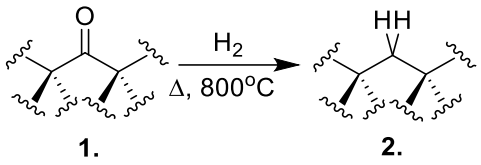

Figure 1.15: Hydrogen termination from oxygen terminated diamond

It was also found that the C-H bonds present on the diamond surface were all sp^3 hybridised as opposed to sp^2 hybridised, suggesting the anneal had not graphitised the surface and just hydrogenated it.[162] The surface was found to have a comparatively larger symmetric than anti-symmetric stretch in photoacoustic spectroscopy, which suggests a highly orientated surface as would be expected.[162] A randomly orientated material would have equal sized symmetric and anti-symmetric stretches.

1.7.2 Oxygen termination of diamond

Oxygen termination of diamond is comparatively easier compared to hydrogen termination with a large number of treatments available to generate oxygen terminated surfaces including: oxygen plasma treatments,[163–166] high temperature annealing in oxygen,[167] boiling in acid,[168,169] alumina polishing,[13] photochemical oxidation[143] and anodic polarization.[132,163–165] Oxygen termination produces a range of different oxygen containing functional groups[163,165,166,168,170–175] including but not limited to: hydroxyl (C-OH),[163,176] ether (C-O-C),[163–165,170,173,175] carbonyl (>C=O)[153,161,163–165,175] and carboxylic acid (COOH).[168,174] Polycrystalline samples containing a range of groups as expected of a sample that consists of a mixture of crystal faces.[163,164]

Single crystal diamond (100) surfaces have been shown to predominantly have C-O-C and C=O terminations, the ratio of which depends on the treatment used. Oxygen plasma treatment has been shown to give largely ether terminated surfaces with only a very small C=O component,[163,165] whereas anodic polarization has been shown to give a higher proportion of reactive >C=O groups although C-O-C groups still dominate. This is important as certain functional groups can be desirable for post-functionalization, for example Notsu *et al.* reported the use of surface C=O groups to

attach dinitrophenylhydrazine to the diamond surface.[164] It must also be taken into account that some C=O groups on the plasma treated surface may not have been reactive and not detected, due to disorder introduced by the etching effects of the plasma.

Anodic polymerisation was shown to give a higher proportion of C-OH groups on polycrystalline samples compared to plasma and UV photochemical treatments.[163] In addition, when anodic polarization in acid was carried out COOH groups[174] were seen in the XPS. Boiling in acid has also been shown to introduce a comparatively high proportion of COOH groups (9.2 and 4.7 %) on the (100) and (111) surfaces respectively.[168] C-OH groups have been shown to be the most common on (111) surfaces.[176] On annealing a 2×1 reconstruction occurs, leading to a much higher proportion of C=O groups observed in XPS.

1.8 Measuring defect and dopant density in BDD

1.8.1 Raman spectroscopy of heavily boron doped diamond

Raman spectroscopy is a powerful technique for probing diamond, due to its relatively large raman scattering cross section and the ability to relate peaks directly to defects in the lattice. The zero phonon line of pure diamond is located at 1332 cm^{-1}, however there are a large number of circumstances under which this can shift.[177] These shifts can be related to physical properties in the diamond such as stress, strain and doping density. Generally only the Brillouin zone centre line is observed (1332 cm^{-1}) in the first order raman spectrum of diamond. The raman active phonon in diamond corresponds to the two interpenetrating cubic sub-lattices of diamond vibrating against each other.[177]

In heavily doped diamond the 1332 cm^{-1} shifts to lower wavenumbers and decreases in intensity. The shift of this peak can be used to determine doping density, however this peak also shifts due to stress in the diamond and as such can be difficult to deconvolute to give an accurate doping density.[178] Heavily BDD also possesses a peak in the region 450-550 cm^{-1} that appears when boron is introduced into the diamond lattice. It has been shown to be possible to fit this peak with a Gaussian and Lorentzian component,[179] where the position (x_l) of the Lorentzian component has been shown to have a direct empirical relationship with the boron concentration (Equation 1.17).

$$[B]\ cm^{-3} = 8.44 \times 10^{30} e^{-0.048 x_l} \qquad [1.17]$$

1.8.2 Electrochemical assessment of BDD dopant density

Electrochemical assessment is particularly useful. If the material contains sufficient available charge carriers to show metal-like characteristics, electrochemical reversibility (diffusion-limited), with a fast ET outer sphere redox couple,[14] will be seen. $Ru(NH_3)_6^{3+/2+}$ is particularly useful as the redox couple as its E^0 lies just within the bandgap of semi-conducting BDD.[13] As semi-conducting BDD has insufficient charge carriers available to maintain electrochemical reversibility, the resulting CV for $Ru(NH_3)_6^{3+/2+}$ shows increased peak to peak separations, >> 59 mV (at 25 ^oC), compared to the reversible case.[128]. Note, it is important to carry out this assessment with an oxygen (O-) terminated surface.

Spatially mapping boron dopant density is also important as with polycrystalline material or defected single crystal electrodes, the different crystallographic orientations take up boron differently; the (111) orientation incorporates approximately 10× more than the (100) orientation. Scanning electrochemical microscopy has been elegantly used to map boron concentration variations qualitatively[128] by correlating the grain dependent (or defect dependent) boron dopant concentration to the ET kinetic rate constant for OS redox couples.[140,180].

1.9 sp^2 carbon in BDD

sp^2 presence at the surface of a BDD electrode can enhance the electrocatalytic activity of the electrode.[181] An ORR signal is now clearly observable. sp^2 presence also causes an increase in background currents (capacitance) and decreasing SW, due to water hydrolysis being facilitated more favourably at the catalytic sp^2 sites.[13,182] Interestingly, for a long time the presence of sp^2 in the sp^3-BDD was long considered problematic.[183] However, it is not until more recently that work has explored the positive impact sp^2 content may have on specific electroanalytical applications[14,142,181] that require a more catalytically active surface.

1.9.1 Measuring the sp^2 content of BDD

Traditionally in the diamond community, Raman spectroscopy is used to assess sp^2 content in BDD, often by comparing the ratio of the sp^3 (1332 cm^{-1}) peak to the G (1580 cm^{-1}) peak.[184] This method is however qualitative,[185] works best when comparing electrodes of the same dopant density and samples only a small area with one measurement (~μm^2 – tens of μm^2 depending on magnification) which is

especially problematic when the sp^2 content is spatially heterogeneous,[14] The biggest problem however, is that the Raman laser penetrates up to several microns[186] into the surface and is therefore not surface sensitive to sp^2; information on surface sp^2 content is essential to the electrochemist. To this end X-ray photoelectron spectroscopy has been explored, but the method is relatively expensive, time-consuming and requires trained operators. It can also be difficult to resolve the sp^2 and sp^3 signatures, and peak deconvolution is required, leading to variations in peak assignments throughout the literature.[187–189]

1.9.2 Sp^2 carbon in BDD to intentionally increase the electrocatalytic activity

The pursuit of high quality BDD electrodes has driven the synthesis of minimal sp^2 content films for electroanalytical applications for low limit of detection measurements. However, the lack of catalytic activity means the material is not suitable for all applications, and therefore there has been considerable interest in finding methods to increase the catalytic activity of BDD, whilst maintaining as many of the favorable properties of material as possible. Common approaches to this problem have been electrodeposition or ion implantation of nanoparticles (NPs)[190,191] and more recently intentional sp^2 incorporation.[19,181]

For electrodes which require the deliberate inclusion of sp^2 content into the surface, growth conditions can be controlled[192], to qualitatively vary sp^2 content. Growth, however, does not enable sufficient spatial control over sp^2 content,[193] which is often required to fully optimise the electrode performance properties and maintain reproducibility. Very recent work has shown, ~ micron resolution control over sp^2 surface content using a 3D positionable laser to locally graphitise regions of the surface. [18,19]

Further improvements in resolution, using this methodology, can be made through the use of adaptive optics to reduce spot size in combination with ultrashort laser pulses, to facilitate 3D writing of structures on and within the diamond.[194] In this way graphitic sub-micron diameter wires,[194] have been formed, which run all the way through insulating diamond; although these latter structures have not yet been investigated electrochemically. In alternative work, a deep beam ion lithography approach has been employed, which uses a focused 1.2 MeV helium ion beam, to create highly damaged sub-superficial structures that after subsequent annealing form

graphitic structures within the diamond. The structures emerge at the surface of the diamond and in this way, a graphitic MEA (sixteen electrodes in single crystal diamond) could be fabricated for proposed neurotransmitter detection experiments.[195]

An application where the introduction of sp^2 carbon into BDD has been utilised is neural stimulation, as a large potential window and capacitance are required to pass large amounts of charge for stimulation. BDD has not traditionally been associated with neural stimulation, due to its inherently low capacitance, however, by engineering the diamond properties accordingly the material can be used for this application. Very heavily doped BDD ([B]= 5.5×10^{21} cm^{-3}) has been shown to exhibit high capacitance,[196] due most likely to the large amount of boron leading to the creation of sp^2 carbon defect sites, naturally raising the capacitance. The deliberate inclusion of large amounts of sp^2 carbon into nanocrystalline diamond films, through the inclusion of nitrogen in the growth mixture, has led to conductive materials with extremely high capacitances. This material has been used in the fabrication of MEAs for retinal stimulation implants,[8] incorporating 256 independently controlled electrodes, as has exceedingly high surface area BDD[197]. As a proof of concept diamond has also been deposited onto flexible polyimide based 3D retinal implants[198].

1.10 Processing of diamond wafers

There are two main methods to process diamond into structures for devices: (i) laser micromachining and (ii) etching. This thesis will focus on the former.

Laser machining of materials is most often employed in conjunction with metals and ceramics[199] by an ablation mechanism with localised heating leading to material removal. Lasers used for machining are either continuous wave systems, which benefit from high average power for fast machining or pulsed laser systems which generally have lower average powers but high peak powers allowing for the machining of thicker and more challenging materials.[200–202] Laser micromachining offers significant advantages for the machining of diamond due to its direct write, single step processing procedures that can machine structures to depths of millimetres.[203]

Insulating diamond is transparent in the visible region with an absorption threshold of 225 nm, therefore it is commonly proposed that diamond is machined by wavelengths longer than the absorption threshold using the ‘graphitic piston’ model,[204] where the diamond is graphitised due to the first laser pulses and then runaway absorption by the

graphite leads to ablation. The process is then repeated. Laser micromachining thus has drawbacks in terms of the quality of the surfaces remaining, as a mixed sp^3/sp^2 surface is created with modified local properties from thermal damage.[205,206] Interestingly, fs laser machining on metals has been shown to produce cleaner holes with less recast due to a smaller heat affected zone, as the absorption occurs on a shorter timescale meaning electron-lattice coupling can be neglected.[207] Femtosecond laser micromachining has been used on diamond for machining.[208–213] Note, most work that has been conducted using laser micromachining on diamond has been using transparent insulating diamond.[210,212,214–219] This has very different absorption properties to "black" BDD, thus doping with boron is likely to affect how the material machines (ablates).

For many applications the BDD needs to be machined into the correct electrode geometry [129,131,227,228,139,220–226] for example, for the production of macroelectrodes,[220–222] microelectrode arrays,[131,220,222–227] tubular flow devices,[228] microelectromechanical devices,[229–231] microfluidics[139,213] and periodic bulb and tube structures.[129] To date, there has been very little research into the impact of possible surface modifications made by the laser on the electrochemical properties and there is very little literature discussing the mechanism of laser machining on boron doped diamond.

1.11 Electrode Geometry

With any electrode material, the ease at which the geometry and scale of the electrode can be manipulated the wider the range of possible applications. Most research based applications use macro-scale thin film electrodes where the electrode is created by e.g. isolating the required electrode geometry using a clamp cell[232] or Kapton tape.[18,193] Thicker, freestanding material, which has been removed from the growth wafer, offers the option of being laser micromachined into a cylinder and then sealed in glass[233], Teflon or epoxy[234] to create a co-planar disc electrode. For some applications, in particular where high quality and robust commercial electrodes are desired inferior sealing insulators are not sufficient, and electrically insulating diamond has been employed instead.[131,227]

1.12 Aims and Objectives

Advances in the synthesis of BDD coupled with innovations in post-growth processing and structuring has been driven by electrochemical applications that make use of the key properties of BDD. This has impacted significantly in many areas, for example, in the biological field for example with the production of multi array implantable electrodes; in the sensing area with deliberate incorporation of controllable catalytic sp^2 sites into the electrode surface and for energy storage, high surface area supercapacitors. Given the intrinsic link between the surface properties of the BDD and the ET capabilities of the material, improvements in BDD material characterization methodology are required which directly benefit the electrochemist, and in Chapter 3 the development of an electrochemical methodology to provide information on sp^2 surface content in BDD electrodes is discussed.

The local graphitization of a pristine sp^3 BDD electrode with a pattern of graphitic spots (50 μm in diameter) using laser micromachining, was previously introduced[19] as a means of producing a very stable, voltammetric pH sensor, which survives even after placement in boiling acid solutions. The sp^2 regions of the BDD surface contain pH responsive quinone groups which shift position in a Nernstian fashion with pH in buffered solutions.[19] Importantly these groups respond only to protons and in this way, the electrode shows proton selectivity even in complex media. Chapter 4 looks to gain a deeper understanding of the PCET process for surface integrated quinone groups on sp^2-BDD and how Γ (controllable using the laser micromachinery) impacts the performance of the pH electrode under the significantly more challenging unbuffered solution conditions. Both cyclic and square wave voltammetric techniques are explored and their impact on the measurement discussed. This is with the aim of producing an electrode which functions in a Nernstian fashion for pH detection across the pH range 4-10. In Chapter 5 this work is further developed by exploring the potential of sp^2-BDD electrodes to catalytically detect dissolved oxygen, via ORR, and in one scan provide simultaneous oxygen and pH sensing capabilities.

Finally in Chapter 6 the use of square wave voltammetry to provide additional electrochemical information is explored particularly in the non-faradaic window of the voltammogram, where we show additional analytical signatures such as the electrode capacitance, uncompensated resistance and solution conductivity can be extracted

from the measurement (Chapter 6) through the capture of the entire current-time response.

The electrochemical possibilities revealed through the use of BDD electrodes is an area which continues to grow and truly highlights BDD as an electrode material that can be specifically tailored for the application of interest.

1.13 References

(1) Balmer, R. S.; Brandon, J. R.; Clewes, S. L.; Dhillon, H. K.; Dodson, J. M.; Friel, I.; Inglis, P. N.; Madgwick, T. D.; Markham, M. L.; Mollart, T. P.; Perkins, N.; Scarsbrook, G. A.; Twitchen, D. J.; Whitehead, A. J.; Wilman, J. J.; Woollard, S. M. Chemical Vapour Deposition Synthetic Diamond: Materials, Technology and Applications. *J. Physics-Condensed Matter* **2009**, *21* (36). https://doi.org/10.1088/0953-8984/21/36/364221.

(2) Kraft, A. Doped Diamond: A Compact Review on a New, Versatile Electrode Material - Open Access Library. *Int. J. Electrochem. Sci.* **2007**, *2*, 355–385. https://doi.org/10.1021/jo026183k.

(3) Gicquel, A.; Hassouni, K.; Silva, F.; Achard, J. CVD Diamond Films: From Growth to Applications. *Curr. Appl. Phys.* **2001**, *1*, 479–496.

(4) Adam, W.; Bauer, C.; Berdermann, E.; Bergonzo, P.; Bogani, F.; Borchi, E.; Brambilla, A.; Bruzzi, M.; Colledani, C.; Conway, J.; et al. Review of the Development of Diamond Radiation Sensors. *Nucl. Instruments Methods Phys. Res. Sect. A Accel. Spectrometers, Detect. Assoc. Equip.* **1999**, *434* (1), 131–145. https://doi.org/10.1016/S0168-9002(99)00447-7.

(5) Shimaoka, T.; Kaneko, J. H.; Tsubota, M.; Shimmyo, H.; Watanabe, H.; Chayahara, A.; Umezawa, H.; Shikata, S. I. High-Performance Diamond Radiation Detectors Produced by Lift-off Method. *EPL* **2016**, *113* (6), 62001. https://doi.org/10.1209/0295-5075/113/62001.

(6) Woerner, E.; Wild, C.; Mueller-Sebert, W.; Koidl, P. CVD-Diamond Optical Lenses. *Diam. Relat. Mater.* **2001**, *10* (3–7), 557–560. https://doi.org/10.1016/S0925-9635(00)00393-9.

(7) Shvyd'ko, Y. V; Stoupin, S.; Cunsolo, A.; Said, A. H.; Huang, X. High-Reflectivity High-Resolution X-Ray Crystal Optics with Diamonds. *Nat. Phys.* **2010**, *6* (3), 196–199. https://doi.org/10.1038/nphys1506.

(8) Ganesan, K.; Garrett, D. J.; Ahnood, A.; Shivdasani, M. N.; Tong, W.; Turnley, A. M.; Fox, K.; Meffin, H.; Prawer, S. An All-Diamond, Hermetic Electrical Feedthrough Array for a Retinal Prosthesis. *Biomaterials* **2014**, *35* (3), 908–915. https://doi.org/10.1016/j.biomaterials.2013.10.040.

(9) Bergonzo, P.; Bongrain, A.; Scorsone, E.; Bendali, A.; Rousseau, L.; Lissorgues, G.; Mailley, P.; Li, Y.; Kauffmann, T.; Goy, F.; Yvert, B.; Sahel, J. A.; Picaud, S. 3D Shaped Mechanically Flexible Diamond Microelectrode Arrays for Eye Implant Applications: The MEDINAS Project. *Irbm* **2011**, *32* (2), 91–94. https://doi.org/10.1016/j.irbm.2011.01.032.

(10) Lagrange, J.-P.; Deneuville, A.; Gheeraert, E. Activation Energy in Low Compensated Homoepitaxial Boron-Doped Diamond Films. *Diam. Relat. Mater.* **1998**, *7* (9), 1390–1393. https://doi.org/10.1016/S0925-9635(98)00225-8.

(11) Williams, a W. S.; Lightowlers, E. C.; Collins, a T. Impurity Conduction in Synthetic Semiconducting Diamond. *J. Phys. C Solid State Phys.* **2001**, *3* (8), 1727–1735. https://doi.org/10.1088/0022-3719/3/8/011.

(12) Macpherson, J. V. The Use of Conducting Diamond in Electrochemistry. In *Electrochemistry at carbon electrodes*; 2015; Vol. 16, pp 163–210. https://doi.org/10.1002/9783527697489.ch5.

(13) Hutton, L. A.; Iacobini, J. G.; Bitziou, E.; Channon, R. B.; Newton, M. E.; Macpherson, J. V. Examination of the Factors Affecting the Electrochemical Performance of Oxygen-Terminated Polycrystalline Boron-Doped Diamond Electrodes. *Anal. Chem.* **2013**, *85* (15), 7230–7240. https://doi.org/10.1021/ac4010421.

(14) Macpherson, J. V. A Practical Guide to Using Boron Doped Diamond in Electrochemical Research. *Phys. Chem. Chem. Phys.* **2015**, *17* (5), 2935–2949. https://doi.org/10.1039/c4cp04022h.

(15) Shin, D.; Tryk, D. A.; Fujishima, A.; Merkoci, A.; Wang, J. Resistance to Surfactant and Protein Fouling Effects at Conducting Diamond Electrodes. *Electroanalysis* **2005**, *17* (4), 305–311. https://doi.org/10.1002/elan.200403104.

(16) Trouillon, R.; O'Hare, D. Comparison of Glassy Carbon and Boron Doped Diamond Electrodes: Resistance to Biofouling. *Electrochim. Acta* **2010**, *55* (22), 6586–6595. https://doi.org/10.1016/j.electacta.2010.06.016.

(17) May, P. W. Diamond Thin Films : A 21st-Century Material Author (s): Paul W . May Source : Philosophical Transactions : Mathematical , Physical and Engineering Sciences , Vol . 358 , No . 1766 , Science into the Next Millennium : Young Scientists Give Their Visions. **2000**, *358* (1766), 473–495.

(18) Ayres, Z. J.; Cobb, S. J.; Newton, M. E.; Macpherson, J. V. Quinone Electrochemistry for the Comparative Assessment of Sp2 Surface Content of Boron Doped Diamond Electrodes. *Electrochem. Commun.* **2016**, *72*, 59–63. https://doi.org/10.1016/j.elecom.2016.08.024.

(19) Ayres, Z. J.; Borrill, A. J.; Newland, J. C.; Newton, M. E.; Macpherson, J. V. Controlled Sp2 Functionalization of Boron Doped Diamond as a Route for the Fabrication of Robust and Nernstian PH Electrodes. *Anal. Chem.* **2016**, *88* (1), 974–980. https://doi.org/10.1021/acs.analchem.5b03732.

(20) Cobb, S. J.; Ayres, Z. J.; Newton, M. E.; Macpherson, J. V. Deconvoluting Surface-Bound Quinone Proton Coupled Electron Transfer in Unbuffered Solutions: Towards a Universal Voltammetric PH Electrode. *J. Am. Chem. Soc.* **2019**, *141* (2), 1035–1044. https://doi.org/10.1021/jacs.8b11518.

(21) Biesheuvel, P. M.; Dykstra, J. E. The Difference between Faradaic and Nonfaradaic Processes in Electrochemistry. **2018**, 1–10.

(22) Bard, A. J.; Faulkner, L. R. *Electrochemical Methods: Fundamentals and Applications*, 2nd ed.; Wiley: New York, 1980.

(23) Pandey, S. Analytical Applications of Room-Temperature Ionic Liquids: A Review of Recent Efforts. *Anal. Chim. Acta* **2006**, *556* (1), 38–45. https://doi.org/10.1016/j.aca.2005.06.038.

(24) Bilewicz, R.; Wikiel, K.; Osteryoung, R.; Osteryoung, J. General Equivalence of Linear Scan and Staircase Voltammetry: Experimental Results. *Anal. Chem.* **1989**, *61* (9), 965–972. https://doi.org/10.1021/ac00184a010.

(25) Kalousek, M. Processses at the Dropping Electrode with a Discontinuously Changing Potential. *Collect. Czech Chem. Commun* **1948**, *13*, 105–115.

(26) Ruić, I. On the Theory of Kalousek Commutator, Square-Wave and Related Techniques. I. Equations for Current-Potential Curves. *J. Electroanal. Chem.* **1972**, *39* (1), 111–122. https://doi.org/10.1016/S0022-0728(72)80480-7.

(27) Barker, G. C.; Gardner, A. W. Forty Years of Square-Wave Polarography. *Analyst* **1992**, *117*, 1811–1828. https://doi.org/10.1039/AN9921701811.

(28) Ramaley, L.; Krause, M. S. Theory of Square Wave Voltammetry. *Anal. Chem.* **1969**, *41* (11), 1362–1365. https://doi.org/10.1021/ac60280a005.

(29) Krause Jr, M. S.; Ramaley, L. Analytical Application of Square Wave Voltammetry. **1969**, *41* (11), 1365–1369. https://doi.org/10.1021/ac60280a008.

(30) Christie, J. H.; Turner, J. A.; Osteryoung, R. A. Square Wave Voltammetry at the Dropping Mercury Electrode: Theory. *Anal. Chem.* **1977**, *49* (13), 1899–1903. https://doi.org/10.1021/ac50021a008.

(31) Mirceski, V.; Komorsky-Lovric, S.; Lovric, M. *Square Wave Voltammetry: Theory and Application*; Berlin; Heidelberg, 2007. https://doi.org/10.1007/978-3-540-73740-7.

(32) Osteryoung, J. G.; O'Dea, J. J. Square-Wave Voltammetry. In *Electroanalytical Chemistry*; Bard, A. J., Ed.; Marcel-Dekker: New York, 1986; p 209.

(33) Aoki, K.; Maeda, K.; Osteryoung, J. Characterization of Nernstian Square-Wave Voltammograms. *J. Electroanal. Chem.* **1989**, *272* (1–2), 17–28. https://doi.org/10.1016/0022-0728(89)87065-2.

(34) Zachowski, E. J.; Wojciechowski, M.; Osteryoung, J. The Analytical Application of Square-Wave Voltammetry. *Anal. Chim. Acta* **1986**, *183* (C), 47–57. https://doi.org/10.1016/0003-2670(86)80073-3.

(35) Lovric, M. Current Sampling in Square-Wave Voltammetry. *Ann. Chim.* **1994**, *84* (7), 379–382.

(36) IUPAC. Compendium of Chemical Terminology. *Gold Book*. 2nd ed. Blackwell Scientific Publications: Oxford 2006.

(37) Fieser, L. F. The Tautomerism of Hydroxy Quinones. *J. Am. Chem. Soc.* **1928**, *50* (2), 439–465. https://doi.org/10.1021/ja01389a033.

(38) Nohl, H.; Jordan, W.; Youngman, R. J. Quinones in Biology: Functions in Electron Transfer and Oxygen Activation. *Adv. Free Radic. Biol. Med.* **1986**, *2* (1), 211–279. https://doi.org/10.1016/S8755-9668(86)80030-8.

(39) Søballe, B.; Poole, R. K. Microbial Ubiquinones: Multiple Roles in Respiration, Gene Regulation and Oxidative Stress Management. *Microbiology* **1999**, *145* (8), 1817–1830. https://doi.org/10.1099/13500872-145-8-1817.

(40) Powis, G. Free Radical Formation by Antitumor Quinones. *Free Radic. Biol. Med.* **1989**, *6* (1), 63–101. https://doi.org/10.1016/0891-5849(89)90162-7.

(41) Goor, G.; Kunkel, W.; Weiberg, O. Ullmann's Encyclopedia of Industrial Chemistry, Vol. A13. In *Ullmann's Encyclopedia of Industrial Chemistry, Vol. A13*; Elvers, B., Hawkins, S., Ravenscroft, M., Schulz, G., Eds.; VCH: Weinheim, 1989; pp 443–466.

(42) Lin, K.; Chen, Q.; Gerhardt, M. R.; Tong, L.; Kim, S. B.; Eisenach, L.; Valle, A. W.; Hardee, D.; Gordon, R. G.; Aziz, M. J.; Marshak, M. P.; Bok, S. Alkaline Quinone Flow Battery. *Science* **2015**, *349* (6255), 1529–1532. https://doi.org/10.1126/science.aab3033.

(43) Campos-Martin, J. M.; Blanco-Brieva, G.; Fierro, J. L. G. Hydrogen Peroxide Synthesis: An Outlook beyond the Anthraquinone Process. *Angew. Chemie - Int. Ed.* **2006**, *45* (42), 6962–6984. https://doi.org/10.1002/anie.200503779.

(44) Kahlert, H. Functionalized Carbon Electrodes for PH Determination. *J. Solid State Electrochem.* **2008**, *12* (10), 1255–1266. https://doi.org/10.1007/s10008-008-0566-7.

(45) Jacq, J. Schema Carre. *J. Electroanal. Chem. Interfacial Electrochem.* **1971**, *29* (1), 149–180. https://doi.org/10.1016/S0022-0728(71)80080-3.

(46) Laviron, E. Electrochemical Reactions with Protonations at Equilibrium. *J. Electroanal. Chem. Interfacial Electrochem.* **1983**, *146* (1), 15–36. https://doi.org/10.1016/S0022-0728(83)80110-7.

(47) Guin, P. S.; Das, S.; Mandal, P. C. Electrochemical Reduction of Quinones in Different Media: A Review. *Int. J. Electrochem.* **2011**, *2011*, 1–22. https://doi.org/10.4061/2011/816202.

(48) Gupta, N.; Linschitz, H. Hydrogen-Bonding and Protonation Effects in Electrochemistry of Quinones in Aprotic Solvents. *J. Am. Chem. Soc.* **1997**, *119* (27), 6384–6391. https://doi.org/10.1021/ja970028j.

(49) Mastragostino, M.; Nadjo, L.; Saveant, J. M. Disproportionation and ECE Mechanisms-I. Theoretical Analysis. Relationships for Linear Sweep Voltammetry. *Electrochim. Acta* **1968**, *13* (4), 721–749. https://doi.org/10.1016/0013-4686(68)85007-8.

(50) Sandona, G.; Amatore, C.; Vianello, E.; Severin, M. G.; Capobianco, G.; Saveant, J. M.; Farnia, G. Kinetics and Mechanism of Self-Protonation Reactions in Organic Electrochemical Processes. *J. Am. Chem. Soc.* **1985**, *107* (7), 1815–1824. https://doi.org/10.1021/ja00293a003.

(51) Bailey, S. I.; Ritchie, I. M. A Cyclic Voltammetric Study of the Aqueous Electrochemistry of Some Quinones. *Electrochim. Acta* **1985**, *30* (1), 3–12. https://doi.org/10.1016/0013-4686(85)80051-7.

(52) He, P.; Crooks, R. M.; Faulkner, L. R. Adsorption and Electrode Reactions of Disulfonated Anthraquinones at Mercury Electrodes. *J. Phys. Chem.* **1990**, *94* (3), 1135–1141. https://doi.org/10.1021/j100366a023.

(53) Howell Furman, N.; Stone, K. G. A Polarographic Study of Certain Anthraquinones. *J. Am. Chem. Soc.* **1948**, *70* (9), 3055–3061. https://doi.org/10.1021/ja01189a064.

(54) Bishop, C. A.; Tong, L. K. J. Equilibria of Substituted Semiquinones at High PH. *J. Am. Chem. Soc.* **1965**, *87* (3), 501–505. https://doi.org/10.1021/ja01081a018.

(55) Gill, R.; Stonehill, H. I. A Polarographic Investigation of the Tautomerism of 2-Hydroxy- and 2:6-Dihydroxy-Anthraquinol. *J. Chem. Soc.* **1952**, *341*, 1857–1863.

(56) Quan, M.; Sanchez, D.; Wasylkiw, M. F.; Smith, D. K. Voltammetry of Quinones in Unbuffered Aqueous Solution. *J. Am. Chem. Soc.* **2007**, *129* (8), 12847–12856. https://doi.org/10.1021/ja0743083.

(57) Müller, O. H. Oxidation-Reduction Potentials Measured with the Dropping Mercury Electrode. III. Polarographic Study of Quinhydrone in Buffered and Unbuffered Solutions. *J. Am. Chem. Soc.* **1940**, *62* (9), 2434–2441. https://doi.org/10.1021/ja01866a048.

(58) Kolthoff, I. M.; Orlemann, E. F. The Use of the Dropping Mercury Electrode as an Indicator Electrode in Poorly Poised Systems. *J. Am. Chem. Soc.* **1941**, *63* (3), 664–667. https://doi.org/10.1021/ja01848a009.

(59) Robertson, R. T.; Pendley, B. D. Microelectrodes as Probes in Low Electrolyte Solutions: The Reduction of Quinone in Aqueous Sulfuric Acid Solution. *J. Electroanal. Chem.* **1994**, *374* (1–2), 173–177. https://doi.org/10.1016/0022-0728(94)03335-8.

(60) Sato, Y.; Fujita, M.; Mizutani, F.; Uosaki, K. Electrochemical Properties of the 2-Mercaptohydroquinone Monolayer on a Gold Electrode. Effect of Solution PH,

Adsorption Time and Concentration of the Modifying Solution. *J. Electroanal. Chem.* **1996**, *409* (1–2), 145–154. https://doi.org/10.1016/0022-0728(95)04421-3.

(61) Tang, Y.; Wu, Y.; Wang, Z. Spectroelectrochemistry for Electroreduction of P-Benzoquinone in Unbuffered Aqueous Solution. *J. Electrochem. Soc.* **2001**, *148* (4), E133. https://doi.org/10.1149/1.1353575.

(62) Forster, R. J.; O'Kelly, J. P. Protonation Reactions of Anthraquinone-2,7-Disulphonic Acid in Solution and within Monolayers. *J. Electroanal. Chem.* **2001**, *498* (1–2), 127–135. https://doi.org/10.1016/S0022-0728(00)00331-4.

(63) Batchelor-Mcauley, C.; Kozub, B. R.; Menshykau, D.; Compton, R. G. Voltammetric Responses of Surface-Bound and Solution-Phase Anthraquinone Moieties in the Presence of Unbuffered Aqueous Media. *J. Phys. Chem. C* **2011**, *115* (3), 714–718. https://doi.org/10.1021/jp1096585.

(64) Abbott, J. C.; Collat, J. W. Indirect Polarographic Determination of Acids. *Anal. Chem.* **1963**, *35* (7), 859–863. https://doi.org/10.1021/ac60200a028.

(65) Menshykau, D.; Batchelor-Mcauley, C.; Compton, R. G. Voltammetry of Surface-Bound Species: Proton-Coupled Electrochemical Reduction. *J. Electroanal. Chem.* **2011**, *651* (2), 118–130. https://doi.org/10.1016/j.jelechem.2010.11.024.

(66) Shim, Y.-B.; Park, S.-M. Spectroelectrochemical Studies of P-Benzoquinone Reduction in Aqueous Media. *J. Electroanal. Chem.* **1997**, *425* (1–2), 201–207. https://doi.org/10.1016/S0022-0728(96)04956-X.

(67) Park, H.; Won, M.; Cheong, C.; Shim, Y. In-Situ ESR Detection of Radical Species of p -Benzoquinone in Aqueous Media. *Electroanalysis* **2002**, *14* (21), 1501–1507.

(68) Ricco, A. J.; Crooks, R. M.; Kim, T.; Yang, H. C.; Dermody, D. L.; Wells, M. Interactions between Organized, Surface-Confined Monolayers and Vapor-Phase Probe Molecules. 9. Structure/Reactivity Relationship between Three Surface-Confined Isomers of Mercaptobenzoic Acid and Vapor-Phase Decylamine. *Langmuir* **1996**, *12* (8), 1989–1996. https://doi.org/10.1021/la9507951.

(69) Himmel, H. J.; Terfort, A.; Arnold, R.; Wöll, C. Chemical Properties of Hydrogen-Bonded Organic Bilayers Fabricated via Self-Assembly of COOH-Functionalised Oligophenylthiols on Au Substrates. *Mater. Sci. Eng. C* **1999**, *8–9*, 431–435. https://doi.org/10.1016/S0928-4931(99)00044-2.

(70) Forster, R. J.; Faulkner, L. R. Interfacial Field Effects on Reductive Chloride Elimination from Spontaneously Adsorbed Monolayers. *Langmuir* **1995**, *11* (3), 1014–1023. https://doi.org/10.1021/la00003a053.

(71) Leventis, H. C.; Streeter, I.; Wildgoose, G. G.; Lawrence, N. S.; Jiang, L.; Jones, T. G. .; Compton, R. G. Derivatised Carbon Powder Electrodes: Reagentless

PH Sensors. *Talanta* **2004**, *63* (4), 1039–1051. https://doi.org/10.1016/J.TALANTA.2004.01.017.

(72) Smalley, J. F. Indirect Laser-Induced Temperature Jump Study of the Chain-Length Dependence of the PKa's of ω-Mercaptoalkanoic Acid Monolayers Self-Assembled on Gold. *Langmuir* **2003**, *19* (22), 9284–9289. https://doi.org/10.1021/la0348968.

(73) Brown, A. P.; Koval, C. A.; Anson, F. C. Illustrative Electrochemical Behaviour of Reactants Irreversibly Adsorbed on Graphite Electrode Surfaces. *J. Electroanal. Chem.* **1976**, *72* (5340), 379–387.

(74) Gomathi, H.; Rao, G. P. Chemical and Electrochemical Modification of the Glassy. *J. Electroanal. Chem.* **1985**, *190*, 85–94.

(75) Zhang, J.; Anson, F. C. Voltammetry and In-Situ Fourier Transform IR Spectroscopy of Two Anthraquinone Disulfonates Adsorbed on Graphite Electrodes. *J. Electroanal. Chem.* **1992**, *331* (1–2), 945–957. https://doi.org/10.1016/0022-0728(92)85016-V.

(76) Larsen, A. G.; Gothelf, K. V. Electrochemical Properties of Mixed Self-Assembled Monolayers on Gold Electrodes Containing Mercaptooctylhydroquinone and Alkylthiols. *Langmuir* **2005**, *21* (3), 1015–1021. https://doi.org/10.1021/la048221w.

(77) Trammell, S. A.; Lowy, D. A.; Seferos, D. S.; Moore, M.; Bazan, G. C.; Lebedev, N. Heterogeneous Electron Transfer of Quinone-Hydroquinone in Alkaline Solutions at Gold Electrode Surfaces: Comparison of Saturated and Unsaturated Bridges. *J. Electroanal. Chem.* **2007**, *606* (1), 33–38. https://doi.org/10.1016/j.jelechem.2007.04.008.

(78) Darwish, N.; Eggers, P. K.; Ciampi, S.; Tong, Y.; Ye, S.; Paddon-Row, M. N.; Gooding, J. J. Probing the Effect of the Solution Environment around Redox-Active Moieties Using Rigid Anthraquinone Terminated Molecular Rulers. *J. Am. Chem. Soc.* **2012**, *134* (44), 18401–18409. https://doi.org/10.1021/ja307665k.

(79) Abhayawardhana, A. D.; Sutherland, T. C. Heterogeneous Proton-Coupled Electron Transfer of an Aminoanthraquinone Self-Assembled Monolayer. *J. Phys. Chem. C* **2009**, *113* (12), 4915–4924. https://doi.org/10.1021/jp807287p.

(80) Abhayawardhana, A. D.; Sutherland, T. C. Heterogeneous Proton-Coupled Electron Transfer of a Hydroxy-Anthraquinone Self-Assembled Monolayer. *J. Electroanal. Chem.* **2011**, *653* (1–2), 50–55. https://doi.org/10.1016/j.jelechem.2011.01.009.

(81) Nagata, M.; Kondo, M.; Suemori, Y.; Ochiai, T.; Dewa, T.; Ohtsuka, T.; Nango, M. Electron Transfer of Quinone Self-Assembled Monolayers on a Gold Electrode. *Colloids Surfaces B Biointerfaces* **2008**, *64* (1), 16–21. https://doi.org/10.1016/j.colsurfb.2007.12.017.

(82) Hong, H. G.; Park, W. Electrochemical Characteristics of Hydroquinone-Terminated Self-Assembled Monolayers on Gold. *Langmuir* **2001**, *17* (8), 2485–2492. https://doi.org/10.1021/la001466y.

(83) Kaifer, A. E.; Gomez-Kaifer, M. *Supramolecular Electrochemistry*; WILEY-VCH: Chichester, 1999.

(84) Laviron, E. Surface Linear Potential Sweep Voltammetry. Equation of the Peaks for a Reversible Reaction When Interactions between the Adsorbed Molecules Are Taken into Account. *J. Electroanal. Chem.* **1974**, *52* (3), 395–402. https://doi.org/10.1016/S0022-0728(74)80449-3.

(85) Chidsey, C. E. D.; Bertozzi, C. R.; Putvinski, T. M.; Mujsce, A. M. Coadsorption of Ferrocene-Terminated and Unsubstituted Alkanethiols on Gold: Electroactive Self-Assembled Monolayers. *J. Am. Chem. Soc.* **1990**, *112* (11), 4301–4306. https://doi.org/10.1021/ja00167a028.

(86) Häkkinen, H. The Gold-Sulfur Interface at the Nanoscale. *Nat. Chem.* **2012**, *4* (6), 443–455. https://doi.org/10.1038/nchem.1352.

(87) Phares, N.; White, R. J.; Plaxco, K. W. Improving the Stability and Sensing of Electrochemical Biosensors by Employing Trithiol-Anchoring Groups in a Six-Carbon Self-Assembled Monolayer. *Anal. Chem.* **2009**, *81* (3), 1095–1100. https://doi.org/10.1021/ac8021983.

(88) Streeter, I.; Leventis, H. C.; Wildgoose, G. G.; Pandurangappa, M.; Lawrence, N. S.; Jiang, L.; Jones, T. G. J.; Compton, R. G. A Sensitive Reagentless PH Probe with a ca. 120 MV/PH Unit Response. *J. Solid State Electrochem.* **2004**, *8* (10), 718–721. https://doi.org/10.1007/s10008-004-0536-7.

(89) Downard, A. J. Electrochemically Assisted Covalent Modification of Carbon Electrodes. *Electroanalysis* **2000**, *12* (14), 1085–1096. https://doi.org/10.1002/1521-4109(200010)12:14<1085::AID-ELAN1085>3.0.CO;2-A.

(90) Delamar, M.; Hitmi, R.; Pinson, J.; Savéant, J. Covalent Modification of Carbon Surfaces by Grafting of Functionalized Aryl Radicals Produced from Electrochemical Reduction of Diazonium Salts. *J. Am. Chem. Soc.* **1992**, *114* (14), 5883–5884. https://doi.org/10.1021/ja00040a074.

(91) Foord, J. S.; Hao, W.; Hurst, S. Studies of the Chemical Functionalisation of Diamond Electrodes. *Diam. Relat. Mater.* **2007**, *16* (4-7 SPEC. ISS.), 877–880. https://doi.org/10.1016/j.diamond.2007.01.011.

(92) Pandurangappa, M.; Lawrence, N. S.; Compton, R. G. Homogeneous Chemical Derivatisation of Carbon Particles: A Novel Method for Funtionalising Carbon Surfaces. *Analyst* **2002**, *127* (12), 1568–1571. https://doi.org/10.1039/b209711g.

(93) Wildgoose, G. G.; Pandurangappa, M.; Lawrence, N. S.; Jiang, L.; Jones, T. G. J.; Compton, R. G. Anthraquinone-Derivatised Carbon Powder: Reagentless Voltammetric PH Electrodes. *Talanta* **2003**, *60* (5), 887–893. https://doi.org/10.1016/S0039-9140(03)00150-4.

(94) Lawrence, N. S.; Pagels, M.; Hackett, S. F. J.; McCormack, S.; Meredith, A.; Jones, T. G. J.; Wildgoose, G. G.; Compton, R. G.; Jiang, L. Triple Component Carbon Epoxy PH Probe. *Electroanalysis* **2007**, *19* (4), 424–428. https://doi.org/10.1002/elan.200603725.

(95) Dai, C.; Song, P.; Wadhawan, J. D.; Fisher, A. C.; Lawrence, N. S. Screen Printed Alizarin-Based Carbon Electrodes: Monitoring PH in Unbuffered Media. *Electroanalysis* **2015**, *27* (4), 917–923. https://doi.org/10.1002/elan.201400704.

(96) Lu, M.; Compton, R. G. Voltammetric PH Sensor Based on an Edge Plane Pyrolytic Graphite Electrode. *Analyst* **2014**, *139* (10), 2397–2403. https://doi.org/10.1039/c4an00147h.

(97) Lu, M.; Compton, R. G. Voltammetric PH Sensing Using Carbon Electrodes: Glassy Carbon Behaves Similarly to EPPG. *Analyst* **2014**, *139* (18), 4599–4605. https://doi.org/10.1039/C4AN00866A.

(98) Masheter, A. T.; Abiman, P.; Wildgoose, G. G.; Wong, E.; Xiao, L.; Rees, N. V.; Taylor, R.; Attard, G. A.; Baron, R.; Crossley, A.; Jones, J. H.; Compton, R. G. Investigating the Reactive Sites and the Anomalously Large Changes in Surface PKa Values of Chemically Modified Carbon Nanotubes of Different Morphologies. *J. Mater. Chem.* **2007**, *17* (25), 2616. https://doi.org/10.1039/b702492d.

(99) Chidsey, C. E. D. Free Energy and Temperature Dependence of Electron Transfer at the Metal-Electrolyte Interface. *Science* **1991**, *251* (4996), 919–922.

(100) Jackson, M. N.; Oh, S.; Kaminsky, C. J.; Chu, S. B.; Zhang, G.; Miller, J. T.; Surendranath, Y. Strong Electronic Coupling of Molecular Sites to Graphitic Electrodes via Pyrazine Conjugation. *J. Am. Chem. Soc.* **2018**, *140* (3), 1004–1010. https://doi.org/10.1021/jacs.7b10723.

(101) Feldman, I. Use and Abuse of PH Measurements. *Anal. Chem.* **1956**, *28* (12), 1859–1866. https://doi.org/10.1021/ac60120a014.

(102) Boyes, W. *Instrumentation Reference Book.*; Butterworth-Heinemann, 2003.

(103) Cremer, M. Über Die Ursache Der Elektromotorischen Eigenschaften Der Gewebe, Zugleich Ein Beitrag Zur Lehre von Polyphasischen Elektrolytketten. *Z. Biol.* **1906**, *47* (29), 562–608.

(104) Licht, S. PH Measurement in Concentrated Alkaline Solutions. *Anal. Chem.* **1985**, *57* (2), 514–519. https://doi.org/10.1021/ac50001a045.

(105) Bergveld, P. Thirty Years of ISFETOLOGY. *Sensors Actuators B Chem.* **2002**, *88* (1), 1–20. https://doi.org/10.1016/s0925-4005(02)00301-5.

(106) Gláb, S.; Hulanicki, A.; Edwall, G.; Folke, F.; Ingman, I.; Koch, W. F. Metal-Metal Oxide and Metal Oxide Electrodes as PH Sensors. *Crit. Rev. Anal. Chem.* **1989**, *21* (1), 29–47. https://doi.org/10.1080/10408348908048815.

(107) Marzouk, S. A. M.; Ufer, S.; Buck, R. P.; Johnson, T. A.; Dunlap, L. A.; Cascio, W. E. Electrodeposited Iridium Oxide PH Electrode for Measurement of Extracellular Myocardial Acidosis during Acute Ischemia. *Anal. Chem.* **1998**, *70* (23), 5054–5061. https://doi.org/10.1021/ac980608e.

(108) VanHoudt, P.; Lewandowski, Z.; Little, B. Iridium Oxide PH Microelectrode. *Biotechnol. Bioeng.* **1992**, *40* (5), 601–608. https://doi.org/10.1002/bit.260400507.

(109) Hitchman, M. L.; Ramanathan, S. Evaluation of Iridium Oxide Electrodes Formed by Potential Cycling as PH Probes. *Analyst* **1988**, *113* (1), 35–39. https://doi.org/10.1039/AN9881300035.

(110) Nguyen, C. M.; Rao, S.; Yang, X.; Dubey, S.; Mays, J.; Cao, H.; Chiao, J. C. Sol-Gel Deposition of Iridium Oxide for Biomedical Micro-Devices. *Sensors (Switzerland)* **2015**, *15* (2), 4212–4228. https://doi.org/10.3390/s150204212.

(111) Wencel, D.; Mcdonagh, C. Optical Chemical Sensors: A Look Back. In *Optochemical Nanosensors*; 2000; pp 52–96.

(112) Lin, J. Recent Development and Applications of Optical and Fiber-Optic PH Sensors. *TrAC - Trends Anal. Chem.* **2000**, *19* (9), 541–552. https://doi.org/10.1016/S0165-9936(00)00034-0.

(113) Biilmann, E. Studies on the Quinhydrone Electrode. *Ann. Chim.* **1921**, *15*, 109.

(114) Diederich, L.; Kuttel, O. M.; Ruffieux, P.; Pillo, T.; Aebi, P.; Schlapbach, L. Photoelectron Emission from Nitrogen- and Boron-Doped Diamond (100) Surfaces. *Surf. Sci.* **1998**, *417* (1), 41–52. https://doi.org/10.1016/s0039-6028(98)00638-4.

(115) Koizumi, S. Growth and Characterization of Phosphorus Doped N-Type Diamond Thin Films. *Phys. Status Solidi a-Applied Res.* **1999**, *172* (1), 71–78. https://doi.org/10.1002/(sici)1521-396x(199903)172:1<71::aid-pssa71>3.3.co;2-e.

(116) Ekimov, E. A.; Sidorov, V. A.; Bauer, E. D.; Mel'nik, N. N.; Curro, N. J.; Thompson, J. D.; Stishov, S. M. Superconductivity in Diamond. *Nature* **2004**, *428* (6982), 542–545. https://doi.org/10.1038/nature02449.

(117) Blase, X.; Bustarret, E.; Chapelier, C.; Klein, T.; Marcenat, C. Superconducting Group-IV Semiconductors. *Nat. Mater.* **2009**, *8* (5), 375–382. https://doi.org/10.1038/nmat2425.

(118) Bundy, F. P.; Hall, H. T.; Strong, H. .; Wentorf, R. H. Man-Made Diamonds. *Nature* **1955**, *176*, 51–55.

(119) Li, H. S.; Qi, Y. X.; Gong, J. H.; Wang, M.; Li, M. S. High-Pressure Synthesis and Characterization of Thermal-Stable Boron-Doped Diamond Single Crystals. *Int.*

J. Refract. Met. Hard Mater. **2009**, *27* (3), 564–570. https://doi.org/10.1016/j.ijrmhm.2008.07.015.

(120) Angus, J. C.; Will, H. A.; Stanko, W. S. Growth of Diamond Seed Crystals by Vapor Deposition. *J. Appl. Phys.* **1968**, *39* (6), 2915–2922. https://doi.org/10.1063/1.1656693.

(121) May, P.; Mankelevich, Y. From Ultrananocrystalline Diamond to Single Crystal Diamond Growth in Hot Filament and Microwave Plasma-Enhanced CVD Reactors: A Unified Model for Growth Rates. *J. Phys. Chem. C* **2008**, 12432–12441. https://doi.org/10.1021/jp803735a.

(122) Ochiai, T.; Ishii, Y.; Tago, S.; Hara, M.; Sato, T.; Hirota, K.; Nakata, K.; Murakami, T.; Einaga, Y.; Fujishima, A. Application of Boron-Doped Diamond Microelectrodes for Dental Treatment with Pinpoint Ozone-Water Production. *ChemPhysChem* **2013**, *14* (10), 2094–2096. https://doi.org/10.1002/cphc.201200845.

(123) Fan, B.; Zhu, Y.; Rechenberg, R.; Rusinek, C. A.; Becker, M. F.; Li, W. Lab on a Chip Neurotransmitter Sensing. *Lab Chip* **2017**, *17*, 3159–3167. https://doi.org/10.1039/C7LC00229G.

(124) Yanagisawa, M.; Jiang, L.; Tryk, D. a.; Hashimoto, K.; Fujishima, a. Surface Morphology and Electrochemical Properties of Highly Boron-Doped Homoepitaxial Diamond Films. *Diam. Relat. Mater.* **1999**, *8* (11), 2059–2063. https://doi.org/10.1016/S0925-9635(99)00172-7.

(125) Cleri, F.; Keblinski, P.; Colombo, L.; Wolf, D.; Phillpot, S. R. On the Electrical Activity of Sp^2 -Bonded Grain Boundaries in Nanocrystalline Diamond. *Europhys. Lett.* **1999**, *46* (5), 671–677. https://doi.org/10.1209/epl/i1999-00318-5.

(126) Cobb, S. J.; Ayres, Z. J.; Macpherson, J. V. Boron Doped Diamond: A Designer Electrode Material for the Twenty-First Century. *Annu. Rev. Anal. Chem.* **2018**, *11* (1), annurev-anchem-061417-010107. https://doi.org/10.1146/annurev-anchem-061417-010107.

(127) Kondo, T.; Hoshi, H.; Honda, K.; Einaga, Y.; Fujishima, A.; Kawai, T. Photochemical Modification of a Boron-Doped Diamond Electrode Surface with Vinylferrocene Photochemical Modification of a Boron-Doped Diamond Electrode Surface With. *J. Phys. Chem. C* **2008**, *112*, 11887. https://doi.org/10.1021/jp802875c.

(128) Patten, H. V; Lai, S. C. S.; Macpherson, J. V; Unwin, P. R. Active Sites for Outer-Sphere, Inner-Sphere, and Complex Multistage Electrochemical Reactions at Polycrystalline Boron-Doped Diamond Electrodes (PBDD) Revealed with Scanning Electrochemical Cell Microscopy (SECCM). *Anal. Chem.* **2012**, *84* (12), 5427–5432. https://doi.org/10.1021/ac3010555.

(129) Fujishima, A.; Rao, T. N. New Directions in Structuring and Electrochemical Applications of Boron-Doped Diamond Thin Films. *Diam. Relat. Mater.* **2001**, *10* (9–10), 1799–1803. https://doi.org/10.1016/s0925-9635(01)00452-6.

(130) Wang, J.; Liu, F.; Chen, H.; Chen, D. The Electron Transfer Behavior of the Hydrogen-Terminated Boron-Doped Diamond Film Electrode. *Mater. Chem. Phys.* **2009**, *115* (2–3), 590–598. https://doi.org/10.1016/j.matchemphys.2008.12.033.

(131) Simm, A. O.; Banks, C. E.; Ward-Jones, S.; Davies, T. J.; Lawrence, N. S.; Jones, T. G. J.; Jiang, L.; Compton, R. G. Boron-Doped Diamond Microdisc Arrays: Electrochemical Characterisation and Their Use as a Substrate for the Production of Microelectrode Arrays of Diverse Metals (Ag, Au, Cu) via Electrodeposition. *Analyst* **2005**, *130* (9), 1303–1311. https://doi.org/10.1039/b506956d.

(132) Duo, I.; Levy-Clement, C.; Fujishima, A.; Comninellis, C. Electron Transfer Kinetics on Boron-Doped Diamond Part I: Influence of Anodic Treatment. *J. Appl. Electrochem.* **2004**, *34* (9), 935–943. https://doi.org/10.1023/b:jach.0000040525.76264.16.

(133) Hutton, L.; O'Neil, G.; Read, T. Electrochemical X-Ray Fluorescence Spectroscopy (EC-XRF) for Trace Heavy Metal Analysis: Enhancing XRF Detection Capabilities by Four Orders of Magnitude. *Anal. Chem.* **2014**, *86*, 4566–4572. https://doi.org/10.1021/ac500608d.

(134) Sbartai, A.; Namour, P.; Errachid, A.; Krejči, J.; Šejnohová, R.; Renaud, L.; Larbi Hamlaoui, M.; Loir, A. S.; Garrelie, F.; Donnet, C.; Soder, H.; Audouard, E.; Granier, J.; Jaffrezic-Renault, N. Electrochemical Boron-Doped Diamond Film Microcells Micromachined with Femtosecond Laser: Application to the Determination of Water Framework Directive Metals. *Anal. Chem.* **2012**, *84* (11), 4805–4811. https://doi.org/10.1021/ac3003598.

(135) Pust, S. E.; Szunerits, S.; Boukherroub, R.; Wittstock, G. Electro-Oxidative Nanopatterning of Silane Monolayers on Boron-Doped Diamond Electrodes. *Nanotechnology* **2009**, *20* (7). https://doi.org/10.1088/0957-4484/20/7/075302.

(136) Zhou, Y.; Zhi, J. The Application of Boron-Doped Diamond Electrodes in Amperometric Biosensors. *Talanta* **2009**, *79* (5), 1189–1196. https://doi.org/10.1016/j.talanta.2009.05.026.

(137) Suffredini, H. B.; Pedrosa, V. A.; Codognoto, L.; Machado, S. A. S.; Rocha, R. C.; Avaca, L. A. Enhanced Electrochemical Response of Boron-Doped Diamond Electrodes Brought on by a Cathodic Surface Pre-Treatment. *Electrochim. Acta* **2004**, *49* (22–23), 4021–4026. https://doi.org/10.1016/j.electacta.2004.01.082.

(138) Babyak, C.; Smart, R. R. Electrochemical Detection of Trace Concentrations of Cadmium and Lead with a Boron-Doped Diamond Electrode: Effect of KCl and KNO3 Electrolytes, Interferences and Measurement in River Water. *Electroanalysis* **2004**, *16* (3), 175–182. https://doi.org/10.1002/elan.200302794.

(139) Forsberg, P.; Jorge, E. O.; Nyholm, L.; Nikolajeff, F.; Karlsson, M. Fabrication of Boron Doped Diamond Microband Electrodes for Electrochemical Detection in a

Microfluidic Channel. *Diam. Relat. Mater.* **2011**, *20* (8), 1121–1124. https://doi.org/10.1016/j.diamond.2011.06.024.

(140) Patten, H. V.; Meadows, K. E.; Hutton, L. A.; Iacobini, J. G.; Battistel, D.; McKelvey, K.; Colburn, A. W.; Newton, M. E.; MacPherson, J. V.; Unwin, P. R. Electrochemical Mapping Reveals Direct Correlation between Heterogeneous Electron-Transfer Kinetics and Local Density of States in Diamond Electrodes. *Angew. Chemie - Int. Ed.* **2012**, *51* (28), 7002–7006. https://doi.org/10.1002/anie.201203057.

(141) Gerischer, H. The Impact of Semiconductors on the Concepts of Electrochemistry. *Electrochim. Acta* **1990**, *35* (11–12), 1677–1699. https://doi.org/10.1016/0013-4686(90)87067-C.

(142) Bennett, J. A.; Wang, J.; Show, Y.; Swain, G. M. Effect of Sp2-Bonded Nondiamond Carbon Impurity on the Response of Boron-Doped Polycrystalline Diamond Thin-Film Electrodes. *J. Electrochem. Soc.* **2004**, *151* (9), E306. https://doi.org/10.1149/1.1780111.

(143) Boukherroub, R.; Wallart, X.; Szunerits, S.; Marcus, B.; Bouvier, P.; Mermoux, M. Photochemical Oxidation of Hydrogenated Boron-Doped Diamond Surfaces. *Electrochem. Commun.* **2005**, *7* (9), 937–940. https://doi.org/10.1016/j.elecom.2005.05.010.

(144) Diederich, L.; Kuttel, O.; Aebi, P.; Schlapbach, L. Electron Affinity and Work Function of Differently Oriented and Doped Diamond Surfaces Determined by Photoelectron Spectroscopy. *Surf. Sci.* **1998**, *418* (1), 219–239. https://doi.org/10.1016/s0039-6028(98)00718-3.

(145) Koeck, F. A. M.; Garguilo, J. M.; Nemanich, R. J. On the Thermionic Emission from Nitrogen-Doped Diamond Films with Respect to Energy Conversion. *Diam. Relat. Mater.* **2004**, *13* (11–12), 2052–2055. https://doi.org/10.1016/j.diamond.2004.06.027.

(146) Bandis, C.; Pate, B. Photoelectric-Emission from Negative-Electron Affinity Diamond (111) Surfaces- Exciton Breakup versus Conduction-Band Emission. *Phys. Rev. B* **1995**, *52* (16), 12056–12071. https://doi.org/10.1103/PhysRevB.52.12056.

(147) Andrade, H. D.; Othman, M. Z.; O'Donnell, K. M.; Lay, J. H.; May, P. W.; Fox, N. A.; Morin, J.; Renault, O. Use of Energy-Filtered Photoelectron Emission Microscopy and Kelvin Probe Force Microscopy to Visualise Work Function Changes on Diamond Thin Films Terminated with Oxygen and Lithium Mono-Layers for Thermionic Energy Conversion. *Int. J. Nanotechnol.* **2014**, *11* (9–11), 796–807. https://doi.org/10.1504/ijnt.2014.063789.

(148) Robinson, V. S.; Show, Y.; Swain, G. M.; Reifenberger, R. G.; Fisher, T. S. Thermionic Emission from Surface-Terminated Nanocrystalline Diamond. *Diam.*

Relat. Mater. **2006**, *15* (10), 1601–1608. https://doi.org/10.1016/j.diamond.2006.01.017.

(149) Zhu, D.; Zhang, L. H.; Ruther, R. E.; Hamers, R. J. Photo-Illuminated Diamond as a Solid-State Source of Solvated Electrons in Water for Nitrogen Reduction. *Nat. Mater.* **2013**, *12* (9), 836–841. https://doi.org/10.1038/nmat3696.

(150) Maier, F.; Riedel, M.; Mantel, B.; Ristein, J.; Ley, L. Origin of Surface Conductivity in Diamond. *Phys. Rev. Lett.* **2000**, *85* (16), 3472–3475. https://doi.org/10.1103/PhysRevLett.85.3472.

(151) Ristein, J. Diamond Surfaces: Familiar and Amazing. *Appl. Phys. a-Materials Sci. Process.* **2006**, *82* (3), 377–384. https://doi.org/10.1007/s00339-005-3363-5.

(152) Ristein, J. Surface Transfer Doping of Diamond. *J. Phys. D-Applied Phys.* **2006**, *39* (4), R71–R81. https://doi.org/10.1088/0022-3727/39/4/r01.

(153) John, P.; Stoikou, M. D. Hydrogen Plasma Interaction with (100) Diamond Surfaces. *Phys. Chem. Chem. Phys.* **2011**, *13* (24), 11503–11510. https://doi.org/10.1039/c1cp20099b.

(154) Gaisinskaya, A.; Akhylediani, R.; Edrei, R.; Alagem, E.; Joselzon, Z.; Hoffman, A. Chemical Composition, Thermal Stability and Hydrogen Plasma Treatment of Laser-Cut Single-Crystal Diamond Surface Studied by X-Ray Photoelectron Spectroscopy and Atomic Force Microscopy. *Diam. Relat. Mater.* **2010**, *19* (4), 305–313. https://doi.org/10.1016/j.diamond.2009.12.007.

(155) Zhao, L.; Peng, H.; Chen, Y.; Luo, Y.; Chen, B.; Xu, R.; Huang, J.; Wang, L.; Xia, Y.; Jin, Z. Effect of Hydrogen Plasma Treatment on the Field Emission of Diamond-like Films Deposited by High Power Excimer Laser Ablation. *New Carbon Mater.* **2010**, *25* (4), 317–320.

(156) Ostrovskaya, L.; Perevertailo, V.; Ralchenko, V.; Dementjev, A.; Loginova, O. Wettability and Surface Energy of Oxidized and Hydrogen Plasma-Treated Diamond Films. *Diam. Relat. Mater.* **2002**, *11* (3–6), 845–850. https://doi.org/10.1016/s0925-9635(01)00636-7.

(157) Maier, F.; Ristein, J.; Ley, L. Electron Affinity of Plasma-Hydrogenated and Chemically Oxidized Diamond (100) Surfaces. *Phys. Rev. B* **2001**, *64* (16). https://doi.org/10.1103/PhysRevB.64.165411.

(158) Goeting, C. H.; Marken, F.; Gutierrez-Sosa, A.; Compton, R. G.; Foord, J. S. Electrochemically Induced Surface Modifications of Boron-Doped Diamond Electrodes: An X-Ray Photoelectron Spectroscopy Study. *Diam. Relat. Mater.* **2000**, *9* (3–6), 390–396. https://doi.org/10.1016/s0925-9635(99)00267-8.

(159) Salazar-Banda, G. R.; Andrade, L. S.; Nascente, P. A. P.; Pizani, P. S.; Rocha, R. C.; Avaca, L. A. On the Changing Electrochemical Behaviour of Boron-Doped

Diamond Surfaces with Time after Cathodic Pre-Treatments. *Electrochim. Acta* **2006**, *51* (22), 4612–4619. https://doi.org/10.1016/j.electacta.2005.12.039.

(160) Hoffmann, R.; Kriele, A.; Obloh, H.; Hees, J.; Wolfer, M.; Smirnov, W.; Yang, N.; Nebel, C. E. Electrochemical Hydrogen Termination of Boron-Doped Diamond. *Appl. Phys. Lett.* **2010**, *97* (5). https://doi.org/10.1063/1.3476346.

(161) Ando, T.; Ishii, M.; Kamo, M.; Sato, Y. Thermal Hydrogenation of Diamond Surfaces Studied By Diffuse Reflectance Fourier-Transform Infrared, Temperature-Programmed Desorption and Laser Raman-Spectroscopy. *J. Chem. Soc. Trans.* **1993**, *89* (11), 1783–1789. https://doi.org/10.1039/ft9938901783.

(162) Ando, T.; Inoue, S.; Ishii, M.; Kamo, M.; Sato, Y.; Yamada, O.; Nakano, T. Fourier-Transform Infrared Photoacoustic Studies of Hydrogenated Diamond Surfaces. *J. Chem. Soc. Trans.* **1993**, *89* (4), 749–751. https://doi.org/10.1039/ft9938900749.

(163) Wang, M.; Simon, N.; Decorse-Pascanut, C.; Bouttemy, M.; Etcheberry, A.; Li, M.; Boukherroub, R.; Szunerits, S. Comparison of the Chemical Composition of Boron-Doped Diamond Surfaces upon Different Oxidation Processes. *Electrochim. Acta* **2009**, *54* (24), 5818–5824. https://doi.org/10.1016/j.electacta.2009.05.037.

(164) Notsu, H.; Yagi, I.; Tatsuma, T.; Tryk, D. A.; Fujishima, A. Surface Carbonyl Groups on Oxidized Diamond Electrodes. *J. Electroanal. Chem.* **2000**, *492* (1), 31–37. https://doi.org/10.1016/s0022-0728(00)00254-0.

(165) Notsu, H.; Yagi, I.; Tatsuma, T.; Tryk, D. A.; Fujishima, A. Introduction of Oxygen-Containing Functional Groups onto Diamond Electrode Surfaces by Oxygen Plasma and Anodic Polarization. *Electrochem. Solid State Lett.* **1999**, *2* (10), 522–524. https://doi.org/10.1149/1.1390890.

(166) Salvadori, M. C.; Araujo, W. W. R.; Teixeira, F. S.; Cattani, M.; Pasquarelli, A.; Oks, E. M.; Brown, I. G. Termination of Diamond Surfaces with Hydrogen, Oxygen and Fluorine Using a Small, Simple Plasma Gun. *Diam. Relat. Mater.* **2010**, *19* (4), 324–328. https://doi.org/10.1016/j.diamond.2010.01.002.

(167) Ando, T.; Yamamoto, K.; Ishii, M.; Kamo, M.; Sato, Y. Vapor-Phase Oxidation Of Diamond Surfaces In O2 Studied By Diffuse-Reflectance Fourier-Transform Infrared And Temperature-Programmed Desorption Spectroscopy. *J. Chem. Soc. Trans.* **1993**, *89* (19), 3635–3640. https://doi.org/10.1039/ft9938903635.

(168) Wang, X.; Ruslinda, A. R.; Ishiyama, Y.; Ishii, Y.; Kawarada, H. Higher Coverage of Carboxylic Acid Groups on Oxidized Single Crystal Diamond (001). *Diam. Relat. Mater.* **2011**, *20* (10), 1319–1324. https://doi.org/10.1016/j.diamond.2011.08.011.

(169) Liu, F. B.; Wang, J. D.; Liu, B.; Li, X. M.; Chen, D. R. Effect of Electronic Structures on Electrochemical Behaviors of Surface-Terminated Boron-Doped

Diamond Film Electrodes. *Diam. Relat. Mater.* **2007**, *16* (3), 454–460. https://doi.org/10.1016/j.diamond.2006.08.016.

(170) Speranza, G.; Torrengo, S.; Miotello, A.; Minati, L.; Bernagozzi, I.; Ferrari, M.; Dipalo, M.; Kohn, E. XPS and UPS in Situ Study of Oxygen Thermal Desorption from Nanocrystalline Diamond Surface Oxidized by Different Process. *Diam. Relat. Mater.* **2011**, *20* (4), 560–563. https://doi.org/10.1016/j.diamond.2011.03.001.

(171) Yagi, I.; Notsu, H.; Kondo, T.; Tryk, D. A.; Fujishima, A. Electrochemical Selectivity for Redox Systems at Oxygen-Terminated Diamond Electrodes. *J. Electroanal. Chem.* **1999**, *473* (1–2), 173–178. https://doi.org/10.1016/s0022-0728(99)00027-3.

(172) John, P.; Polwart, N.; Troupe, C. E.; Wilson, J. I. B. The Oxidation of Diamond: The Geometry and Stretching Frequency of Carbonyl on the (100) Surface. *J. Am. Chem. Soc.* **2003**, *125* (22), 6600–6601. https://doi.org/10.1021/ja029586a.

(173) Torrengo, S.; Canteri, R.; Dell'Anna, R.; Minati, L.; Pasquarelli, A.; Speranza, G. XPS and ToF-SIMS Investigation of Nanocrystalline Diamond Oxidized Surfaces. *Appl. Surf. Sci.* **2013**, *276*, 101–111. https://doi.org/10.1016/j.apsusc.2013.03.041.

(174) Ballutaud, D.; Simon, N.; Girard, H.; Rzepka, E.; Bouchet-Fabre, B. Photoelectron Spectroscopy of Hydrogen at the Polycrystalline Diamond Surface. *Diam. Relat. Mater.* **2006**, *15* (4–8), 716–719. https://doi.org/10.1016/j.diamond.2006.01.004.

(175) Thomas, R. E.; Rudder, R. A.; Markunas, R. J. Thermal-Desorption From Hydrogenated And Oxygenated Diamond (100) Surfaces. *J. Vac. Sci. Technol. a-Vacuum Surfaces Film.* **1992**, *10* (4), 2451–2457. https://doi.org/10.1116/1.577983.

(176) Takeuchi, D.; Ri, S. G.; Tokuda, N.; Yamasaki, S. Recovery of Negative Electron Affinity by Annealing on (111) Oxidized Diamond Surfaces. *Diam. Relat. Mater.* **2009**, *18* (2–3), 206–209. https://doi.org/10.1016/j.diamond.2008.10.007.

(177) Zaitsev, A. M. *Optical Properties of Diamond: A Data Handbook*; Springer Berlin Heidelberg: Berlin, 2001.

(178) Szirmai, P.; Pichler, T.; Williams, O. A.; Mandal, S.; Bäuerle, C.; Simon, F. A Detailed Analysis of the Raman Spectra in Superconducting Boron Doped Nanocrystalline Diamond. *Phys. Status Solidi Basic Res.* **2012**, *249* (12), 2656–2659. https://doi.org/10.1002/pssb.201200461.

(179) Bernard, M.; Deneuville, A.; Muret, P. Non-Destructive Determination of the Boron Concentration of Heavily Doped Metallic Diamond Thin Films from Raman Spectroscopy. *Diam. Relat. Mater.* **2004**, *13* (2), 282–286. https://doi.org/10.1016/j.diamond.2003.10.051.

(180) Tomlinson, L. I.; Patten, H. V.; Green, B. L.; Iacobini, J.; Meadows, K. E.; McKelvey, K.; Unwin, P. R.; Newton, M. E.; Macpherson, J. V. Intermittent-Contact

Scanning Electrochemical Microscopy (IC-SECM) as a Quantitative Probe of Defects in Single Crystal Boron Doped Diamond Electrodes. *Electroanalysis* **2016**, *28* (10), 2297–2302. https://doi.org/10.1002/elan.201600291.

(181) Garcia-Segura, S.; Vieira dos Santos, E.; Martínez-Huitle, C. A. Role of Sp3/Sp2 Ratio on the Electrocatalytic Properties of Boron-Doped Diamond Electrodes: A Mini Review. *Electrochem. Commun.* **2015**, *59*, 52–55. https://doi.org/10.1016/j.elecom.2015.07.002.

(182) Martin, H.; Argoitia, A.; Landau, U.; Anderson, A.; Angus, J. Hydrogen and Oxygen Evolution on Boron-Doped Diamond Electrodes. *J. Electrochem. Soc.* **1996**, *143* (6), 134.

(183) Fujishima, A. *Diamond Electrochemistry*; Elsevier, 2005.

(184) Prawer, S.; Nemanich, R. J. Raman Spectroscopy of Diamond and Doped Diamond. *Philos. Trans. A. Math. Phys. Eng. Sci.* **2004**, *362* (1824), 2537–2565. https://doi.org/10.1098/rsta.2004.1451.

(185) Cuesta, A.; Dhamelincourt, P.; Laureyns, J.; Martinez-Alonso, A.; Tascon, J. M. D. Raman Microprobe Studies on Carbon Materials. *Carbon N. Y.* **1994**, *32* (8), 1523–1532. https://doi.org/10.1016/0008-6223(94)90148-1.

(186) Ferreira, N. G.; Abramof, E.; Corat, E. J.; Trava-Airoldi, V. J. Residual Stresses and Crystalline Quality of Heavily Boron Doped Diamond Films Analysed by Micro-Raman Spectroscopy and X-Ray Diffraction. *Carbon N. Y.* **2003**, *41*, 1301–1308. https://doi.org/doi:10.1016/S0008-6223(03)00071-X.

(187) Fujimoto, A.; Yamada, Y.; Koinuma, M.; Sato, S. Origins of Sp3C Peaks in C1s X-Ray Photoelectron Spectra of Carbon Materials. *Anal. Chem.* **2016**, *88* (12), 6110–6114. https://doi.org/10.1021/acs.analchem.6b01327.

(188) Ivandini, T. A.; Sato, R.; Makide, Y.; Fujishima, A.; Einaga, Y. Electrochemical Detection of Arsenic(III) Using Iridium-Implanted Boron-Doped Diamond Electrodes. *Anal. Chem.* **2006**, *78* (18), 6291–6298. https://doi.org/10.1021/ac0519514.

(189) Toghill, K. E.; Compton, R. G. Metal Nanoparticle Modified Boron Doped Diamond Electrodes for Use in Electroanalysis. *Electroanalysis* **2010**, *22* (17–18), 1947–1956. https://doi.org/10.1002/elan.201000072.

(190) May, P. W. Diamond Thin Films : A 21st-Century Material. *Philos. Trans. Math. , Phys. Eng. Sci.* **2000**, *358* (1766), 473–495.

(191) Ayres, Z. J.; Newland, J. C.; Newton, M. E.; Mandal, S.; Williams, O. A.; Macpherson, J. V. Impact of Chemical Vapour Deposition Plasma Inhomogeneity on the Spatial Variation of Sp 2 Carbon in Boron Doped Diamond Electrodes. *Carbon N. Y.* **2017**, *121*, 434–442. https://doi.org/10.1016/j.carbon.2017.06.008.

(192) Sun, B.; Salter, P. S.; Booth, M. J. High Conductivity Micro-Wires in Diamond Following Arbitrary Paths. *Appl. Phys. Lett.* **2014**, *105* (23). https://doi.org/10.1063/1.4902998.

(193) Picollo, F.; Battiato, A.; Carbone, E.; Croin, L.; Enrico, E.; Forneris, J.; Gosso, S.; Olivero, P.; Pasquarelli, A.; Carabelli, V. Development and Characterization of a Diamond-Insulated Graphitic Multi Electrode Array Realized with Ion Beam Lithography. *Sensors* . 2015. https://doi.org/10.3390/s150100515.

(194) Watanabe, T.; Shimizu, T. K.; Tateyama, Y.; Kim, Y.; Kawai, M.; Einaga, Y. Giant Electric Double-Layer Capacitance of Heavily Boron-Doped Diamond Electrode. *Diam. Relat. Mater.* **2010**, *19* (7–9), 772–777. https://doi.org/10.1016/j.diamond.2010.02.022.

(195) Rousseau, L.; Scorsone, E.; Bendali, A.; Djilas, M.; Girard, H.; Cottance, M.; Joucla, S.; Dubus, E.; Degardin, J.; Yvert, B.; Lissorgues, G.; Bergonzo, P.; Picaud, S. Soft 3D Retinal Implants with Diamond Electrode a Way for Focal Stimulation. *2013 Transducers Eurosensors XXVII 17th Int. Conf. Solid-State Sensors, Actuators Microsystems, TRANSDUCERS EUROSENSORS 2013* **2013**, No. June, 1227–1230. https://doi.org/10.1109/Transducers.2013.6626996.

(196) Bendali, A.; Rousseau, L.; Lissorgues, G.; Scorsone, E.; Djilas, M.; Dégardin, J.; Dubus, E.; Fouquet, S.; Benosman, R.; Bergonzo, P.; Sahel, J. A.; Picaud, S. Synthetic 3D Diamond-Based Electrodes for Flexible Retinal Neuroprostheses: Model, Production and in Vivo Biocompatibility. *Biomaterials* **2015**, *67*, 73–83. https://doi.org/10.1016/j.biomaterials.2015.07.018.

(197) Dubey, A. K.; Yadava, V. Laser Beam Machining - A Review. *Int. J. Mach. Tools Manuf.* **2008**, *48* (6), 609–628. https://doi.org/10.1016/j.ijmachtools.2007.10.017.

(198) Windholz, R. Nanosecond Pulsed Excimer Laser Machining of Chemical Vapour Deposited Diamond and Highly Oriented Pyrolytic Graphite. *J. Mater. Sci.* **1997**, *2*, 4295–4301.

(199) Odake, S.; Ohfuji, H.; Okuchi, T.; Kagi, H.; Sumiya, H.; Irifune, T. Pulsed Laser Processing of Nano-Polycrystalline Diamond: A Comparative Study with Single Crystal Diamond. *Diam. Relat. Mater.* **2009**, *18* (5–8), 877–880. https://doi.org/10.1016/j.diamond.2008.10.066.

(200) Harrison, P. M.; Henry, M.; Brownell, M. Laser Processing of Polycrystalline Diamond, Tungsten Carbide, and a Related Composite Material. *J. Laser Appl.* **2006**, *18* (2), 117–126. https://doi.org/10.2351/1.2164472.

(201) Sudheer, S. K.; Kakadia, B.; Mahadevan Pillai, V. P.; Shafeev, G. A.; Simakin, A. V. Processing of Natural Diamonds Using Nanosecond and Picosecond Lasers - Relative Merits and Demerits. *Proc. SPIE* **2008**, *6881* (2008), 68811G. https://doi.org/10.1117/12.786994.

(202) Windholz, R.; Molian, P. A. Nanosecond Pulsed Excimer Laser Machining of Chemically Vapour-Deposited Diamond and Graphite: Part II. Analysis and Modelling. *J. Mater. Sci.* **1998**, *33*, 523–528.

(203) Strekalov, V. N.; Konov, V. I.; Kononenko, V. V.; Pimenov, S. M. Early Stages of Laser Graphitization of Diamond. *Appl. Phys. a-Materials Sci. Process.* **2003**, *76* (4), 603–607. https://doi.org/10.1007/s00339-002-2014-3.

(204) Kononenko, V. V; Kononenko, T. V; Pimenov, S. M.; Sinyavskii, M. N.; Konov, V. I.; Dausinger, F. Effect of the Pulse Duration on Graphitisation of Diamond during Laser Ablation. *Quantum Electron.* **2005**, *35* (3), 252–256. https://doi.org/10.1070/QE2005v035n03ABEH002900.

(205) Chichkov, B. N.; Momma, C.; Nolte, S.; von Alvensleben, F.; Tunnermann, A. Femtosecond, Picosecond and Nanosecond Laser Ablation of Solids. *Appl. Phys. a-Materials Sci. Process.* **1996**, *63* (2), 109–115. https://doi.org/10.1007/bf01567637.

(206) Kononenko, V. V; Gololobov, V. M.; Komlenok, M. S.; Konov, V. I. Nonlinear Photooxidation of Diamond Surface Exposed to Femtosecond Laser Pulses. *Laser Phys. Lett.* **2015**, *12* (9), 096101. https://doi.org/10.1088/1612-2011/12/9/096101.

(207) Ozkan, A. M.; Malshe, A. P.; Railkar, T. A.; Brown, W. D.; Shirk, M. D.; Molian, P. A. Femtosecond Laser-Induced Periodic Structure Writing on Diamond Crystals and Microclusters. *Appl. Phys. Lett.* **1999**, *75* (23), 3716–3718. https://doi.org/10.1063/1.125439.

(208) Kononenko, T. V.; Meier, M.; Komlenok, M. S.; Pimenov, S. M.; Romano, V.; Pashinin, V. P.; Konov, V. I. Microstructuring of Diamond Bulk by IR Femtosecond Laser Pulses. *Appl. Phys. A Mater. Sci. Process.* **2008**, *90* (4), 645–651. https://doi.org/10.1007/s00339-007-4350-9.

(209) Wu, Q. H.; Ma, Y. R.; Fang, R. C.; Liao, Y.; Yu, Q. X.; Chen, X. L.; Wang, K. Femtosecond Laser-Induced Periodic Surface Structure on Diamond Film. *Appl. Phys. Lett.* **2003**, *82* (11), 1703. https://doi.org/10.1063/1.1561581.

(210) Gattass, R. R.; Mazur, E. Femtosecond Laser Micromachining in Transparent Materials. *Nat. Photonics* **2008**, *2* (4), 219–225. https://doi.org/10.1038/nphoton.2008.47.

(211) Su, S.; Li, J.; Lee, G. C. B.; Sugden, K.; Webb, D.; Ye, H. Femtosecond Laser-Induced Microstructures on Diamond for Microfluidic Sensing Device Applications. *Appl. Phys. Lett.* **2013**, *102* (23), 231913. https://doi.org/10.1063/1.4811170.

(212) Malshe, A.; Deshpande, D. Nano and Microscale Surface and Sub-Surface Modifications Induced in Optical Materials by Femtosecond Laser Machining. *J. Mater. Process. Technol.* **2004**, *149* (1–3), 585–590. https://doi.org/10.1016/j.jmatprotec.2003.11.050.

(213) Lee, G. C. B. B.; Su, S.; Li, J. L.; Sugden, K.; Roohpour, N.; Yan, H. X.; Ye, H. T. Analysis of Femtosecond Laser Surface Patterning on Bulk Single-Crystalline Diamond. *J. Exp. Nanosci.* **2012**, *7* (6), 662–672. https://doi.org/10.1080/17458080.2012.724181.

(214) Mathis, A.; Courvoisier, F.; Froehly, L.; Furfaro, L.; Jacquot, M.; Lacourt, P. A.; Dudley, J. M. Micromachining along a Curve: Femtosecond Laser Micromachining of Curved Profiles in Diamond and Silicon Using Accelerating Beams. *Appl. Phys. Lett.* **2012**, *101* (7). https://doi.org/10.1063/1.4745925.

(215) Ramanathan, D.; Molian, P. a. Micro- and Sub-Micromachining of Type IIa Single Crystal Diamond Using a Ti : Sapphire Femtosecond Laser. *J. Manuf. Sci. Eng. Asme* **2002**, *124* (2), 389–396. https://doi.org/10.1115/1.1459083.

(216) Zalloum, O. H. Y.; Parrish, M.; Terekhov, A.; Hofmeister, W. On Femtosecond Micromachining of HPHT Single-Crystal Diamond with Direct Laser Writing Using Tight Focusing. *Opt. Express* **2010**, *18* (12), 13122–13135. https://doi.org/10.1364/oe.18.013122.

(217) Della Valle, G.; Osellame, R.; Laporta, P. Micromachining of Photonic Devices by Femtosecond Laser Pulses. *J. Opt. a-Pure Appl. Opt.* **2009**, *11* (1), 013001. https://doi.org/10.1088/1464-4258/11/1/013001.

(218) Joseph, M. B.; Bitziou, E.; Read, T. L.; Meng, L.; Palmer, N. L.; Mollart, T. P.; Newton, M. E.; Macpherson, J. V. Fabrication Route for the Production of Coplanar, Diamond Insulated, Boron Doped Diamond Macro- and Microelectrodes of Any Geometry. *Anal. Chem.* **2014**, *86* (11), 5238–5244. https://doi.org/10.1021/ac501092y.

(219) Hutton, L. A.; Newton, M. E.; Unwin, P. R.; Macpherson, J. V. Factors Controlling Stripping Voltammetry of Lead at Polycrystalline Boron Doped Diamond Electrodes: New Insights from High-Resolution Microscopy. *Anal. Chem.* **2011**, *83* (3), 735–745. https://doi.org/10.1021/ac101626s.

(220) Provent, C.; Haenni, W.; Santoli, E.; Rychen, P. Boron-Doped Diamond Electrodes and Microelectrode-Arrays for the Measurement of Sulfate and Peroxodisulfate. *Electrochim. Acta* **2004**, *49* (22–23), 3737–3744. https://doi.org/10.1016/j.electacta.2004.02.047.

(221) Cvacka, J.; Quaiserova, V.; Park, J. W.; Show, Y.; Muck, A.; Swain, G. M.; Cva??ka, J.; Quaiserov??, V.; Park, J. W.; Show, Y.; Muck, A.; Swain, G. M. Boron-Doped Diamond Microelectrodes for Use in Capillary Electrophoresis with Electrochemical Detection. *Anal. Chem.* **2003**, *75* (11), 2678–2687. https://doi.org/10.1021/ac030024z.

(222) Hess, A. E.; Sabens, D. M.; Martin, H. B.; Zorman, C. A. Diamond-on-Polymer Microelectrode Arrays Fabricated Using a Chemical Release Transfer

Process. *J. Microelectromechanical Syst.* **2011**, *20* (4), 867–875. https://doi.org/10.1109/jmems.2011.2159099.

(223) Khamis, D.; Mahe, E.; Dardoize, F.; Devilliers, D. Peroxodisulfate Generation on Boron-Doped Diamond Microelectrodes Array and Detection by Scanning Electrochemical Microscopy. *J. Appl. Electrochem.* **2010**, *40* (10), 1829–1838. https://doi.org/10.1007/s10800-010-0114-x.

(224) Soh, K. L.; Kang, W. P.; Davidson, J. L.; Basu, S.; Wong, Y. M.; Cliffel, D. E.; Bonds, A. B.; Swain, G. M. Diamond-Derived Microelectrodes Array for Electrochemical Analysis. *Diam. Relat. Mater.* **2004**, *13* (11–12), 2009–2015. https://doi.org/10.1016/j.diamond.2004.07.025.

(225) Pagels, M.; Hall, C. E.; Lawrence, N. S.; Meredith, A.; Jones, T. G. J.; Godfried, H. P.; Pickles, C. S. J.; Wilman, J.; Banks, C. E.; Compton, R. G.; Jiang, L. All-Diamond Microelectrode Array Device. *Anal. Chem.* **2005**, *77* (11), 3705–3708. https://doi.org/10.1021/ac0502100.

(226) Hutton, L. A.; Vidotti, M.; Iacobini, J. G.; Kelly, C.; Newton, M. E.; Unwin, P. R.; Macpherson, J. V. Fabrication and Characterization of an All-Diamond Tubular Flow Microelectrode for Electroanalysis. *Anal. Chem.* **2011**, *83* (14), 5804–5808. https://doi.org/10.1021/ac2010247.

(227) Sepulveda, N.; Aslam, D.; Sullivan, J. P. Polycrystalline Diamond MEMS Resonator Technology for Sensor Applications. *Diam. Relat. Mater.* **2006**, *15* (2–3), 398–403. https://doi.org/10.1016/j.diamond.2005.08.032.

(228) Kohn, E.; Gluche, P.; Adamschik, M. Diamond MEMS — a New Emerging Technology. *Diam. Relat. Mater.* **1999**, *8* (2–5), 934–940. https://doi.org/10.1016/S0925-9635(98)00294-5.

(229) Auciello, O.; Birrell, J.; Carlisle, J. a; Gerbi, J. E.; Xiao, X.; Peng, B.; Espinosa, H. D. Materials Science and Fabrication Processes for a New MEMS Technology Based on Ultrananocrystalline Diamond Thin Films. *J. Phys. Condens. Matter* **2004**, *16* (16), R539–R552. https://doi.org/10.1088/0953-8984/16/16/R02.

(230) Granger, M. C.; Witek, M.; Xu, J.; Wang, J.; Hupert, M.; Hanks, A.; Koppang, M. D.; Butler, J. E.; Lucazeau, G.; Mermoux, M.; Strojek, J. W.; Swain, G. M. Standard Electrochemical Behavior of High-Quality, Boron-Doped Polycrystalline Diamond Thin-Film Electrodes. *Anal. Chem.* **2000**, *72* (16), 3793–3804. https://doi.org/10.1021/ac0000675.

(231) Hutton, L.; Newton, M. E.; Unwin, P. R.; Macpherson, J. V. Amperometric Oxygen Sensor Based on a Platinum Nanoparticle- Modified Polycrystalline Boron Doped Diamond Disk Electrode Amperometric Oxygen Sensor Based on a Platinum Nanoparticle-Modified Polycrystalline Boron Doped Diamond Disk Electrode. *Anal. Chem.* **2009**, *81* (3), 1023–1032. https://doi.org/10.1021/ac8020906.

(232) Wakerley, D.; Güell, A. G.; Hutton, L. A.; Miller, T. S.; Bard, A. J.; Macpherson, J. V. Boron Doped Diamond Ultramicroelectrodes: A Generic Platform for Sensing Single Nanoparticle Electrocatalytic Collisions. *Chem. Commun.* **2013**, *49* (50), 5657. https://doi.org/10.1039/c3cc42915f.

Chapter 2: Experimental

This chapter contains experimental information that forms standard techniques and procedures that apply throughout the entire thesis. Further experimental information is provided within each chapter.

2.1 Materials and Chemicals

2.1.1 Chemicals

All aqueous solutions were prepared using Milli-Q water, resistivity 18.2 MΩ cm at 25 ^{o}C (Millipore). Chemicals were used as provided unless stated otherwise and were measured using a four figure balance (Mettler-Toledo). A list of chemicals can be found in Table 2.1. Bulk solution pH values were measured using a commercial pH probe (Mettler-Toledo seven easy (Chapters 3 and 7) and Hach HQ411d (Chapters 4-6))

Chemical	Supplier	Extra information
Potassium Nitrate (KNO_3)	Fisher Scientific	>99.0%
Potassium Chloride (KCl)	Sigma Aldrich	>99%
Potassium Sulphate (K_2SO_4)	VWR	>99.0%
Potassium Hydroxide (KOH)	Alfa Aesar	>99.98% metals basis
Sulphuric Acid (H_2SO_4)	Sigma Aldrich	98%
Sodium Chloride (NaCl)	Alfa Aesar	>99.0%
Boric Acid (H_3BO_3)	Sigma Aldrich	>99.97%
Alumina Micropolish	Buehler	0.05 µm
Hexaaminеruthenium(III)Chloride ($Ru(NH_3)_6.Cl_3$)	Strem Chemicals Ltd.	>97%
Citric Acid ($C_6H_8O_7$)	Sigma Aldrich	>99.5%
Tertiary Sodium Phosphate (Na_3PO_4)	Sigma Aldrich	>95%
Tetrabutylammonium hexafluorophosphate (TBAHFP)	Sigma Aldrich	>99.0%
Acetonitrile (MeCN)	Fisher scientific	>99.0%
4Å Molecular sieves	Sigma Aldrich	
p-toluenesulfonic acid (p-TsOH)	Sigma Aldrich	>99.0%
Silver epoxy	CircuitWorks	
5 min fast setting Araldite	RS Components	

Table 2.1: List of chemicals used in this thesis and their suppliers

2.1.2 Boron doped diamond samples

In Chapters 3-6 high quality negligible sp^2 content freestanding microcrystalline BDD wafers (Electroanalytical Grade, Element Six Ltd., UK) was used as the base material for laser micro-machined electrodes. This material was grown by MWCVD (Section 1.6.1) with a boron dopant density of ~3×10^{20} cm^{-3}. The material was ~350 µm thick and polished to ~nm roughness on the growth face and lapped to µm roughness on the nucleation face. In Chapter 3 other grades of BDD from Element Six Ltd., UK and ultrananocrystalline thin film BDD on silicon from Advanced Diamond Technologies

Inc., Illinois, USA, were also used (see Section 3.3.1). All material was metallically doped and as such suitable for electrochemical studies.

2.2 Laser micromachining

Due to the extreme properties of diamond, fabrication of usable electrode geometries from diamond wafers is challenging, with laser micro-machining being one of the few suitable methods for electrode preparation. In this thesis two Oxford Lasers Ltd. laser micro-machining systems have been used: A-532 (Chapter 3, Figure 2.1a) and E-355-ATHI-O (Chapter 4-6, Figure 2.1b).

Figure 2.1:(a) Oxford Lasers A-532 Laser Micro-machining System (b) Oxford Lasers E-355-ATHI-O Laser Micro-machining System

The A-532 system has a frequency doubled (532 nm) Nd:YAG 20 ns pulsed laser head, with a maximum power of ~3 W and a nominal spot size of 10 µm. The E-355-ATHI-O system has a frequency tripled (355 nm) Nd:YAG 34 ns pulsed laser head with a maximum power of ~8 W and nominal spot size of 6 µm. Both systems can be operated using G-Code, a common computer numerical control programming language, that can be written using computer aided design software or manually to define the geometry of the feature to be machined.

2.2.1 Sample cutting

For ease of sample handling the six inch polished BDD wafers from Element Six Ltd. were diced into useful sample sizes (on the order of mm). For glass sealed electrodes 1 mm diameter BDD cylinders were cut from the wafer using a laser micro-machiner (A-532 in Chapter 3 and E-355H-ATHI-O in Chapters 4-6). For efficient cutting high pulse fluences and pulse densities (1200 J cm^{-2} and 3×10^7 cm^{-2} respectively) were used.

2.2.2 Milling

For the machining of structures that go part way through the diamond wafer, and the controlled introduction of sp^2 into the surface of BDD electrodes (glass sealed and Kapton masked, for use in chapters 3-6), laser micro-machining was again used (A-532 in Chapter 3 and E-355H-ATHI-O in Chapters 4-6). However the laser fluences and pulse densities used were lower than in Section 2.2.1 (14-980 J cm^{-2} and 1-2 $\times 10^6$ cm^{-2}). This allowed for the production of spatial control of regions of sp^2 containing BDD with an electrode geometry defined by the machining code.

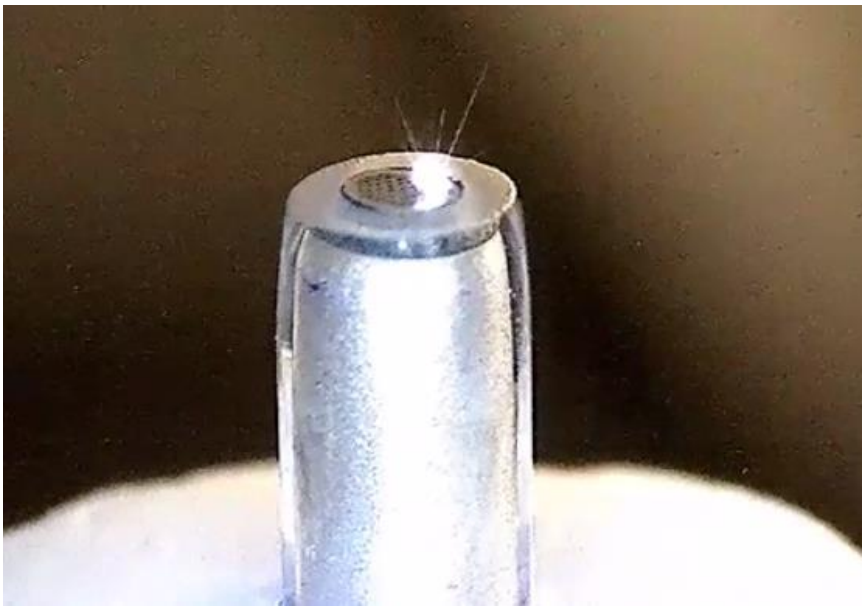

Figure 2.2: Laser Micro-machining of spatially controlled sp^2 containing features into a BDD electrode

2.3 Acid cleaning

After laser micromachining all BDD samples were acid cleaned to remove loosely bound sp^2. This involved heating the sample at ~200°C for 30 min in concentrated H_2SO_4 (98%) saturated with KNO_3 before the heat was turned on.[1] Samples were then thoroughly rinsed with ultrapure water. This process also was necessary to produce a consistent O-terminated surface.

2.4 Applying an ohmic contact to BDD

For all electrochemical experiments BDD was ohmically contacted. Ti (10 nm) / Au (400 nm) was sputtered (Moorfields MiniLab 060 platform sputter/evaporator) onto the back of the BDD samples and annealed at 400°C for 5 h, to allow the titanium to react with the BDD to form titanium carbide, creating a reliable ohmic contact.

2.5 Electrode manufacture

In this thesis, three forms of BDD electrode were used: (1) Glass sealed (see Section 2.5.1, used in Chapter's 4 and 5); (2) Kapton masked (see section 2.5.2, used in Chapter 3) and (3) all-diamond (as described previously,[2] Chapter 6). Different electrode geometries have different advantage and disadvantages. The glass sealed electrodes are robust and can be used in conventional electrochemical cells, however they have the disadvantage of a time-consuming fabrication process. Kapton tape electrodes allowed for fast 'droplet' experiments to be conducted on larger BDD surfaces, however it is very challenging to use degassed solutions and the seal can be prone to leaking. All diamond electrodes were extremely robust and had excellent electrochemical properties, although the fabrication route was complex, resulting in a limited supply of electrodes. Therefore experimental machining of the surface was not feasible with such a reduced number.

2.5.1 Glass sealed electrode manufacture

Ohmically contacted (Section 2.4) 1 mm BDD cylinders were sealed in glass capillaries (o.d. 2 mm; i.d. 1.16 mm; Harvard Apparatus Ltd., Kent, UK) and the top surface exposed by polishing away the glass with carbide grit paper disks and alumina (0.05 μm) paste (Buehler, Germany).[3] Any laser milling to controllably introduce sp^2 carbon into the polished growth surface (see Section 2.2.2) and subsequent acid cleaning (section 2.3) was conducted at this point in the procedure. A copper wire was

used to contact the back face of the BDD cylinder in the capillary using silver epoxy to form a conductive and permanent bond. The top of the capillary was then sealed using Araldite to prevent solution access to the inside of the capillary.

2.5.2 Kapton tape electrodes.

Samples cut from a BDD wafer (Section 2.1.2) with laser micromachined features in the surface (Section 2.2.2) were mounted to a Ti/Au sputtered slide using an ohmic contact on the back face of the BDD sample (Section 2.4) after acid cleaning (Section 2.3). The area of interest was masked using a kapton mask with a laser cut 1 mm diameter hole to define the electrode area.

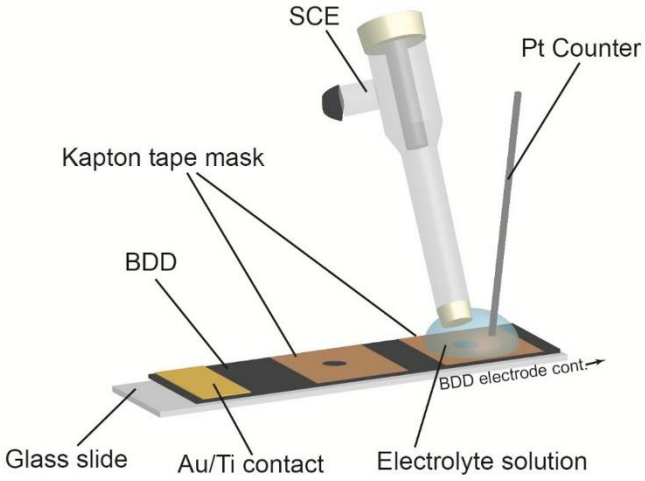

Figure 2.3 Electrochemical set up for Kapton tape masked electrode experiments from Ayres et al.[4]

2.6 Electrochemical set up

All electrochemical experiments were conducted with a 3-electrode set up, with working electrodes of different forms (Section 2.5). For Chapters 3 and 5-6 a saturated calomel reference electrode was used ($Hg|Hg_2Cl_2$, E^0= + 0.244.4 V *vs* SHE) in aqueous solution and in chapter 4 a silver/silver chloride ($Ag|AgCl$, E^0= + 0.210 V *vs* SHE) in aqueous solution and silver/silver nitrate ($Ag|Ag^+$, 10mM $AgNO_3$, E^0= 0.545 V *vs* SHE) in acetonitrile (MeCN)

2.7 Electrochemical Characterisation of BDD Electrodes

All BDD electrodes in this thesis were characterised before use by following a standard electrochemical characterisation procedure. Briefly, this consisted of a

measurement of the solvent window in 0.1 M KNO_3 at 0.1 V s^{-1}, the double layer capacitance from a CV at 0 V *vs* SCE, and the response of a redox mediator. The exact procedure is described in previously published work.[5,6]

2.8 Micro-Raman Spectroscopy

Raman spectroscopy is based upon the inelastic scattering of monochromated light by a sample. When a laser beam is used to illuminate a sample, some proportion (sample dependent) is reflected and of that portion a small component (ca. 1 in 10 million photons) interacts with a phonon in the material, leading to a characteristic shift in the energy of the reflected photon. These shifts are used to provide information on the sample. In chapter 3 micro-raman spectroscopy is used to assess the sp^2 content of BDD material. All micro-raman spectroscopy was performed using a Renishaw inVia Raman Microscope with an excitation wavelength of 532 nm and 10 mW power. The laser spot size was approximately 3 μm.

2.9 White-Light Interferometry

White Light Interferometry (WLI), is an optical method for investigating surface topography. WLI can image areas of up to 500 μm^2 with a maximum height resolution of 1 nm. In this measurement technique the white light from a source is collimated and then split in two, with half reflected from a reference mirror and half from the sample. The beams are then recombined and the constructive and destructive interference fringes from the difference in path length is used to infer the surface topography across the entire imaged area. The time taken to collect an image is on the order of seconds, compared to AFM that would take hours to image a comparable area. This larger area and faster measurement time is at the expense of X-Y resolution, which is limited by the CCD detector of the interferometer and is dependent on the magnification. WLI can be operated in two modes phase shifted interferometry (PSI) and vertical scanning interferometry (VSI). PSI operates by moving the reference mirror using a piezoelectric positioner to alter the relative path lengths and allows for high Z resolution imaging (ca. 1 nm) over short distances (ca. 1 μm). VSI mode operates by using a stepper motor to change the distance to the sample while holding the reference path constant and can resolve large distances (10s of mm) with reduced Z resolution (ca. 10 nm). All WLI in this thesis was performed with a Bruker Contour GT.

2.10 References

(1) Ayres, Z. J.; Borrill, A. J.; Newland, J. C.; Newton, M. E.; Macpherson, J. V. Controlled Sp2 Functionalization of Boron Doped Diamond as a Route for the Fabrication of Robust and Nernstian PH Electrodes. *Anal. Chem.* **2016**, *88* (1), 974–980. https://doi.org/10.1021/acs.analchem.5b03732.

(2) Joseph, M. B.; Bitziou, E.; Read, T. L.; Meng, L.; Palmer, N. L.; Mollart, T. P.; Newton, M. E.; Macpherson, J. V. Fabrication Route for the Production of Coplanar, Diamond Insulated, Boron Doped Diamond Macro- and Microelectrodes of Any Geometry. *Anal. Chem.* **2014**, *86* (11), 5238–5244. https://doi.org/10.1021/ac501092y.

(3) Hutton, L.; Newton, M. E.; Unwin, P. R.; Macpherson, J. V. Amperometric Oxygen Sensor Based on a Platinum Nanoparticle- Modified Polycrystalline Boron Doped Diamond Disk Electrode Amperometric Oxygen Sensor Based on a Platinum Nanoparticle-Modified Polycrystalline Boron Doped Diamond Disk Electrode. *Anal. Chem.* **2009**, *81* (3), 1023–1032. https://doi.org/10.1021/ac8020906.

(4) Ayres, Z. J.; Newland, J. C.; Newton, M. E.; Mandal, S.; Williams, O. A.; Macpherson, J. V. Impact of Chemical Vapour Deposition Plasma Inhomogeneity on the Spatial Variation of Sp 2 Carbon in Boron Doped Diamond Electrodes. *Carbon N. Y.* **2017**, *121*, 434–442. https://doi.org/10.1016/j.carbon.2017.06.008.

(5) Hutton, L. A.; Iacobini, J. G.; Bitziou, E.; Channon, R. B.; Newton, M. E.; Macpherson, J. V. Examination of the Factors Affecting the Electrochemical Performance of Oxygen-Terminated Polycrystalline Boron-Doped Diamond Electrodes. *Anal. Chem.* **2013**, *85* (15), 7230–7240. https://doi.org/10.1021/ac4010421.

(6) Macpherson, J. V. A Practical Guide to Using Boron Doped Diamond in Electrochemical Research. *Phys. Chem. Chem. Phys.* **2015**, *17* (5), 2935–2949. https://doi.org/10.1039/c4cp04022h.

Chapter 3: Quinone electrochemistry for the comparative assessment of sp^2 surface content of boron doped diamond electrodes.

3.1 Overview

The electrochemically active surface groups on an sp^2 carbon material controllably introduced by laser micromachining or as grown into a boron doped diamond (BDD) electrode are characterised and the surface coverage of electroactive quinone groups used to inform on the sp^2 surface content of electrodes. Laser micromachining of an electrode surface is used to systematically increase the amount of sp^2 carbon present by increasing the area machined. A linear relationship between quinone surface coverage and surface area machined is determined (r^2 = 0.9999) for use of characterising the amount of sp^2 carbon introduced. This electrochemical material characterisation technique is compared to raman spectroscopy, the most commonly used approach. Quinone surface coverage measurements can also be used for comparative assessment of as-grown electrodes containing different amounts of surface sp^2 carbon.

3.2 Introduction

Polycrystalline boron doped diamond (BDD) has emerged as a popular material for the electrochemist in recent years[1,2] due to its intriguing electroanalytical properties compared to other more conventional electrode materials including: extended solvent window (SW), low background currents, high chemical inertness and mechanical robustness, as well as increased resistance to fouling. For this reason, BDD electrodes have found use in a wide range of applications, such as electroanalysis,[3] biosensing,[4] wastewater processing[5] and spectroelectrochemistry.[6] Many of these properties arise from the sp^3 bonded carbon structure. However, achieving a pure sp^3 material during diamond synthesis especially in combination with high boron dopant levels, is challenging and almost impossible for nano and smaller sized grain material.[7,8] Increasing sp^2 content has its disadvantages e.g. increased background current, reduced solvent window, increased susceptibility to corrosion etc., but can also be advantageous [9] e.g. enhanced electrocatalytic properties,[10] provision of pH active functional groups.[11] Thus for each electrochemical application the sp^2 surface content of BDD needs to be carefully considered, characterised, and controlled, if possible.

Raman spectroscopy is widely used to assess sp^2 content in BDD electrodes,[12] often by comparing the ratio of the 1332 cm^{-1} (sp^3) peak to the G (sp^2) peak.[13] This method is however qualitative,[14] works best when comparing electrodes of the same dopant density and samples only a small area with one measurement (~μm^2 – tens of μm^2 depending on magnification) which is especially problematic when sp^2 content is spatially heterogeneous.[15] Raman can also penetrate up to several microns[16] into the surface. The latter is especially non-ideal for the electrochemist, who cares only about sp^2 surface content. It is therefore imperative that *surface sensitive* characterisation methods are employed when assessing BDD material quality for *electrochemical* applications. To this end photoelectron spectroscopy has been explored,[17] but the method is relatively expensive, time-consuming and requires trained operators. It is also difficult to resolve the sp^2 and sp^3 signatures[18] and peak deconvolution is required, leading to variations in peak assignments throughout the literature.[19,20]

In contrast electrochemistry represents a low cost, rapid characterisation technique providing information about charge transfer processes occurring at the electrode-solution interface. The presence of sp^2 carbon at the electrode surface has been shown previously to modify the solvent window (SW) and capacitance (*C*) of BDD

electrodes[2,21] and result in surface bound quinone groups, which show a pH dependent redox signature, when suitably activated.[11] However, to date, no attempt has been made to correlate these observations with sp^2 surface content. In this chapter the use of the quinone redox signature to provide information on BDD sp^2 surface coverage is demonstrated by systematically increasing the sp^2 content using laser ablation (micromachining) techniques. Direct comparisons with SW and *C* are also made.

3.3 Experimental

3.3.1 Materials

All solutions were prepared from Milli-Q water (Millipore Corp.), resistivity 18.2 MΩ cm at 25 °C. Four different BDD electrodes, numbered 1-4, were grown under different chemical vapour deposition (CVD) conditions, in order to deliberate vary the sp^2 content of the electrodes. Electrodes 1-3 were all grown using microwave-CVD (Element Six, Harwell, UK). They contained ca. 3×10^{20} boron atoms cm^{-3}, and were grown thick enough (in the range 250 – 500 μm) so that they could be removed from the growth substrate and polished to ~ nm roughness. Due to the thickness of the material, large grain sizes result, μm's to tens of μm's. Electrode 1 was used as the baseline material for all laser machining studies and was expected to contain minimal sp^2 carbon (Diafilm EA grade material).[21] Electrode 4 was also grown using microwave CVD (Advanced Diamond Technologies Inc., Illinois, USA) but this time in ultrananocrystalline (UNC), thin film form (2 μm), with a boron dopant concentration of 1.6×10^{21} boron atoms cm^{-3}).[21] The surface was left as-grown (surface roughness 9.3 ± 0.4 nm) and the electrode was left attached to its niobium growth substrate.

C and SW measurements were run in 0.1 M potassium nitrate (KNO_3, Fisher Scientific) solution. For quinone surface coverage (Γ) measurements, a pH 2 Carmody buffer was prepared,[22] using boric acid (99.97%, Sigma Aldrich), citric acid (≥99.5%, Sigma Aldrich) and tertiary sodium phosphate (≥95%, Sigma Aldrich), and the final solution pH measured using a pH meter (SevenEasy, Mettler Toledo).

3.3.2 Electrode preparation

Electrode 1 was laser machined using a 532 nm Nd:YAG nanosecond laser micromachiner (A-532 system, Oxford Lasers Ltd). Laser micromachining is known to result in sp^2 formation on the surface.[23] To systematically increase sp^2 content, six squares (n = 3 for each *i.e.* 18 squares in total) of increasing size (length dimension 200 μm increasing to 700 μm) were machined into 18 individual electrodes of uniform geometric diameter, as shown in Figure 3.1. Identical laser parameters were employed (1000 Hz / 0.195 W with a machining speed of 0.3 mm s^{-1}) optimised to maximise sp^2 production.[24] Once machined, the electrodes were acid treated in boiling concentrated H_2SO_4 (98%) saturated with KNO_3 to oxygen-terminate the surface and remove any loosely contacted sp^2 introduced during machining.[11] Electrodes 2 and 3 were also

subject to acid cleaning prior to use. A less aggressive acid clean was used for Electrode 4 to avoid damaging the thin film material. To provide a reliable ohmic contact, Ti (10 nm) / Au (300 nm) was sputtered (MiniLab 060 Platform, Moorfield Nanotechnology Ltd.) onto the back face of Electrodes 1-3 and top face of Electrode 4, and annealed at 400 °C for 5 h.[21]

For comparative electrode measurements (*vide infra*), all electrodes were acid treated in the same way prior to experiment. This involved running cyclic voltammetry (CV) experiments in 0.1 M H_2SO_4 at 0.1 V s^{-1}, from 0 V to -2 V and then 2 V, before returning to 0 V for 20 cycles.

3.3.3 Electrochemical setup

All electrochemical measurements were performed using a platinum counter and a saturated calomel reference electrode (SCE). The BDD electrodes were mounted onto a Ti/Au sputtered glass slide, using silver epoxy (RS Components Ltd.). In order to restrict the electrode area, Kapton tape (RS Components Ltd.) was laser machined to create 1 mm diameter holes and positioned on the electrodes accordingly (Figure 3.1). All potentials are quoted versus SCE, with all experiments conducted at room temperature (25±2°C). SW values are calculated using a current density threshold of ±0.4 mA cm^{-2}.[21] Analysis of the quinone CV data was carried out after baseline correction and smoothing (Origin Pro software).[25] The baseline correction involved subtracting a linear baseline from the raw data (from +0.25 V to +0.62 V) whilst the current signal was smoothed using a ten point adjacent averaging procedure[25,26]

3.3.4 White Light Interferometry (WLI)

A Bruker ContourGT (Bruker Nano Inc., USA) was used to record WLI profiles. 3D rendering of interferometry data was performed and the increase in electrode area after machining calculated using Gwyddion 2.42. [27]

3.3.5 Optical Images

Optical images of the laser features and electrodes 1-4 were collected using an Olympus BH-2 UMA light microscope (Olympus Corporation, Japan) with both a 50 × and 100 × objective.

3.3.6 Raman spectroscopy

Raman spectroscopy was performed on electrodes 1-4 using a Renishaw inVia Reflex Raman Microscope equipped with a 532 nm solid state laser and a 50 × objective. 20 accumulations were used per spectra to improve the signal to noise ratio.

3.4 Results and discussion

3.4.1 Characterisation of laser features

The total surface area for each sample was calculated using Gwyddion 2.42 (Czech Metrology Institute, CZE) based on the topographical information collected by WLI.

The surface area data collected by WLI was then used to calculate the percentage of the 1 mm masked area which had been exposed to laser ablation, including both the base of the pits and the sidewalls. Samples were processed by Laplace interpolation using Gwyddion 2.42 to fill any missing data points and a three point level was applied to the bare diamond surface to set the data zero point. A mask was applied in Gwyddion fully covering the laser feature. The surface area increase was then calculated by subtracting the projected mask area from the mask surface area (incorporating the laser feature and corresponding roughness from WLI). The calculated surface area increase (laser feature) was added to the area of the 1 mm diameter circular Kapton mask to give the total area of the electrode. These areas are summarised in Table 3.1.

Laser feature side length / µm	**700**	**600**	**500**	**400**	**300**	**200**
Average electrode area / cm²	0.0123± 7.4×10^{-6}	0.0117± 8.0×10^{-6}	0.0109± 1.1×10^{-4}	0.0099± 4.9×10^{-5}	0.0092± 2.9×10^{-5}	0.0086± 1.1×10^{-5}

Table 3.1: Total electrode area including laser features, calculated by WLI

The process was repeated, with the projected area restricted to the size of the laser features. WLI data was then used to calculate the total area of the laser feature. The percentage of the full laser area to the laser machined area was then calculated using Equation 3.1. The percentage area of the laser feature with respect to the total area of the electrode is subsequently referred to as the machined surface area (%).

$$Machined\ surface\ area\ (\%) = \frac{machined\ surface\ area}{total\ electrode\ surface\ area} \times 100 \qquad [3.1]$$

Figure 3.1 shows optical images of the six laser machined BDD electrodes (length of machined square = 200, 300, 400, 500, 600 and 700 µm; *n* = 3 for each square). The machined surface area expressed as a percentage of the total surface area, calculated according to Equation 3.1 using WLI data, equates to 14, 25, 37, 50, 64 and 76 % respectively:

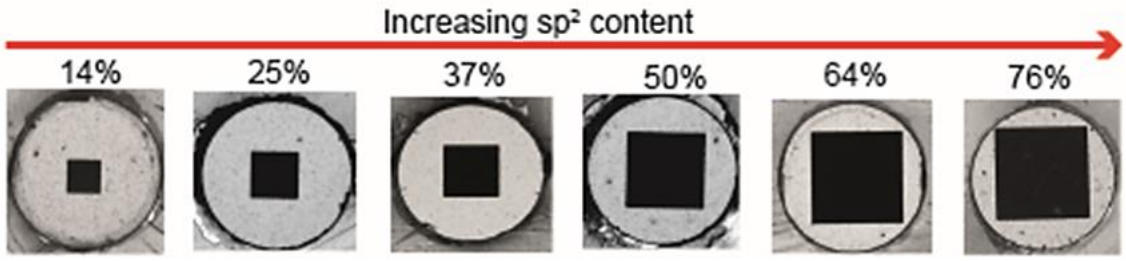

Figure 3.1: Optical images of the machined BDD electrodes, increasing in size (side length: left to right) from 200, 300, 400, 500, 600 to 700 µm, masked by Kapton exposing a 1 mm diameter circular area for electrochemical measurements

3.4.2 Interferometry data for laser micromachined electrodes

To investigate the uniformity of the laser micro-machining process, interferometry line scan data was collected for each of the laser micromachined boron doped diamond (BDD) samples, shown in Figure 3.2.

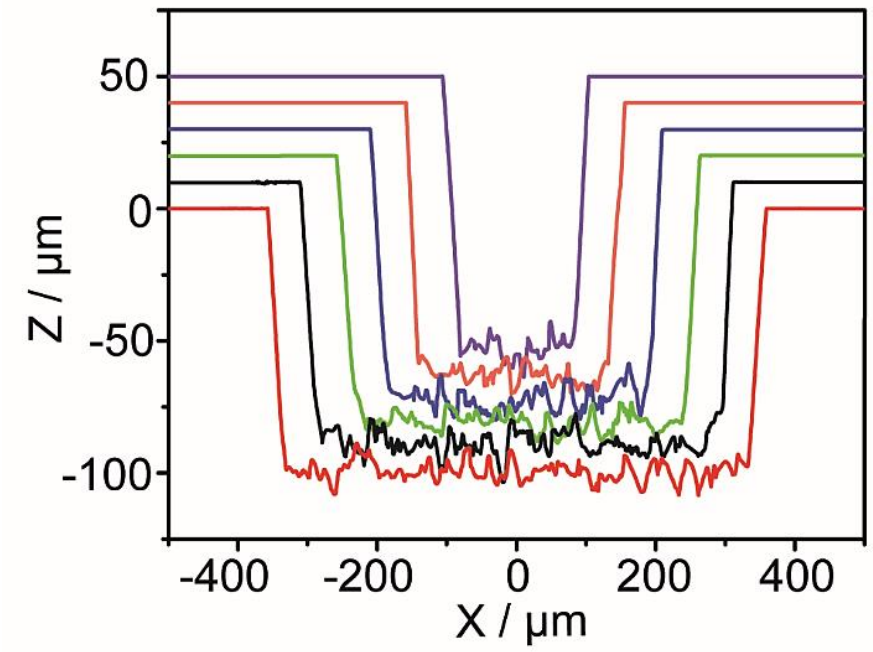

Figure 3.2: Interferometry data for the lasered pits 200, 300, 400, 500, 600, 700 µm, corresponding to purple, orange, blue, green, black and red respectively, offset in the Z axis for clarity.

The laser micromachining was found to have an acceptable consistency with average pit depths of 101 ± 1.9 µm and a root mean squared (rms) roughness of 3.9 ± 0.18 µm across the samples. The average rms roughness values and pit depths for each of the samples (n=3) are summarised in Table 3.2.

Laser feature side length / µm	*Average rms / µm*	*Average pit depth / µm*
700	3.7±0.06	98.6±0.06
600	3.8±0.2	99.5±0.2
500	3.8±0.2	100.4±0.1
400	4.1±0.06	101.8±0.4
300	4.0±0.2	102.5±0.7
200	4.0±0.06	104±1.8

Table 3.2: Summary of average rms and pit depth for laser features using WLI

Some variation was seen in the depth of the laser features, decreasing in a linear manner from 104 ± 1.8 µm in the 200 µm sidelength sample to 98.6 ± 0.06 in the 700 µm sample. This can be attributed to the sample not being completely perpendicular to the laser beam during machining, leading to the surface of the sample being slightly out of focus when the XY coordinates were changed away from the point at which the laser was originally focused. It was decided that the variation was not significant enough to cause an issue that couldn't be accounted for when area correction was carried out in the electrochemical measurements.

3.4.3 Raman spectroscopy

Raman spectroscopy has traditionally been used to characterise diamond by comparing the sp^2 (1580 cm^{-1}, G) to sp^3 (1332 cm^{-1}) peak ratio.

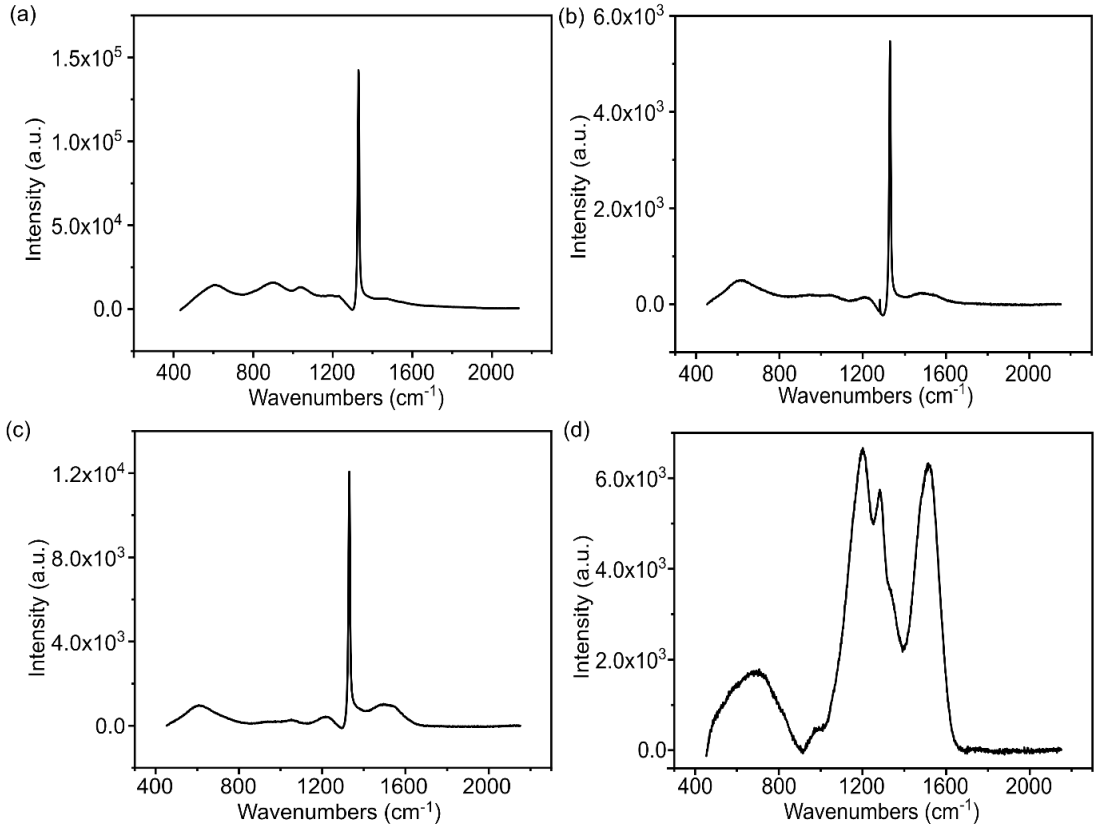

Figure 3.3: Averaged Raman spectra (n=20) for electrodes (a) 1, (b) 2, (c) 3, (d) 4, used to calculate Raman sp^2:sp^3 ratios.

The average of 20 spots at random locations across electrodes 1-4 was plotted in Figure 3.3. From this the sp^2:sp^3 ratios were plotted using the Brillouin zone centre peak height for the sp^3 peak and the G peak for the sp^2 peak. This gave values of 0.019:1, 0.044:1, 0.085:1 and 1.1:1 for electrodes 1-4 respectively. This follows the expected trend however, there are numerous problems with attempting to extract quantitative information from these spectra. Firstly it must be remembered that the Raman cross section of sp^3 and sp^2 carbon is vastly different, with sp^2 having an ~40 × higher Raman cross section.[28] The size of the peaks is also dependent on the Raman laser wavelength used, as this affects the Raman cross-sections of both features differently. Material properties must also be considered as it has been shown that increasing boron concentration shifts the Brillouin zone centre peak to lower wavenumbers and leads to a decrease in its intensity, making comparing between samples with different boron concentrations (such as electrodes 1-3 compared to 4) impossible.

Raman spectroscopy was carried out with an n = 20 random sample across the machined area. It was found that there was a large variation in the sp^2:sp^3 ratio, with some areas showing no sp^2 related features and others prominent peaks (Figure 3.4). This is in part due to the polycrystalline nature of the material with differently doped grains machining differently and giving differing Raman responses. For this reason along with the large penetration depth compared to electrochemistry and difficulties quantifying the sp^2 content the technique must be treated with caution. This highlights the need for an electrochemical method of characterising diamond quality.

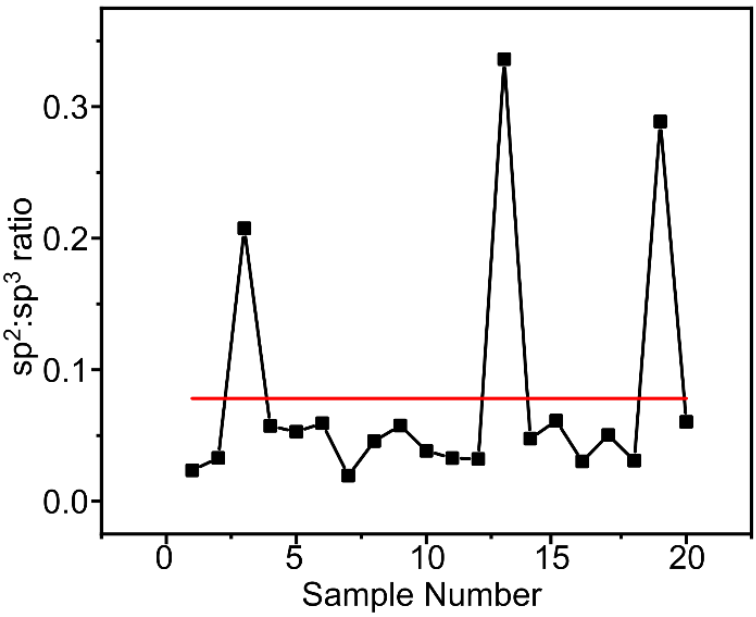

Figure 3.4: Black- Variation of the sp^2:sp^3 ratio across electrode 3 calculated by raman spectroscopy Red- Average sp^2:sp^3 ratio.

A CV was performed in 0.1 M KNO_3 (pH= 6.5), degassed with nitrogen to remove contributions from oxygen reduction reaction (ORR) and allow the peaks from surface bound quinone groups usually masked by the ORR to be seen. Three peaks were seen in the CV with an $E_{1/2}$ of -0.22, 0.17 and 0.40 V *vs* SCE (Figure 3.5) attributed to different processes, the assignment of which is non-trivial as the groups found on the machined surface cannot easily be compared to solution phase model compounds to determine what species are generating the peaks witnessed.

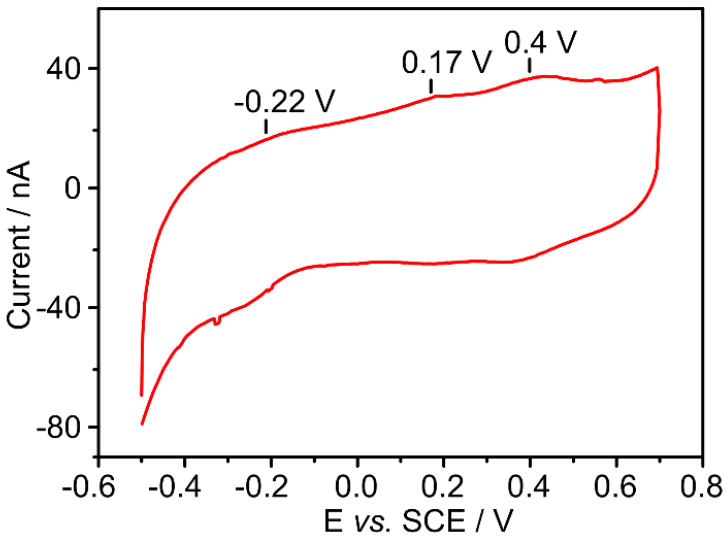

Figure 3.5: CV showing three oxidation and reduction peaks for the 500µm sidelength machined electrode in 0.1M KNO_3 in the absence of oxygen, at a scan rate of 0.1 V s^{-1}.

For the measurement of the surface sp^2 concentration it was necessary to select one process to monitor. The peak at -0.22 V was immediately rejected due to the peak being convoluted with other reactions even in a degassed solution of KNO_3, the peak is even less clear when measurements was made in pH 2 buffer in the presence of oxygen, as used for the Γ measurements.

3.4.4 The +0.17 V peak

When experiments were performed in pH 2 buffer in the presence of oxygen the oxidation peak of the quinone species at 0.17 V was larger and had an asymmetrical peak shape (Figure 3.6a) observed in the presence of Oxygen, with a second peak at ~0.09 V convoluting the broad quinone peak. While this still provided the expected trend of increasing current with increasing machined area (Figure 3.6b) the size of the peak changed considerably on cycling, meaning the charge measured was dependent on which cycle the value was taken from. It was decided to investigate this peak further.

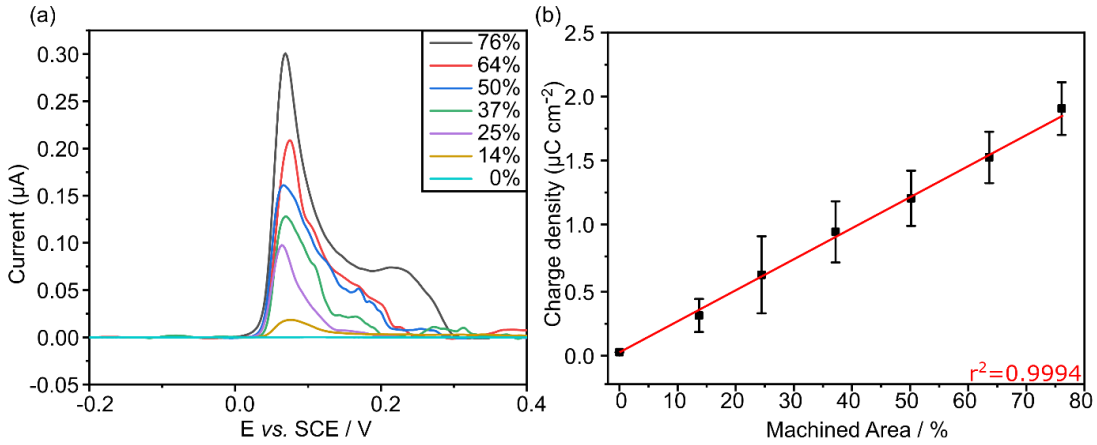

Figure 3.6:(a) Quinone peak shape seen for +0.17 V peak of electrodes with different machined areas in pH 2 buffer in presence of oxygen. (b) linear correlation of machined area with charge passed.

It was found that if the electrode was not cycled to potentials more negative than -0.1 V the single quinone-like peak was witnessed, this is investigated further in Chapter 4. It was therefore suggested that a process happening more negative of -0.1 V *vs* SCE was responsible for the generation of a species that was subsequently oxidised, convoluting the peak. The fact that this peak shape is not seen when the sample is degassed (Figure 3.5) suggests that oxygen is involved in the reduction reaction that causes this effect, this is further supported by the fact that when a degassed sample is cycled to extreme positive potentials the peak is also seen due to the oxygen evolution reaction occurring at the potentials reached in the positive window. The correlation of machined area with the charge passed (Figure 3.6) indicates the peak is related to a reaction occurring on the machined area.

Anthraquinone like species are used commercially to generate hydrogen peroxide using hydrogenation catalysts,[29] this has also been demonstrated electrochemically.[30,31] Therefore it was hypothesised that ORR was occurring via a $2e^-$ pathway, electrogenerating H_2O_2[32] which was being reduced at ~-0.28 V forming OH^- (Scheme 3.1).[33]

$$Q + e^- \rightarrow Q^{\cdot -}$$

$$Q^{\cdot -} + O_2 \rightarrow Q + O_2^{\cdot -}$$

$$O_2^{\cdot -} + H_2O \rightarrow HO_2^- + OH^-$$

$$HO_2^- + H^+ \rightarrow H_2O_2$$

$$H_2O_2 + 2e^- \rightarrow 2OH^-$$

Scheme 3.1: Electrogeneration of hydrogen peroxide by quinone species followed by its reduction to form hydroxyl ions.[33]

To test this a linear sweep voltammogram (LSV) was run from 0.2 V to -0.8 V in 0.1 M KNO_3 in the presence and absence of 0.3% w/w H_2O_2. In the absence of H_2O_2 no reduction peak was seen at 0.28 V (Figure 3.7: red) however when the H_2O_2 was added (Figure 3.7: blue) a peak with the same reduction potential and shape as the peak in the CV (Figure 3.7: black) was seen. This suggests that this peak in the CV comes from the reduction of H_2O_2 due to the similarities in the peak. This hypothesis is further supported as the quinone oxidation and reduction peak positions are known to be sensitive to the solution pH. If H_2O_2 was being reduced to produce hydroxyl, the solution pH would increase and as such the quinone oxidation peak would shift to a more negative potential in the absence of buffer. The quinone oxidation peak in unbuffered KNO_3 (Figure 3.7: black) can be seen to be shrinking in size and shifting to a more negative potential upon cycling. This supports the conclusion that H_2O_2 is being converted to OH^- as the pH can be seen to be increasing from the shift in the quinone peak. The effect of ORR on the quinone peak position in unbuffered solutions has been studied further in Chapter 4. The mechanism of ORR on sp^2 machined electrode surfaces was studied further in Chapter 5.

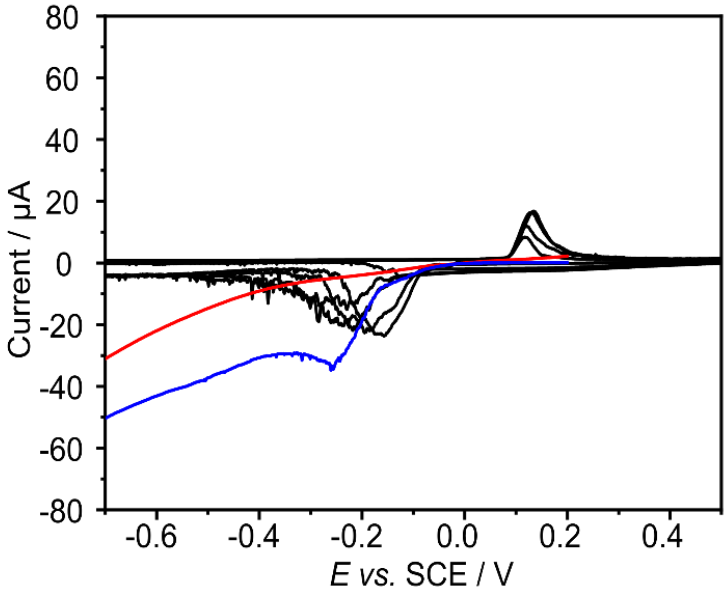

Figure 3.7: Black 50% machined area laser feature CV in 0.1 M KNO_3 at 0.1 Vs^{-1} between 2 and -2 V; Red LSV of 50% laser feature in 0.1 M KNO_3 at a scan rate of 0.1 Vs^{-1}; Blue LSV of 50% laser feature in 0.1 M KNO_3 with 0.3% w/w H_2O_2 at a scan rate of 0.1 Vs^{-1}

The propensity of this surface bound electroactive species to generate H_2O_2 by ORR supports the hypothesis that this species is a quinone. This property is most commonly associated with anthraquinones, although there is no direct evidence to support a particular structure of the surface group.

Due to the complications associated with the peak at +0.17 V it was decided that, while a reasonable linear relationship was shown, a CV would be carried out between 0 and 0.7 V vs SCE and the peak at 0.4 V used to calculate the Γ of that particular quinone species for comparison of the sp^2 content of different diamond samples.

3.4.5 Comparison of surface sp^2 content of diamond using Γ measurements.

For each electrode, CVs in pH 2 buffer were carried out (scan rate of 0.1 V s^{-1}), cycling from 0 to 0.7 V. Figure 3.8a shows typical quinone oxidation peaks for each machined area, along with the bare BDD response. The peaks were integrated (from +0.25 to +0.62 V vs. SCE) to obtain the charge passed, *Q*, and converted to Γ (mol cm^{-2}) using Equation 3.2:[34]

$$Q = nAF\Gamma \qquad [3.2]$$

where n = the number of electrons transferred = 2; A = the total electrode surface area (cm^2); calculated from WLI and F = Faraday's constant (96485 C mol^{-1}).

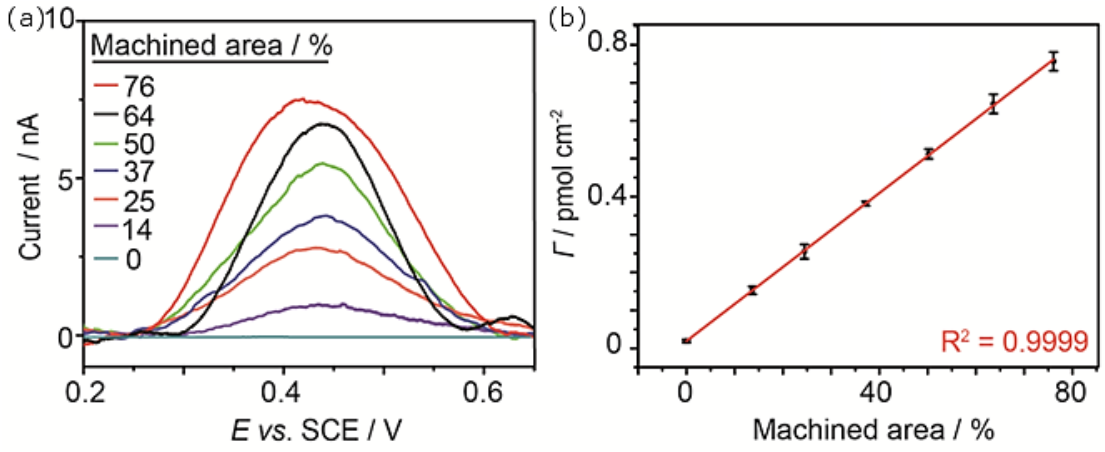

Figure 3.8:(a) Representative background subtracted quinone oxidation peaks for the six machined electrodes and blank, in pH 2 buffer, at a scan rate of 0.1 V s-1. (b) Plot of machined surface area (%) versus Γ.

Figure 3.8b shows Γ vs % machined surface area. As the area machined increases Γ also increases linearly (R^2 = 0.9999) suggesting a strong correlation between Γ on the electrode surface and the amount of sp^2 created due to the laser ablation process. This suggests that Γ can be used to inform on sp^2 carbon present at the electrode surface. Also in contrast to Figure 3.6 this peak is Gaussian in shape and was stable after cycling for repeat cycles (n=20).

C and SW measurements (Figure 3.9a and b respectively) were also made with the same 18 electrodes, and subsequently compared to Γ data, shown in Figure 3.9c. It is apparent that C also follows a similar trend to Γ, with % machined surface area, with a linear response observed (R^2 = 0.9992). This is supported by literature, with quinone groups shown to increase the total *C* observed.[35,36] While *C* has been shown to have a strong correlation with machined area under ideal conditions it cannot necessarily be considered on real world samples. This is due to a number of convoluting factors that can affect the *C* values including: the material thickness; boron doping concentration; surface roughness; quality of the electrical contact. In this experiment all these factors were controlled, however when comparing other samples these parameters may influence the *C* value as opposed to Γ which is exclusively due to sp^2 content, assuming the electrode surfaces have been prepared the same way.

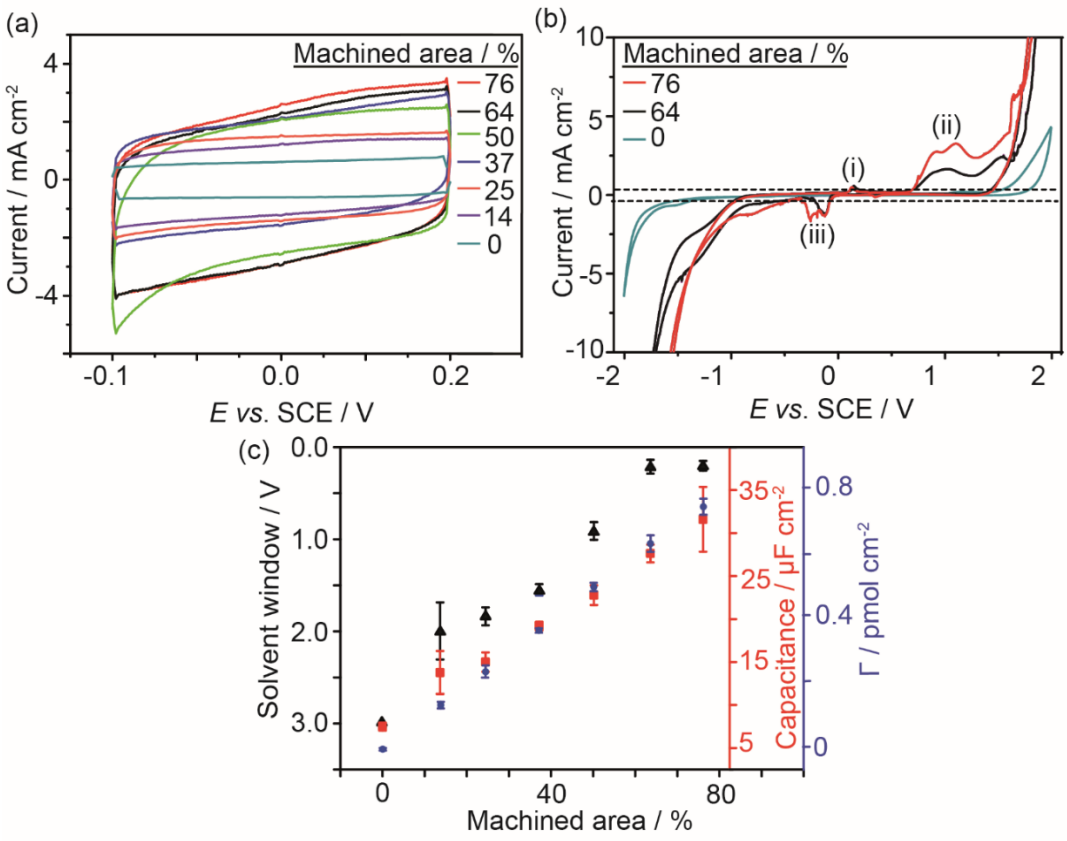

Figure 3.9: Electrochemical measurements (scan rate of 0.1 V s^{-1}) collected for six BDD electrodes with increasing machined area (0-76%) including: (a) C data, (b) selected SW data for clarity, showing the ±0.4 mA cm^{-2} threshold (dotted lines) and (c) comparison of SW, C and Γ with machined surface area%.

The SW is defined as the potential window in which a current of no more than of ±0.4 mA cm^{-2} is passed[21] (the threshold current, marked by a dotted line in Figure 3.9b). From Figure 3.9c, the SW data does not follow the same trend as Γ and *C* plateauing for machined areas ≥ 64%. This is due to the complexity of the SW's observed when sp^2 carbon is present, especially at significant levels (Figure 3.9b). At high sp^2 levels, in addition to current signals attributed to the oxidation of graphitic/quinone type groups on the surface (labelled i) significant oxidation features close to the anodic solvent window (labelled ii) are observed.[21] The feature labelled (iii) we ascribe to the reduction of reactive oxygen species such as hydrogen peroxide electrogenerated due to the quinone groups present.[37] So although there are clear differences in the current magnitude of the SW features, especially anodically for 64% and 76% laser machined electrodes, there is little variation in the SW values recorded. Furthermore, no threshold current could be found which enabled a linear response between SW and machined surface area percentage.[9]

It is also important to demonstrate whether the approach advocated in Figure 3.8 for Γ could be used to distinguish between electrodes that have naturally present sp^2 from the growth process. Thus BDD electrodes 1-4, grown using procedures which should result in an increasing sp^2 content (and are both thin film and thick freestanding) were analysed (Figure 3.10). Changes in the synthesis conditions and resulting thickness of Electrodes 1-4 are also reflected optically in the resulting grain structures observed

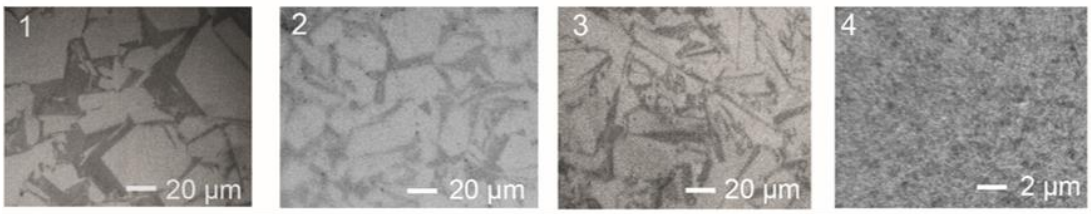

Figure 3.10: Investigation of BDD Electrodes 1-4 including optical images (× 50 and × 100 objective) showing grain structures

3.4.6 Effect of pretreatment

Electrode 4 could not be subjected to the usual high temperature oxidising acid etch procedure (see Section 2.3) due to the material still being attached to its growth substrate which was not robust enough to survive the extreme cleaning procedure. Both of these procedures are known to oxygen terminate the surface, introducing surface bound quinone groups to the material. Instead an electrochemical acid cleaning procedure was used (see Section 3.3.2). This pretreatment was used on all electrodes for the comparison of the naturally present sp^2 content in the material to ensure electrodes were treated identically.

To assess the difference between electrodes pre-treated by electrochemical acid cycling and those pre-treated by high temperature oxidising acid etched electrodes 1-3 that could be treated by both methods were acid etched and the Γ measured. The sample was then electrochemically acid cycled and the Γ of the same area measured again with the results reported in Table 3.3.

Diamond Grade	*Quinone surface coverage- acid clean (mol cm^{-2})*	*Quinone surface coverage- acid cycling (mol cm^{-2})*
MR14	$1.8 \times 10^{-16} \pm 2 \times 10^{-17}$	1.6×10^{-16} +/- 2×10^{-17}
MR11	$2.9 \times 10^{-16} \pm 2 \times 10^{-17}$	2.8×10^{-16} +/- 2×10^{-17}
MR12	$7.0 \times 10^{-16} \pm 2 \times 10^{-17}$	6.8×10^{-16} +/- 2×10^{-17}

Table 3.3: Comparison of Γ for Electrodes 1-3 after an oxidising acid etch and acid cycling

It was found that the average Γ measured after acid cycling were all lower than the Γ measured after an oxidising acid etch, however all measurements on the same sample regardless of acid pretreatment were within error of each other and as such cannot be considered to be significantly different. Therefore, it could be argued that electrode 4 after acid cycling could be compared to electrodes 1-3 after an oxidising acid etch. However, it was decided all electrodes should be treated identically where possible.

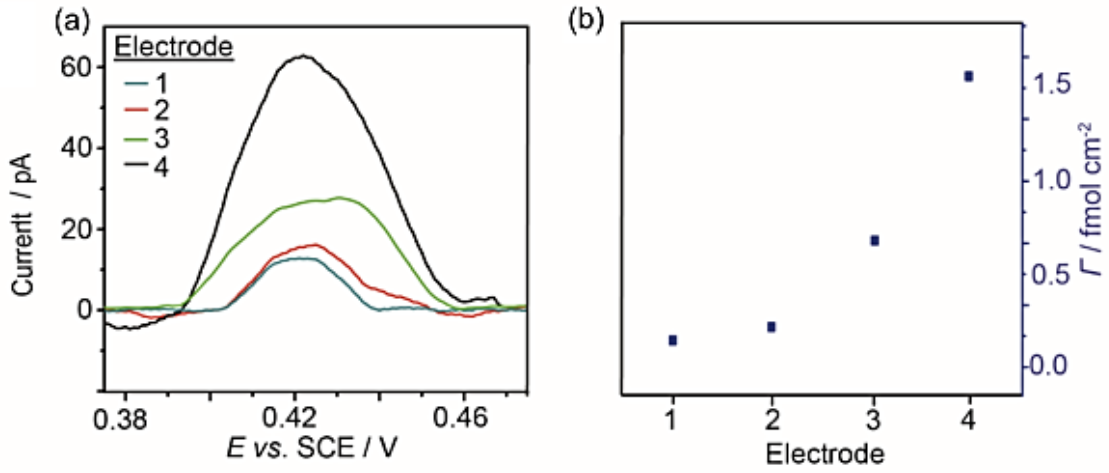

Figure 3.11:(a)The background subtracted quinone oxidation responses at a scan rate of 0.1 V s^{-1} and (b) Γ measurements versus Electrode 1-4.

Figure 3.11 shows the quinone oxidation response for the four electrodes, demonstrating small (picoamp), but measurable currents when background subtracted. A clear increase in quinone oxidation peak, i.e. increasing Γ, with increasing sp^2, is observed, with Γ values of 1.8×10^{-16}, 2.9×10^{-16}, 7.0×10^{-16} and 1.6×10^{-15} mol cm^{-2} recorded for electrodes 1-4 respectively. Note the data recorded on the UNC

Electrode 4 suggests electrochemically active sp^2 coverages almost an order of magnitude higher than the minimal sp^2 content Electrode 1. By comparison, Raman analysis demonstrated a sp^2 signal in all of $n = 20$ Raman spot measurements at random locations for Electrode 4, whilst Electrodes 1-3 all showed spatial variations, with a fraction of spots (per electrode) showing no sp^2 signal at all. Furthermore as the boron concentration was higher in Electrode 4 than Electrodes 1-3, the 1332 cm^{-1} peak was reduced in intensity compared to electrodes 1-3, making 1332 cm^{-1}: G peak ratio comparisons between electrodes inappropriate.

The change in peak width on these electrodes supports the use of charge as a measure of the sp^2 content. Quinone proton coupled electron transfer exhibits traditionally broad waves, often attributed to the electrostatic interactions of neighbouring groups,[38,39] local surface heterogeneities[40] and non-equivalent functional groups.[41,42] At the exceedingly low surface coverages seen on high quality as-grown electrodes these effects could be expected to be reduced, changing the peak width. At these exceedingly low surface coverages the FWHM is close to the theoretically predicted 45.3 mV for a surface bound $2e^-$ process[34] although accurate determination at the current scales used is extremely challenging.

3.5 Conclusions

A new method for assessing the sp^2 surface content of BDD electrodes is introduced. A laser machining process is used to systematically increase the sp^2 content of a BDD electrode by ablating progressively larger squares of graphitised carbon into the surface of a minimal sp^2 content BDD electrode. The graphitised surface contains quinone groups which can be oxidised. The nature of these surface quinone groups is studied with 3 features seen and the ability of the surface to catalyse oxygen reduction demonstrated. The area under the oxidation peak at +0.4 V vs SCE, which equates to Γ, scales linearly (R^2 = 0.9999) with sp^2 surface content (under acidic conditions) expressed as % of machined surface area compared to total electrode area. It has been shown that this approach is also applicable to BDD electrodes which contain inherent sp^2 resulting from the growth process. Γ measurements were able to clearly distinguish between four different electrodes and place them in order of increasing sp^2 surface content. Γ values as low as 0.18 fmol cm^{-2} were recorded on the minimal content BDD electrode rising to 1.6 fmol cm^{-2} for the UNC material, demonstrating both excellent sensitivity and selectivity for BDD film characterisation. We suggest Γ measurements as a preferred method, compared to Raman spectroscopy, for electrode surfaces, as the latter is unfortunately not purely surface sensitive and therefore requires the assumption to be made sp^2 content is spatially uniform throughout the electrode, which is often not the case. Furthermore, compared to the electrochemical characterisation methods available, Γ measurements provide an unambiguous alternative for the assessment of surface sp^2 in BDD electrodes.

3.6 References

(1) Einaga, Y.; Foord, J. S.; Swain, G. M. Diamond Electrodes: Diversity and Maturity. *MRS Bull.* **2014**, *39* (06), 525–532. https://doi.org/10.1557/mrs.2014.94.

(2) Macpherson, J. V. A Practical Guide to Using Boron Doped Diamond in Electrochemical Research. *Phys. Chem. Chem. Phys.* **2015**, *17* (5), 2935–2949. https://doi.org/10.1039/c4cp04022h.

(3) Compton, R. G.; Foord, J. S.; Marken, F. Electroanalysis at Diamond-like and Doped-Diamond Electrodes. *Electroanalysis* **2003**, *15* (17), 1349–1363. https://doi.org/10.1002/elan.200302830.

(4) Zhou, Y.; Zhi, J. The Application of Boron-Doped Diamond Electrodes in Amperometric Biosensors. *Talanta* **2009**, *79* (5), 1189–1196. https://doi.org/10.1016/j.talanta.2009.05.026.

(5) Gandini, D.; Mahé, E.; Michaud, P. A.; Haenni, W.; Perret, A.; Comninellis, C. Oxidation of Carboxylic Acids at Boron-Doped Diamond Electrodes for Wastewater Treatment. *J. Appl. Electrochem.* **2000**, *30* (12), 1345–1350. https://doi.org/10.1023/A:1026526729357.

(6) Hutton, L.; O'Neil, G.; Read, T. Electrochemical X-Ray Fluorescence Spectroscopy (EC-XRF) for Trace Heavy Metal Analysis: Enhancing XRF Detection Capabilities by Four Orders of Magnitude. *Anal. Chem.* **2014**, *86*, 4566–4572. https://doi.org/10.1021/ac500608d.

(7) Watanabe, T.; Honda, Y.; Kanda, K.; Einaga, Y. Tailored Design of Boron-Doped Diamond Electrodes for Various Electrochemical Applications with Boron-Doping Level and Sp2-Bonded Carbon Impurities. *Phys. Status Solidi Appl. Mater. Sci.* **2014**, *211* (12), 2709–2717. https://doi.org/10.1002/pssa.201431455.

(8) Williams, O. A.; Nesladek, M.; Daenen, M.; Michaelson, S.; Hoffman, A.; Osawa, E.; Haenen, K.; Jackman, R. B. Growth, Electronic Properties and Applications of Nanodiamond. *Diam. Relat. Mater.* **2008**, *17* (7–10), 1080–1088. https://doi.org/10.1016/j.diamond.2008.01.103.

(9) Bennett, J. A.; Wang, J.; Show, Y.; Swain, G. M. Effect of Sp2-Bonded Nondiamond Carbon Impurity on the Response of Boron-Doped Polycrystalline Diamond Thin-Film Electrodes. *J. Electrochem. Soc.* **2004**, *151* (9), E306. https://doi.org/10.1149/1.1780111.

(10) Garcia-Segura, S.; Vieira dos Santos, E.; Martínez-Huitle, C. A. Role of Sp3/Sp2 Ratio on the Electrocatalytic Properties of Boron-Doped Diamond Electrodes: A Mini Review. *Electrochem. Commun.* **2015**, *59*, 52–55. https://doi.org/10.1016/j.elecom.2015.07.002.

(11) Ayres, Z. J.; Borrill, A. J.; Newland, J. C.; Newton, M. E.; Macpherson, J. V. Controlled Sp2Functionalization of Boron Doped Diamond as a Route for the Fabrication of Robust and Nernstian PH Electrodes. *Anal. Chem.* **2016**, *88* (1), 974–980. https://doi.org/10.1021/acs.analchem.5b03732.

(12) Ferrari, A. C.; Robertson, J. Raman Spectroscopy of Amorphous, Nanostructured, Diamond-like Carbon, and Nanodiamond. *Philos. Trans. R. Soc. a-*

Mathematical Phys. Eng. Sci. **2004**, *362* (1824), 2477–2512. https://doi.org/10.1098/rsta.2004.1452.

(13) Prawer, S.; Nemanich, R. J. Raman Spectroscopy of Diamond and Doped Diamond. *Philos. Trans. A. Math. Phys. Eng. Sci.* **2004**, *362* (1824), 2537–2565. https://doi.org/10.1098/rsta.2004.1451.

(14) Cuesta, A.; Dhamelincourt, P.; Laureyns, J.; Martinez-Alonso, A.; Tascon, J. M. D. Raman Microprobe Studies on Carbon Materials. *Carbon N. Y.* **1994**, *32* (8), 1523–1532. https://doi.org/10.1016/0008-6223(94)90148-1.

(15) Patten, H. V; Hutton, L. A.; Webb, J. R.; Newton, M. E.; Unwin, P. R.; Macpherson, J. V. Electrochemical "read-Write''' Microscale Patterning of Boron Doped Diamond Electrodes." *Chem. Commun.* **2015**, *51* (1), 164–167. https://doi.org/10.1039/c4cc07830f.

(16) Ferreira, N. G.; Abramof, E.; Corat, E. J.; Trava-Airoldi, V. J. Residual Stresses and Crystalline Quality of Heavily Boron Doped Diamond Films Analysed by Micro-Raman Spectroscopy and X-Ray Diffraction. *Carbon N. Y.* **2003**, *41*, 1301–1308. https://doi.org/doi:10.1016/S0008-6223(03)00071-X.

(17) Briggs, D.; Seah, M. P. Practical Surface Analysis by AES and XPS. *Willey, Chichester* **1983**.

(18) Calliari, L. AES and Core Level Photoemission in the Study of A-C and a-C : H. *Diam. Relat. Mater.* **2005**, *14* (8), 1232–1240. https://doi.org/10.1016/j.diamond.2004.10.046.

(19) Jackson, S. T.; Nuzzo, R. G. Determining Hybridization Differences for Amorphous Carbon from the XPS C 1s Envelope. *Appl. Surf. Sci.* **1995**, *90* (2), 195–203. https://doi.org/10.1016/0169-4332(95)00079-8.

(20) Mérel, P.; Tabbal, M.; Chaker, M.; Moisa, S.; Margot, J. Direct Evaluation of the Sp3 Content in Diamond-like-Carbon Films by XPS. *Appl. Surf. Sci.* **1998**, *136* (1–2), 105–110. https://doi.org/10.1016/S0169-4332(98)00319-5.

(21) Hutton, L. A.; Iacobini, J. G.; Bitziou, E.; Channon, R. B.; Newton, M. E.; Macpherson, J. V. Examination of the Factors Affecting the Electrochemical Performance of Oxygen-Terminated Polycrystalline Boron-Doped Diamond Electrodes. *Anal. Chem.* **2013**, *85* (15), 7230–7240. https://doi.org/10.1021/ac4010421.

(22) Carmody, W. R. Easily Prepared Wide Range Buffer Series. *J. Chem. Educ.* **1961**, *38* (11), 559. https://doi.org/10.1021/ed038p559.

(23) Butler-Smith, P. W.; Axinte, D. A.; Pacella, M.; Fay, M. W. Micro/Nanometric Investigations of the Effects of Laser Ablation in the Generation of Micro-Tools from Solid CVD Diamond Structures. *J. Mater. Process. Technol.* **2013**, *213* (2), 194–200. https://doi.org/10.1016/j.jmatprotec.2012.08.010.

(24) Wang, C. Z.; Ho, K. M.; Shirk, M. D.; Molian, P. A. Laser-Induced Graphitization on a Diamond (111) Surface. *Phys. Rev. Lett.* **2000**, *85* (19), 4092–4095. https://doi.org/10.1103/PhysRevLett.85.4092.

(25) Lu, M.; Compton, R. G. Voltammetric PH Sensor Based on an Edge Plane Pyrolytic Graphite Electrode. *Analyst* **2014**, *139* (10), 2397–2403. https://doi.org/10.1039/c4an00147h.

(26) Jakubowska, M. Signal Processing in Electrochemistry. *Electroanalysis* **2011**, *23* (3), 553–572. https://doi.org/10.1002/elan.201000465.

(27) Nečas, D.; Klapetek, P. Gwyddion: An Open-Source Software for SPM Data Analysis. *Cent. Eur. J. Phys.* **2012**, *10* (1), 181–188. https://doi.org/10.2478/s11534-011-0096-2.

(28) Klar, P.; Lidorikis, E.; Eckmann, A.; Verzhbitskiy, I. A.; Ferrari, A. C.; Casiraghi, C. Raman Scattering Efficiency of Graphene. *Phys. Rev. B - Condens. Matter Mater. Phys.* **2013**, *87* (20), 1–12. https://doi.org/10.1103/PhysRevB.87.205435.

(29) Goor, G.; Kunkel, W.; Weiberg, O. Ullmann's Encyclopedia of Industrial Chemistry, Vol. A13. In *Ullmann's Encyclopedia of Industrial Chemistry, Vol. A13*; Elvers, B., Hawkins, S., Ravenscroft, M., Schulz, G., Eds.; VCH: Weinheim, 1989; pp 443–466.

(30) Campos-Martin, J. M.; Blanco-Brieva, G.; Fierro, J. L. G. Hydrogen Peroxide Synthesis: An Outlook beyond the Anthraquinone Process. *Angew. Chemie - Int. Ed.* **2006**, *45* (42), 6962–6984. https://doi.org/10.1002/anie.200503779.

(31) Mooste, M.; Kibena, E.; Sarapuu, A.; Matisen, L.; Tammeveski, K. Oxygen Reduction on Thick Anthraquinone Films Electrografted to Glassy Carbon. *J. Electroanal. Chem.* **2013**, *702*, 8–14. https://doi.org/10.1016/j.jelechem.2013.04.031.

(32) Morcos, I.; Yeager, E. Kinetic Studies of the Oxygen-Peroxide Couple On Pyrolytic Graphite. *Electrochim. Acta* **1970**, *15*, 953–975.

(33) Yeager, E. Electrocatalysts for O2 Reduction. *Electrochim. Acta* **1984**, *29* (11), 1527–1537. https://doi.org/10.1016/0013-4686(84)85006-9.

(34) Bard, A. J.; Faulkner, L. R. *Electrochemical Methods: Fundamentals and Applications*; Wiley: New York, 1980.

(35) Le Comte, A.; Chhin, D.; Gagnon, A.; Retoux, R.; Brousse, T.; Bélanger, D. Spontaneous Grafting of 9,10-Phenanthrenequinone on Porous Carbon as an Active Electrode Material in an Electrochemical Capacitor in an Alkaline Electrolyte. *J. Mater. Chem. A* **2015**, *3* (11), 6146–6156. https://doi.org/10.1039/C4TA05536E.

(36) Algharaibeh, Z.; Pickup, P. G. An Asymmetric Supercapacitor with Anthraquinone and Dihydroxybenzene Modified Carbon Fabric Electrodes. *Electrochem. Commun.* **2011**, *13* (2), 147–149. https://doi.org/10.1016/j.elecom.2010.11.036.

(37) Vaik, K.; Sarapuu, A.; Tammeveski, K.; Mirkhalaf, F.; Schiffrin, D. J. Oxygen Reduction on Phenanthrenequinone-Modified Glassy Carbon Electrodes in 0.1 M KOH. *J. Electroanal. Chem.* **2004**, *564* (1–2), 159–166. https://doi.org/10.1016/j.jelechem.2003.08.024.

(38) Laviron, E. Surface Linear Potential Sweep Voltammetry. Equation of the Peaks for a Reversible Reaction When Interactions between the Adsorbed Molecules

Are Taken into Account. *J. Electroanal. Chem.* **1974**, *52* (3), 395–402. https://doi.org/10.1016/S0022-0728(74)80449-3.

(39) Chidsey, C. E. D.; Bertozzi, C. R.; Putvinski, T. M.; Mujsce, A. M. Coadsorption of Ferrocene-Terminated and Unsubstituted Alkanethiols on Gold: Electroactive Self-Assembled Monolayers. *J. Am. Chem. Soc.* **1990**, *112* (11), 4301–4306. https://doi.org/10.1021/ja00167a028.

(40) Benítez, G.; Vericat, C.; Tanco, S.; Lenicov, F. R.; Castez, M. F.; Vela, M. E.; Salvarezza, R. C. Role of Surface Heterogeneity and Molecular Interactions in the Charge-Transfer Process through Self-Assembled Thiolate Monolayers on Au(111). *Langmuir* **2004**, *20* (12), 5030–5037. https://doi.org/10.1021/la036440w.

(41) Albery, W. J.; Boutelle, M. G.; Colby, P. J.; Hillman, A. R. The Kinetics of Electron Transfer in the Thionine-Coated Electrode. *J. Electroanal. Chem.* **1982**, *133* (1), 135–145. https://doi.org/10.1016/0022-0728(82)87012-5.

(42) Peerce, P.; Bard, A. Polymer Films on Electrodes: Part III. Digital Simulation Model for Cyclic Voltammetry of Electroactive Polymer Film and Electrochemistry of Poly (Vinylferrocene) on Platinum. *J. Electroanal. Chem.* **1980**, *114*, 89–115. https://doi.org/http://dx.doi.org/10.1016/S0022-0728(80)80438-4.

Chapter 4: Deconvoluting surface-bound quinone proton coupled electron transfer in unbuffered solutions: towards a universal voltammetric pH electrode

4.1 Overview

Whilst quinone proton coupled electron transfer under buffered conditions, is well understood, the situation is more complicated in unbuffered solutions. With a view to producing a quinone based voltammetric pH sensitive electrode that can function universally in both buffered and unbuffered solutions by following a two electron ($2e^-$) / two proton ($2H^+$), Nernstian pathway over a wide pH range, the voltammetric response of surface-bound quinones directly integrated into a boron doped diamond (BDD) electrode is investigated. A laser ablation process enables both integration of quinones into the BDD electrode surface with a high pKa_1 (first protonation state) and with controllable, very low surface coverages. Under buffered conditions, the $2e^-/2H^+$ pathway is followed across the entire pH range. The measured electron transfer (ET) rate constant values, from Laviron analysis, are also high, indicative of fast ET pathways. Under unbuffered conditions, deviations are seen in the neutral region (pH 6-8), away from the expected $2e^-/2H^+$ behavior. We show that this is due to a local pH change caused by the consumption and generation of protons at the electrode surface during the redox electrochemistry of the quinone. By reducing surface coverage, down to two orders of magnitude below that of a monolayer ($\sim 4 \times 10^{-12}$ mol cm^{-2}; the limit of our laser ablation process) local pH changes can be reduced but are not eradicated completely. By moving to a pulsed voltammetric technique, where for each potential step, protons consumed at the electrode are immediately replaced, it is possible, provided the surface coverage is low enough, to obtain a Nernstian $2e^-/2H^+$ response across a wide pH range in unbuffered solution.

4.2 Introduction

Quinones are one of the most important and ubiquitous organic redox couples and have been subject to over a century of electrochemical research.[1,2] Their electron transfer properties in buffered aqueous environments are key to a range of biological systems, such as mitochondrial ATP synthesis[3] and electron transport[4] . Moreover, the redox electrochemistry of quinones has been utilized in redox flow batteries[5] and their biological activity underpins some forms of cancer chemotherapy treatments.[6] Quinones are also used commercially to generate hydrogen peroxide on the ton scale,[7] via the quinone-catalyzed oxygen reduction reaction (ORR).[8]

The electrochemistry of quinones has been extensively studied, with the nine-membered square scheme (Figure 4.1) proposed by Jacq,[9] used as a basis for interpreting their electrochemical response in aqueous solutions.[10] Quinones can undergo a two electron reduction, accompanied by reaction with up to two protons ($2e^-/2H^+$), dependent on the solution pH relative to the pK_a of the quinone employed. Such reactions, denoted proton coupled electron transfer (PCET), can proceed in either a stepwise fashion, with either proton or electron transfer occurring first (Figure 4.1, green dotted line)[11] or via a concerted process where the proton(s) and electron(s) are transferred in a single kinetic step (Figure 4.1, blue dotted line).[12,13] In the case of buffered systems only one voltammetric peak is typically observed.

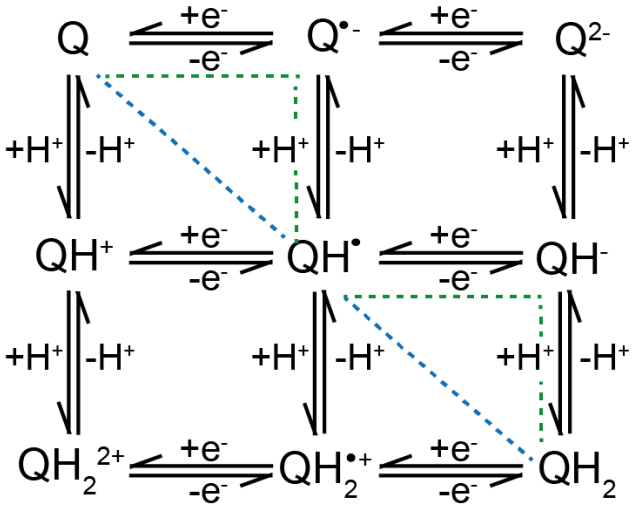

Figure 4.1: Quinone nine-membered scheme of squares, showing the proton (H+) dependent stepwise (green dotted line) and concerted (blue dotted line) PCET routes.

Utilizing the Nernst equation, the redox potential and thus the position of the quinone oxidation/reduction peaks will shift by 59 mV / pH unit at 298 K,[14] provided p$K_{a,1}$ (the first protonation state of the quinone) has not been reached. Note, it is this proton dependence on the peak potential, that has resulted in quinone electrochemistry being utilized in the development of voltammetric-based pH electrodes.[15–19] As the pH exceeds p$K_{a,1}$ the mechanism switches to a $2e^-/1H^+$ reaction forming QH^- and equating to a 30 mV / pH unit shift.[14] If the basicity is increased further, and p$K_{a,2}$ is reached the reaction becomes pH independent and $2e^-$ only (0 mV / pH unit), forming Q^{2-}.[14] This is akin to the quinone response found in aprotic (organic) media, which typically results in a simple two-electron transfer reaction, defined by two redox peaks. [20] However, in contrast, in aqueous media only one voltammetric peak is seen for the $2e^-$ reduction process. This is attributed to the strong hydrogen bonding of in particular Q^- with water, shifting the second reduction potential (Q^-/Q^{2-}) much more positive than the first (Q/Q^-), so they are indistinguishable.[21,22]

The understanding of quinone PCET in unbuffered aqueous media is significantly more challenging, with the complexity of the system highlighted by the limited number of studies conducted in the area, compared to buffered media.[23–34] Many studies observe a deviation from a $2e^-/2H^+$ response, well before the pH exceeds pK_{a1},[23,24,27] which coincides with the appearance of a second wave in the cyclic voltammogram (CV).[14,23,24,27,28] Precise understanding of why this occurs is subject to debate.[23,24] However, most interpretations agree that an insufficient number of protons for the reduction of all the quinones by the $2e^-/ 2H^+$ pathway is responsible.[14,23,28] The first wave is typically attributed to the $2e^-/2H^+$ route, whilst the second is thought to represent the proton independent, $2e^-$ reduction to Q^{2-}, with Q^{2-} existing in an equilibrium mixture of QH_2, QH^- and Q^{2-} dependent on the basicity of Q^{2-}. The prominence of the second wave (Q/Q^{2-}) and its position on the potential axis, i.e. the ease at which Q undergoes reduction to Q^{2-}, is thought to be controlled by the relative concentrations of Q, QH^-, Q^{2-} and OH^- and the associated pK_a values.[23] With increasing pH, the first wave disappears. In contrast, in buffered solutions, for all pH values, one wave results, due to either $2e^-/2H^+$, $1H^+$ or $0H^+$ depending on whether $pK_{a,1}$ / $pK_{a,2}$ has been exceeded.

To explain the origin of the lack of available protons in unbuffered solution, researchers highlight two factors, which themselves are interconnected: (i) the

importance of the ratio of quinone concentration [Q] to [H^+] in bulk solution.[23] Experiments show quinone electrochemical responses in unbuffered solution mimic those in buffered solution provided [H^+]>[Q];[23] as [H^+] ~ [Q] the second wave emerges. (ii) Local pH changes in the electrode/electrolyte reaction layer.[24,28] In particular, simulations have shown that by making the electrochemical measurement, the local pH is increased, due to the consumption of protons during quinone reduction.[24,27,29,30] For example, the interfacial pH can increase by up to 5–6 pH units[24] compared to the buffered solution, during the electrochemical reduction of solution-phase quinone molecules at neutral pH. This phenomenon was also used to explain the appearance of a second wave in the CV for hydrazine (also a PCET process) as the buffer capacity of the system was decreased.[35] Furthermore, as quinones can also catalyze ORR[36,37] and ORR itself consumes protons, the presence of oxygen may also lead to additional local pH increases along with contribution of an ORR faradaic signal to the quinone response.[31] ORR induced pH changes are either neglected in the interpretation of PCET in unbuffered solutions, or circumvented by deaerating the solution.[16,17]

Much of the work exploring the quinone redox mechanism in unbuffered solution is performed with solution-phase quinone species, where pK_{a1} typically falls in the pH range 7.7-9.9.[23,38] In contrast, it is well-documented that surface-bound quinone species exhibit pK_{a1} values higher than their solution-phase counterparts.[39] This can be attributed to changes in the local environment when the quinone is tethered to an electrode surface, where entropic changes are significantly different to those in bulk solution.[39] To date, only a limited number of studies have explored the pH response of surface tethered quinones in unbuffered solutions[24,27,28,32,33], using either physical adsorption or chemical and electrochemical functionalization at mercury,[28] screen printed carbon,[33] gold[27] and edge plane pyrolytic graphite (EPPG) electrodes.[24] Interestingly, as with solution studies, similar anomalous behavior is also observed, with a second wave emerging as the pH is increased, again well before the pH exceeds pK_{a1}, which with further pH increases results in a single wave.[27] Surface coverages of $\Gamma = 2.8 \times 10^{-10}$ mol cm^{-2} [27] (monolayer on gold) and $\Gamma = 2.5 \times 10^{-9}$ mol cm^{-2} [24] (multi-layer on EPPG) were reported.

Given that sp^2 carbon materials, such as glassy carbon (GC) and EPPG also naturally contain a variety of high-order oxides, including quinone groups, these un-

functionalized electrodes have also been used in studies. The quinones on these electrodes are found at sub-monolayer surface coverages (e.g. $\Gamma = 5.9 \times 10^{-11}$ mol cm^{-2} for EPPG).[17] Such electrodes have also been used to measure solution pH under buffered, deaerated conditions, given the high reported pKa_1 values (pKa_1 ~13).[16,17] Recent results suggest that when a quinone molecule is strongly electronically coupled to an electrode surface, as is likely to be the case with a surface group directly integrated into the electrode, for PCET, ET cannot happen unless accompanied by ion transfer i.e. the electron only pathway is not viable.[40]

In this chapter, we explore the mechanism of surface bound quinone electrochemistry with a view to developing a measurement methodology that can be used to accurately measure solution pH across an environmentally relevant pH range (4-10) in both unbuffered and aerated solutions. Given that [Q] and ORR, are important considerations we explore the effect of quinone surface coverage $[Q]_{surface}$ on the response, both in the absence and presence of oxygen. For these studies we use a boron doped diamond (BDD) base material,[41] which is itself insensitive to ORR,[42] and controllably introduce surface bound quinone groups into the surface using a laser ablation approach[18,43]. These groups are directly integrated into the surface and are therefore expected to be strongly electronically coupled to the electrode. These electrodes are denoted BDD-quinone (BDD-Q). This approach enables us to go below the monolayer limit by ~two orders of magnitude; such low coverages have not been reported before using conventional physical or chemical functionalization routes.

4.3 Experimental

4.3.1 Materials and solutions.

All solutions were prepared from Milli-Q water (Millipore Corp.) with a resistivity of 18.2 MΩ cm at 25°C. Negligible sp^2 carbon content,[42,43] freestanding (470 μm thick) BDD was used as the base material in this study, with a boron dopant concentration of ~3×10^{20} boron atoms cm^{-3} i.e. metallic doping (Element Six Ltd, Harwell, UK). Carmody buffers were prepared over the range 4-10 using boric acid (H_3BO_3, 99.97%; Sigma Aldrich), citric acid ($C_6H_8O_7$, ≥99.5%; Sigma-Aldrich) and tertiary sodium phosphate (Na_3PO_4, ≥95%; Sigma-Aldrich) with a buffer capacity of 25-30 mM per pH unit.[44] For unbuffered solutions 0.1 M potassium nitrate (KNO_3, ≥99.5%; Puratronic) was pH adjusted with 1 M sulfuric acid (H_2SO_4, 98%, Sigma-Aldrich) or 1 M KOH (≥99.97%; Sigma-Aldrich) to create unbuffered pH values across the 4-10 range. The conductivity of the solutions was maintained at ca. 10 mS cm^{-1}. The pH of all aqueous solutions was tested against a glass pH probe (HQ411d benchtop pH probe, Hach Company), calibrated using pH 4, 7 and 10 standard buffer solutions. Non-aqueous experiments were carried out in degassed 0.1 M Tetrabutylammonium hexafluorophosphate (TBAHFP) (Sigma-Aldrich, UK, >99.0%) in acetonitrile (Fisher-Scientific, UK) dried over 4Å Molecular sieves (Sigma-Aldrich, UK). For experiments in the presence of protons of 0.02 M p-toluenesulfonic acid (p-TsOH) (Sigma-Aldrich, UK, >99.0%) was added.

4.3.2 Electrode fabrication.

BDD cylinders of 1 mm diameter, lapped on the top (growth) surface to approximately nanometer scale roughness, were machined from a six inch BDD wafer using a 355 nm Nd:YAG 34 nanosecond laser micromachiner (E-355H-ATHI-O system, Oxford lasers). The BDD cylinders were acid cleaned in boiling concentrated H_2SO_4 (98%), saturated with KNO_3, to oxygen terminate the surface and remove any loosely contacted sp^2 carbon introduced during the laser micromachining step. Ti (10 nm) / Au (400 nm) was sputtered (Moorfields MiniLab 060 platform sputter/evaporator) onto the back of the BDD cylinders and annealed at 400°C for 5 h, to form a reliable ohmic contact. The BDD cylinders were then sealed in glass capillaries (o.d. 2 mm; i.d. 1.16 mm; Harvard Apparatus Ltd., Kent, UK) and the top surface exposed by polishing away the glass with carbide grit paper disks and alumina (0.05 μm) paste

(Buehler, Germany). Hexagonal arrays containing a fixed number of 50 μm diameter laser pits with a centre to centre spacing of 100 μm (Figure 4.2, inset), were ablated into the BDD surface using laser power densities in the range 14-980 J cm^{-2}. The power density was altered by changing laser power and laser pitch overlap (how each laser pulse overlaps with the next) to produce BDD-Q electrodes containing different quinone surface coverages. After laser micromachining sp^2 carbon regions of the electrode were again cleaned to remove loosely bound sp^2 carbon and oxidatively "activated" to form stable quinone groups on the electrode surfaces. This involved heating the electrode at ~200°C for 15 min in concentrated H_2SO_4 (98%) saturated with KNO_3,[18] followed by anodic polarization under constant current conditions (+0.1 mA for 60 s) in 0.1 M H_2SO_4.[18]

4.3.3 Electrochemical setup.

For electrochemical measurements a three-electrode configuration was utilized with BDD-Q as the working electrode, a platinum wire as the counter electrode and a silver/silver chloride (Ag|AgCl) electrode as the reference in aqueous solutions, in non-aqueous solutions a homemade Ag|$AgNO_3$(10 mM $AgNO_3$, Sigma-Aldrich, UK) reference was used. For ORR measurements, a GC electrode (3 mm diameter: ALS, Japan), mechanically polished using alumina (0.05 μm) paste, was also employed. A CHI 760C potentiostat was used for all measurements, except current-time where an Ivium compactstat was utilized. For anodic polarization a Galvanostat was employed (Keithley 6220 Precision Current Source). Quinone surface coverage (Γ) measurements were made by running a CV in pH 2 Carmody buffer from 0.7 V to 0 V and back to 0.7 V.[43] The charge passed (q) was determined by integrating the oxidative peak and calculated using $\Gamma=q/nAF$ where n = number of electrons used in the reaction (2), A = the electrode area, calculated by interferometry (cm^2) and F = Faraday's constant (96485 C mol^{-1}); as shown in Figure 4.4 for the three BDD-Q electrodes used in this study. For electrochemical measurements square wave voltammetry (SWV) was employed at a frequency of 150 Hz, amplitude of 0.1 V, step potential of 1 mV. The current was averaged over the last 61- 100% of each pulse.

4.3.4 White Light Interferometry (WLI).

A Bruker ContourGT (Bruker Nano Inc., USA) was used to record WLI profiles. 3D rendering of interferometry data was performed, and electrode area calculated using Gwyddion 2.46.[45]

4.4 Results and Discussion

4.4.1 Controlling Quinone Surface Coverage, Γ:

During the laser ablation procedure (Figure 4.2), carbon leaves the surface in the form of both solid particulates and carbon containing gases. Plasma generation, promotes further etching of the BDD surface and re-deposition of carbon in a non-diamond-carbon (graphitic – sp^2) form. Shallow, at the μm level, sp^2 containing 'pits' are thus created in the electrode surface, When exposed to oxidizing conditions (such as acid treatment and anodic polarization) these regions become terminated with quinone groups, which are not intrinsically present on the bare BDD electrode surface (Figure 4.2).

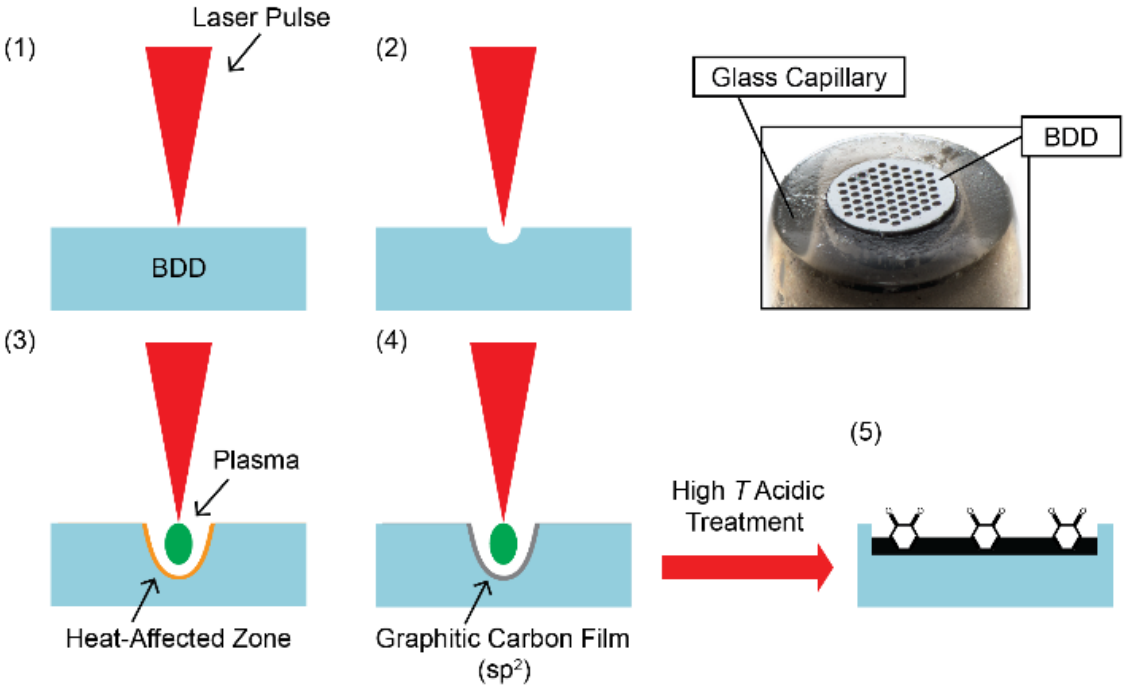

Figure 4.2: Schematic of the nanosecond laser ablation process on BDD. (1) A laser pulse is focused on the BDD (2) ablation occurs (3) a plasma is generated, locally heating and etching further into the BDD. (4) Re-deposition of a graphitic carbon film occurs. (5) After activation BDD-Q results. Inset: Glass-sealed BDD-Q electrode, showing the 1 mm BDD disk electrode and the laser machined hexagonal array of sp^2 carbon containing pits.

To assist in determining appropriate BDD-Q Γ values for investigation, we first present a simple calculation which enables us to consider how proton surface concentration $[H^+]_{surface}$ relates to $[Q]_{surface}$. To do this we assume a typical diffusion

length, δ, and calculate the number of protons per unit area (= $\delta \times$ bulk concentration). To calculate δ, we assume the flux of protons arriving at the surface is diffusion-limited, and there is diffusional overlap between pits. Under such conditions the following equation applies:

$$\delta = D^{1/2} F / 2.69 \times 10^5 n^{1/2} v^{1/2} \qquad [4.1]$$

where D is the diffusion coefficient of protons (=7.8 x 10^{-5} cm^2 s^{-1}),[46] and v is a typical scan rate (=1 V s^{-1}; *vide infra*); δ = 0.0022 cm. Thus for pH values of 4, 7 and 10, $[H^+]_s$ = 2.2 × 10^{-10} mol cm^{-2}, 2.2 × 10^{-13} and 2.2 × 10^{-16} mol cm^{-2} s^{-1} respectively. Given monolayer coverage is ca. 10^{-10} mol cm^{-2}, [47] we deliberately work with much lower quinone surface coverages in order to operate across a pH range where $[Q]_{surface}$ is both > $[H^+]_{surface}$ and < $[H^+]_{surface}$.

To alter Γ, the laser fluence (power per unit area) can be changed (Figure 4.3), and therefore BDD surface sp^2 content and Γ can be finely controlled. The lower limit of fluence is set by the ablation threshold of the material; 12.1 J cm^{-2} for BDD, calculated by the D^2 method.[48] From the ablation threshold until ~280 J cm^{-2} there is a linear relationship between laser fluence and Γ, with increasing laser fluence leading to an increased Γ. This can be attributed to a greater degree of material heat damage and the breaking of more sp^3 carbon bonds to leave more stable sp^2 carbon. Above 280 J cm^{-2} Γ reaches a plateau, this can be considered to be a surface with the same degree of heat damage being translated down through the material. The maximum fluence is limited by the power of the laser system used. In addition to changing laser fluence, the pulse density can be also altered to change Γ.

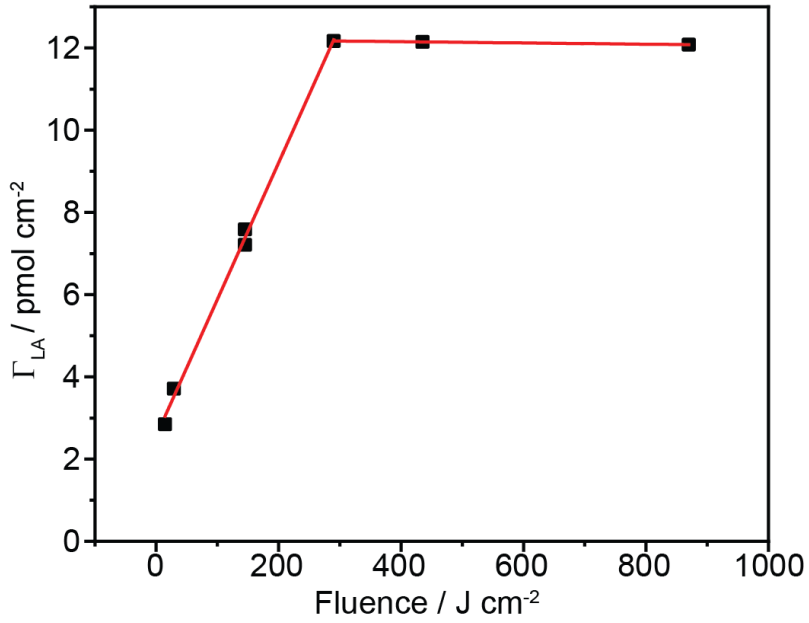

Figure 4.3: The relationship between Γ and laser fluence at a pulse density of 2 × 10^6 cm^{-2}

Under the ablation conditions employed, by changing the laser fluence, Γ values varying between 1.2×10^{-11} mol cm^{-2} and 3×10^{-12} mol cm^{-2} could be reliably obtained. The latter at the ablation threshold of the material, representing the lowest surface coverage possible using this nanosecond laser ablation approach. Γ is calculated by consideration of the sp^2 created areas *only*; sp^3 BDD contains negligible quinone content.[43] These surface coverages are all sub-monolayer and two orders of magnitude lower than a typical monolayer coverage. Such low surface coverages would be extremely challenging to achieve using traditional surface chemical functionalization routes.

Through control of the laser fluence 3 electrodes of differing Γ were created (Figure 4.4). The surface coverages were (a) $1.02 \times 10^{-11} \pm 3 \times 10^{-13}$ mol cm^{-2} (highest – BDD-Q1, red) (b) $8.78 \times 10^{-12} \pm 2 \times 10^{-13}$ mol cm^{-2} (BDD-Q2, blue) and (c) $4.21 \times 10^{-12} \pm 9 \times 10^{-14}$ mol cm^{-2} (lowest – BDD-Q3, green).

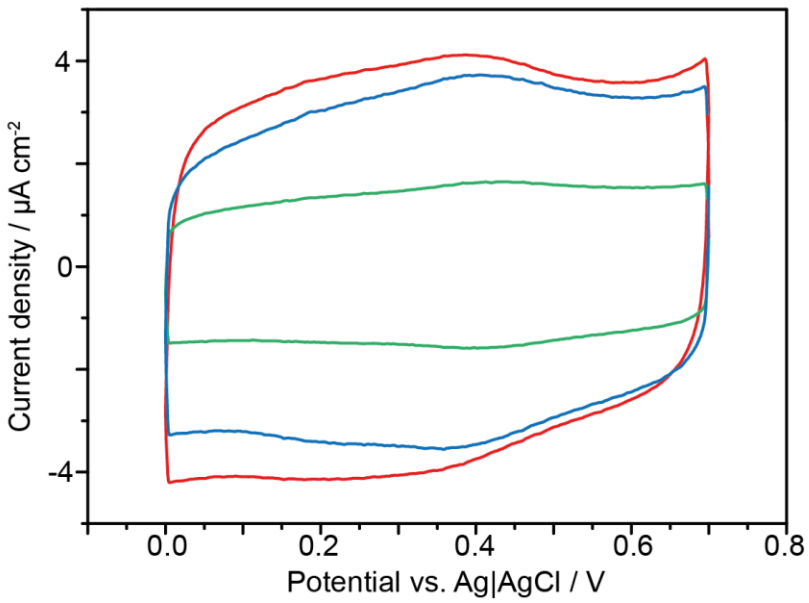

Figure 4.4:CVs of electrodes BDD-Q1 (red) BDD-Q2 (blue) and BDD-Q3 (green) in pH 2 buffer, recorded at 0.1 V s^{-1}, showing the presence of a reductive/oxidative quinone peaks

4.4.2 Cyclic Voltammetry.

The effect of Γ on the unbuffered CV response for three BDD-Q electrodes of different Γ values *vide supra* was recorded over the pH range 4-10 (a CV every ~0.3 pH unit). A fast scan rate of 1 V s^{-1} was employed to discern the quinone PCET faradaic signal due to the low surface coverages employed. Typical CV responses for the three different electrodes are shown in Figure 4.5 for (a) BDD-Q1, (b) BDD-Q2 and (c) BDD-Q3 in unbuffered and aerated solutions. All 57 CVs recorded showed *one* wave only. In all pH solutions (buffered and unbuffered), the peak full width half maximum is broader (190 ± 20 mV) than that theoretically predicted, 45.3 mV for a $2e^-$ process;[49] as is often witnessed for surface bound quinone species in buffered solutions.[50,51] Although there is debate in the literature whether this broadening is due to electrostatic interactions between neighbouring groups,[52,53] given the low densities involved it is more likely non-equivalent active sites[54,55] or surface heterogeneities are responsible.[56]

Figure 4.5d displays the anodic (oxidation) peak position (Ep_a, filled symbols) and cathodic (reduction) peak position (Ep_c, unfilled symbols), as a function of pH for all three electrodes, over the pH range 4-10. The green line represents the buffered

(aerated) response of the three BDD-Q electrodes for pH's 4, 7 and 10. Under buffered conditions, a Nernstian pH dependence of 62 ± 3 mV per pH unit is observed for both the reductive and oxidative peaks, as expected for $2e^-/2H^+$ transfer. The linear buffered data also indicates these quinone groups, which have been directly integrated into the BDD electrode surface, have a $pKa_1 \geq 10$. Under unbuffered conditions, deviations away from the expected Nernstian response (green line) are most significant in the neutral region (defined as the pH range 6 - 8). Whereas in both the acidic (pH range 4 – 6) and alkali regions (pH range 8 – 10) the response, especially for the anodic potentials appears to return to the ideal 59 mV response, indicative of $2e^-/2H^+$ Nernstian behavior. The deviations are most apparent for BDD-Q1, which has the highest Γ, and least for BDD-Q3, which has the lowest Γ, therefore suggesting Γ is playing a role in the resulting electrochemical response. As the pH is increased past 8, the response especially for the anodic potentials, returns to close to $2e^-/2H^+$ Nernstian. Deviations are also seen in the pH neutral region when plotting the mid-point of the two peaks, $E_{1/2}$ i.e. $(Ep_a + Ep_c / 2)$ as shown in Figure 4.5e.

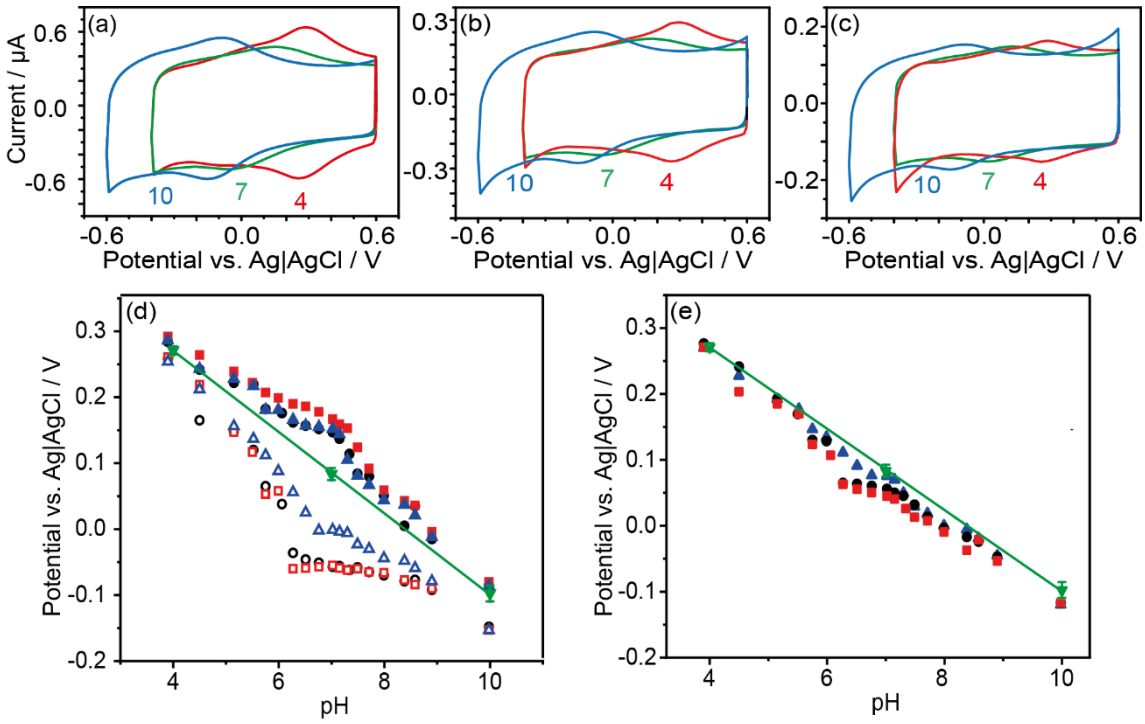

Figure 4.5: CV response in unbuffered solutions at pH 4, 7 and 10 for (a) BDD-Q1, (b) BDD-Q2 and (3) BDD-Q3. (d) Anodic (filled) and cathodic (unfilled) peak positions for BDD-Q1 (red,▪), BDD-Q2 (black, ●), and BDD-Q3 (blue, ▲) across the 4-10 pH range. The peak centre in buffered solutions averaged across all 3 electrodes is plotted in green (gradient= 62 mV). (e) Peak centre potentials for BDD-Q1 (red,▪), BDD-Q2 (black, ●), and BDD-Q3 (blue, ▲) across the 4-10 pH range.

Interestingly, in contrast to all other studies, even when the CV behaviour starts to deviate from the $2e^-/2H^+$ line in this study, the emergence and then dominance of a second wave in the CV is never observed. This suggests that in this system, whilst some form of proton depletion must be present due to the observed deviation, this effect is not significant enough to force the system down a proton independent, $2e^-$ only pathway.[23] The question is why is this behaviour observed in this system, whereas other unbuffered surface (and solution) studies do not? It is believed the answer lies in the extremely low $[Q]_{surface}$ implemented here, up to two orders of magnitude smaller than monolayer. At such low surface coverages, it is more meaningful to think of the electrode as a sparse array of active sites (where each active site represents a quinone group) embedded within an electrochemically inert matrix (the sp^2 regions). Under these conditions, the flux of H^+ per quinone molecule (assuming they are diffusionally isolated) is significantly higher than the situation where the whole surface is considered active, by 5 orders of magnitude. This leads to $[H^+]_{surface}$ values much

higher than originally considered and a greater compensation of proton depletion effects.

Furthermore, the CV data in Figure 4.6a shows the absence and then appearance of a PCET wave for BDD-Q3, in non-aqueous solvent as protons are added to the solvent. Such behavior indicates the quinones are strongly coupled to the electrode surface, as the PCET mechanism is concerted and proton transfer is required to facilitate ET. Hence if the system in unbuffered aqueous solutions did switch to $2e^-$ only, there should be no redox response observed in the CV. In this study a wave is observed for all pH values considered.

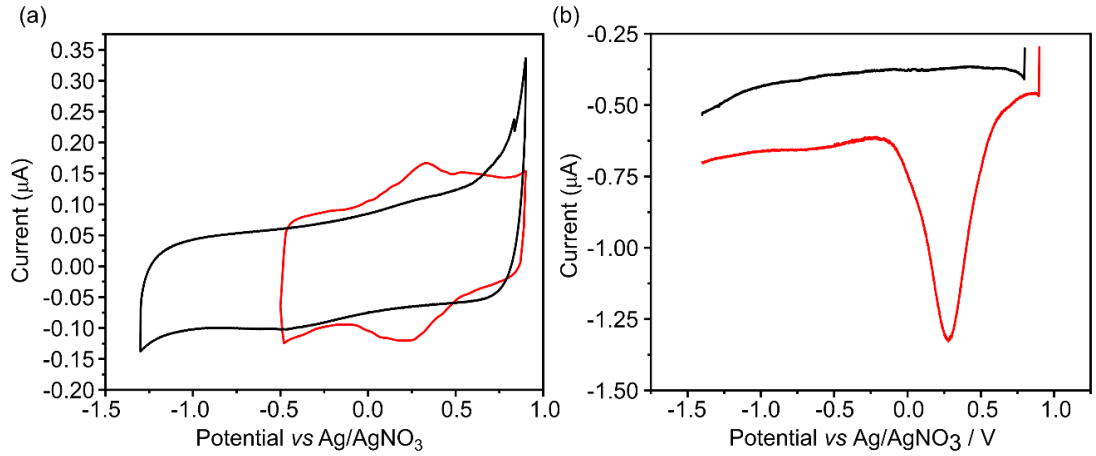

Figure 4.6: CV(a) and SWV(b) of BDD-Q3 in 0.1 M TBAHFP in Acetonitrile (black) and with 0.02 M p-TsOH (red).

In the absence of protons, no voltammetric wave is observed for the quinone reduction (CV, Figure 4.6a-black; SWV, Figure 4.6b-black). This suggests that the quinone groups cannot undergo a $2e^-$ proton independent reduction, and as such the groups are strongly electronically coupled to the electrode and the reaction occurs by a concerted PCET mechanism. This explains the absence of a second wave across the entire pH range in unbuffered solutions, as this wave is attributed to the $2e^-$ proton independent reaction to Q^{2-}, a reaction that is demonstrated to not occur in this system. On the addition of 0.02 M p-TsOH a new wave appears in the CV (Figure 4.6a, red) and SWV (Figure 4.6b, red) at ~0.25 V vs $Ag/AgNO_3$. This wave can be attributed to the concerted $2e^-/2H^+$ reduction of surface quinone groups.

Due to the absence of a proton independent route for our system, the deviations in the neutral region of Figure 4.5 are therefore suggestive of a change in the equilibrium potential of the $2e^-/2H^+$ reaction due to a change in the local proton concentration as a result of the quinone electrochemical reaction. Under acidic pH, consumption /generation of protons, during reduction/oxidation at the interface is clearly not in sufficient quantities to perturb the interfacial acidic pH. Under alkaline conditions, excess protons produced during oxidation will be immediately neutralized by the high concentrations of hydroxide ions, which are also in high enough concentration to prevent local proton depletion effects, during reduction, being registered as a local pH change. However, in the neutral region, where the equilibrium concentrations of H^+ and OH^- are most finely balanced e.g. at neutral pH (both equal 1×10^{-7} mol L^{-1}), the data suggests there are not enough protons or hydroxide ions to accommodate the local pH changes and the quinone electrochemistry therefore reflects this change. Hence under reductive conditions (proton consumption) the local pH increases compared to bulk, resulting in a more alkaline local solution and a decrease in E_{pc}, whilst under oxidative conditions (proton generation) the local pH becomes more acidic, and E_{pa} increases. Away from this region, at higher and lower bulk pH, local proton perturbation effects are less strongly felt.

It is also important to note that the shifts in Ep_a and Ep_c, with pH, are not equivalent. Deviations in Ep_c from the Nernstian ($2e^-/2H^+$) line are much larger, suggesting the system locally shifts more alkaline from the bulk pH than acidic, for a given pH during quinone PCET in the deviation region. One explanation for this is the possible presence of side reactions in the cathodic region also contributing to a local pH increase, such as ORR discussed in further detail *vide infra*.

The peak to peak separation, ΔE_p, in the buffered systems for all three electrodes is 9 ± 2 mV, close to the expected 0 mV for a surface bound ET system.[49] For the unbuffered solutions, at pH 4 , ΔE_p is 31 mV (BDD-Q1), 26 mV (BDD-Q2) and 24 mV (BDD-Q3) At pH 7, ΔE_p has increased to 222 mV (BDD-Q1), 204 mV (BDD-Q2) and 153 mV (BDD-Q3), whilst at pH 10, ΔE_p decreases back to 73 mV (BDD-Q1), 63 mV (BDD-Q2) and 34 mV (BDD-Q3). For each pH the largest ΔE_p values are recorded for the highest Γ BDD-Q electrode. This trend of ΔE_p increasing from pH 4-7 and then decreasing from pH 7-10 correlates qualitatively with the data observed in Figure 4.5d

and e. Thus the pH change in the local environment, could play a role in the changing peak separation during the timescale of the measurement, which is more pronounced under neutral conditions (Figure 4.5d). [12]

It is also interesting to consider the ET kinetics of the quinone PCET reaction (k_{et}) as a function of pH in both buffered and unbuffered solutions. Figure 4.7 shows Laviron plots (E_{pa} and E_{pc} versus log scan rate, *v* over the *v* range 0.1 – 100 V s^{-1})[57] for BDD-Q3, for pH 4, 7 and 10 in both buffered (filled symbols) and unbuffered (unfilled symbols) solutions. BDD-Q3 was chosen as it shows the smallest deviations from Nernstian behavior in unbuffered solutions and therefore subsequently the smallest local pH environment changes throughout the scan. From the Laviron plots information on k_{et}, the ET rate coefficient α (values given in Table 4.1) and ET mechanism can be obtained. In buffered solutions, the linear portions of the Laviron plots for all three pH values gives a ~60 mV per decade response, very close to that expected for a $2e^-/2H^+$ process. From these gradients, which are equal to $RT/\alpha nF$, α was calculated to be 0.50 ± 0.02 for both the anodic (black, E_{pa}) and cathodic (red, E_{pc}) linear branches.

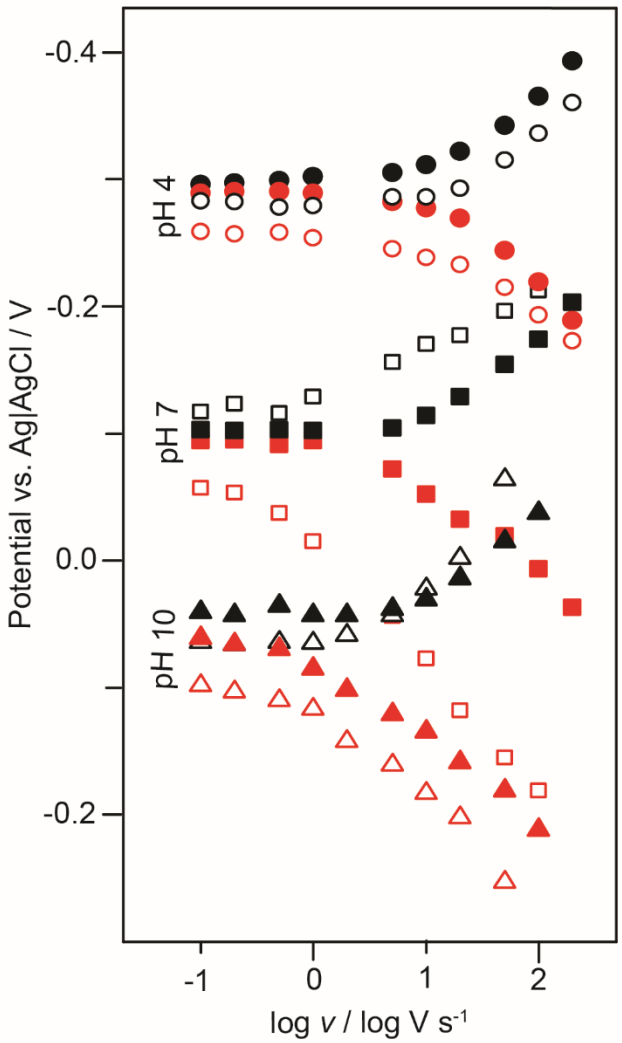

Figure 4.7: Laviron plots for pH 4 (●), 7 (▪) and 10 (▲) in both buffered (filled symbols) and unbuffered (unfilled symbols), collected at scan rates 0.1 to 100 V s^{-1}, for BDD-Q3, showing the anodic (black) cathodic (red) peak potential positions

From the intercepts of the linear regions of the Laviron plots, k_{et} can be calculated. In buffered solution, for the oxidation reaction, no change in k_{et} is observed for pH 4, 7 and 10 ($k_{et,ox}$ = ~220 – 250 s^{-1}). Note this value is high for k_{et} when compared against typical quinones chemically tethered to an electrode surface via a linker chain.[58,59] This value supports the theory that the quinone here is directly integrated into the electrode surface. However, for the reduction reaction, k_{et} slows down with increasing pH from 260 s^{-1} at pH 4 to 73 s^{-1} at pH 7, and 28 s^{-1} at pH 10 (Table 4.1). One possible explanation is that in buffered solutions, it is the proton concentration that rate limits. For oxidation as the quinones are already in their reduced form (QH_2), H^+ are simply released back into solution. In contrast, for reduction, there must be sufficient protons to support the reduction reaction; proton concentration decrease logarithmically as the

pH increases. This data also suggests that in this system, PCET is concerted due to the dependence of the ET rate on pH not following the predicted W-shape as expected for a stepwise process.[60] PCET on a strongly electronically coupled system has also been shown to exhibit concerted ET across a wide pH range, resulting in a single wave.[40]

In unbuffered solutions, at pH 4, the measured parameters (Table 4.1) are close to those of a buffered system, however at pH 7 this is no longer holds, k_{et} has dropped significantly to 5.4 (anodic) and 4.8 (cathodic), with concomitant changes in α to 0.29 (anodic) and 0.71 (cathodic) indicating changes in reorganization energy for the reactions. At pH 7 the largest changes in the system from Nernstian behavior were observed (Figure 4.5d and e). As the local pH of the solution is changing throughout the measurement, this also leads to a thermodynamic change in the peak potentials which can convolute changes in the kinetics, which are also dependent on the local pH.[61] At pH 10, k_{et} rises to 57 (anodic) and 14 s^{-1} (cathodic). We therefore note the difficulty of interpreting a PCET system in unbuffered aqueous media, due to the convolution of kinetic and local environment (pH) changes.

pH		α	$k_{et,(Ox)}$ (s^{-1})	$k_{et,(red)}$ (s^{-1})
4	Buffered	0.52	250	260
	Unbuffered	0.51	250	190
7	Buffered	0.52	230	73
	Unbuffered	0.71	5.4	4.8
10	Buffered	0.52	220	28
	Unbuffered	0.48	57	14

Table 4.1:Electron transfer rates in buffered and unbuffered solutions at pH 4, 7 and 10 (2 s.f.).

4.4.3 Pulsed Voltammetry

The CV data in unbuffered solutions (Figure 4.5) strongly suggest there is perturbation of the local pH during the quinone electrochemical measurement, even with significantly reduced surface coverages compared to all previous work. Whilst it is conceivable to go to even higher scan rates (> 1 V s^{-1}) in order to increase proton diffusional fluxes with a view to minimizing local pH changes, capacitive currents become a significant consideration. Going to lower Γ using the laser ablation

technique would also be very challenging, as we are very close to the laser ablation threshold with the lowest fluence employed. It is therefore prudent to consider alternative electrochemical waveforms as a means to minimize, and ultimately negate, the local pH change. The use of a pulse technique, such as square wave voltammetry (SWV) offers distinct advantages over CV; for each step potential, the potential is pulsed first in one direction and then the other, with a defined potential pulse amplitude (Figure 4.8a). The current is averaged in both directions, i_1 and i_2, over a defined portion of the current-time component of the decay curve, which is free from capacitive currents. The output current per potential step, Δi is thus:

$$\Delta i = i_1 - i_2 \qquad [4.2]$$

where i_1 is the forward current and i_2 is the reverse current. In this way a current (Δi) – voltage curve is constructed, as shown in Figure 4.8b.

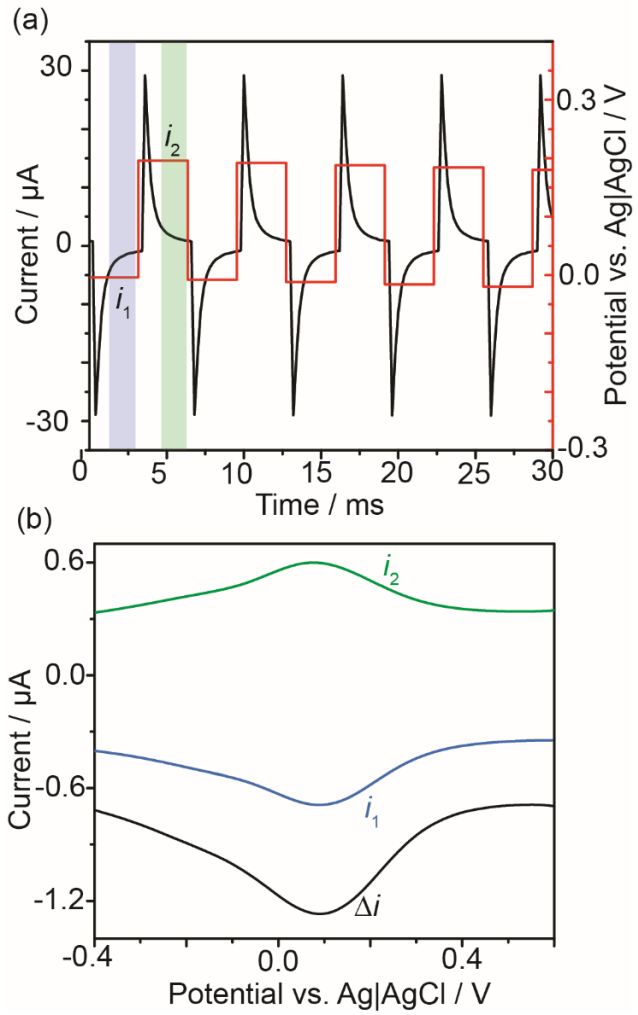

Figure 4.8:(a) Current-time transients for SWV showing the pulse sequence and (b) SWV response showing i_1 (cathodic, blue) and i_2 (anodic, green) currents recorded during the SWV cycle along with the Δi (black) for buffered pH 7 solution on the BDD-Q3 electrode.

For the surface bound quinone, over the voltage range of interest, the SWV can be pulsed in both the reductive and oxidative directions of the quinone PCET process, per step potential. This means it should be possible to both consume and generate protons at the electrode surface, with the aim to minimize, and ultimately negate, the local pH change. We chose a peak amplitude of 0.1 V, which is sufficient to capture both the quinone reduction (blue line) and oxidation (green line) processes per step potential, Figure 4.8b, along with a high pulse frequency of 150 Hz. This equates to each individual current-time trace lasting 3.33 ms (with sampling over the last 61%-100% of the trace). The high frequency leads to large currents, but isn't too high that the analyzed signal is dominated by capacitive contributions.

Figure 4.9a shows typical SWVs, scanning in a cathodic direction, for BDD-Q 1,2 and 3 electrodes in both buffered (dotted lines) and unbuffered (full lines) solutions. The smaller currents for the unbuffered response could be due to a decrease in the ET transfer kinetics (Table 1), which will affect the current-time decay profile. Figure 4.9b shows the peak SWV potentials plotted versus pH (over the range 4-10). The dotted line indicates the $2e^-/2H^+$ Nernstian (60 ± 2 mV pH^{-1}) line for the buffered data, $R^2 = 0.9999$. In unbuffered solutions, BDD-Q3 which has the lowest Γ and showed the lowest deviations in Figure 4.5d and e, when operated under potential pulse control now shows a response which is linear over the pH range investigated, $R^2 = 0.9999$. The electrodes BDD-Q1 and 2 show smaller deviations in the neutral region, compared to Figure 4.5d, but they are still apparent. We attribute this to the higher quinone surface coverages present on these electrodes, which are inducing larger local pH changes at the interface that cannot be compensated completely by the potential pulse method. This data thus represents a means by which linear pH-potential behaviour can be obtained using surface functionalized quinones in unbuffered aerated solutions, over a wide pH range.

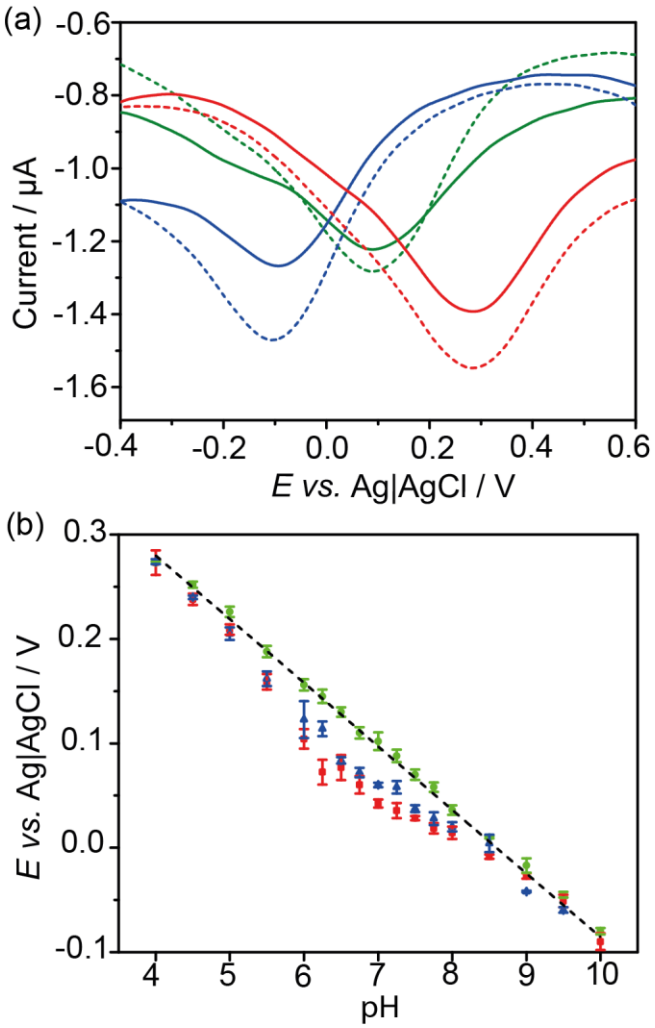

Figure 4.9:(a) Buffered (dashed line) and unbuffered (solid line) SWV responses for the BDD-Q3 electrode. (b) The potential-pH response for BDD-Q1 (red, ▪), BDD-Q2 (blue, ▲) and BDD-Q3 (green, ●) electrodes using SWV (150 Hz, 0.1 V amplitude) in unbuffered aqueous solution. The Nernstian buffered response averaged across all 3 electrodes (dashed line) is also shown.

4.4.4 Impact of the oxygen reduction reaction.

ORR is an inner sphere ET reaction,[62] therefore, the ET kinetics of the reaction are electrode surface dependent. High-quality (sp^3 carbon) BDD is electrocatalytically inert,[41] therefore on BDD, ORR is significantly kinetically hindered compared to sp^2 carbon electrodes. Those sp^2 electrodes that contain higher order oxide groups can show an even higher activity due to the electrocatalytic effect of quinones on ORR.[36] Figure 4.10a shows the ORR response of bare BDD, BDD-Q electrodes 1, 2 and 3 and a GC electrode in a solution containing 0.1 M KNO_3, pH adjusted to 7.0 and oxygen aerated. The dominant wave for ORR is clearly seen on the GC and BDD-Q1

electrodes, with the half wave potential for ORR significantly more cathodic (kinetically hindered) on BDD-Q1 (~-1.0 V) than for GC (~-0.7 V). The ORR responses are significantly smaller on electrodes BDD-Q2 and Q3 and represent the reduced sp^2 content of these electrodes.

Whilst ORR can generate a localized pH change due to the production of OH-,[63] ORR on BDD-Q, as shown in Figure 4.10a, is occurring in a potential window outside that of the quinone PCET (Figure 4.9a). However, quinone groups are also catalytic to ORR[37]. As the quinone content is only a small fraction of the sp^2 content of the laser ablated areas, we expect any quinone-catalysed ORR to show significantly smaller currents than that at the sp^2 carbon areas of the electrode, and occur in a kinetically more favorable position. In Figure 4.9a, very small peaks are seen in the unbuffered SWV's on the left hand side of the main peak. Figure 4.10b shows the SWV response for the BDD-Q3 electrode in an aerated and de-aerated 0.1 M KNO_3 solution, pH corrected to 7.0, with 30 repeat scans. Clearly the peak on the cathodic side of the main peak, labelled (i), can now be ascribed to an oxygen related process, due to its disappearance when deaerating. This peak is postulated to be due to PCET on a quinone species. Repeat scanning, in aerated solution, causes the main peak position to shift in a negative direction, indicative of an increasingly alkaline environment (the shift of -74 mV over 30 scans, equates to a pH change from 7.0 to 8.25). Whilst pulse voltammetry can negate quinone proton depletion / accumulation effects, as ORR is irreversible, OH^- produced cannot be compensated for during pulse voltammetry and is the reason why, after the first scan, repeat scans cause the local pH to rise. It is thus likely quinone-catalyzed ORR is responsible for the larger cathodic offset compared to the anodic offset, from the CV data in unbuffered media, as shown in Figure 4.5d.

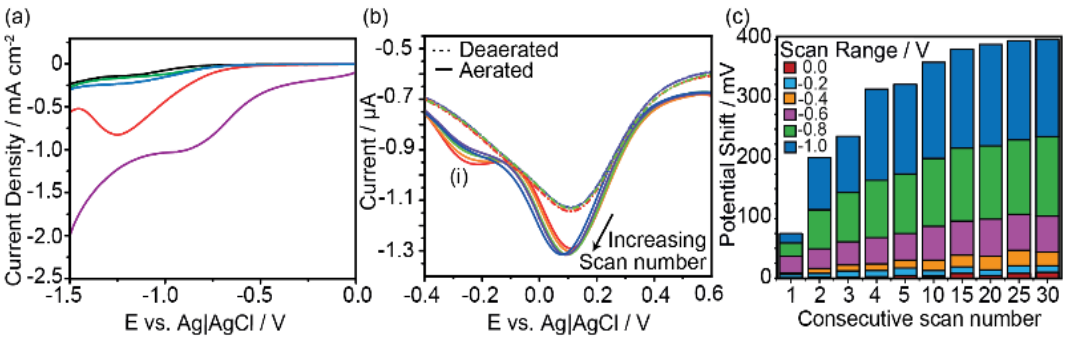

Figure 4.10: (a) LSV of GC (purple), BDD-Q1 (red), BDD-Q2 (blue), BDD-Q3 (green) and bare BDD (black) collected in 0.1 M KNO_3 (adjusted to pH 7); (b) SWV data in aerated and deaerated at solution, pH 7 in 0.1 M KNO_3 for BDD-Q3 and (c) potential shift in mV per consecutive SWV for different scan ranges.

We further illustrate ORR producing local alkali shifts, in figure 4.10c, by systematically increasing the negative end point of the scan range for the SWV from 0.7 V to 0.0, −0.2, −0.4, −0.6, −0.8 and −1.0 V. Each scan is repeated × 30 to exacerbate the local pH change. As we drive the potential more negative, we increase the amount that quinone catalyzed ORR is electrochemically driven, and start to initiate sp^2 driven ORR. For 0.0 V, where little ORR is occurring, the alkali potential shift observed is only 10 mV (pH change 0.17) after 30 consecutive scans. This increases to 11 mV (0.19 pH units), 23 mV (0.39 pH units), 60 mV (1.02 pH units), 133 mV (2.25 pH units) and 170 mV (2.88 pH units) as the potential scan range is swept out further to −0.2, −0.4, −0.6, −0.8 and −1.0 V respectively. We therefore advocate to study PCET on quinone species in unbuffered aqueous solutions consideration must also be given to the impact of side reactions such as ORR on the reaction mechanism. However, by careful control of the potential scan window, and by limiting the number of scans per measurement, ORR induced local pH changes, can be avoided.

4.5 Conclusions

Surface integrated quinone groups produced on a BDD electrode via a laser ablation process, provide a unique opportunity to investigate the mechanism of quinone PCET in an unbuffered environment. This is due to the attributes these electrodes bring, including: a high pKa_1 (>10); strong electronic coupling; and an extremely low surface coverage, down to 10^{-12} mol cm^{-2} (two orders of magnitude lower than typical monolayer coverages).

In buffered solutions over the pH range 4-10, the electrodes show a $2e^-/2H^+$ PCET Nernstian response, whilst in unbuffered solution they exhibit a deviation in the neutral pH region (pH 6- 8), but return to Nernstian as the pH increases. In all cases one wave is observed. The deviation is less severe the lower the quinone surface coverage. Such behavior is unlikely to indicate the response moving away from the $2e^-/2H^+$ path to $2e^-$ only, due to a combination of factors. These include: the high pKa_1 values arising as a result of surface stabilization; the observance of one wave not two even in the deviation region; the fact the $2e^-$ pathway is not supported on the BDD-Q electrode and finally; the extremely high proton fluxes likely to be generated at such sparse surface coverages. We therefore ascribe the reported potential deviation in the unbuffered neutral region (negative for the cathodic scan and positive for the anodic scan) to local proton depletion and accumulation effects at the BDD electrolyte interface. In this region given the finite balance of proton and hydroxide ions, perturbations in proton concentration are most significant. Deviations in the cathodic region are more severe than those in the anodic, attributed to quinone-catalyzed ORR also causing the local pH to rise. Such effects can be reduced by careful attention to the scan range employed and number of scans made per measurement.

To negate this behaviour, lowering the surface coverage even further would be a possibility, however the reported surface coverages are already the lowest seen in the literature to-date and represent the technical limitation of the nanosecond laser ablation system. We therefore advocate use of a pulsed voltammetric approach where for each step potential of the CV, the potential pulses into first quinone reduction (consuming protons) and then immediately switches to quinone oxidation (to generate protons). Combining this approach with a very low surface coverage BDD-Q electrode

(4.21×10^{-12} mol cm^{-2}) we show we are able to negate proton accumulation / depletion effects in unbuffered aerated media, and demonstrate a PCET response which follows the $2e^-/2H^+$ pathway over the pH range 4-10. Furthermore, the potential window for BDD-Q PCET is within an extremely useful working range of 0.4 to -0.3 V. Inner sphere voltammetric interference molecules will be strongly electrocatalytically retarded on this electrode, and thus significantly pushed out, away from the pH response. This approach paves the way for development of a universally useful BDD-Q based voltammetric pH sensor.

4.6 References

1) Hammes-Schiffer, S.; Soudackov, A. V. Proton-Coupled Electron Transfer in Solution, Proteins, and Electrochemistry. *J. Phys. Chem. B* **2008**, *112* (45), 14108–14123. https://doi.org/10.1021/jp805876e.

(2) Guin, P. S.; Das, S.; Mandal, P. C. Electrochemical Reduction of Quinones in Different Media: A Review. *Int. J. Electrochem.* **2011**, *2011*, 1–22. https://doi.org/10.4061/2011/816202.

(3) Nohl, H.; Jordan, W.; Youngman, R. J. Quinones in Biology: Functions in Electron Transfer and Oxygen Activation. *Adv. Free Radic. Biol. Med.* **1986**, *2* (1), 211–279. https://doi.org/10.1016/S8755-9668(86)80030-8.

(4) Søballe, B.; Poole, R. K. Microbial Ubiquinones: Multiple Roles in Respiration, Gene Regulation and Oxidative Stress Management. *Microbiology* **1999**, *145* (8), 1817–1830. https://doi.org/10.1099/13500872-145-8-1817.

(5) Lin, K.; Chen, Q.; Gerhardt, M. R.; Tong, L.; Bok, S. Alkaline Quinone Flow Battery. *Science* **2015**, *349* (6255), 1529–1532. https://doi.org/10.1126/science.aab3033.

(6) Powis, G. Free Radical Formation by Antitumor Quinones. *Free Radic. Biol. Med.* **1989**, *6* (1), 63–101. https://doi.org/10.1016/0891-5849(89)90162-7.

(7) Goor, G.; Kunkel, W.; Weiberg, O. Ullmann's Encyclopedia of Industrial Chemistry, Vol. A13. In *Ullmann's Encyclopedia of Industrial Chemistry, Vol. A13*; Elvers, B., Hawkins, S., Ravenscroft, M., Schulz, G., Eds.; VCH: Weinheim, 1989; pp 443–466.

(8) Campos-Martin, J. M.; Blanco-Brieva, G.; Fierro, J. L. G. Hydrogen Peroxide Synthesis: An Outlook beyond the Anthraquinone Process. *Angew. Chemie - Int. Ed.* **2006**, *45* (42), 6962–6984. https://doi.org/10.1002/anie.200503779.

(9) Jacq, J. Schema Carre. *J. Electroanal. Chem. Interfacial Electrochem.* **1971**, *29* (1), 149–180. https://doi.org/10.1016/S0022-0728(71)80080-3.

(10) Laviron, E. Electrochemical Reactions with Protonations at Equilibrium. *J. Electroanal. Chem. Interfacial Electrochem.* **1983**, *146* (1), 15–36. https://doi.org/10.1016/S0022-0728(83)80110-7.

(11) Costentin, C. Electrochemical Approach to the Mechanistic Study of Proton-Coupled Electron Transfer. *Chem. Rev.* **2008**, *108* (7), 2145–2179. https://doi.org/10.1021/cr068065t.

(12) Costentin, C.; Louault, C.; Robert, M.; Savéant, J.-M. The Electrochemical Approach to Concerted Proton--Electron Transfers in the Oxidation of Phenols in Water. *Proc. Natl. Acad. Sci.* **2009**, *106* (43), 18143–18148. https://doi.org/10.1073/pnas.0910065106.

(13) Jackson, M. N.; Surendranath, Y. Donor-Dependent Kinetics of Interfacial Proton-Coupled Electron Transfer. *J. Am. Chem. Soc.* **2016**, *138* (9), 3228–3234. https://doi.org/10.1021/jacs.6b00167.

(14) Bailey, S. I.; Ritchie, I. M. A Cyclic Voltammetric Study of the Aqueous Electrochemistry of Some Quinones. *Electrochim. Acta* **1985**, *30* (1), 3–12. https://doi.org/10.1016/0013-4686(85)80051-7.

(15) Lafitte, V. G. H.; Wang, W.; Yashina, A. S.; Lawrence, N. S. Anthraquinone-Ferrocene Film Electrodes: Utility in PH and Oxygen Sensing. *Electrochem. Commun.* **2008**, *10* (12), 1831–1834. https://doi.org/10.1016/j.elecom.2008.09.031.

(16) Lu, M.; Compton, R. G. Voltammetric PH Sensing Using Carbon Electrodes: Glassy Carbon Behaves Similarly to EPPG. *Analyst* **2014**, *139* (18), 4599–4605. https://doi.org/10.1039/C4AN00866A.

(17) Lu, M.; Compton, R. G. Voltammetric PH Sensor Based on an Edge Plane Pyrolytic Graphite Electrode. *Analyst* **2014**, *139* (10), 2397–2403. https://doi.org/10.1039/c4an00147h.

(18) Ayres, Z. J.; Borrill, A. J.; Newland, J. C.; Newton, M. E.; Macpherson, J. V. Controlled Sp2Functionalization of Boron Doped Diamond as a Route for the Fabrication of Robust and Nernstian PH Electrodes. *Anal. Chem.* **2016**, *88* (1), 974–980. https://doi.org/10.1021/acs.analchem.5b03732.

(19) Kahlert, H. Functionalized Carbon Electrodes for PH Determination. *J. Solid State Electrochem.* **2008**, *12* (10), 1255–1266. https://doi.org/10.1007/s10008-008-0566-7.

(20) Gupta, N.; Linschitz, H. Hydrogen-Bonding and Protonation Effects in Electrochemistry of Quinones in Aprotic Solvents. *J. Am. Chem. Soc.* **1997**, *119* (27), 6384–6391. https://doi.org/10.1021/ja970028j.

(21) Hui, Y.; Chng, E. L. K.; Chng, C. Y. L.; Poh, H. L.; Webster, R. D. Hydrogen-Bonding Interactions between Water and the One and Two-Electron-Reduced Forms of Vitamin K1. *J. Am. Chem. Soc.* **2009**, *131*, 1523–1534.

(22) Yang, J. E.; Yoon, J. H.; Won, M. S.; Shim, Y. B. Electrochemical and Spectroelectrochemical Behaviors of Vitamin K 1/Lipid Modified Electrodes and the Formation of Radical Anion in Aqueous Media. *Bull. Korean Chem. Soc.* **2010**, *31* (11), 3133–3138. https://doi.org/10.5012/bkcs.2010.31.11.3133.

(23) Quan, M.; Sanchez, D.; Wasylkiw, M. F.; Smith, D. K. Voltammetry of Quinones in Unbuffered Aqueous Solution: Reassessing the Roles of Proton Transfer and Hydrogen Bonding in the Aqueous Electrochemistry of Quinones. *J. Am. Chem. Soc.* **2007**, *129* (42), 12847–12856. https://doi.org/10.1021/ja0743083.

(24) Batchelor-Mcauley, C.; Kozub, B. R.; Menshykau, D.; Compton, R. G. Voltammetric Responses of Surface-Bound and Solution-Phase Anthraquinone Moieties in the Presence of Unbuffered Aqueous Media. *J. Phys. Chem. C* **2011**, *115* (3), 714–718. https://doi.org/10.1021/jp1096585.

(25) Park, H.; Won, M.; Cheong, C.; Shim, Y. In-Situ ESR Detection of Radical Species of p -Benzoquinone in Aqueous Media. *Electroanalysis* **2002**, *14* (21), 1501–1507.

(26) Tang, Y.; Wu, Y.; Wang, Z. Spectroelectrochemistry for Electroreduction of P-Benzoquinone in Unbuffered Aqueous Solution. *J. Electrochem. Soc.* **2001**, *148* (4), E133. https://doi.org/10.1149/1.1353575.

(27) Sato, Y.; Fujita, M.; Mizutani, F.; Uosaki, K. Electrochemical Properties of the 2-Mercaptohydroquinone Monolayer on a Gold Electrode. Effect of Solution PH, Adsorption Time and Concentration of the Modifying Solution. *J. Electroanal. Chem.* **1996**, *409* (1–2), 145–154. https://doi.org/10.1016/0022-0728(95)04421-3.

(28) Forster, R. J.; O'Kelly, J. P. Protonation Reactions of Anthraquinone-2,7-Disulphonic Acid in Solution and within Monolayers. *J. Electroanal. Chem.* **2001**, *498* (1–2), 127–135. https://doi.org/10.1016/S0022-0728(00)00331-4.

(29) Müller, O. H. Oxidation-Reduction Potentials Measured with the Dropping Mercury Electrode. III. Polarographic Study of Quinhydrone in Buffered and Unbuffered Solutions. *J. Am. Chem. Soc.* **1940**, *62* (9), 2434–2441. https://doi.org/10.1021/ja01866a048.

(30) Robertson, R. T.; Pendley, B. D. Microelectrodes as Probes in Low Electrolyte Solutions: The Reduction of Quinone in Aqueous Sulfuric Acid Solution. *J. Electroanal. Chem.* **1994**, *374* (1–2), 173–177. https://doi.org/10.1016/0022-0728(94)03335-8.

(31) Kolthoff, I. M.; Orlemann, E. F. The Use of the Dropping Mercury Electrode as an Indicator Electrode in Poorly Poised Systems. *J. Am. Chem. Soc.* **1941**, *63* (3), 664–667. https://doi.org/10.1021/ja01848a009.

(32) Dai, C.; Chan, C. W. I.; Barrow, W.; Smith, A.; Song, P.; Potier, F.; Wadhawan, J. D.; Fisher, A. C.; Lawrence, N. S. A Route to Unbuffered PH Monitoring: A Novel Electrochemical Approach. *Electrochim. Acta* **2016**, *190*, 879–886. https://doi.org/10.1016/j.electacta.2016.01.004.

(33) Dai, C.; Song, P.; Wadhawan, J. D.; Fisher, A. C.; Lawrence, N. S. Screen Printed Alizarin-Based Carbon Electrodes: Monitoring PH in Unbuffered Media. *Electroanalysis* **2015**, *27* (4), 917–923. https://doi.org/10.1002/elan.201400704.

(34) Shim, Y.-B.; Park, S.-M. Spectroelectrochemical Studies of P-Benzoquinone Reduction in Aqueous Media. *J. Electroanal. Chem.* **1997**, *425* (1–2), 201–207. https://doi.org/10.1016/S0022-0728(96)04956-X.

(35) Arulrajan, A. C.; Renault, C.; Lai, S. C. S. How Changes in Interfacial PH Lead to New Voltammetric Features: The Case of the Electrochemical Oxidation of Hydrazine. *Phys. Chem. Chem. Phys.* **2018**, *20* (17), 11787–11793. https://doi.org/10.1039/c8cp01835a.

(36) Vaik, K.; Sarapuu, A.; Tammeveski, K.; Mirkhalaf, F.; Schiffrin, D. J. Oxygen Reduction on Phenanthrenequinone-Modified Glassy Carbon Electrodes in 0.1 M KOH. *J. Electroanal. Chem.* **2004**, *564* (1–2), 159–166. https://doi.org/10.1016/j.jelechem.2003.08.024.

(37) Jürmann, G.; Schiffrin, D. J.; Tammeveski, K. The PH-Dependence of Oxygen Reduction on Quinone-Modified Glassy Carbon Electrodes. *Electrochim. Acta* **2007**, *53* (2), 390–399. https://doi.org/10.1016/j.electacta.2007.03.053.

(38) Gamage, R. S. K. A.; McQuillan, A. J.; Peake, B. M. Ultraviolet–visible and Electron Paramagnetic Resonance Spectroelectrochemical Studies of the Reduction Products of Some Anthraquinone Sulphonates in Aqueous Solutions. *J. Chem. Soc., Faraday Trans.* **1991**, *87* (22), 3653–3660. https://doi.org/10.1039/FT9918703653.

(39) Masheter, A. T.; Abiman, P.; Wildgoose, G. G.; Wong, E.; Xiao, L.; Rees, N. V.; Taylor, R.; Attard, G. A.; Baron, R.; Crossley, A.; Jones, J. H.; Compton, R. G. Investigating the Reactive Sites and the Anomalously Large Changes in Surface PKa Values of Chemically Modified Carbon Nanotubes of Different Morphologies. *J. Mater. Chem.* **2007**, *17* (25), 2616. https://doi.org/10.1039/b702492d.

(40) Jackson, M. N.; Oh, S.; Kaminsky, C. J.; Chu, S. B.; Zhang, G.; Miller, J. T.; Surendranath, Y. Strong Electronic Coupling of Molecular Sites to Graphitic Electrodes via Pyrazine Conjugation. *J. Am. Chem. Soc.* **2018**, *140* (3), 1004–1010. https://doi.org/10.1021/jacs.7b10723.

(41) Macpherson, J. V. A Practical Guide to Using Boron Doped Diamond in Electrochemical Research. *Phys. Chem. Chem. Phys.* **2015**, *17* (5), 2935–2949. https://doi.org/10.1039/c4cp04022h.

(42) Hutton, L. A.; Iacobini, J. G.; Bitziou, E.; Channon, R. B.; Newton, M. E.; Macpherson, J. V. Examination of the Factors Affecting the Electrochemical Performance of Oxygen-Terminated Polycrystalline Boron-Doped Diamond Electrodes. *Anal. Chem.* **2013**, *85* (15), 7230–7240. https://doi.org/10.1021/ac4010421.

(43) Ayres, Z. J.; Cobb, S. J.; Newton, M. E.; Macpherson, J. V. Quinone Electrochemistry for the Comparative Assessment of Sp2 Surface Content of Boron Doped Diamond Electrodes. *Electrochem. Commun.* **2016**, *72*, 59–63. https://doi.org/10.1016/j.elecom.2016.08.024.

(44) Carmody, W. R. Easily Prepared Wide Range Buffer Series. *J. Chem. Educ.* **1961**, *38* (11), 559. https://doi.org/10.1021/ed038p559.

(45) Nečas, D.; Klapetek, P. Gwyddion: An Open-Source Software for SPM Data Analysis. *Cent. Eur. J. Phys.* **2012**, *10* (1), 181–188. https://doi.org/10.2478/s11534-011-0096-2.

(46) Macpherson, J. V; Unwin, P. R. Determination of the Diffusion Coefficient of Hydrogen in Aqueous Solution Using Single and Double Potential Step Chronoamperometry at a Disk Ultramicroelectrode. *Anal. Chem.* **1997**, *69* (11), 2063–2069. https://doi.org/10.1021/ac961211i.

(47) Ernst, S.; Aldous, L.; Compton, R. G. The Voltammetry of Surface Bound 2-Anthraquinonyl Groups in Room Temperature Ionic Liquids: Cation Size Effects. *Chem. Phys. Lett.* **2011**, *511* (4–6), 461–465. https://doi.org/10.1016/j.cplett.2011.06.073.

(48) Ben-Yakar, A.; Byer, R. L. Femtosecond Laser Ablation Properties of Borosilicate Glass. *J. Appl. Phys.* **2004**, *96* (9), 5316–5323. https://doi.org/10.1063/1.1787145.

(49) Bard, A. J.; Faulkner, L. R. *Electrochemical Methods: Fundamentals and Applications*; Wiley: New York, 1980.

(50) Larsen, A. G.; Gothelf, K. V. Electrochemical Properties of Mixed Self-Assembled Monolayers on Gold Electrodes Containing Mercaptooctylhydroquinone and Alkylthiols. *Langmuir* **2005**, *21* (3), 1015–1021. https://doi.org/10.1021/la048221w.

(51) Zhang, W.; Rosendahl, S. M.; Burgess, I. J. Coupled Electron / Proton Transfer Studies of Benzoquinone-Modified Monolayers. *J. Phys. Chem. C* **2010**, *114* (6), 2738–2745.

(52) Laviron, E. Surface Linear Potential Sweep Voltammetry. Equation of the Peaks for a Reversible Reaction When Interactions between the Adsorbed Molecules Are Taken into Account. *J. Electroanal. Chem.* **1974**, *52* (3), 395–402. https://doi.org/10.1016/S0022-0728(74)80449-3.

(53) Chidsey, C. E. D.; Bertozzi, C. R.; Putvinski, T. M.; Mujsce, A. M. Coadsorption of Ferrocene-Terminated and Unsubstituted Alkanethiols on Gold: Electroactive Self-Assembled Monolayers. *J. Am. Chem. Soc.* **1990**, *112* (11), 4301–4306. https://doi.org/10.1021/ja00167a028.

(54) Albery, W. J.; Boutelle, M. G.; Colby, P. J.; Hillman, A. R. The Kinetics of Electron Transfer in the Thionine-Coated Electrode. *J. Electroanal. Chem.* **1982**, *133* (1), 135–145. https://doi.org/10.1016/0022-0728(82)87012-5.

(55) Peerce, P.; Bard, A. Polymer Films on Electrodes: Part III. Digital Simulation Model for Cyclic Voltammetry of Electroactive Polymer Film and Electrochemistry of Poly (Vinylferrocene) on Platinum. *J. Electroanal. Chem.* **1980**, *114*, 89–115. https://doi.org/http://dx.doi.org/10.1016/S0022-0728(80)80438-4.

(56) Benítez, G.; Vericat, C.; Tanco, S.; Lenicov, F. R.; Castez, M. F.; Vela, M. E.; Salvarezza, R. C. Role of Surface Heterogeneity and Molecular Interactions in the Charge-Transfer Process through Self-Assembled Thiolate Monolayers on Au(111). *Langmuir* **2004**, *20* (12), 5030–5037. https://doi.org/10.1021/la036440w.

(57) Laviron, E. General Expression of the Linear Potential Sweep Voltammogram in the Case of Diffusionless Electrochemical Systems. *J. Electroanal. Chem.* **1979**, *101* (1), 19–28. https://doi.org/10.1016/S0022-0728(79)80075-3.

(58) Darwish, N.; Eggers, P. K.; Ciampi, S.; Tong, Y.; Ye, S.; Paddon-Row, M. N.; Gooding, J. J. Probing the Effect of the Solution Environment around Redox-Active Moieties Using Rigid Anthraquinone Terminated Molecular Rulers. *J. Am. Chem. Soc.* **2012**, *134* (44), 18401–18409. https://doi.org/10.1021/ja307665k.

(59) Abhayawardhana, A. D.; Sutherland, T. C. Heterogeneous Proton-Coupled Electron Transfer of an Aminoanthraquinone Self-Assembled Monolayer. *J. Phys. Chem. C* **2009**, *113* (12), 4915–4924. https://doi.org/10.1021/jp807287p.

(60) Finklea, H. O. Theory of Coupled Electron-Proton Transfer with Potential-Dependent Transfer Coefficients for Redox Couples Attached to Electrodes. *J. Phys. Chem. B* **2001**, *105* (37), 8685–8693. https://doi.org/10.1021/jp010768l.

(61) Trammell, S. A.; Lowy, D. A.; Seferos, D. S.; Moore, M.; Bazan, G. C.; Lebedev, N. Heterogeneous Electron Transfer of Quinone-Hydroquinone in Alkaline Solutions at Gold Electrode Surfaces: Comparison of Saturated and Unsaturated Bridges. *J. Electroanal. Chem.* **2007**, *606* (1), 33–38. https://doi.org/10.1016/j.jelechem.2007.04.008.

(62) Yeager, E. Electrocatalysts for O2 Reduction. *Electrochim. Acta* **1984**, *29* (11), 1527–1537. https://doi.org/10.1016/0013-4686(84)85006-9.

(63) Mooste, M.; Kibena, E.; Sarapuu, A.; Matisen, L.; Tammeveski, K. Oxygen Reduction on Thick Anthraquinone Films Electrografted to Glassy Carbon. *J. Electroanal. Chem.* **2013**, *702*, 8–14. https://doi.org/10.1016/j.jelechem.2013.04.031.

Chapter 5: An sp^2 Patterned Boron Doped Diamond Electrode for the Simultaneous Detection of Dissolved Oxygen and pH

5.1 Outline

A hybrid sp^2-sp^3 electrochemical sensor comprising patterned regions of non-diamond-carbon (sp^2) in a boron doped diamond (sp^3) matrix is described for the simultaneous voltammetric detection of dissolved oxygen (DO) and pH in buffered aqueous solutions. Using a laser micropatterning process it is possible to write mechanically robust regions of sp^2 carbon into a BDD electrode. These regions both promote the electrocatalytic reduction of oxygen and facilitate the proton coupled electron transfer of quinone groups, integrated into the surface of the sp^2 carbon. In this way, in one voltammetric sweep (time of measurement ~ 4 s) it is possible to determine both the DO concentration and solution pH. By varying the sp^2 pattern the response can be optimised towards both analytes. Using a closely-spaced sp^2 microspot array a linear response towards DO, across the range 0.0 to 8.0 mg L^{-1} (0.0 to 0.25 mM; sensitivity = -8.77×10^{-8} A L mg^{-1}, $R^2 = 0.9991$) and pH range 4 – 10 (sensitivity = 59.7 mV pH^{-1}, $R^2 = 0.9983$) is demonstrated. Finally, we show how the peak position for ORR is independent of pH and thus via measurement of the difference in ORR and pH peak position, internal referencing is possible. Such electrodes show great promise for use in applications ranging from bio-medical sensing to water analysis.

5.2 Introduction

The stability of an ecological or biological system, whether it be natural waters[1] or body fluids e.g. blood,[2] is governed by its ability to maintain a carefully controlled homeostasis. A number of fundamental factors influence this homeostasis, and can be used as indicators of system health. These include, for example, temperature,[3] pH,[4,5] and dissolved oxygen (DO) concentration.[6,7] DO is most commonly measured either optically using a luminescent probe or electrochemically via adaptations of the membrane-based Clark cell method. pH is commonly measured using the potentiometric glass pH probe.[8] Whilst all probes offer good sensitivity and selectivity, their large size, fragility, susceptibility to fouling and need for frequent calibration due to drift can lead to difficulties in complex media.

For many applications, sampling frequency is an important issue. For arterial blood analysis of hospitalized patients, DO, pH, CO_2 and temperature are measured using a conventional blood gas analyser, which employs a Clark cell for DO[9] and a glass potentiometric probe for pH.[10] The latter measurement also enables the indirect determination of blood CO_2.[11] Such parameters are vital indicators of underlying problems, and can change rapidly as a result of medical conditions or trauma.[12,13] In blood gas analysis, withdrawal of large quantities (up to 5 ml) of blood is typically required, with the sample transported to the instrument for analysis. This limits sampling frequency to, at best ca. one test per hour, which is not sufficient for early detection of deteriorating health conditions. This underscores the importance of continuous, on-line, and reliable measurements.

Whilst there have been developments in the field of smaller, more robust DO sensors most still have associated issues which make their use in continuous on-line detection difficult. Variations on Clark-type DO electrodes include methods of miniaturisation, [14–19] or those based on non-noble metals.[20] However, issues with membrane use and fragility are still a concern. Miniaturisation of membrane-free e.g. Pt microdisc,[21] Pt microarrays,[22,23] and metal-polymer[24,25] electrodes have also been explored for DO analysis in a range of fields including oceanography, biology, and biomedicine. A number of optical sensing methods, due to their ability to measure DO without consumption, or the generation of toxic species, such as hydrogen peroxide, have also been investigated for biological cell culture analysis.[26] However, in all cases DO reliability in a continuous on-line setting is still affected by one or more issue including

fragility, biotoxicity, size, susceptibility to damage or fouling, or complicated preparation and use.

For the widely used glass pH probe, alternatives have also been explored aimed primarily at miniaturisation and on-line analysis. One of the most popular includes pH sensitive iridium oxide (IrOx).[27] Whilst IrOx enables miniaturisation and offers good sensitivity with a super-nernstian response, it suffers drawbacks of biocompatibility and long term film stability; film dissolution and delamination are problematic. Quinone functionalised electrodes have also been proposed as pH sensors due to proton coupled electron transfer (PCET) during quinone reduction.[28] However, quinones chemically tethered to an electrode surface can also present long term stability and robustness issues. Recent work saw the introduction of boron doped diamond-quinone (BDD-Q) electrodes, where the quinone groups were robustly integrated into the BDD surface via a laser ablation process.[29–31] These strongly electronically coupled BDD-Q electrodes were shown to measure solution pH in both buffered[29] and unbuffered media.[31]

In general, BDD is an increasingly popular electrode material choice for electroanalysis, due to the interesting properties which arise from its sp^3 nature, including mechanical robustness, wide solvent window with low background currents, chemical inertness, low fouling, and biocompatibility.[32–34] However, the sp^3 BDD surface renders the electrode much more catalytically insensitive to inner sphere redox reactions, compared to metal electrodes and sp^2 carbon electrodes. For example, the oxygen reduction reaction (ORR) is significantly retarded on BDD and can be difficult to detect within the aqueous solvent window since the sp^3 structure lacks electron transfer mediating binding sites.[32] In contrast, on sp^2 electrodes, such as graphite or glassy carbon, ORR is thought to go via a two-electron transfer pathway,[35–38] Equation 5.1.

$$O_2 + 2H^+ + 2e^- \rightarrow H_2O_2 \qquad pH = 7,\ E^o = 0.456\ V\ vs\ SCE \qquad [5.1]$$

This study aims to produce a membrane-less electrochemical approach to the measurement of pH and DO, which is suitable for high frequency, on-line analysis, and is capable of detecting both species in one voltammetric measurement only. Hybrid, robust sp^2 functionalised BDD electrodes will be used to improve catalytic efficiency of ORR on BDD and promote pH sensitivity. Of interest is how the spatial

arrangement of sp^2 sites in the BDD base material impacts optimisation of the ORR and pH signals. Buffered solutions over the pH range 6-8, are employed, given the significance of pH and DO measurements in the biological field. The possibility of using the difference between both signals to correct for reference electrode drift is also explored.

5.3 Experimental

5.3.1 Solutions

Solutions were prepared using ultrapure water (Milli-Q, resistivity of ≥18.2 MΩ cm at 25 °C). Buffers covering the pH range 2 - 10 were prepared according to the Carmody method.[29,39] After laser ablation, each electrode was conditioned by cycling in 0.1 M H_2SO_4 (98%, Sigma-Aldrich, UK).[29,32] Electrode analyses were conducted in 0.1 M KNO_3 (99%, Sigma-Aldrich, UK), 0.1 M H_2SO_4 (Fisher Scientific, UK), 1 mM $Ru(NH_3)_6^{3+/2+}$ (99%, Strem Chemicals, UK) with 0.1 M KNO_3, and pH 2 Carmody buffer respectively. All chemicals were used as received unless otherwise stated.

5.3.2 Electrode Preparation

BDD cylinders of 1 mm diameter, polished on the top (growth) surface to approximately nanometer scale roughness, were machined from a six inch freestanding BDD wafer (357 μm thick) using a 355 nm Nd:YAG 34 nanosecond laser micromachiner (E-355H-ATHI-O system, Oxford lasers). The BDD cylinders were acid cleaned in boiling concentrated H_2SO_4 (98%), saturated with KNO_3, to oxygen terminate the surface and remove any loosely contacted sp^2 carbon introduced during the laser micromachining step. Ti (10 nm) / Au (400 nm) was sputtered (Moorfields MiniLab 060 platform sputter/evaporator) onto the back of the BDD cylinders and annealed at 400°C for 5 h, to form a reliable ohmic contact. The BDD cylinders were then sealed in glass capillaries (o.d. 2 mm; i.d. 1.16 mm; Harvard Apparatus Ltd., Kent, UK) and the top surface exposed by polishing away the glass with carbide grit paper disks and alumina (0.05 μm) paste (Buehler, Germany). The glass capillary was back filled with silver epoxy (Chemtronics, CircuitWorks), a copper wire added for electrical connection, and the capillary sealed with non-conductive epoxy (Araldite).

A laser micromachiner was used to pattern sp^2 carbon features into the BDD surface. All electrodes were machined with a pulse fluence of 14 J cm^{-2}, just above the ablation threshold of BDD.[31] Electrodes 1 and 2, were produced by rastering the laser beam in a circular pattern with a nominal pulse density of 2×10^6 pulses per cm^{-2} and 1×10^6 pulses per cm^{-2} respectively. The nominal pulse density was altered to account for differences in the stage acceleration effects on different sized features, with the aim of achieving a similar surface sp^2 content on both electrodes. Electrode 3 was fabricated using isolated laser pulses to produce an array of microspots. After laser micromachining the electrodes were again acid cleaned to both remove loosely bound

sp^2 carbon and oxidatively "activate" by heating the electrode at ~200 °C for 15 minutes in concentrated H_2SO_4 (98 %) saturated with KNO_3.[29] Prior to electrochemical characterization the electrode surface and pit profiles were analyzed via optical microscopy (Leica DM4000M) and white light interferometry (WLI: Contour GT, Bruker).

5.3.3 Electrochemical Measurements

Electrochemical measurements were conducted using a CH1040a potentiostat (CH Instruments Inc., USA), and a saturated calomel reference electrode (SCE: IJ Cambria Scientific Ltd., UK). DO concentration and solution pH were measured using a luminescent DO (LDO) probe (HQ40d; Hach, USA) and a glass pH probe (SevenCompact; Mettler Toledo, UK), respectively. The DO concentration was regulated through the use of Ar and O_2 gases piped into a sealed reaction vessel using mass-flow controllers (MKS Instruments) with a total flow rate of 500 sccm. An outlet pipe with non-return valve was also connected to the reaction vessel to remove excess gas and avoid pressure build-up. All measurements were conducted versus a standard SCE reference electrode and a Pt wire counter electrode. BDD electrodes were polished before use with alumina (0.05 µm) paste (Buehler, Germany). For measurement of the diffusion coefficient of O_2, a 28 µm diameter Pt microelectrode was prepared before use by cycling in 0.1 M H_2SO_4 (>99 %, Sigma Aldrich, UK). For Koutecky-Levich analysis the glass sealed hybrid sp^2-BDD electrode was rotated at frequencies in the range 12-30 Hz employing a commercial rotator (Pine Instruments, USA) in conjunction with a 3D printed in-house customized electrode holder to attach the electrode to rotator. Electrodes were assessed in terms of their quinone surface coverage, Γ, using a method previously described,[30] where Γ is calculated using Equation 5.2 from the charge passed, Q, during oxidation of the quinone groups,where n is the number of electrons transferred (n = 2), A is the total electrode surface area (cm^2, measured using WLI and F is the Faraday constant (96485 C mol^{-1}).

$$Q = nAF\Gamma \qquad [5.2]$$

5.3.4 Data Analysis

Data analysis was conducted using Python 3.6 and the SciPy stack. Data was smoothed using a rolling mean with a window of 10 data points in order to remove low amplitude noise. The pH and ORR peaks were identified using the first derivative method within

the bounds +0.3 V to -0.2 V, and -0.85 V to -1.1 V *vs* SCE respectively. Where the first derivative is equal to zero a turning point occurs, minima are identified by a positive second derivative at that point (i.e. an increasing first derivative through the turning point). For each peak the current and potential value were recorded. Calibration curves were fitted using linear regression.

5.4 Results and Discussion

ORR on minimal sp^2 content BDD base material is significantly kinetically retarded, occurring very close to the cathodic solvent window (Figure 5.1, where the half wave potential, $E_{1/2}$ for ORR = -1.414 V). A limiting current of 0.67 µA is observed.

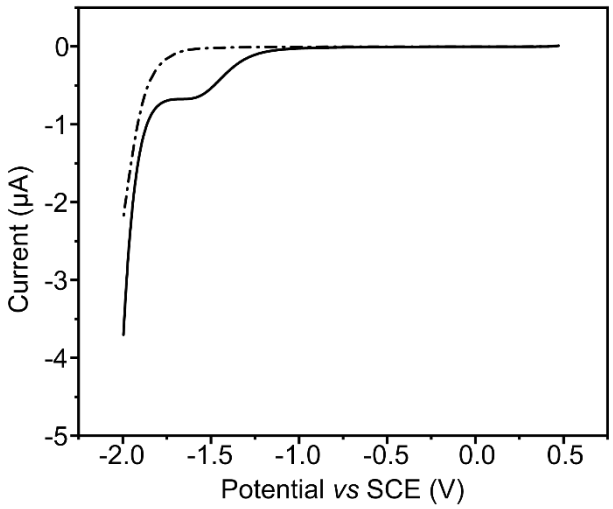

Figure 5.1: Linear sweep voltammogram for an sp^2 free electrode conducted at 0.05 V s^{-1} between 0.5 V and -2 V vs SCE in pH 7.00 Carmody buffer under ambient (solid line) and degassed (−·−·) conditions.

Laser ablation enables patterning of sp^2 carbon regions into the BDD base material, with any shape, limited only by the spot size of the laser process *ca* ~ 5 µm (for the laser system employed).[29,30] Associated with these sp^2 regions are surface-integrated quinones; BDD-Q.[29,31] Initial experiments explored how sp^2 pattern affects the voltammetric response of a BDD macroelectrode (1 mm geometric diameter), with respect to ORR.

WLI was used to determine the geometry of the three laser micro-machined electrode patterns, (Figure 5.2) (a) Electrode 1 a centrally located single lasered sp^2 macrospot. (b) Electrode 2 a hexagonal array of sp^2 microspots, and (c) electrode 3 a hexagonal array of smaller sp^2 microspots. 3D rendered images (top) illustrate the locations at which depth profiles of the surface were measured (pink and black solid lines), these correspond to the line profile (line length *vs* surface depth) plots presented below. In each case, two line profiles are presented to demonstrate consistency.

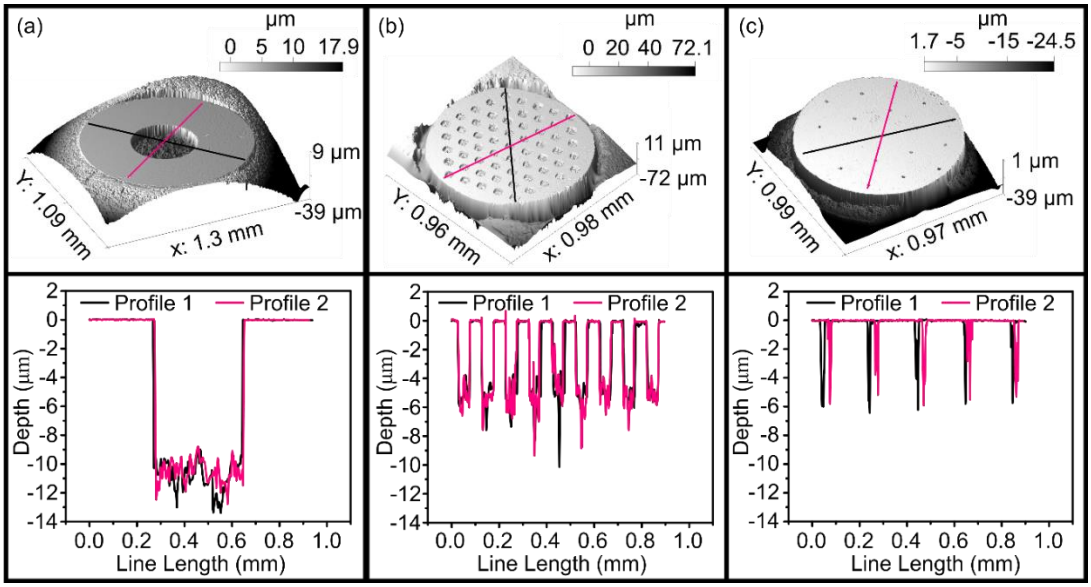

Figure 5.2: WLI data showing a rendered 3D image (top), and the lasered pit profiles (bottom) of (a) a single spot electrode, (b) an array electrode of equivalent quinone surface coverage to (a), and (c) a microarray electrode.

Electrodes (1) and (2) exhibit an equivalent Γ for quinone groups but (1) is a single, centrally located single macrospot, 370 ± 2 µm in diameter, 10 ± 2 µm deep, whilst (2) is an hexagonal array of sixty-one microspots, 50 ± 2 µm in diameter and 5 ± 2 µm deep, with a centre to centre spacing = 100 µm. On a typical voltammetric timescale employed here (= 0.05 V s^{-1}), diffusional overlap between neighbouring sites will be significant. Electrode (3) represents a hexagonal array of nineteen microspots, 10 ± 2 µm in diameter (5 ± 2 µm deep) with a centre to centre spacing of 200 µm. The size and spacing is such that diffusional overlap is not expected. The three electrode designs considered, are shown optically in Figure 5.3(top);

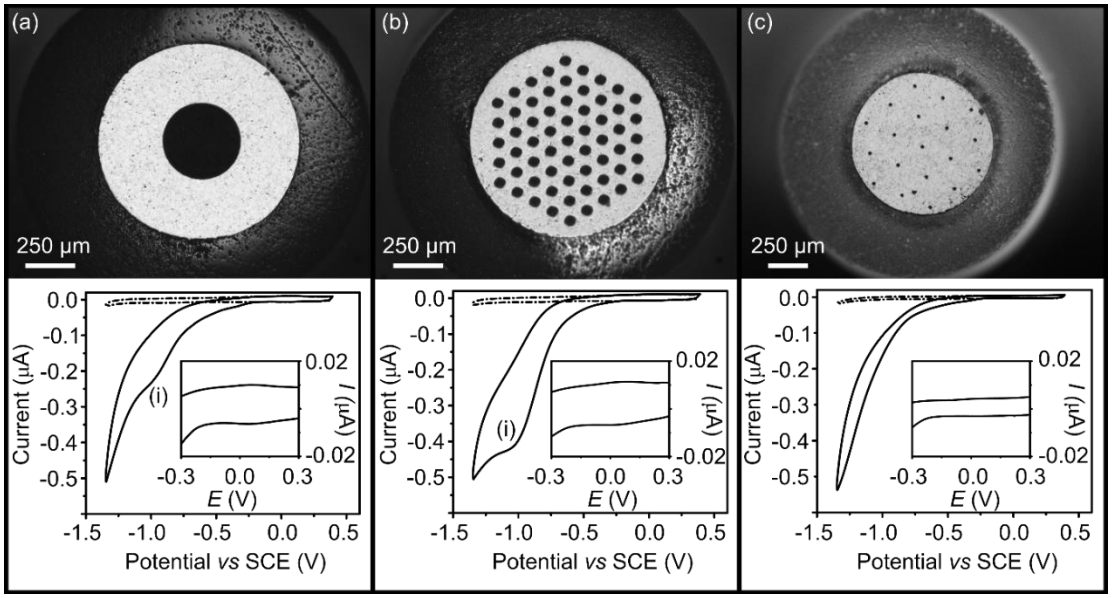

Figure 5.3: Optical microscope images and cyclic voltammograms (CVs) for (a) single macrospot sp^2-BDD electrode, (b) microarray sp^2-BDD electrode of equivalent Γ to (a), and (c) smaller spot size microarray sp^2-BDD electrode. CVs were run at 0.05 V s^{-1} between +0.4 V and -1.35 V in pH 7.00 Carmody buffer under ambient (solid) and degassed (−·−·) conditions. CV insets show CV zoomed in around the quinone oxidation-reduction peaks (+0.3 V to -0.3 V).

Figure 5.3 (bottom) shows the resulting cyclic voltammetry (CV) responses recorded in oxygen-containing (ambient conditions) and degassed (low oxygen conditions) pH 7.00 Carmody buffer solutions, at a scan rate of 0.05 V s^{-1}. It is clear, from comparison with the bare BDD electrode[40] (Figure 5.1), and from CVs recorded in deaerated solutions (−·−·) that the waves labelled (i) in Figure 5.3(a) and (b) are associated with ORR on sp^2-BDD ($E_{1/2}$ = -0.821 V and -0.839 V respectively). They are shifted by ~0.6 V more positive under the same solution conditions, compared to bare BDD, indicating significantly faster electron transfer (ET) kinetics compared to BDD alone. Note, relative to E^o, electron transfer is still slow. These patterned electrodes can be considered as containing ORR-active sp^2 Electrode(s) embedded within an inert BDD background, for the voltammetric scan range presented in Figure 5.3. In this way, design 2, is similar to a more traditional high density microelectrode array where the active material e.g. Pt, Au, carbon fibre is embedded within an insulating material such as glass, or epoxy.[41,42] On the smaller microarray electrode (3), ORR due to the sp^2 microsites on BDD cannot be suitably discerned.

The diffusion coefficient, *D*, of O_2 in pH 7 Carmody buffer was calculated from the steady state current, i_{ss}, for ORR process at a 27.8 µm diameter Pt disk microelectrode (Figure 5.4). On Pt, *n* for ORR is assumed to be 4.[36]

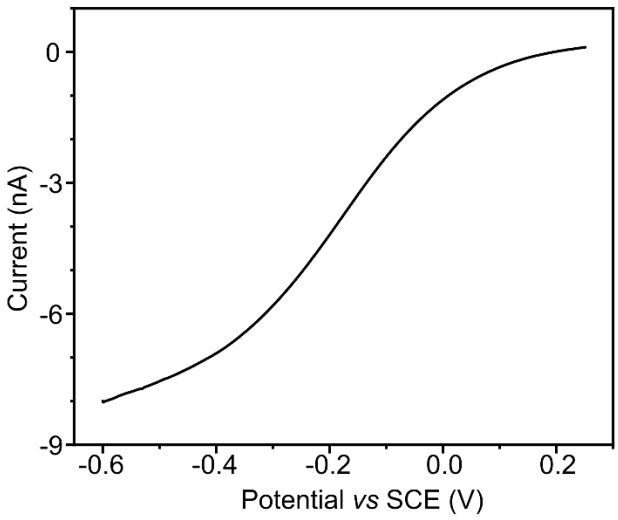

Figure 5.4: CV of ORR on a 27.8 µm Pt microelectrode conducted at 50 mV s^{-1} between 0.25 V and -0.6 V in pH 7.00 Carmody buffer under ambient conditions (8.14 mg L^{-1}).

From the measured i_{ss}, *D* for O_2 could be calculated using Equation 5.3:

$$i_{ss} = 4naFDC^* \qquad [5.3]$$

Where i_{ss} = 7.4 nA, *n* = 4, *a* is the electrode radius, *F* is the Faraday constant (96485 C mol^{-1}) and C^* is the concentration (8.14 mg L^{-1} = 0.255 mol dm^{-3}). *D* was calculated to be 1.36×10^{-5} cm^2 s^{-1}.

Whilst sp^2 carbons are assumed to follow a $2e^-$ ORR process,[35,36] the exact structure of the robust non-diamond-form of carbon produced on the surface from the BDD during laser ablation has yet to be elucidated. It was therefore necessary to identify the number of electrons involved in ORR on the hybrid sp^2-BDD electrode in order to quantify further the current responses observed. Due to the slow kinetics of ET, Koutecky-Levich analysis can be used to determine *n* for ORR on the sp^2-BDD electrode.

A rotating disc electrode was used to measure the ET kinetics of ORR on an sp^2-BDD microarray electrode (Electrode 2). The ORR response was measured by linear sweep voltammetry at a range of rotation rates (75 – 189 rad s-1), Figure 5.5(a). The

Koutecky-Levich equation, Equation 5.4, was used to calculate the number of electrons, n, transferred from the average inverse current slopes at different potentials along the ORR wave (0.95-1.15 V *vs* SCE, Figure 5.5(b)).

$$\frac{1}{i} = \frac{1}{i_k} + \frac{1}{(0.620nFAD^{2/3}v^{-1/6}C)}\omega^{-1/2} \qquad [5.4]$$

where i is the measured current, i_k is the kinetic current, F is the Faraday constant (96485 C mol^{-1}), A is the electrode area (only sp^2 regions assumed active = 0.00225 cm^{-2} from interferometry), D is the diffusion coefficient (1.36 × 10^{-5} cm^2 s^{-1}, measured using a Pt microelectrode (*vide supra*)), v is the kinematic viscosity (assumed to be 0.01 cm^2 s^{-1}), C is the DO concentration (8.3 mg L^{-1}, 0.26 mM from LDO probe) and ω is the rotation rate (rad s^{-1}). From this equation n = 2.04.

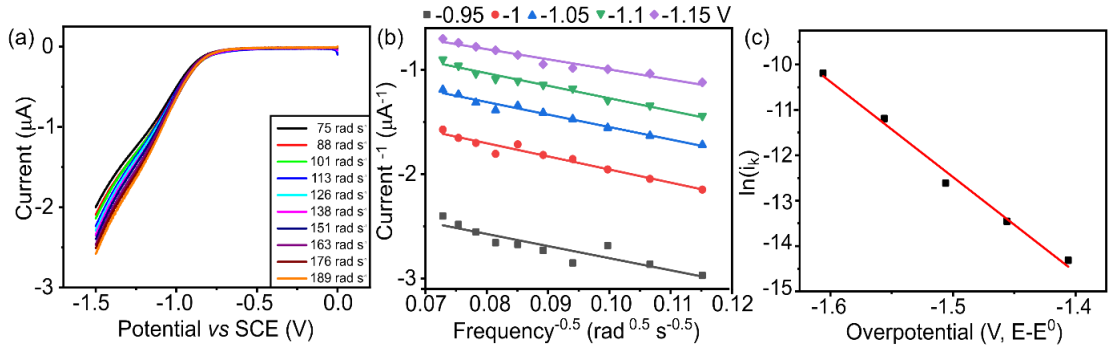

Figure 5.5:(a) LSV of Electrode 2 in pH 7 Carmody buffer at varying rotation rates (75-189 rad s-1). (b) Koutecky-Levich plot of the inverse current at different potentials along the ORR wave (0.95-1.15 V vs SCE). (c) Natural logarithm of kinetic current against overpotential for the calculation of kinetic parameters.

The Tafel equation (Equation 5.5), where (E - E^0) is the overpotential was used to produce a Tafel slope (Figure 5.5(c)) from plotting i_k at different overpotentials along the ORR wave, determined from the intercepts of Figure 5.5(b). From the slope it was possible to determine a transfer coefficient (α) of 0.27 and a heterogeneous rate constant (k_0) of 7.0 ×10^{-16} cm s^{-1} from the intercept.

$$i_k = nFk_0Ce^{-\propto nF/RT(E-E^0)} \qquad [5.5]$$

Assuming only the sp^2 carbon contributes to the ORR currents observed in Figure 5.3 and ET is irreversible and diffusion controlled, the latter which can be considered predominantly planar, the expected peak current can be calculated using equation 5.6:[30,43]

$$i_p = 0.496(\alpha n')^{0.5} nFAC(\frac{FDv}{RT})^{0.5} \qquad [5.6]$$

where α is the transfer coefficient, n' is the number of electrons transferred before the rate determining step (n' = 1),[37,38] n is the total number of electrons transferred (n = 2),[35–38] C is the concentration, D is the diffusion coefficient (1.36 × 10^{-5} cm^2 s^{-1}, measured using a Pt microelectrode, *vide supra*), v is the scan rate (0.05 V s^{-1}), R is the gas constant (8.314 J mol^{-1} K^{-1}) and T is the temperature (298 K). The calculated i_p for electrode (1) is = 0.204 µA (for a DO concentration of 8.3 mg L^{-1} = 0.26 mM and geometric electrode area governed by the laser ablated area of 1.07 × 10^{-3} cm^2), this compares closely to the current recorded= 0.206 µA, after the background current at -0.55 V vs. SCE was subtracted. For Electrode (2) the measured background subtracted current is 0.42 µA. Given diffusional overlap is expected, if we assume a geometric electrode area based on a 0.85 mm diameter electrode (the external diameter of the machined region), a current of 0.52 µA is predicted. For Electrode (3) a limiting current of 13 nA is expected based on the cumulative response of nineteen diffusionally-isolated microelectrodes of diameter 10 µm. The magnitude of this wave is of the same order as the background currents, explaining the absence of an observable wave in Figure 5.3(c).

In the potential region, 0.3 V to -0.3 V for all three electrodes there is also evidence of another voltammetric process, highlighted in the insets to the CVs in Figure 5.3a-c. The CVs are characteristic of a surface bound ET process; peak to peak separations for the three electrodes are (1) 27 mV; (2) 54 mV and (3) n/a, as only the anodic peak was discernible from the background current. This response has previously been associated with PCET for surface integrated, strongly electronically coupled,[31,44] quinones residing in the sp^2 regions of the BDD electrode. From analysis of the anodic CV sweep, it is possible to calculate, Γ for the Q-groups for the three electrodes, equation 5.2, where Γ is (1) 2.63 × 10^{-13} mol cm^{-2} (A = 1.25 × 10^{-3} cm^2); (2) 2.71 × 10^{-13} mol cm^{-2} (A = 2.07 × 10^{-3} cm^2) and (3) 1.23 × 10^{-13} mol cm^{-2} (A = 3.66 × 10^{-4}

cm^2). The information in brackets represents the machined surface area for each electrode.

Comparing the currents passed for both ORR and the quinone PCET response, the largest ORR current is seen for Electrode (2). The quinone PCET response is much harder to distinguish against the background current, for all electrodes, and becomes increasingly more difficult as the quinone content decreases. To increase the signals, especially for the quinone response, square wave voltammetry (SWV) was employed, with a focus on electrode (2), given its promise from the CV data for both ORR and pH. Figure 5.6, shows both the CV (0.05 V s^{-1}) and SWV (100 Hz, 0.1 V amplitude, and 0.004 V increment) responses for the microarray Electrode (2) in pH 7.00 Carmody buffer under ambient conditions in aerated solution over the potential range 0.4 V to -1.35 V (measurement time = 1.88 s). A high frequency was chosen for SWV data in order to increase the current magnitude, but not so high that the analysed component of the current contained non-faradaic current components at the solution conductivities employed. As clearly shown, SWV amplifies the current for both ET processes, importantly enabling the quinone PCET process to be easily resolvable against the background. Interestingly, now evident on the left hand side of the pH peak is a smaller second peak, which has previously been shown to be related to quinone catalysed ORR.[31]

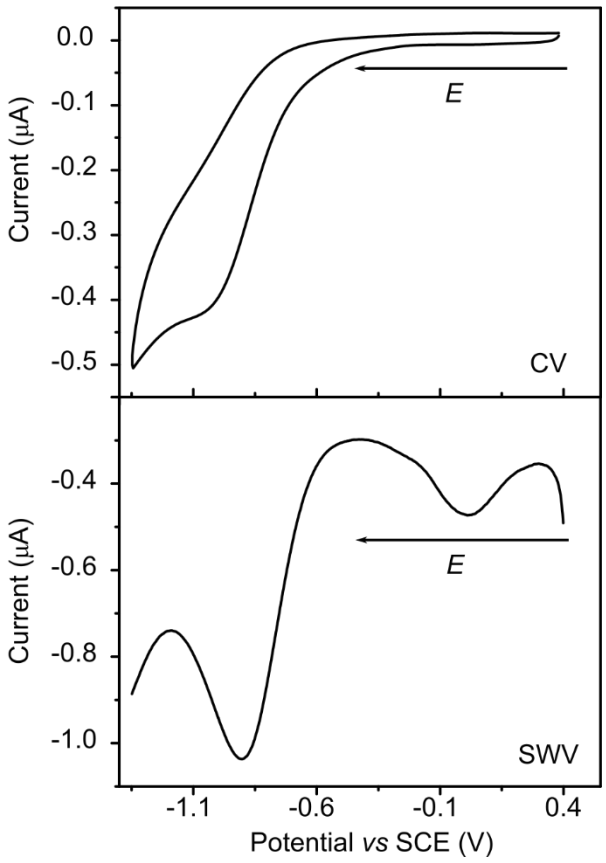

Figure 5.6: Comparison of CV and SWV response between 0.4 V and -1.35 V for microarray electrode 2, in pH 7.00 Carmody buffer under ambient conditions. CV (top) run at 0.05 V s-1 with 0.004 V increment. SWV (bottom) run at 100 Hz, 0.1 V amplitude, and 0.004 V increment.

To further investigate the ability of Electrode (2) to quantify DO concentration and pH in one measurement, Figure 5.7 shows the SWV response (100 Hz, 0.1 V amplitude, and 0.004 V increment) in pH 6.02, 7.12, and 8.10 buffers (chosen for their biological pH relevance) over a range of DO concentrations between 0 (deaerated: 100 % Ar) and 8 mg L^{-1} O_2 (= 0.25 mM); the solution was bubbled with O_2 and Ar gases at a flow rate of 500 sccm in ratios between 0 % O_2: 100 % Ar and 20 % O_2: 80 % Ar.

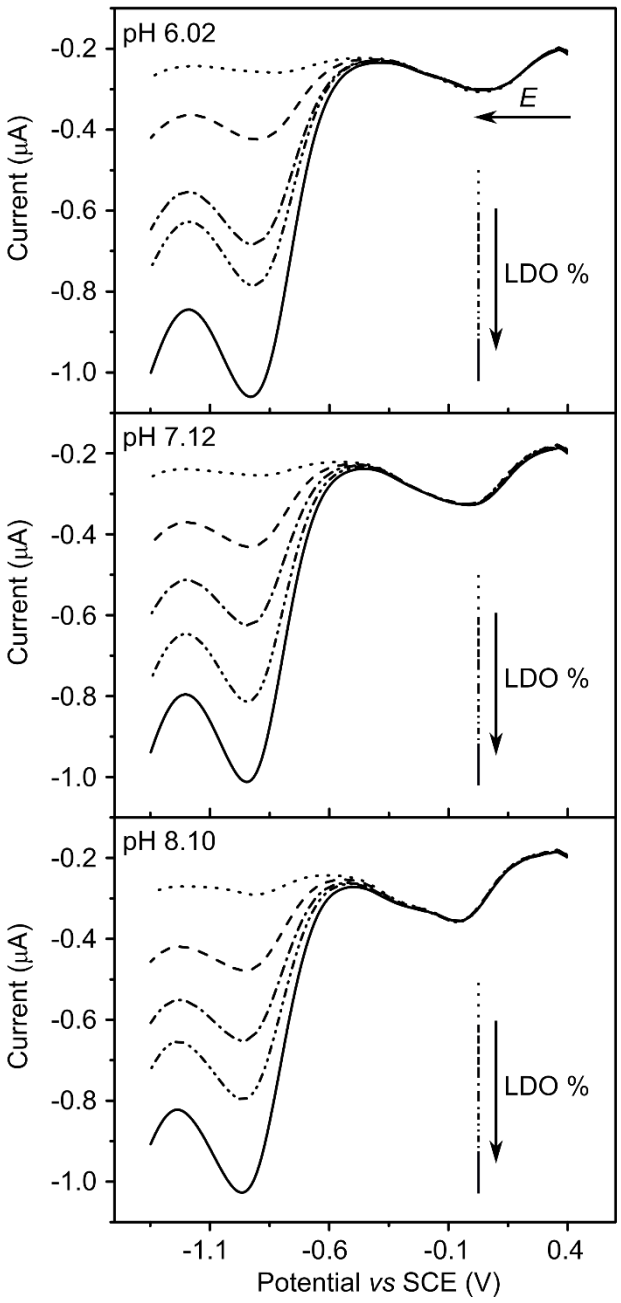

Figure 5.7: SWV data showing the pH response and ORR response in pH 6.02 (top), pH 7.12 (middle), and pH 8.10 (bottom) Carmody buffer solution over a range of DO concentrations. SWVs were run at 100 Hz, 0.1 V amplitude, 0.004 V increment, between 0.4 V and -1.35 V.

The ORR peak near -1.0 V clearly increases in current magnitude with increasing DO concentration, confirming that it is due to ORR on laser incorporated sp^2 carbon. Note a small DO current is observable under 0 % O_2:100% Ar conditions, indicating it was

not possible to completely remove all the DO from the system; confirmed also from the LDO independent measurement. The pH peak is unaffected in either current magnitude or peak potential by the changing DO concentration. In contrast, as the pH is increased a shift in the negative potential direction is observed, consistent with the Nernst equation[43] for a $2e^-/2H^+$ process.[29,31] The data presented in Figure 5.8 was repeated such that three measurements were recorded for each pH: pH 4 (4.16, 4.18. 4.21), pH 6 (6.00, 6.02, 6.04), pH 7 (7.12, 7.12, 7.15), pH 8 (8.06, 8.10, 8.13), and pH 10 (10.16, 10.17, 10.18) and for each of the fifteen pH measurements made, five O_2:Ar ratios between 0 % O_2: 100 % Ar and 20 % O_2: 80 % Ar (0:100, 4:96, 10:90, 14:86, 20:80) were also assessed (seventy five measurements in total). The resulting ORR currents (background subtracted) are presented in Figure 5.8a versus the measured LDO values, for the different pH solutions over the range 4.00-10.20. Each measurement was background subtracted at -0.55 V (such that the current value at -0.55 V = 0 µA for all measurements), chosen such that neither DO nor pH related processes were occurring. This method was chosen over the subtraction of a linear baseline as the changing shape of the curve baseline at more negative potentials than the ORR peak, with changing DO concentration, caused artificial shifting of the peak.

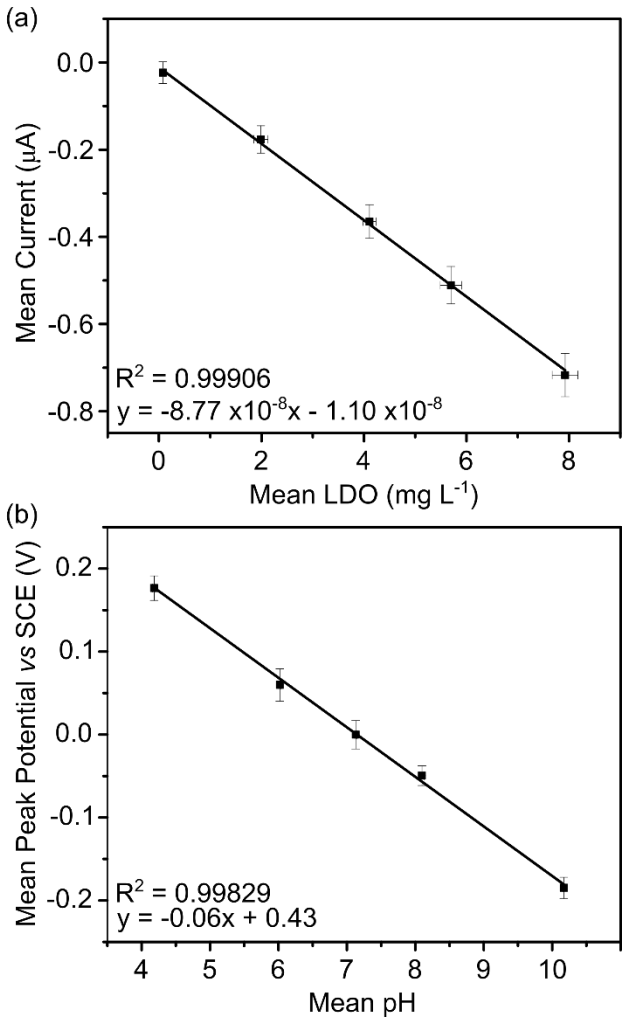

Figure 5.8:(a) Mean ORR peak current vs mean measured LDO (mg L^{-1}), and (b) mean pH vs mean pH peak potential both from the same series of SWV experiments as described in Figure 5.7. Experiments were conducted in pH buffer solutions between pH 4.00 and 10.20 (pH 4: 4.16, 4.18. 4.21, pH 6: 6.00, 6.02, 6.04, pH 7: 7.12, 7.12, 7.15, pH 8: 8.06, 8.10, 8.13, and pH 10: 10.16, 10.17, 10.18) each for five oxygen concentrations over the range 0.1 - 8 mg L^{-1}. Data was background subtracted at -0.55 V, where no pH or DO related processes are occurring.

For the five pH values investigated (in the range 4 - 10) a linear relationship between the aggregate mean ORR peak current and the mean DO concentration (mg L^{-1}), calculated across all pH values for each DO concentration, is observed with a gradient of -8.77×10^{-8} A L mg^{-1}, $R^2 = 0.9991$. This enables the assumption to be made that the magnitude of the oxygen current response is unaffected by pH over the pH range 4-10.[37] The data in Figure 5.8b is constructed similarly from the fifteen data sets by calculating the aggregate mean of the quinone PCET peak potential across all DO concentrations for each group of pH values and plotting *vs* the mean pH for each

group. Here a gradient of 59.7 mV pH^{-1} results with an R^2 of 0.9983. Theory predicts that the PCET pH response should follow a Nernstian (59 mV pH^{-1} for 298 K) relationship.

Finally, it is interesting to consider, now we have two peaks recorded in one SWV scan, whether it is possible to use the voltage difference between the peaks as a means to accommodate any possible reference electrode drift issues. Drift is problematic when determining pH from the position of a voltammetric wave. This concept was first proposed by Wrighton *et al.*[45] and has been used by others for pH determination using quinone PCET where a pH insensitive redox molecule is deliberately added to the system.[45–47] Although Equation 5.1 indicates the involvement of H^+ in the reaction, as there are no H^+ transfer reactions occurring before or in the rate determining step,[37,38] $[H^+]$ should not affect the peak position for ORR ET. The peak potential for ORR *vs* SCE from the first set of data collected for Figure 5.8 (pH 4.16, 6.00, 7.15, 8.06, and 10.18, at four different DO concentrations in the range 1.5 – 8.0 mg L^{-1}) was analysed for a statistically significant dependence. Here a Kruskal-Wallis analysis of variance (ANOVA) and a One-Way ANOVA at a 5 % significance level, with the Bonferroni correction for multiple comparisons, were employed. No statistical dependence of ORR peak potential on either DO concentration or pH was observed, Figure 5.9(a) and (b) respectively, where the DO concentration or pH are compared with the ORR peak potential. Figure 5.9c shows the separation between the pH and ORR peaks in one voltammetric scan, ΔE_p, as a function of DO concentration, for fixed pH values between 4.16 to 10.18. ΔE_p can thus be used to inform on solution pH, as shown in Figure 5.9(d), where a close to Nernstian gradient of 57.0 mV is observed when plotting average ΔE_p for all DO concentrations as a function of pH. Figure 5.9 highlights the potential for using the ORR signal as an internal reference for voltammetric pH measurements.

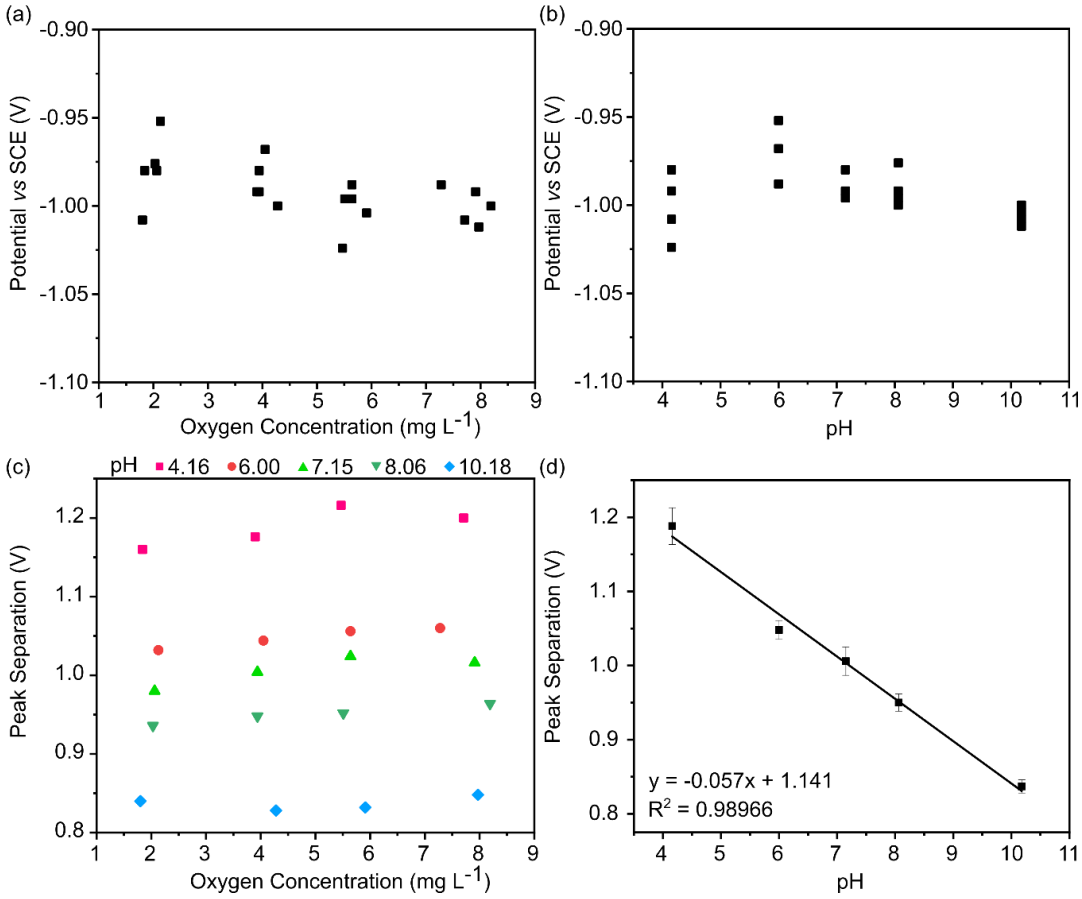

Figure 5.9: Potential dependence of ORR peak on: (a) DO concentration for pH solutions in the range 4.16 to 10.18. (b) pH for DO concentrations in the range 1.5-8.0 mg L^{-1}. (c) Effect of DO concentration on ΔE_p. (d) Effect of pH on average ΔE_p for all DO concentrations, error bars are standard deviation of all ΔE_p for each pH.

5.5 Conclusions

Simultaneous measurement of DO concentration and pH, in the same voltammetric scan, using a hybrid sp^2-BDD electrode containing laser patterned sp^2 regions, was demonstrated in buffered solutions across the pH range 4-10 and DO concentrations of 0 – 8 mg L^{-1} (0 – 0.25 mM). Linear responses to both were observed. The spatial arrangement of sp^2 regions on the BDD, and the voltammetric measurement technique, were both investigated to produce an optimised response for ORR and pH. A diffusional-overlapping microspot sp^2 array in conjunction with SWV was found to produce the largest signals for analysis. As both analytes could be detected in one voltammetric scan (time of scan ~ 4.4 s) this approach offers significant potential benefits over current methods including, for example; the need for only one working electrode and significantly decreased analysis. As there is no membrane, a stabilisation time due to diffusion of species through or across a membrane, is no longer required.

The relationship between peak positions of the DO and pH SWV responses were explored in more detail with the ORR peak position being found to be independent of both DO concentration and pH peak position. A linear relationship was demonstrated between the peak separation between the ORR and pH signals (in the same scan) and pH, indicating promise as a possible avenue for internal referencing and correcting against reference electrode drift. Furthermore, the high thermal conductivity of BDD means placement of a temperature probe on the rear face of the BDD (within the probe) would allow for accurate temperature measurement of the front facing solution, making the sensor a truly standalone multi-purpose device.

5.6 References

(1) Izraėl′, I. A. (I͡Uriĭ A. *Ecology and Control of the Natural Environment*; Springer Netherlands, 1992.

(2) Chiras, D. D. *Human Biology*; Jones and Bartlett Publishers, 2005.

(3) Houdas, Y.; Ring, E. F. J. Human Body Temperature - Its Measurement and Regulation. Plenum Press 1982, p . https://doi.org/10.1007/978-3-319-95729-6.

(4) Hamm, L. L.; Nakhoul, N.; Hering-Smith, K. S. Acid-Base Homeostasis. *Clin. J. Am. Soc. Nephrol.* **2015**, *10* (12), 2232–2242. https://doi.org/10.2215/CJN.07400715.

(5) National Research Council (U.S.). Committee on the Development of an Integrated Science Strategy for Ocean Acidification Monitoring, R. *Ocean Acidification : A National Strategy to Meet the Challenges of a Changing Ocean*; National Academies Press, 2010.

(6) Abele, D.; Vazquez-Medina, J. P.; Zenteno-Savin, T. *Oxidative Stress in Aquatic Ecosystems.*; John Wiley & Sons, 2011.

(7) Maltepe, E.; Saugstad, O. D. Oxygen in Health and Disease: Regulation of Oxygen Homeostasis-Clinical Implications. *Pediatr. Res.* **2009**, *65* (3), 261–268. https://doi.org/10.1203/PDR.0b013e31818fc83f.

(8) Skoog, D. A.; Holler, F. J.; Crouch, S. R. Principles of Instrumental Analysis - Douglas A. Skoog, F. James Holler, Stanley R. Crouch - Google Books, 7th ed.; Cengage Learning: Boston, USA, 2016.

(9) Severinghaus, J. W.; Astrup, P. B. History of Blood Gas Analysis. IV. Leland Clark's Oxygen Electrode. *J. Clin. Monit.* **1986**, *2* (2), 125–139. https://doi.org/10.1007/BF01637680.

(10) Langton, J. A.; Hutton, F. A.; Frca, M. M. Respiratory Gas Analysis. https://doi.org/10.1093/bjaceaccp/mkn048.

(11) Severinghaus, J. W.; Freeman Bradley, A. *Electrodes for Blood PO, and PC0, Determination*; 1958.

(12) Tisherman, S. A.; Forsythe, R. M. *Trauma Intensive Care*; Oxford University Press, 2013.

(13) Peitzman, A. B. *The Trauma Manual : Trauma and Acute Care Surgery*; Wolters Kluwer Health/Lippincott Williams & Wilkins, 2008.

(14) Wu, C.-C.; Yasukawa, T.; Shiku, H.; Matsue, T. Fabrication of Miniature Clark Oxygen Sensor Integrated with Microstructure. *Sensors Actuators B Chem.* **2005**, *110* (2), 342–349. https://doi.org/10.1016/J.SNB.2005.02.014.

(15) Obeidat, Y. M.; Evans, A. J.; Tedjo, W.; Chicco, A. J.; Carnevale, E.; Chen, T. W. Monitoring Oocyte/Embryo Respiration Using Electrochemical-Based Oxygen Sensors. *Sensors Actuators B Chem.* **2018**, *276*, 72–81. https://doi.org/10.1016/J.SNB.2018.07.157.

(16) Jobst, G.; Urban, G.; Jachimowicz, A.; Kohl, F.; Tilado, O.; Lettenbichler, I.; Nauer, G. Thin-Film Clark-Type Oxygen Sensor Based on Novel Polymer Membrane

Systems for in Vivo and Biosensor Applications. *Biosens. Bioelectron.* **1993**, *8* (3–4), 123–128. https://doi.org/10.1016/0956-5663(93)85024-I.

(17) Yang, Z.; Sasaki, S.; Karube, I.; Suzuki, H. Fabrication of Oxygen Electrode Arrays and Their Incorporation into Sensors for Measuring Biochemical Oxygen Demand. *Anal. Chim. Acta* **1997**, *357* (1–2), 41–49. https://doi.org/10.1016/S0003-2670(97)00560-6.

(18) Ramamoorthy, R.; Dutta, P. K.; Akbar, S. A. Oxygen Sensors: Materials, Methods, Designs and Applications. *J. Mater. Sci.* **2003**, *38* (21), 4271–4282. https://doi.org/10.1023/A:1026370729205.

(19) Niazi, A.; Anthony, C. J. Development of Oxygen Sensor by Integrating the Low Cost Printed Circuit Board Technology and Solid Electrolyte Membrane.

(20) Nei, L.; Compton, R. G. An Improved Clark-Type Galvanic Sensor for Dissolved Oxygen. *Sensors Actuators B Chem.* **1996**, *30* (2), 83–87. https://doi.org/10.1016/0925-4005(95)01754-J.

(21) Sosna, M.; Denuault, G.; Pascal, R. W.; Prien, R. D.; Mowlem, M. Development of a Reliable Microelectrode Dissolved Oxygen Sensor. *Sensors Actuators B* **2007**, *123*, 344–351. https://doi.org/10.1016/j.snb.2006.08.033.

(22) Yu-Quan, C.; Guang, L. An Auto-Calibrated Miniature Microhole Cathode Array Sensor System for Measuring Dissolved Oxygen. *Sensors Actuators B Chem.* **1993**, *10* (3), 219–222. https://doi.org/10.1016/0925-4005(93)87009-E.

(23) O'Hare, D.; Winlove, C. P.; Parker, K. H. Electrochemical Method for Direct Measurement of Oxygen Concentration and Diffusivity in the Intervertebral Disc: Electrochemical Characterization and Tissue-Sensor Interactions. *J. Biomed. Eng.* **1991**, *13* (4), 304–312. https://doi.org/10.1016/0141-5425(91)90112-K.

(24) Wang, P.; Liu, Y.; Abruña, H. D.; Spector, J. A.; Olbricht, W. L. Micromachined Dissolved Oxygen Sensor Based on Solid Polymer Electrolyte. *Sensors Actuators B Chem.* **2011**, *153* (1), 145–151. https://doi.org/10.1016/J.SNB.2010.09.075.

(25) Chou, T. .; Ng, K. .; Wang, S. . Gold-Solid Polymer Electrolyte Sensor for Detecting Dissolved Oxygen in Water. *Sensors Actuators B Chem.* **2000**, *66* (1–3), 184–186. https://doi.org/10.1016/S0925-4005(00)00349-X.

(26) Grist, S. M.; Chrostowski, L.; Cheung, K. C. Optical Oxygen Sensors for Applications in Microfluidic Cell Culture. *Sensors (Basel).* **2010**, *10* (10), 9286–9316. https://doi.org/10.3390/s101009286.

(27) O'Hare, D.; Parker, K. H.; Winlove, C. P. Metal–metal Oxide PH Sensors for Physiological Application. *Med. Eng. Phys.* **2006**, *28* (10), 982–988. https://doi.org/10.1016/J.MEDENGPHY.2006.05.003.

(28) Kahlert, H. Functionalized Carbon Electrodes for PH Determination. *J. Solid State Electrochem.* **2008**, *12* (10), 1255–1266. https://doi.org/10.1007/s10008-008-0566-7.

(29) Ayres, Z. J.; Borrill, A. J.; Newland, J. C.; Newton, M. E.; Macpherson, J. V. Controlled Sp ^{2} Functionalization of Boron Doped Diamond as a Route for the

Fabrication of Robust and Nernstian PH Electrodes. *Anal. Chem.* **2016**, *88* (1), 974–980. https://doi.org/10.1021/acs.analchem.5b03732.

(30) Ayres, Z. J.; Cobb, S. J.; Newton, M. E.; Macpherson, J. V. Quinone Electrochemistry for the Comparative Assessment of Sp2 Surface Content of Boron Doped Diamond Electrodes. *Electrochem. Commun.* **2016**, *72*, 59–63. https://doi.org/10.1016/j.elecom.2016.08.024.

(31) Cobb, S.; Ayres, Z. J.; Newton, M. E.; Macpherson, J. V. Deconvoluting Surface-Bound Quinone Proton Coupled Electron Transfer in Unbuffered Solutions: Towards a Universal Voltammetric PH Electrode. *J. Am. Chem. Soc.* **2019**, *141* (2), 1035–1044. https://doi.org/10.1021/jacs.8b11518.

(32) Macpherson, J. V. A Practical Guide to Using Boron Doped Diamond in Electrochemical Research. *Phys. Chem. Chem. Phys.* **2015**, *17* (5), 2935–2949. https://doi.org/10.1039/c4cp04022h.

(33) Cobb, S. J.; Ayres, Z. J.; Macpherson, J. V. Boron Doped Diamond: A Designer Electrode Material for the Twenty-First Century. *Annu. Rev. Anal. Chem.* **2018**, *11* (1), annurev-anchem-061417-010107. https://doi.org/10.1146/annurev-anchem-061417-010107.

(34) Yang, N.; Yu, S.; Macpherson, J. V.; Einaga, Y.; Zhao, H.; Zhao, G.; Swain, G. M.; Jiang, X. Conductive Diamond: Synthesis, Properties, and Electrochemical Applications. *Chem. Soc. Rev.* **2019**, *48* (1), 157–204. https://doi.org/10.1039/C7CS00757D.

(35) Morcos, I.; Yeager, E. Kinetic Studies of the Oxygen-Peroxide Couple On Pyrolytic Graphite. *Electrochim. Acta* **1970**, *15*, 953–975.

(36) Yeager, E. Electrocatalysts for O2 Reduction. *Electrochim. Acta* **1984**, *29* (11), 1527–1537. https://doi.org/10.1016/0013-4686(84)85006-9.

(37) Taylor, R. J.; Humffray, A. A. Electrochemical Studies on Glassy Carbon Electrodes. II. Oxygen Reduction in Solutions of High PH (PH>10). *J. Electroanal. Chem.* **1975**, *64* (1), 63–84. https://doi.org/10.1016/S0022-0728(75)80278-6.

(38) Taylor, R. J.; Humffray, A. A. Electrochemical Studies on Glassy Carbon Electrodes III. Oxygen Reduction in Solutions of Low PH (PH<10). *J. Electroanal. Chem. …* **1975**, *64*, 85–94.

(39) Carmody, W. R. Easily Prepared Wide Range Buffer Series. *J. Chem. Educ.* **1961**, *38* (11), 559. https://doi.org/10.1021/ed038p559.

(40) Joseph, M. B.; Bitziou, E.; Read, T. L.; Meng, L.; Palmer, N. L.; Mollart, T. P.; Newton, M. E.; Macpherson, J. V. Fabrication Route for the Production of Coplanar, Diamond Insulated, Boron Doped Diamond Macro- and Microelectrodes of Any Geometry. *Anal. Chem.* **2014**, *86* (11), 5238–5244. https://doi.org/10.1021/ac501092y.

(41) Huang, X.-J.; O'Mahony, A. M.; Compton, R. G. Microelectrode Arrays for Electrochemistry: Approaches to Fabrication. *Small* **2009**, *5* (7), 776–788. https://doi.org/10.1002/smll.200801593.

(42) Fletcher, S.; Horne, M. D. Random Assemblies of Microelectrodes (RAM™ Electrodes) for Electrochemical Studies. *Electrochem. Commun.* **1999**, *1* (10), 502–512. https://doi.org/10.1016/S1388-2481(99)00100-9.

(43) Bard, A. J.; Faulkner, L. R. Electrochemical Methods: Fundamentals and Applications, 2nd ed.; Wiley.

(44) Jackson, M. N.; Oh, S.; Kaminsky, C. J.; Chu, S. B.; Zhang, G.; Miller, J. T.; Surendranath, Y. Strong Electronic Coupling of Molecular Sites to Graphitic Electrodes via Pyrazine Conjugation. *J. Am. Chem. Soc.* **2018**, *140* (3), 1004–1010. https://doi.org/10.1021/jacs.7b10723.

(45) Hickman, J. J.; Ofer, D.; Laibinis, P. E.; Whitesides, G. M.; Wrighton, M. S. Molecular Self-Assembly of Two-Terminal, Voltammetric Microsensors with Internal References. *Science*. American Association for the Advancement of Science pp 688–691. https://doi.org/10.2307/2875430.

(46) Leventis, H. C.; Streeter, I.; Wildgoose, G. G.; Lawrence, N. S.; Jiang, L.; Jones, T. G. .; Compton, R. G. Derivatised Carbon Powder Electrodes: Reagentless PH Sensors. *Talanta* **2004**, *63* (4), 1039–1051. https://doi.org/10.1016/J.TALANTA.2004.01.017.

(47) Gagné, R. R.; Koval, C. A.; Lisensky, G. C. Ferrocene as an Internal Standard for Electrochemical Measurements. *Inorg. Chem.* **1980**, *19* (14), 2854–2855.

Chapter 6: Enhancing Square Wave Voltammetry Measurements via Electrochemical Analysis of the Non-Faradaic Potential Window

6.1 Overview

Square wave voltammetry (SWV) is a commonly used analytical technique, where a series of potential pulses are applied with the intention of increasing signal to noise ratios and reducing background (non-faradaic currents). The raw current-time (*i*-*t*) data from this method is often discarded, and only the currents over the last part of the potential pulse are used to form a voltammogram. However, discarded data can offer further analytical information if collected. In this chapter it is demonstrated that in regions of the potential window where there are only non-faradaic reactions, information on the resistance and capacitance can be found by fitting the *RC* decay seen in the first part of the *i*-*t* data. This information can be used to inform on the solution conductivity and electrode capacitance, which are useful metrics for electrode condition and tracking effects such as fouling. These measurements are possible at high frequencies (up to 1667 measurements per second) and without the need to conduct further electrochemical experiments, such as electrochemical impedance spectroscopy. Measurement of the *RC* decay can also be used to infer if the square wave parameters are sufficient to have completely removed any non-faradaic contributions to the SWV, allowing simple and fast optimisation of the measurement conditions.

6.2 Introduction

In electroanalysis, pulsed voltammetric techniques are a common way of increasing detection sensitivity,[1] with the aim of excluding the capacitive contribution from the response, resulting in lower detection limits. Square wave voltammetry (SWV), originally developed by Kalousek and Barker,[2] is particularly popular,[3] as it allows faster analysis times compared to other pulse techniques such as differential pulse voltammetry or normal pulse voltammetry.[1] For most analytical applications, staircase SWV, as proposed by Ramaley and Krause,[4,5] and often referred to as SWV (or Osteryoung SWV),[6] has become the *de facto* standard. SWV is widely used in electroanalytical studies, interestingly, often with little or no comment as to how the operational parameters chosen were adopted.

SWV involves the application of a series of potential pulses, formed from a potential staircase (Figure 6.1a, dashed line) overlaid with a square wave pulse, with a forward and then reverse pulse occurring on each tread of the staircase (Figure 6.1a

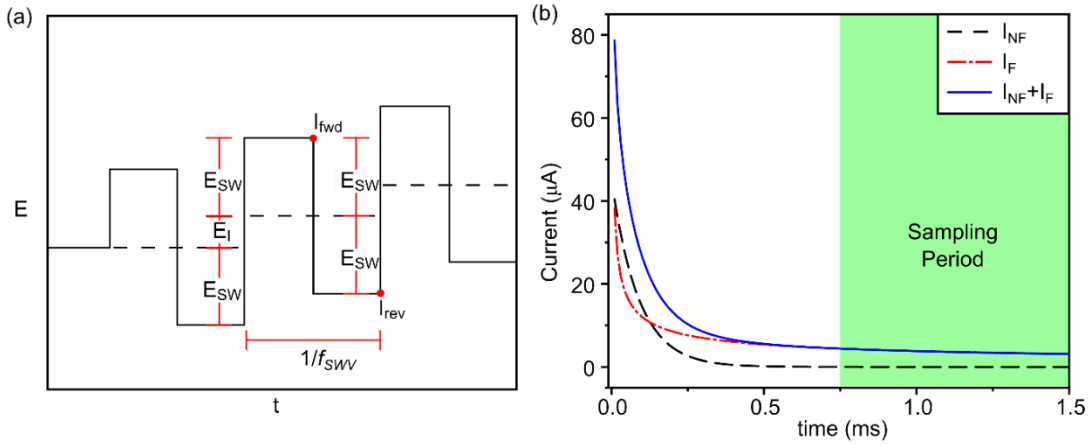

, solid line).[3] Operational variables include the pulse amplitude, (E_{sw}) frequency (f_{SW}) and staircase increment (E_I), creating a large parameter space for SWV optimisation. The raw data consists of a series of current time (*i*-*t*) decays in the anodic and cathodic directions, where the length of the decay is determined by the frequency employed.

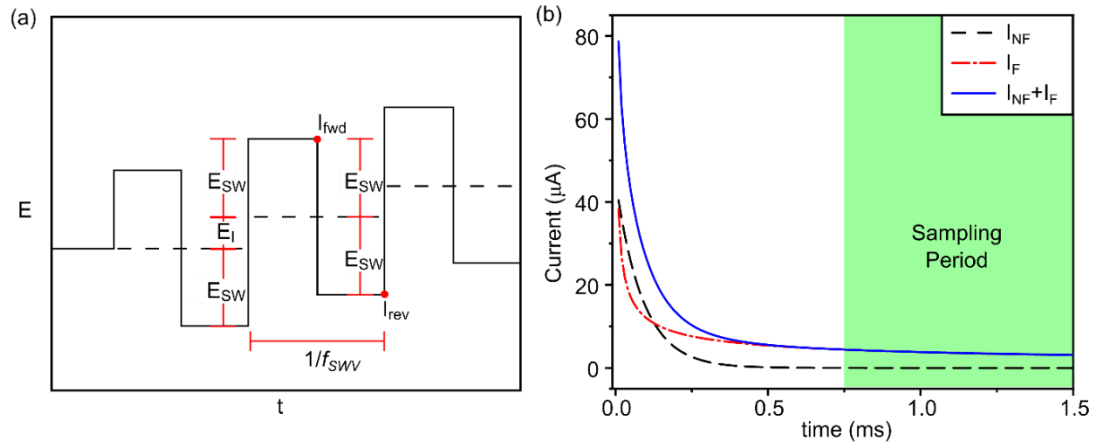

Figure 6.1:(a) SWV potential pulse sequence, where E_{sw} is the amplitude, f_{SW} is the square wave frequency, E_I is the increment, I_{fwd} and I_{rev} are the sampling points for the forward and reverse currents,respectively. (b) Theoretical I_{NF}, I_F and (I_{NF}+I_F) current-time responses for an anodic potential pulse of ΔE= 0.1 V, R= 3kΩ, C_{dl}= 40 nF, Diffusion coefficient= 8 × 10^{-6} cm s^{-1} concentration = 0.1 mM.

An example *i-t* curve in a single square wave pulse (blue line), for detection of a redox active analyte, is shown in Figure 6.1b, where the current passed represents the sum of the faradaic (I_F; red line, diffusional $t^{-1/2}$ decay[7]) and non-faradaic (I_{NF}, black line, exponential *t* decay) current. With the text book definition of SWV, the current at the end of each pulse is sampled and the reverse current subtracted from the forward current and plotted against the staircase potential to give a voltammogram. However, to improve on noise, many commercial potentiostats current average over a defined percentage of the pulse (as much as 50-100% of each individual *i-t* trace).[8] Some potentiostats also record the forward and reverse currents in the output data for inspection by the user.

In a potential range where no faradaic reactions occur, the shape of the *i-t* decay curve on the application of a potential pulse is related to resistance, *R*, and capacitance, *C*, which collectively represent the time constant, *RC*, as shown by equation 1, where ΔE represents the potential pulse height (the forward pulse is larger than the reverse pulse by E_I).

$$i(t) = \frac{\Delta E}{R} e^{-t/RC} \qquad [6.1]$$

In the case of an electrochemical cell *R* is related to the cell geometry, electrode spacing, electrode *R* and solution *R*.[9] This is referred to as the uncompensated *R*, R_u. If the cell geometry is fixed and the electrode *R* negligible, R_u depends only on solution

R. In theory the conditions of SWV should be chosen such that sampling occurs at a time (or time period) in the *i-t* curve where the non-faradaic currents have decayed to ~ 0 and only the faradaic response is analysed. In systems where *R* and / or *C* are high, low frequencies and small amplitudes should be used for sensitive faradaic analysis, however this is at the expense of long measurement times and reduced faradaic currents. In the presence of faradaic electron transfer (ET), kinetic and mechanistic information on ET processes is also possible, for example from analysing the relationship between peak current and frequency,[10–12] or amplitude.[13–15 16]

In SWV, focus is always on the faradaic ET reaction. However, by sampling in a potential region where only non-faradaic (double layer charging) reactions are captured, using appropriate sampling conditions, it should be possible to extract information on *R* and *C*. *R* can be used to inform on solution conductivity (σ), and *C*, on the double layer capacitance (C_{dl}) of the electrode. Information on the former is important for a large number of applications including drinking water quality assessment, process water monitoring, production of ultrapure water, and measurement of the salinity of seawater.[17] In contrast, *C* could be used to inform on changes that are taking place at the electrode surface, as a function of time *e.g.* electrode fouling,[18–20] common in more complex real world solution matrices. Knowledge of *RC* can also be used to provide feedback on the most appropriate parameters for faradaic SWV analysis. Typically, electrochemical impedance spectroscopy (EIS), is used as the method of choice for determining *R* and *C*, along with providing information on charge transfer kinetics.[21] However, EIS measurements can be time consuming, requires an appropriate equivalent circuit to be determined and fitted and are not amenable to electroanalytical detection measurements.

In this chapter the potential of SWV to provide information on σ (through *R*) and electrode modification/fouling (through *C*), during electroanalysis, using the part of the *i-t* trace that is typically discarded in conventional SWV is investigated. We employ a boron doped diamond (BDD) electrode for these proof-of-concept studies, given BDD offers a wide potential range over which non-faradaic processes occur.[22] We show how the non-faradaic *i-t* curve can be utilised to provide optimisation data for subsequent faradaic SWV analysis and demonstrate the ability of SWV to inform on solution conductivity and surface modification processes taking place at the electrode. Finally, using an appropriately sp^2 functionalised BDD electrode[23,24] and by

sampling in the appropriate potential regions, we highlight how SWV with the same electrode, can provide information on both solution pH (faradaic) and solution conductivity (non-faradaic).

6.3 Experimental

6.3.1 Materials and solutions.

All solutions were prepared from Milli-Q water (Millipore Corp.) with a resistivity of 18.2 MΩ cm at 25 °C. Potassium nitrate (KNO_3, 99.97%; Sigma Aldrich) and potassium chloride (KCl, ≥99%; Sigma Aldrich) were used as supporting electrolytes at different concentrations to adjust σ. The σ and resistivity(ρ) of all solutions was measured independently using a commercial four-point graphite probe conductivity sensor (InLab 731, Mettler Toledo). This sensor was specified for σ of $10^1 - 10^6$ µS cm^{-1} with a nominal cell constant (k) of 0.57 cm^{-1}. 0.5% w/v mucin from porcine stomach (≥99%; Sigma-Aldrich) and serotonin hydrochloride (≥98%; Sigma Aldrich) were used for fouling experiments with σ adjusted using KCl. Hexaaminеruthenium(III)Chloride ($Ru(NH_3)_6.Cl_3$, >97%, Strem Chemicals) was used for electrode characterization. Water samples were collected from Bassenthwaite lake, Lake District, UK; Hayle estuary, Cornwall, UK; Kenilworth river, Warwickshire, UK and laboratory taps at the University of Warwick, UK. For the laser micromachined BDD electrode experiments pH 7.09 Carmody buffer was prepared using boric acid (H_3BO_3, 99.97%; Sigma- Aldrich), citric acid ($C_6H_8O_7$, ≥ 99.5%; Sigma-Aldrich), and tertiary sodium phosphate (Na_3PO_4, ≥95%; Sigma-Aldrich) with a buffer capacity of 25−30 mM per pH unit.[25]

6.3.2 Electrochemical setup.

For electrochemical measurements a three-electrode configuration was utilized for all experiments. A 1 mm diameter minimal sp^2 content BDD disk, doped above the metallic threshold and encapsulated with insulating diamond, was used as the working electrode (WE). Fabrication of this electrode is described elsewhere.[26] For sp^2-BDD electrode experiments, a 1 mm BDD disk electrode containing a laser micromachined hexagonal array of sixty-one, 50 µm diameter sp^2 containing laser pits, with a center-to-center spacing of 100 µm was employed; described in detail elsewhere.[23,24] A platinum wire was used as the counter electrode (CE) and a saturated calomel electrode (SCE) as the reference electrode (RE). The electrode spacing was controlled, with the RE at an electrode centre-to-centre distance of 5 mm from the WE. All measurements were performed using an Ivium compactstat (Ivium Technologies B.V.).

A series of potential pulses were applied and the resulting *i-t* traces recorded. The potential levels and pulse times were chosen to simulate a SWV measurement in

amplitude, frequency and increment. For reconstructed SWV in 1 mM $Ru(NH_3)_6^{3+}$ reduction in 5 mM KNO_3. 246 potential pulses were applied between 0 to -0.5 V *vs* SCE with an E_{SW}= 0.1 V, E_I = 4 mV and f_{SW} = 156 Hz and the SWV response, for different current averaged time periods of each *i-t* trace (25% – 100%; 37.5% – 100%; 50% – 100%; 62.5% – 100% and 75 – 100% of the pulse duration). For all studies the potentiostat filter was set to 1 MHz and the high speed mode used for stability to avoid additional processing of the data by the instrument. For $f_{SW} \leq 25$ Hz the sampling frequency (f_{samp}) was 1 kHz, limited by the data transfer rate. At $f_{SW} > 25$ Hz the f_{samp} was 60 × greater than f_{SW}, limited by the onboard potentiostat memory to 8192 data points for the entire scan. Complementary EIS studies were conducted at 0.1 V *vs* SCE with an amplitude of 10 mV at 16 equally spaced frequencies from 10 Hz to 1 MHz.

6.3.3 Data Analysis.

All data was analysed using Matlab R2018a (Mathworks). Each potential pulse was extracted and fitted with exponential decays using the curve fitting toolbox, the coefficients from this were used to extract *R* and *C*.

6.4 Results and discussion

To ensure that when complete *i-t* data is collected for a SWV, a typical voltammogram can be reformed a series of pulses was applied in 1 mM Hexaaminеruthenium(III) Chloride (>99%, Sigma Aldrich, UK) in 5 mM KCl supporting electrolyte. The pulses simulated a SWV scanning cathodically from 0 to -0.5 V with an amplitude of 0.1 V, an increment of 4 mV and a frequency of 156 Hz and the raw *i-t* data was collected (Figure 6.2a). To form a SWV, the first part of the pulse (where non-faradaic processes are a factor) is omitted and the remainder (from 25 to 75% of the pulse, to simulate different potentiostats sampling parameters) averaged to give forward and reverse currents or the current at the end of the pulse used (Figure 6.2b). These currents are assumed to be only faradaic. This assumption is only valid when the *RC* decay is much faster than the frequency. The reverse current is subtracted from the forward current to generate a SWV (Figure 6.2c). By capturing the entire pulse however, the initial part of the scan that is usually omitted can be used to inform on the non-faradaic processes that occur to generate the *RC* decay witnessed i.e. capacitance and resistance. In regions of the scan where there are no faradaic reactions occurring, such as well before the E^0 for the analyte of interest and away from the electrode solvent window, the currents are purely non-faradaic and can be used to infer whether these processes are contributing to the currents used for analyte detection. The *RC* decay may impinge on the portion of the pulse used to form the SWV. This can be used to optimise the measurement conditions for a particular solution.

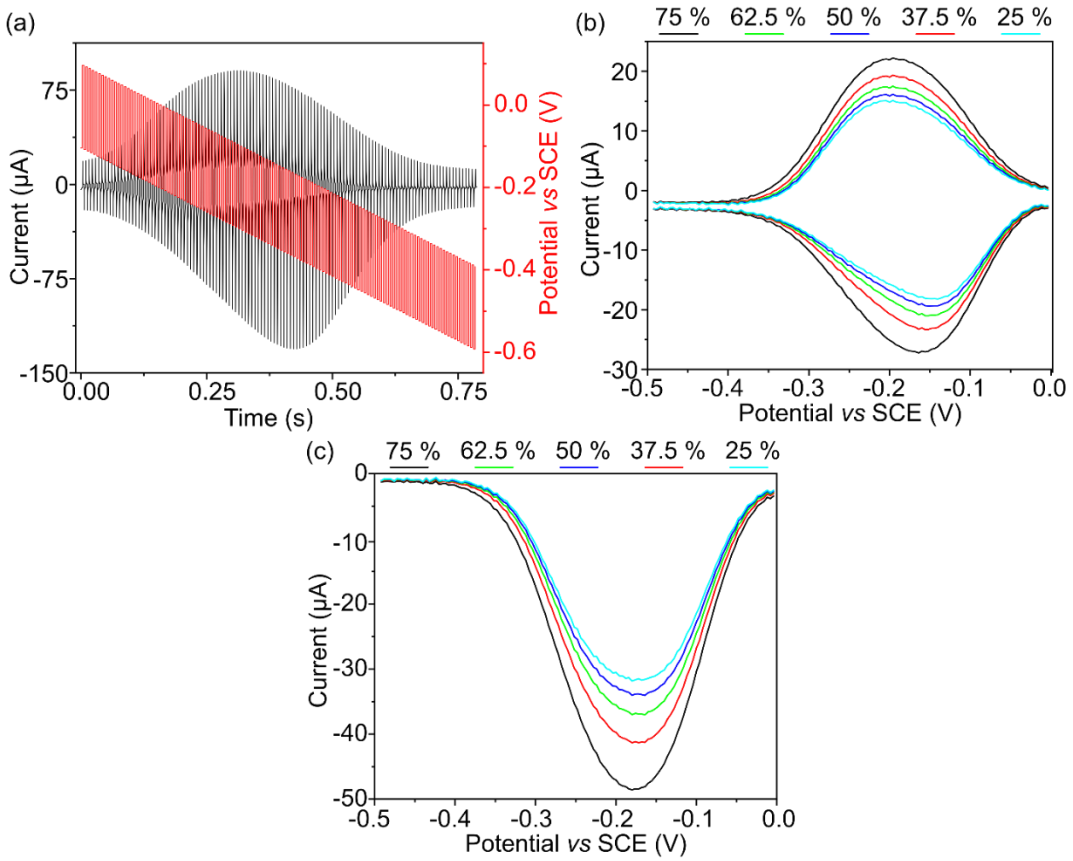

Figure 6.2:(a) Raw i-t data for 1 mM ruthenium(III)hexamine. (b) forward and reverse currents at sample intervals (25-75%). (c) SWV at sample intervals (25-75%).

6.4.1 Extracting σ and C data from a SWV signal

The insert to Figure 6.3 shows the cyclic voltammetric (CV) response for a BDD electrode in 0.1 M KCl electrolyte (scan rate = 0.1 V s^{-1}). The CV is almost featureless as a result of inner sphere redox processes such as water electrolysis and oxygen reduction reaction being kinetically hindered,[22,27] with the cathodic window dominated by hydrogen evolution reaction[28] and the anodic by chloride oxidation.[29] There is a large potential window (~ -1.3 V to +1.0 V *vs* SCE) in which the current response is dominated by double layer capacitance. In this potential range the raw *i-t* data from a SWV will depend only on *R* and *C*. Figure 6.3 shows representative *i-t* data, taken from a single potential step in the SWV (0.0 to 0.2 V *vs* SCE over a time period of 0.3 ms *i.e.* f_{SW}= 1.67 kHz), for *n*=35 solutions of different electrolyte concentrations (i.e. σ) across the range 2 - 24 mS cm^{-1}. As σ decreases, the decay time length increases, in accordance with Equation 6.1. The time at which the data is free from *RC* contributions, which is assumed to be where the non-faradaic current is less than the resolution of the potentiostat 16 bit analogue to digital converter for a 100 μA

current range (3 nA), has a dependence on σ. At the highest σ, 24 mS cm^{-1}, current sampling at times ≥ 120 µs are recommended and at the lowest σ, 20 µS cm^{-1}, times of ≥ 82 ms are required. These times set limits on the SWV sampling frequency for truly *RC* free contributions to the current. Note, for very low (0.1 mS cm^{-1}) conductivity measurements, the f_{SW} required may not be practical for real world measurements.

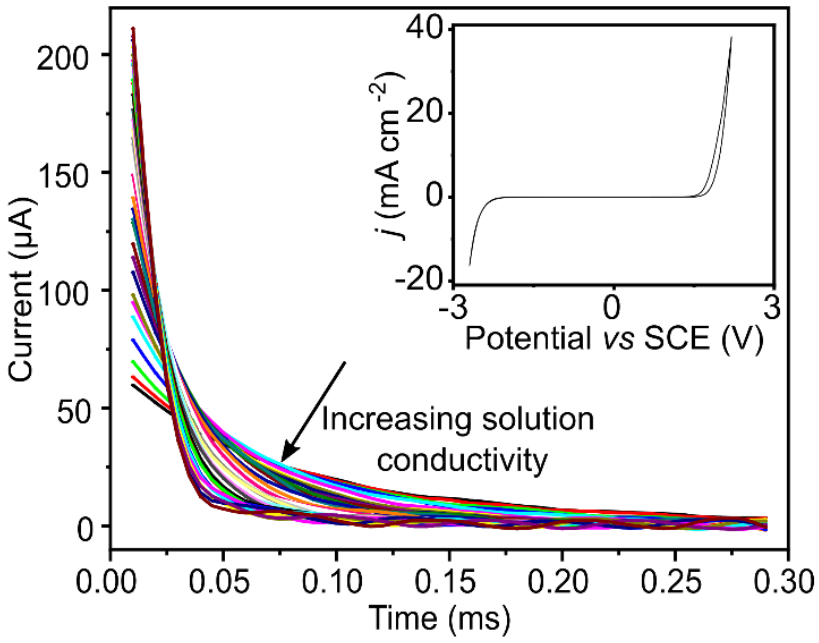

Figure 6.3: i-t decays (n=35) for a single cathodic potential pulse from a SWV measurement in the region where only non-faradaic reactions occur (0 to 0.2 V vs SCE) in solutions from 2-24 mS cm^{-1}. Inset: CV recorded at 0.1 V s^{-1} in 0.1 M KNO_3, for BDD

In SWV, many pulses are recorded, with the exact number being controlled by E_I and the potential scan range of interest. Both the forward and reverse *i-t* curves, per potential step, can be analysed using Equation 6.2. The modulus of the current response in each pulse can be analysed using an exponential fit of the form:

$$|i| = A*exp(B*t) \qquad [6.2]$$

where in accordance with equation 6.1, the pre-exponential term A represents ($\Delta E/R$), where ΔE for a forward pulse is larger than the reverse pulse by the increment, and B is ($-1/RC$). From A as ΔE is known, R can be experimentally determined for each pulse. This is shown in Figure 6.4a, for a solution containing 0.25 M KCl. 246 potential pulses were applied in the cathodic direction over a potential range free from

faradaic contribution, +0.3 to -0.2 V *vs* SCE, with an E_{SW}= 0.1 V and E_I= 4 mV. E_{SW} was chosen to be large enough to give current decays on the 100s of µA scale without stepping into solvent processes at the potential of faradaic reactions and E_I was chosen to give a reasonable (~0.5 V) potential scan range with the 246 pulses that were applied. This data is exemplar of the response across the entire σ range and was chosen as one of the highest σ studied, with the fast *RC* decay making it one of the most challenging solution conditions for this measurement. The black and red data sets correspond to forward and reverse pulses, respectively. Figure 6.4a shows the direction of ΔE does not affect the measured *R* values, nor the absolute potential applied. The extracted *R* values are within the measurement uncertainty across the entire potential range scanned, independent of pulse direction. Thus it is possible to use the mean value for the *R* values obtained from all the pulses to give a single value, $R = 429 \pm 13\ \Omega$ (n=246). The large amount of data collected in one SWV scan provides accurate mean values for *R* on a short timescale; here 246 individual measurements are captured in less than a second.

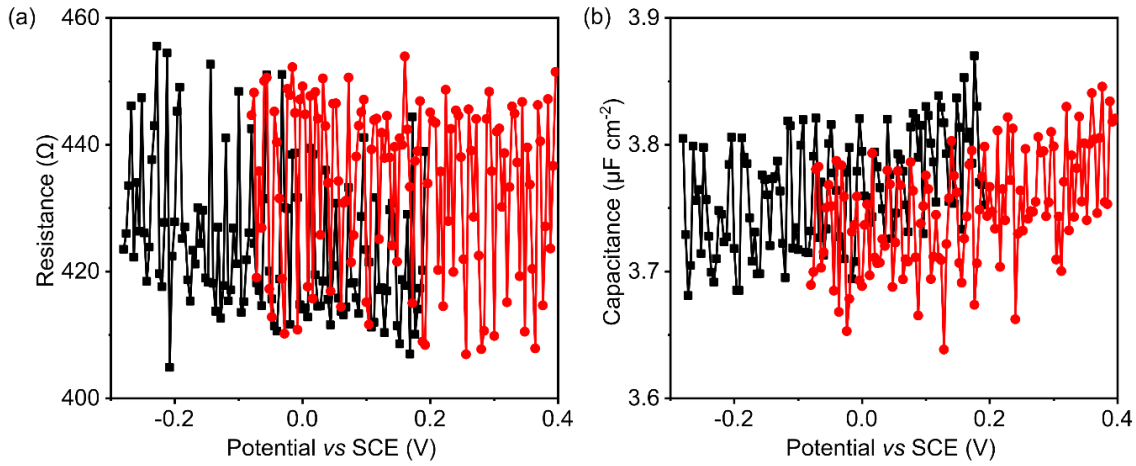

Figure 6.4: Effect of electrode potential on (a) the fitted R values and (b) C values for the forward (black) and reverse (red) pulses in a solution of 0.25 M KCl. E_{SW}= 0.1 V and E_I= 4 mV.

With knowledge of *R* it is possible to determine *C* for each pulse, from the exponential term B in equation 6.2, as shown in Figure 6.4b. Unlike *R*, *C* and in particular, the C_{dl} of the electrode can have a dependence on the absolute potential and step direction.[30] However, BDD in aqueous solutions over the comparatively small potential range employed has been shown to have an almost flat capacitance-potential relationship.[31–33] As such *C* is averaged to give a value for the entire scan, in this case 3.76 ± 0.04

µF cm^{-2} (*n*=246). A complementary EIS measurement for the same 0.25 M KCl solution at 0.1 V *vs* SCE gave a value for *C*, in very close agreement, =3.8 ± 0.11 µF cm^{-2}, when fitted with a simple *RC* circuit (a resistor and capacitor in series).

To ensure the *R* and *C* values output represent components in the proposed equivalent circuit, *R* and *C* values the measurement was run against a dummy cell as described in figure 6.5. A SWV was run across the potential range + 0.3 to -0.2 V with an amplitude of 0.1 V, increment of 0.004 V and frequency of 1.67 kHz.

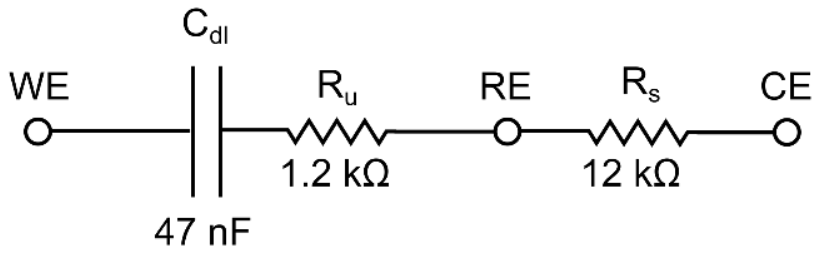

Figure 6.5: Dummy cell circuit where electronic components are used to represent the components of an electrochemical cell where only non-faradaic reactions occur. The double layer capacitance (C_{dl}) by a 47 nF resistor, Ru by a 1.2 kΩ resistor and the compensated solution R (R_s) by a 12 kΩ resistor.

A *R* of 1.196 ± 0.002 kΩ (resistor value 1.2 ± 0.006 kΩ) and *C* of 46.9 ± 0.4 nF (capacitor value 47 ± 2 nF) were recorded from the *i-t* trace. These are within the tolerance on the electronic components. This indicates the measured *C* and *R* equate to C_{dl} and R_u.

The shape of the *RC* decay is dependent on the cell geometry (Figure 6.6) with the working WE to RE distance affecting the measured uncompensated resistance (R_u). When the WE-RE spacing was changed from 5 mm to 45 mm electrode centre to centre spacing the measured *R* changed from 7000 to 7490 Ω. An increase of ~9 × in the inter-electrode distance caused a <10% change in the R_u, suggesting electrode spacing affects the measured *R*, but the system is not particularly sensitive to it. R_u

does not correlate linearly to the electrode position, with the position of all 3 electrodes and cell geometry affecting the value.[9]

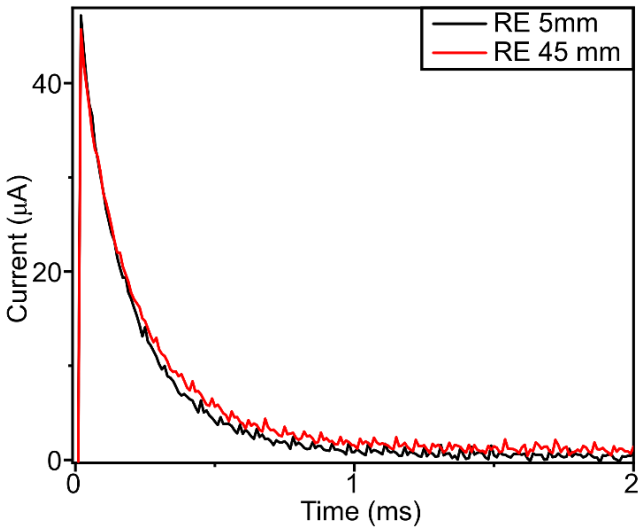

Figure 6.6: i-t curves for 5 mm (Black) and 45 mm (Red) WE-RE centre to centre spacing for a 0.3 V potential step in a 792 μS cm^{-1} KCl solution.

The RE position gave no measurable change in *C*, with values of 3.66 and 3.83 ± 0.23 μF cm^{-2} for 5 and 45 mm spacings respectively. These values are within the error of the measurement.

C_{dl} can have a concentration[34] and electrolyte dependence[35], as the thickness of the Stern layer and ion mobility changes. Due to this some change in *C* is expected with conductivity. The *C* measurements across the entire σ range are shown in Figure 6.7. While small changes in *C* are witnessed no specific trend observed, and an average value of 3.71 ± 0.23 μF cm^{-2} (n = 45510, 185 measurements each of 246 pulses) can be calculated. The small magnitude of these changes means no attempt was made to relate these changes to fundamental solution properties.

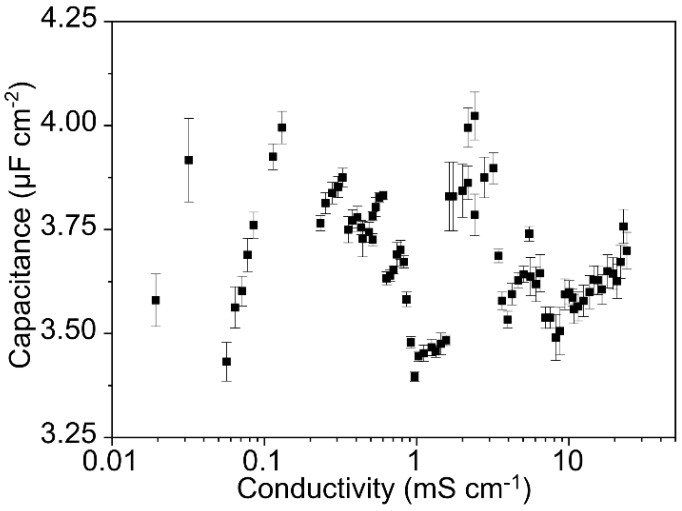

Figure 6.7: Effect of solution σ on the measured C by fitting the RC decay from SWV data.

These values agree well with previously published values for these electrodes using CV over the potential range ± 0.1 V *vs* SCE; C = 7.7-2.7 µF cm^{-2} [26,36]

6.4.2 Measurement of σ using SWV

To assess whether *i-t* traces from SWV could be used to quantify σ, initial experiments considered the KCl electrolyte system over the σ range 20 µS cm^{-1} – 24 mS cm^{-1}. SWV was employed using the conditions *vide supra.* As σ increases, and the *RC* time constant decreases, faster sampling is required to accurately capture the *RC* decay and *vice versa*. The onboard memory of the potentiostat limits the number of possible data points, therefore f_{samp} and f_{SW} must be changed throughout the conductivity range to accurately capture the *RC* decay.

The *R* values from the *RC* decay are the R_u, which represents several series *R* between the WE and RE and at low σ is dominated by the solution *R* and at high σ other system, solution independent, *R* in the system *e.g.* the electrode and wire *R*. Figure 6.8a shows a plot of measured *R* values versus the measured solution resistivity (ρ=1/σ), the latter measured using a commercial conductivity meter, for the range 42 Ω cm – 50kΩ cm (σ= 20 µS cm^{-1} – 24 mS cm^{-1}). The relationship between ρ and *R* is linear (r^2=0.999) and the intercept of this plot (ρ=0, R=168 ± 15 Ω) represents the additional system *R* and when subtracted from the measured *R* values the solution *R* can be determined and the solution conductance (G) plotted against solution σ (Figure 6.8b), the gradient of which is equal to k = 0.176 ± 0.002 cm^{-1}.

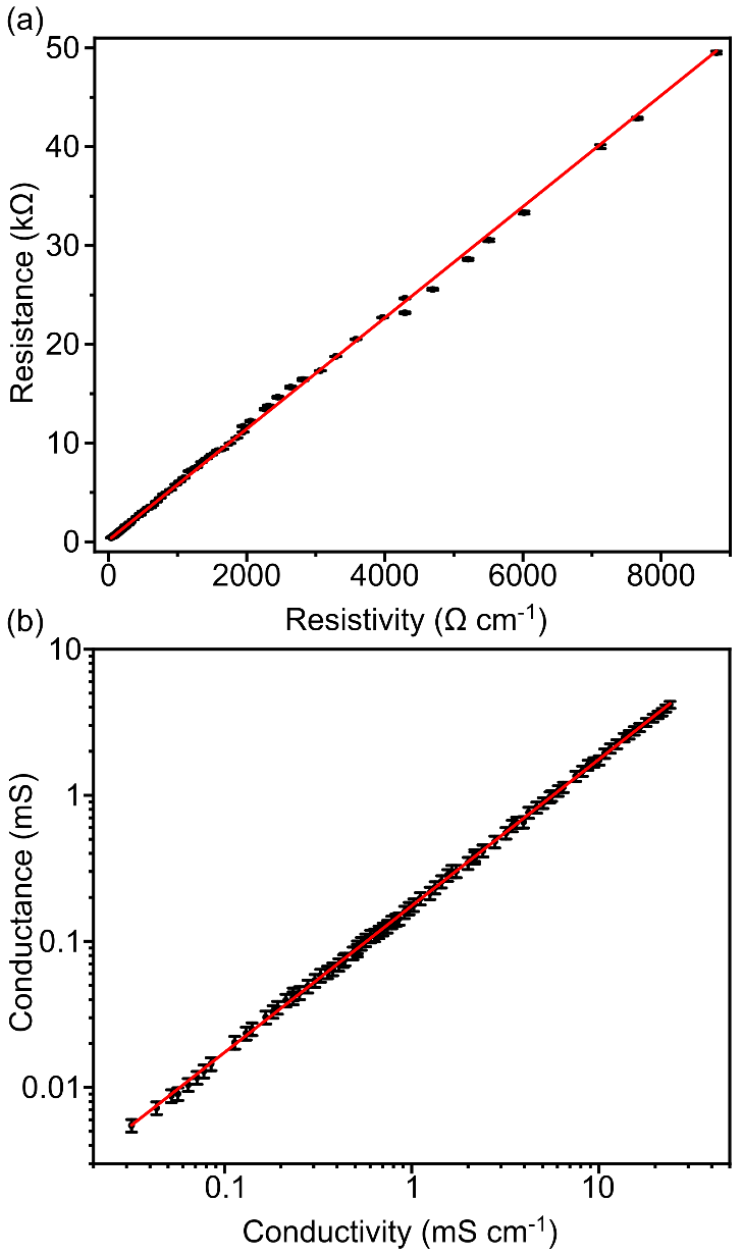

Figure 6.8: (a) Measured R values in solutions of known ρ from SWV, the X intercept of which represents additional system R that when excluded give solution R. (b) Measured solution G in KCl from SWV in solutions of differing σ (gradient= 0.176 ± 0.002, r^2= 0.999).

To test the origin of this system *R* (168 ± 15 Ω) the measured *R* for a BDD electrode and a Au electrode in a solution of the same *σ* (=15.13 mS cm^{-1}) were compared. For the Au electrode the measured *R* was 198 ± 6 Ω and for BDD 418 ± 5 Ω. This suggests the BDD electrode is inherently more resistive than a traditional noble metal electrode.

While the BDD is metallically doped its conductivity is orders of magnitude lower than Au.

To test the electrolyte dependence of the measured solution G on σ the same experiment was performed in KNO_3 (Figure 6.9). A linear response with a similar k (0.174 ± 0.003 cm^{-1}) was observed, demonstrating the electrolyte independence of the measured solution G, as would be expected.

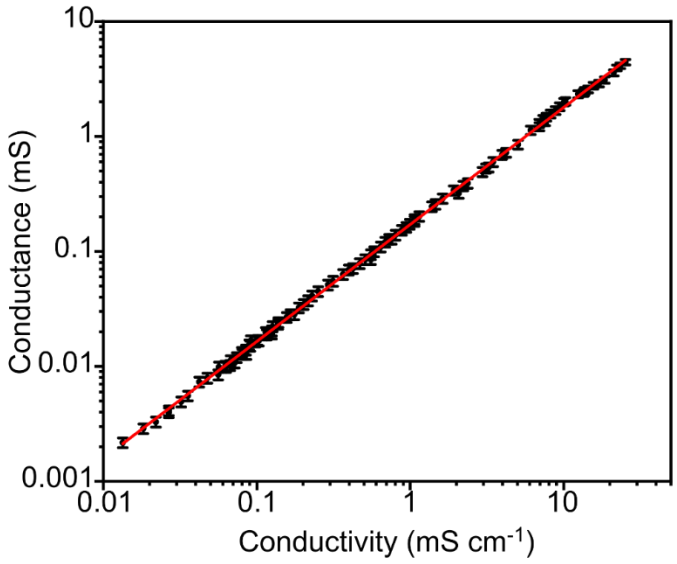

Figure 6.9: Measured solution G in KNO3 from SWV in solutions of differing σ (gradient= 0.174 ± 0.003, r2= 0.999).

As the σ is increased (ρ decreased) further, the response plateaus, an effect found to be dependent on f_{samp}. A five-fold increase in f_{samp} (1 kHz to 5 kHz), increased the σ of the plateau from 0.3 mS cm^{-1} to 1.6 mS cm^{-1} (Figure 6.10).

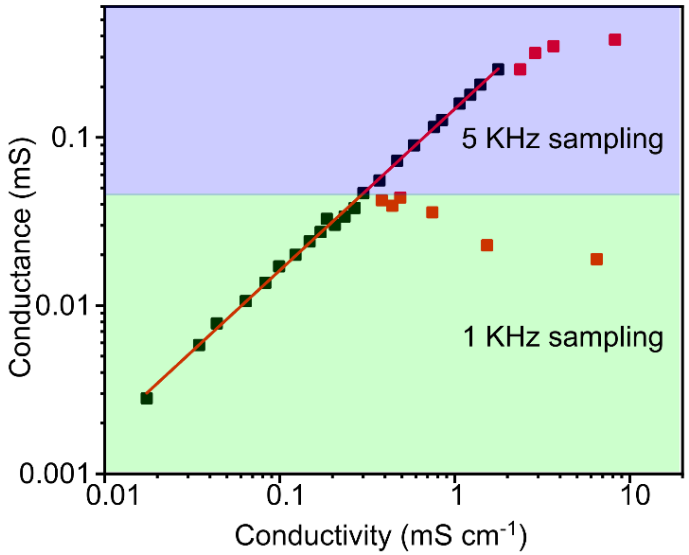

Figure 6.10: Effect of σ on measured solution G, with data deviating from a linear response (red points). Changing the sampling frequency increases the σ at which this occurs.

At the limit of the potentiostat employed (f_{samp} =100 kHz) the data deviates away from linear at σ >25 mS cm^{-1}, defining the upper end of the linear working range, reaching a plateau at ~30 mS cm^{-1}. This is due to the *RC* decay occuring too quickly to be accurately captured and fitted with the maximum f_{samp} of the potentiostat. If the measurement of σ higher than 30 mS cm^{-1} was necessary, a potentiostat with higher bandwidth (>100 KHz) would be required. For measuring σ of many different water systems *e.g.* river, tap and industrial wastewater, as well as typical supporting electrolyte concentrations commonly used in electroanalytical measurements (up to ~0.3 mol dm^{-3}; σ ~30 mS cm^{-1}), an f_{samp} of 100 kHz is sufficient.

To test the capability of the system to measure the σ of different water samples using a SWV measurement, several samples from lakes, rivers and estuaries around the UK in addition to tap water from two different labs in the University of Warwick were measured using a commercial conductivity meter and compared to the conductivity extracted from SWV (Table 6.1), using the SWV parameters outlined in Table 6.1.

Sample	Conductivity Meter (mS cm^{-1})	SWV (mS cm^{-1})	Percentage error (%)
Tap Water (lab 1)	0.503 ± 0.001	0.509 ± 0.03	1.2
Tap Water (lab 2)	0.571 ± 0.001	0.585 ± 0.04	2.5
Bassenthwaite Lake	0.0604 ± 0.0001	0.0592±0.004	2.0
Kenilworth River	0.646 ± 0.001	0.653± 0.04	1.1
Hayle Estuary	0.430 ± 0.001	0.430± 0.02	0.0

Table 2.1: σ of real world water samples of unknown composition, collected from around the UK, measured with a commercial conductivity meter and from fitting the RC decay of a SWV over the potential range +0.3 V to -0.2 V vs SCE.

The σ of the real world water samples extracted from SWV measurements was within 2.5% of that measured by a commercial conductivity meter, therefore proving that this approach can be used to extract the σ from solutions of an unknown composition.

6.4.3 Electrode C measurements for the in-situ monitoring of electrode fouling

Electrode fouling is always a concern when the electrode is directly in contact with the measurement solution. For example, in complex biological media, adsorption of proteins onto the electrode surface can hinder ET, reducing the rate constant and resulting in reduced analytical signals, decreased limits of detection and uncertainties on the measurement.[37] EIS has been used to provide information on electrode fouling by measuring changes in the charge transfer resistance[18,38] or in some cases, C.[18,20] Here, we investigate whether C values extracted from SWV in the non-faradaic potential window, can be used to infer on electrode biofouling. Specifically, the double layer capacitance of an electrode immersed in a solution of 0.5% w/v mucin and 5 mM KCl, was monitored over time (Figure 6.11, E_{SW}= 0.1 V, E_I = 4 mV and f_{SW} = 156 Hz, f_{samp} = 1 kHz) using a potential range of 0.3 to -0.2 V *vs* SCE, and compared to values extracted from EIS at 0.1 V *vs* SCE, when fitted with a simple *RC* equivalent circuit. Mucin is a group of large glycoproteins consisting of a thread-like peptide backbone with segments containing densely packed carbohydrate side chains, these form a mucosal gel blanket on biological surfaces for protection and lubrication[39] and can cause electrode fouling.[40]

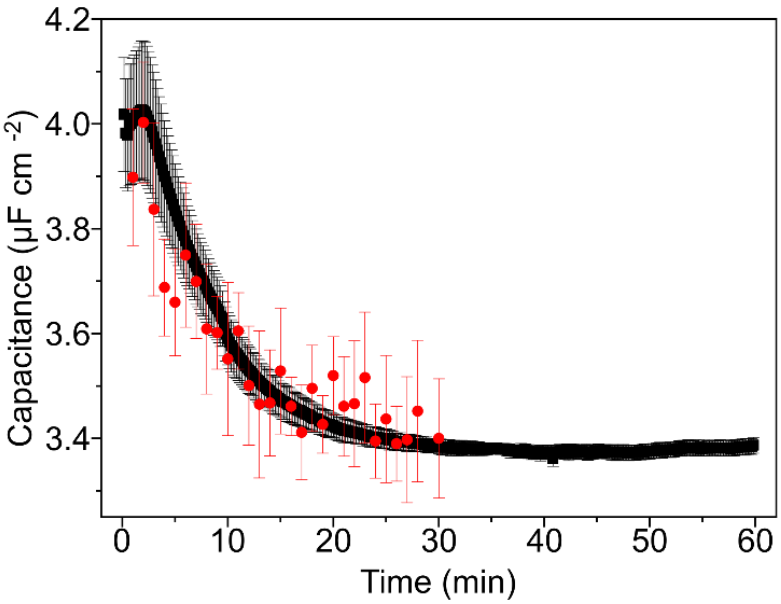

Figure 6.11: C values in 0.5 % w/v mucin measured using SWV (black squares, error bars are the standard deviation in the C values for each scan) and EIS (red circles, error bars are the uncertainty on the equivalent circuit fitting).

As shown in Figure 6.11, upon exposure to mucin, *C* increased slightly in the first 5 minutes and then decreased from a maximum value of 4.03 to 3.37 µF cm^{-2} over a 30 min time period until reaching a plateau. This plateau was maintained over a further 23 hr period (one measurement every 10 s). The initial starting value for *C* was as expected based on the data *vide supra* in the absence of mucin. A very similar decay was observed using EIS, fitted with an *RC* equivalent circuit, suggesting SWV is recording the *C* values accurately. Due to the increased measurement time of EIS only one measurement per minute was possible, as opposed to every 10 s for SWV, with each SWV measurement giving a value for *C* that is an average of 246 measurements. In both cases data fitting is required. For the case of EIS an equivalent circuit must be proposed and the uncertainty on the measurement is determined by the uncertainty on the equivalent circuit fitting. With SWV, the uncertainty can be derived from the standard deviation of the averaged measurements.

It is known that on hydrophobic surfaces it is the bare backbone of the mucin that interacts with the surface, whilst the hydrophilic carbohydrate side chains surround themselves with water.[41] The BDD surface here is oxygen terminated (O-BDD) and thus hydrophilic.[22] In this case interactions with the surface and the water are likely to be via hydrogen bonding between the carbohydrate side chains and the BDD oxygen

groups.[42] A small but quantifiable decrease in *C* is recorded, with time which we attribute to electrode fouling by mucin.

In addition to the change in *C* seen with time upon fouling of the BDD electrode in a solution of 0.5% *w/v* mucin in 5 mM KCl (Figure 6.11) A change in *R*, extracted from the same experiment as figure 6.11, over a comparable timescale (Figure 6.12) was also seen. The SWV measurements (black squares, n=246) were performed every 10 s, with each measurement taking only 0.8 s over the potential range 0.3 to -0.2 V *vs* SCE (E_{SW}= 0.1 V, E_I = 4 mV and f_{SW} = 156 Hz, f_{samp} = 1 kHz. Also shown is EIS data (red circles, error bars are the uncertainty on the fit) at 0.1 V *vs* SCE, recorded every minute over a time period of 60 mins and fitted with an *RC* equivalent circuit. Due to the increased measurement time, the fastest frequency of measurement for EIS is one measurement per minute.

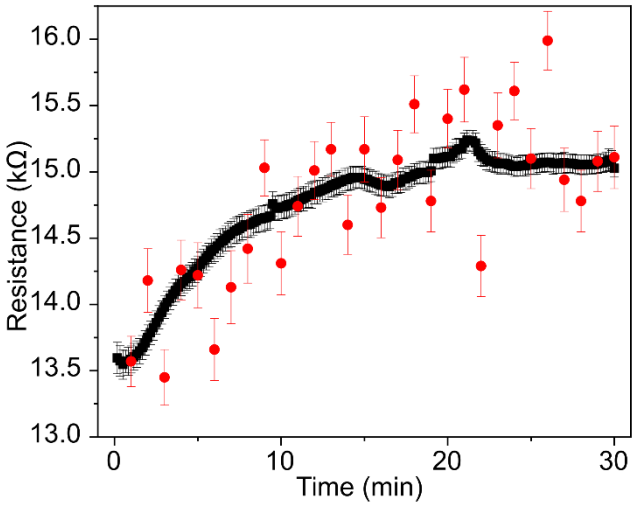

Figure 6.12: R values in 0.5 % w/v mucin and 5 mM KCl measured using SWV (black squares, error bars are the standard deviation in the R values for each scan, σ=0.707 mS cm^{-1}) and EIS (red circles, error bars are the uncertainty on the fit).

R measured by SWV and EIS were in close agreement, with an increase in *R* from 13.5 kΩ to 15 kΩ over the first 30 minutes. This can be explained by an increase in the excluded volume at the electrode surface, reducing the area of the electrode and increasing the effective solution *R*.

Electrochemical fouling can also occur as a result of electrochemical oxidation (or reduction) of the analyte of interest, due to product adsorption. For example, the oxidation of serotonin, a neurotransmitter, results in the formation of an electrically

insulating but porous film due to the formation of a polymer like film,[43] formed from reactive side products and dimers.[44,45] SWV is often used in serotonin detection in order to enhance the electrochemical signature due to the small concentrations detected in typical measurement systems.[46–48] To test whether changes in *C* and *R* could be recorded from the same SWV as faradaic reactions, repeated scans for the oxidation of 1 mM serotonin in 5 mM KCl over the potential range 0.45 – 0.96 V *vs* SCE were performed (Figure 6.13a, E_{SW}= 0.1 V, E_I = 4 mV and f_{SW} = 156 Hz). Over this potential range a peak for the faradaic reaction was seen and a region could be identified where only non-faradaic reactions occurred. This system was chosen as a proof of concept study, where the rate and magnitude of the non-faradaic current were of a magnitude and time constant recordable with the potentiostat used. In addition to the faradaic data, analysis of the *RC* decay curves was conducted using the first 15 reverse pulses (E = 0.35 to 0.410 V *vs* SCE), which by virtue of occurring at a potential negative of the staircase potential by the E_{SW}, are further away from the faradaic peak potential, occurring in a region of the potential window where no faradaic reaction occurs. From these pulses extraction of the *C* and *R* with repeat scans is also possible (Figure 6.13c and d respectively).

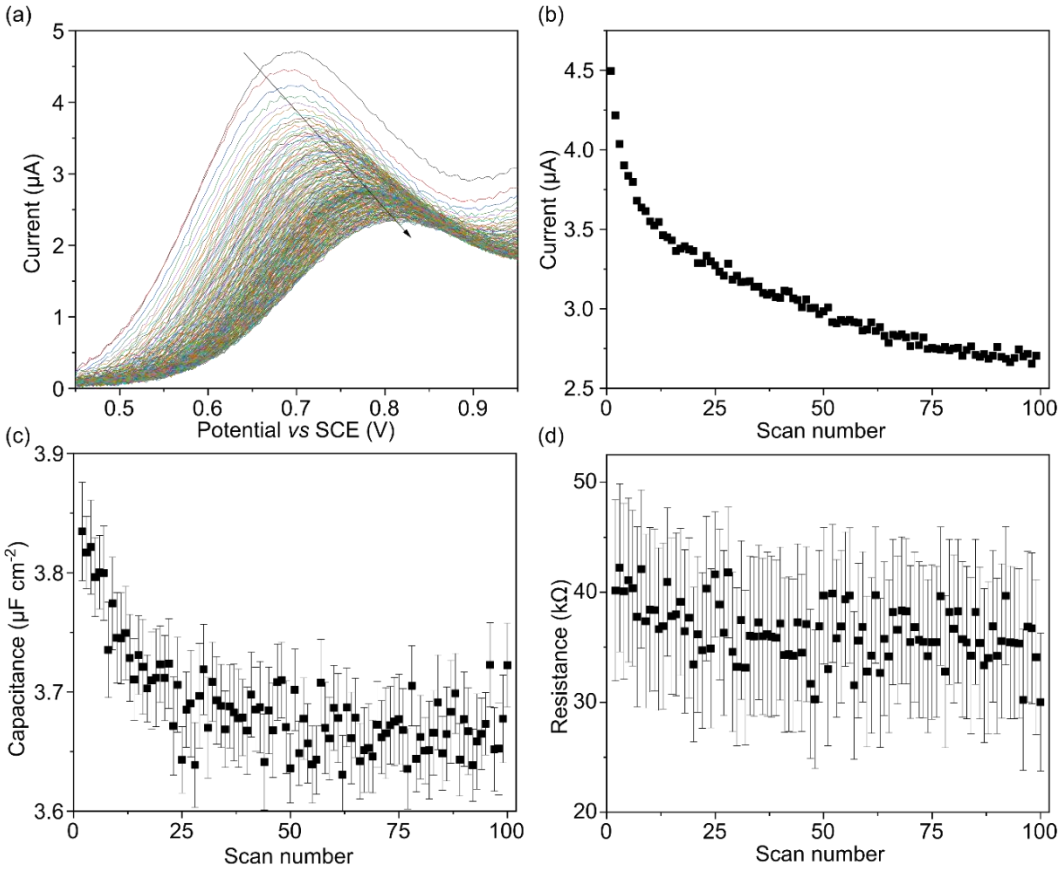

Figure 6.13:(a) 100 SWV scans for 1 mM Serotonin in 5 mM KCl showing a decrease in the peak current. (b) the change in faradaic peak current from SWV with repeated scans. (c) fitted C values from the initial (non-faradaic) portion of the SWV, showing a decrease in C upon electrode fouling with repeated scans. (d) the system R recorded from fouling of the electrode.

It is observed that the current drops with repeat scans, which is attributed to the formation of a porous insulating layer on the surface, reducing the flux to the electrode surface. The *C* (Figure 6.13c) decayed similarly, showing a steep drop with the first scans, followed by a slower decrease, in line with the peak height data (Figure 6.13b). This provides an additional way to measure electrode fouling. Information on *R* was also available from the same measurement (Figure 6.13d). The ability to measure the *R* and *C* in parallel with faradaic reactions provides extra utility from the same measurement by exploiting the often neglected non-faradaic components in the scan. This allows for *in-situ* real time monitoring of electrode condition to determine the degree of electrode fouling and whether a decrease in peak current is due to a change in the serotonin concentration, or electrode fouling. In addition to this the measurement of solution *R* can be used to optimise the measurement conditions and obtain the greatest possible sensitivity for the solution of interest.

6.4.4 Determining pH and solution conductivity with the same electrode and SWV protocols

Previous work has shown that laser ablation of the surface of BDD creates quinone groups in the surface which under proton coupled electron transfer. In this way the sp^2 BDD electrode is voltammetrically pH sensitive. SWV can be used to enhance the pH voltammetric detection signal.[23,24] SWV for this electrode in pH 7.09 Carmody buffer (σ = 8.80 mS cm^{-1}), using the parameters E_{SW}=0.05 V, E_I= 1 mV f_{SWV}= 156 Hz, shows a pH sensitive faradaic peak (Figure 6.14a), where the black line is the output SWV response (current sampled at 75-100% of the pulse). The blue and red lines show the forward and reverse currents. Also clear is a potential window, 0.45 and 0.67 V *vs* SCE, where no faradaic reactions occur (Figure 6.14a, green region). SWV data was recorded in this window using the same parameters as for pH except the frequency was increased to 1.67 kHz to capture the non-faradaic contribution. In this region *R* and *C* could be measured from the raw *i*-*t* of a SWV (Figure 6.14b and c, respectively).

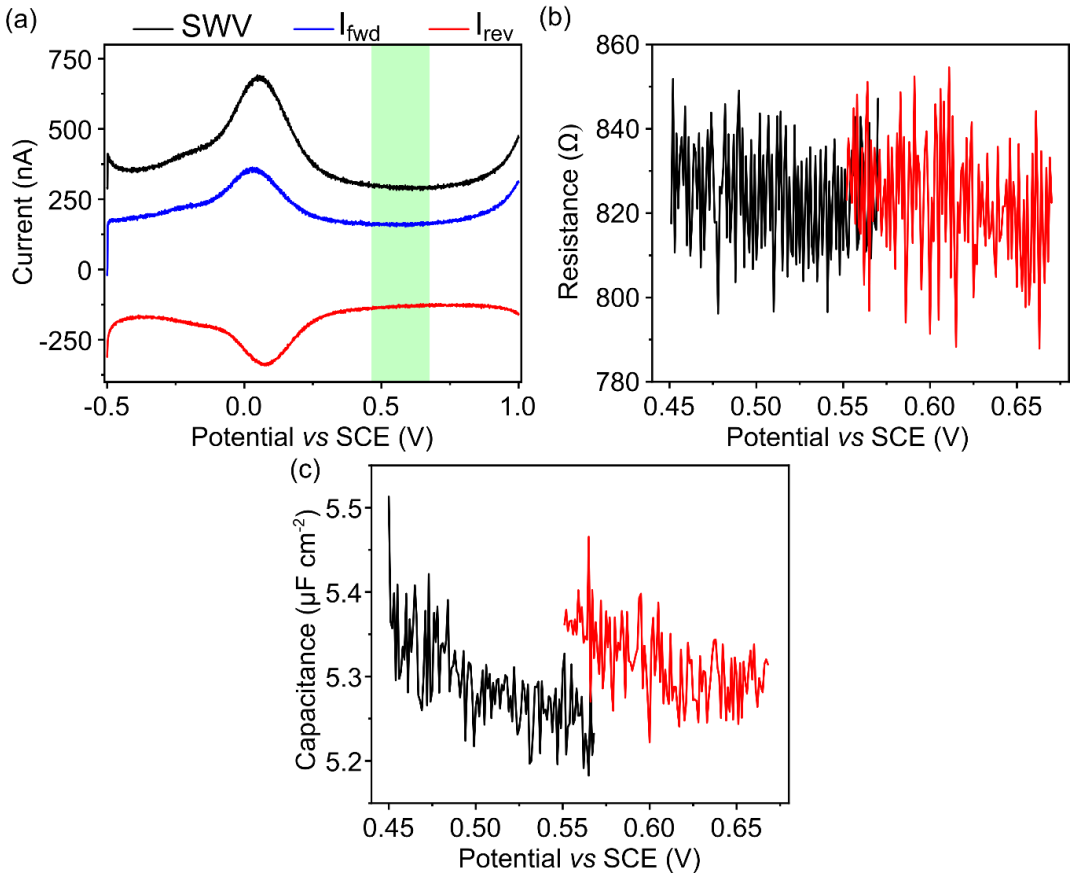

Figure 6.14:(a) SWV of a laser micromachined BDD electrode in pH 7.09 Carmody buffer (σ=8.80 mS cm^{-1}, E_{SW}=0.05 V, E_I= 1 mV f_{SWV}= 156 Hz) with a region free of faradaic reactions highlighted (green). (b) and (c) fitted R (b) and C (c) values from the non-faradaic region of the SWV (E_{SW}=0.05 V, E_I= 1 mV f_{SWV}= 1.67 kHz).

The average value for *R* (820 ± 14 Ω, n=246), could be used to calculate the solution conductivity = 8.73 ± 0.19 mS cm^{-1} which is in close agreement with the value measured using a commercial conductivity meter. The average *C* (n=246) was 5.30 ± 0.05 μF cm^{-2}, higher than the unmachined electrodes used *vide supra* as would be expected for a BDD electrode with an sp^2 surface component.[49]

6.5 Conclusions

SWV is a powerful technique, the current traces of which contain additional information that is often discarded. By recording the entire current trace, the sampling region can be modified at will during data analysis, allowing for optimisation for the greatest sensitivity in the solution of interest. In portions of the scan where there are no faradaic reactions, the *RC* decays can be fitted to inform on solution *R* and *C*. These values can be used to optimise the SWV itself, while also providing additional analytical signals. The fitted conductance data can be used to inform on solution conductivity with a cell constant of 0.176 ± 0.002 cm^{-1}, and can be used to measure real world samples of unknown σ such as lake and river water. Tracking *C* allows for real time monitoring of electrode condition, where changes in *C* occur as electrodes foul, allowing a quick check of the degree of electrode fouling without running additional measurements. The fouling of BDD electrodes will be explored further in future work. Additionally, if the faradaic decay in a pulse is well understood (for instance by fitting the last portion of the pulse), it could be postulated that this could be subtracted from the initial currents to allow the extraction of non-faradaic currents even when faradaic reactions are present. Knowledge of the electrode condition allows a user to understand whether changes in peak height and intensity are due to a change in solution or electrode composition and appropriate corrections to calibrations can be made. It is possible to extract all this additional information using the existing electronics and potential pulse sequences applied in SWV, purely by capturing and analysing this latent data, a much more complete understanding of an analyte.

6.6 References

(1) Osteryoung, J. G.; Schreiner, M. M. Recent Advances in Pulse Voltammetry. *C R C Crit. Rev. Anal. Chem.* **1988**, *19* (1), S1–S27. https://doi.org/10.1080/15476510.1988.10401465.

(2) Barker, G. C.; Gardner, A. W. Forty Years of Square-Wave Polarography. *Analyst* **1992**, *117*, 1811–1828. https://doi.org/10.1039/AN9921701811.

(3) Mirceski, V.; Komorsky-Lovric, S.; Lovric, M. *Square Wave Voltammetry: Theory and Application*; Berlin; Heidelberg, 2007. https://doi.org/10.1007/978-3-540-73740-7.

(4) Ramaley, L.; Krause, M. S. Theory of Square Wave Voltammetry. *Anal. Chem.* **1969**, *41* (11), 1362–1365. https://doi.org/10.1021/ac60280a005.

(5) Krause Jr, M. S.; Ramaley, L. Analytical Application of Square Wave Voltammetry. **1969**, *41* (11), 1365–1369. https://doi.org/10.1021/ac60280a008.

(6) Christie, J. H.; Turner, J. A.; Osteryoung, R. A. Square Wave Voltammetry at the Dropping Mercury Electrode: Theory. *Anal. Chem.* **1977**, *49* (13), 1899–1903. https://doi.org/10.1021/ac50021a008.

(7) Bard, A. J.; Faulkner, L. R. *Electrochemical Methods: Fundamentals and Applications*, 2nd ed.; Wiley: New York, 1980.

(8) Lovric, M. Current Sampling in Square-Wave Voltammetry. *Ann. Chim.* **1994**, *84* (7), 379–382.

(9) Myland, J. C.; Oldham, K. B. Uncompensated Resistance. 1. The Effect of Cell Geometry. *Anal. Chem.* **2000**, *72* (17), 3972–3980. https://doi.org/10.1021/ac0001535.

(10) Komorsky-Lovrić, Š.; Lovrić, M. Measurements of Redox Kinetics of Adsorbed Azobenzene by "a Quasireversible Maximum" in Square-Wave Voltammetry. *Electrochim. Acta* **1995**, *40* (11), 1781–1784. https://doi.org/10.1016/0013-4686(95)00097-X.

(11) Lovrić, M.; Komorsky-Lovric, Š. Square-Wave Voltammetry of an Adsorbed Reactant. *J. Electroanal. Chem.* **1988**, *248* (2), 239–253. https://doi.org/10.1016/0022-0728(88)85089-7.

(12) Phares, N.; White, R. J.; Plaxco, K. W. Improving the Stability and Sensing of Electrochemical Biosensors by Employing Trithiol-Anchoring Groups in a Six-Carbon Self-Assembled Monolayer. *Anal. Chem.* **2009**, *81* (3), 1095–1100. https://doi.org/10.1021/ac8021983.

(13) Mirceski, V.; Laborda, E.; Guziejewski, D.; Compton, R. G. New Approach to Electrode Kinetic Measurements in Square-Wave Voltammetry: Amplitude-Based Quasireversible Maximum. *Anal. Chem.* **2013**, *85* (11), 5586–5594. https://doi.org/10.1021/ac4008573.

(14) Mirčeski, V.; Lovrić, M. Split Square-Wave Voltammograms of Surface Redox Reactions. *Electroanalysis* **1997**, *9* (16), 1283–1287.

https://doi.org/10.1002/elan.1140091613.

(15) Mirceski, V.; Guziejewski, D.; Lisichkov, K. Electrode Kinetic Measurements with Square-Wave Voltammetry at a Constant Scan Rate. *Electrochim. Acta* **2013**, *114*, 667–673. https://doi.org/10.1016/j.electacta.2013.10.046.

(16) Dauphin-Ducharme, P.; Arroyo-Currás, N.; Kurnik, M.; Ortega, G.; Li, H.; Plaxco, K. W. Simulation-Based Approach to Determining Electron Transfer Rates Using Square-Wave Voltammetry. *Langmuir* **2017**, *33* (18), 4407–4413. https://doi.org/10.1021/acs.langmuir.7b00359.

(17) Gray, J. R. Conductivity Analyzers and Their Application. *Environ. Instrum. Anal. Handb.* **2004**, 491–510. https://doi.org/10.1002/0471473332.ch23.

(18) Moulton, S. E.; Barisci, J. N.; Bath, A.; Stella, R.; Wallace, G. G. Studies of Double Layer Capacitance and Electron Transfer at a Gold Electrode Exposed to Protein Solutions. *Electrochim. Acta* **2004**, *49* (24), 4223–4230. https://doi.org/10.1016/j.electacta.2004.03.034.

(19) Contu, F.; Elsener H Bhni, B. Characterization of Implant Materials in Fetal Bovine Serum and Sodium Sulfate by Electrochemical Impedance Spectroscopy. I. Mechanically Polished Samples. *J. Biomed. Mater. Res.* **2002**, *62* (3), 412–421. https://doi.org/10.1002/jbm.10329.

(20) Contu, F.; Elsener, B.; Bohni, H. Characterization of Implant Materials in Fetal Bovine Serum and Sodium Sulfate by Electrochemical Impedance Spectroscopy. II. Coarsely Sandblasted Samples. *J Biomed.Mater.Res* **2003**, *67A* (1), 246–254. https://doi.org/10.1002/jbm.a.10113.

(21) Orazem, M. E.; Tribollet, B. *Electrochemical Impedance Spectroscopy*, 2nd Ed.; Orazem, M. E., Tribollet, B., Eds.; John Wiley & Sons, 2017. https://doi.org/10.1002/9781118694404.ch19.

(22) Macpherson, J. V. A Practical Guide to Using Boron Doped Diamond in Electrochemical Research. *Phys. Chem. Chem. Phys.* **2015**, *17* (5), 2935–2949. https://doi.org/10.1039/c4cp04022h.

(23) Ayres, Z. J.; Borrill, A. J.; Newland, J. C.; Newton, M. E.; Macpherson, J. V. Controlled Sp2 Functionalization of Boron Doped Diamond as a Route for the Fabrication of Robust and Nernstian PH Electrodes. *Anal. Chem.* **2016**, *88* (1), 974–980. https://doi.org/10.1021/acs.analchem.5b03732.

(24) Cobb, S. J.; Ayres, Z. J.; Newton, M. E.; Macpherson, J. V. Deconvoluting Surface-Bound Quinone Proton Coupled Electron Transfer in Unbuffered Solutions: Towards a Universal Voltammetric PH Electrode. *J. Am. Chem. Soc.* **2019**, *141* (2), 1035–1044. https://doi.org/10.1021/jacs.8b11518.

(25) Carmody, W. R. Easily Prepared Wide Range Buffer Series. *J. Chem. Educ.* **1961**, *38* (11), 559. https://doi.org/10.1021/ed038p559.

(26) Joseph, M. B.; Bitziou, E.; Read, T. L.; Meng, L.; Palmer, N. L.; Mollart, T. P.; Newton, M. E.; Macpherson, J. V. Fabrication Route for the Production of Coplanar, Diamond Insulated, Boron Doped Diamond Macro- and Microelectrodes of Any Geometry. *Anal. Chem.* **2014**, *86* (11), 5238–5244. https://doi.org/10.1021/ac501092y.

(27) Cobb, S. J.; Ayres, Z. J.; Macpherson, J. V. Boron Doped Diamond: A Designer Electrode Material for the Twenty-First Century. *Annu. Rev. Anal. Chem.* **2018**, *11* (1), annurev-anchem-061417-010107. https://doi.org/10.1146/annurev-anchem-061417-010107.

(28) Cai, Y.; Anderson, A. B.; Angus, J. C.; Kostadinov, L. N. Hydrogen Evolution on Diamond Electrodes by the Volmer-Heyrovsky Mechanism. *J. Electrochem. Soc.* **2007**, *154* (2), F36. https://doi.org/10.1149/1.2403044.

(29) Liu, D. Q.; Chen, C. H.; Perry, D.; West, G.; Cobb, S. J.; Macpherson, J. V.; Unwin, P. R. Facet-Resolved Electrochemistry of Polycrystalline Boron-Doped Diamond Electrodes: Microscopic Factors Determining the Solvent Window in Aqueous Potassium Chloride Solutions. *ChemElectroChem* **2018**, *5* (20), 3028–3035. https://doi.org/10.1002/celc.201800770.

(30) Garrido, J. A.; Nowy, S.; Härtl, A.; Stutzmann, M. The Diamond/Aqueous Electrolyte Interface: An Impedance Investigation. *Langmuir* **2008**, *24* (8), 3897–3904. https://doi.org/10.1021/la703413y.

(31) Xu, J.; Granger, M. C.; Chen, Q.; Strojek, J. W.; Lister, T. E.; Swain, G. M. Peer Reviewed: Boron-Doped Diamond Thin-Film Electrodes. *Anal. Chem.* **1997**, *69* (19), 591A-597A. https://doi.org/10.1021/ac971791z.

(32) Alehashem, S.; Chambers, F.; Strojek, J. W. J. W.; Swain, G. M.; Ramesham, R. Cyclic Voltammetric Studies of Charge Transfer Reactions at Highly Boron-Doped Polycrystalline Diamond Thin-Film Electrodes. *Anal. Chem.* **1995**, *67* (17), 2812–2821. https://doi.org/10.1021/ac00113a014.

(33) Kondo, T.; Honda, K.; Tryk, D. A.; Fujishima, A. AC Impedance Studies of Anodically Treated Polycrystalline and Homoepitaxial Boron-Doped Diamond Electrodes. *Electrochim. Acta* **2003**, *48* (19), 2739–2748. https://doi.org/10.1016/S0013-4686(03)00391-8.

(34) Brown, M. A.; Goel, A.; Abbas, Z. Effect of Electrolyte Concentration on the Stern Layer Thickness at a Charged Interface. *Angew. Chemie - Int. Ed.* **2016**, *55* (11), 3790–3794. https://doi.org/10.1002/anie.201512025.

(35) Lust, E.; Jänes, A.; Arulepp, M. Influence of Solvent Nature on the Electrochemical Parameters of Electrical Double Layer Capacitors. *J. Electroanal. Chem.* **2004**, *562* (1), 33–42. https://doi.org/10.1016/j.jelechem.2003.07.034.

(36) Bitziou, E.; Joseph, M. B.; Read, T. L.; Palmer, N.; Mollart, T.; Newton, M. E.; Macpherson, J. V. In Situ Optimization of PH for Parts-Per-Billion Electrochemical Detection of Dissolved Hydrogen Sulfide Using Boron Doped Diamond Flow Electrodes. **2014**. https://doi.org/10.1021/ac502941h.

(37) Hanssen, B. L.; Siraj, S.; Wong, D. K. Y. Recent Strategies to Minimise Fouling in Electrochemical Detection Systems. *Rev. Anal. Chem.* **2016**, *35* (1), 1–28. https://doi.org/10.1515/revac-2015-0008.

(38) Kiran, R.; Scorsone, E.; de Sanoit, J.; Arnault, J.-C. J.-C.; Mailley, P.; Bergonzo, P. Boron Doped Diamond Electrodes for Direct Measurement in Biological Fluids: An In Situ Regeneration Approach. *J. Electrochem. Soc.* **2013**, *160* (1), H67–H73. https://doi.org/10.1149/2.014302jes.

(39) Corfield, A. P. Mucins: A Biologically Relevant Glycan Barrier in Mucosal Protection. *Biochim. Biophys. Acta - Gen. Subj.* **2015**, *1850* (1), 236–252. https://doi.org/10.1016/j.bbagen.2014.05.003.

(40) Fagan-Murphy, A.; Watt, F.; Morgan, K. A.; Patel, B. A. Influence of Different Biological Environments on the Stability of Serotonin Detection on Carbon-Based Electrodes. *J. Electroanal. Chem.* **2012**, *684*, 1–5. https://doi.org/10.1016/j.jelechem.2012.08.003.

(41) Shi, L.; Ardehali, R.; Caldwell, K. D.; Valint, P. Mucin Coating on Polymeric Material Surfaces to Suppress Bacterial Adhesion. *Colloids Surfaces B Biointerfaces* **2000**, *17* (4), 229–239. https://doi.org/10.1016/S0927-7765(99)00121-6.

(42) Baszkin, A. Surface Phenomena in Biocomponent-Polymer Systems: A Case Study of Mucin Adsorption on Polymers with Different Hydrophilicities. *Clin. Mater.* **1992**, *11* (1–4), 119–123. https://doi.org/10.1016/0267-6605(92)90036-S.

(43) Patel, A. N.; Unwin, P. R.; Macpherson, J. V. Investigation of Film Formation Properties during Electrochemical Oxidation of Serotonin (5-HT) at Polycrystalline Boron Doped Diamond. *Phys. Chem. Chem. Phys.* **2013**, *15* (41), 18085–18092. https://doi.org/10.1039/c3cp53513d.

(44) Jackson, B. P.; Dietz, S. M.; Wightman, R. M. Fast-Scan Cyclic Voltammetry of 5-Hydroxytryptamine. *Anal. Chem.* **1995**, *67* (6), 1115–1120. https://doi.org/10.1021/ac00102a015.

(45) Wrona, M. Z.; Dryhurst, G. Interactions of 5-Hydroxytryptamine with Oxidative Enzymes. *Biochem. Pharmacol.* **1991**, *41* (8), 1145–1162. https://doi.org/10.1016/0006-2952(91)90653-M.

(46) Park, S. G.; Park, J. E.; Cho, E. I.; Hwang, J. H.; Ohsaka, T. Electrochemical Detection of Ascorbic Acid and Serotonin at a Boron-Doped Diamond Electrode Modified with Poly(N,N-Dimethylaniline). *Res. Chem. Intermed.* **2006**, *32* (5–6), 595–601. https://doi.org/10.1163/156856706777973736.

(47) Goyal, R. N.; Gupta, V. K.; Oyama, M.; Bachheti, N. Gold Nanoparticles Modified Indium Tin Oxide Electrode for the Simultaneous Determination of Dopamine and Serotonin: Application in Pharmaceutical Formulations and Biological Fluids. *Talanta* **2007**, *72* (3), 976–983. https://doi.org/10.1016/j.talanta.2006.12.029.

(48) Tertiș, M.; Cernat, A.; Lacatiș, D.; Florea, A.; Bogdan, D.; Suciu, M.; Săndulescu, R.; Cristea, C. Highly Selective Electrochemical Detection of Serotonin on Polypyrrole and Gold Nanoparticles-Based 3D Architecture. *Electrochem. Commun.* **2017**, *75*, 43–47. https://doi.org/10.1016/j.elecom.2016.12.015.

(49) Ayres, Z. J.; Cobb, S. J.; Newton, M. E.; Macpherson, J. V. Quinone Electrochemistry for the Comparative Assessment of Sp2 Surface Content of Boron Doped Diamond Electrodes. *Electrochem. Commun.* **2016**, *72*, 59–63. https://doi.org/10.1016/j.elecom.2016.08.024.

Chapter 7: Conclusions and Future Directions

7.1 Conclusions

BDD has become a popular material for electroanalytical applications in recent years, mainly due to its very interesting material properties. It has however become apparent that these material properties are highly dependent on the quality of the material and how it has been processed.

In Chapter 3 the effects of sp^2 incorporation on the electrochemical response are investigated through the use of laser micromachining to controllably introduce sp^2 carbon into the BDD electrode surface. An increasing sp^2 content was shown to reduce the solvent window and increase the electrode capacitance. In addition, the amount of surface sp^2 content was shown to quantitatively correlate with the coverage of quinone surface groups on the electrode, which undergo a reversible $2e^-/2H^+$ proton coupled electron transfer (PCET) reaction. The magnitude of the associated quinone reduction/oxidation peak in a voltammogram can be used to determine the quinone surface coverage (Γ) and is thus as a measure of the sp^2 content of the electrode. This method was employed to assess the sp^2 content of different grades of BDD grown using different growth recipes. When BDD was laser machined the electrode was also found to become more catalytic to oxygen reduction reaction (ORR), both via catalysis from the quinone groups and the sp^2 surface itself. For the former, features observed in the voltammogram were attributed to the hydrogen peroxide product of quinone-catalysed ORR and acted to convolute the quinone peak. Oxygen reduction reaction is further studied in Chapter 5.

The quinone peak associated with laser micromachined electrodes has previously been shown to function as a pH sensor[1], however to use it as a practical pH sensor it must perform correctly under all solution conditions. In Chapter 4 the PCET response was studied in unbuffered solutions and a deviation from the expected 59 mV pH^{-1} gradient was witnessed in the mid region. To create a functioning sensor a greater understanding of the system was required. The PCET reaction was shown to be concerted, *i.e.* electron transfer happened simultaneously with proton transfer. No peak was witnessed in the absence of protons, meaning that the quinone could never react by a proton independent pathway and a change in the mechanism could be

excluded. The kinetics of this reaction were investigated in buffered and unbuffered solutions, and was found to have extremely fast kinetics in buffered solutions, with an electron transfer rate constant of 220-250 s^{-1}. Due to the concerted nature of the reaction this rate constant also represents the rate of proton transfer. As the rate was pH independent this can be considered to be limited by the electron transfer rate due to the availability of protons in buffers.

In unbuffered solutions the electron transfer rate was limiting at low pH but at high pH the rate decreased due to the surface $[H^+]$ being rate limiting. These changes in rate could not be used to explain the response seen. The size of the deviation was shown to scale with Γ, and therefore could be attributed to local proton depletion effects from the PCET reaction and also side reactions such as quinone catalysed and sp^2 carbon catalysed ORR, the latter studied further in chapter 5. Square wave voltammetry (SWV) was shown to minimise proton depletion effects and when used in combination with a low Γ and a scan range where ORR was not promoted could be used to give the expected 59 mV pH^{-1} response. Hence proving the development of a pH sensor that could be used in unbuffered solutions.

In Chapter 5 the ORR response on the laser machined sp^2 carbon surface was studied further. An all-diamond BDD electrode of negligible sp^2 content was shown to exhibit a wave in CV very close to the solvent window, with an $E_{1/2}$ of -1.414 V *vs* SCE, which disappeared when the solution was degassed. This was attributed to the ORR response on BDD. When an electrode was laser micromachined a new feature appeared at -0.83 V *vs* SCE that could be attributed to ORR on sp^2 carbon. From the magnitude of the peaks seen in a CV it was demonstrated that the entire sp^2 area was active and Koutecky-Levich analysis was used to determine a heterogeneous rate constant (k_0) of 7.0×10^{-16} cm s^{-1} for this reaction. It was found that the magnitude of the ORR response in a SWV on a laser micromachined BDD electrode could be used to measure the dissolved oxygen concentration of a solution. As these electrodes are similar to those in Chapters 3 and 4 they also exhibited a pH response and as such could be used as a sensor for both dissolved oxygen and pH. Several electrode designs were evaluated and an array of 50 μm laser micromachined pits shown to give a good response for the ORR and pH measurement. Due to the lack of a proton transfer before the rate determining step the peak potential of the ORR reaction was shown to be pH

independent, and therefore could be used as an internal reference for the pH measurement where the peak shifts along the potential axis.

SWV was shown to be important in chapters 4 and 5 for the measurement of dissolved oxygen and pH using laser micromachined electrodes. This technique is commonly used for a large number of electroanalytical applications, often with little understanding of how the technique works. In Chapter 6 it was demonstrated that additional analytical parameters such as the resistance (*R*) and capacitance (*C*) of the system could be determined by using the non-faradaic component of a SWV pulse sequence, that is always neglected. When a potential pulse is applied in the absence of faradaic reactions an exponential current decay with time is observed, the magnitude and time of which depended on *R* and *C*. This decay could be fitted and used to determine the value of *R* and *C*. The *R* measured was the uncompensated resistance, and this could be used to determine the solution conductivity. *C* was related to the double layer capacitance and could be used to monitor electrode fouling. Knowing these parameters is important for optimising a sensor as the response may differ depending on the solution conditions, for instance if the conductivity of the solution is low the measurement may be affected by ohmic drop or migration may have to be accounted for in addition to diffusion. *C* can be used as a monitor of electrode health as the value could be used to tell the user when a cleaning procedure is necessary, or be used to correct a calibration that is changing due to degradation of the electrode. This technique was applied to a laser micro-machined BDD pH electrode in a region of the SWV identified where no faradaic reactions were occurring. Here it was shown that the solution conductivity and electrode *C* could be measured, in addition to using the SWV for pH measurement. Through this technique it could be envisaged that the same electrode and measurement technique (SWV) could be used for the measurement of pH, dissolved oxygen and solution conductivity whilst the electrode health was simultaneously monitored through the electrode *C*.

The work in this thesis aims to provide a greater understanding in the application of BDD electrodes for sensing applications, based around the controlled creation of active sp^2 containing regions by laser micromachining. Quinone PCET offers a measurement technique for the amount of sp^2 carbon introduced by machining, an important parameter to control given its use in many of the envisaged applications of these electrodes. It has been shown that to make robust electrochemical sensors the

fundamental properties of these electrochemical systems must be understood both in terms of the electrode material and how the measurement is performed. However, further work is still required to take this system from a tightly controlled academic environment to a commercial device, but device development can be strongly guided by the studies within. In addition to this the full capabilities of this electrode material have not yet been explored, with other environments and analytes that could potentially be measured using this type of electrode.

7.2 Future Work

The work in this thesis has covered a large number of areas at the proof of concept stage. However many of these areas would benefit from further work.

7.2.1 Further understanding of the electrode material

While the material at the interface of the laser ablated BDD electrodes used throughout this thesis (Chapters 3-6) has been well characterised electronically (it has been shown to be strongly electronically coupled, Chapter 4) and electrochemically (surface functionality- Chapters 3 and 4 and electrocatalytic activity- Chapter 5), characterisation of its microstructure is lacking. Work regarding this is currently ongoing, through the preparation of lamella for transmission electron microscopy characterisation by focused ion beam milling. The completion of this work will further our understanding of this highly scientifically interesting material and will provide information on the nature of the sp^2 carbon on the nanoscale, that has been observed through electrochemical and spectroscopic measurements on the macro and micro scale. This information will help explain the abnormally high stability and robustness of this material, in addition to its electronic and electrochemical performance. This work may also offer structure-based information to guide further application and material design.

7.2.2 The use of raw pulsed voltammetry data to gain further analytical information

In Chapter 6 the non-faradaic potential window was used to gain further information on the solution conductivity and double layer capacitance. This information was shown to provide information on electrode fouling, an area of interest as the fouling of electrodes is a common problem for commercial sensing applications. The ability to monitor fouling processes merits further study, as both the resistance and capacitance of can provide information on the fouling processes with a high time

resolution. This provides a novel way to conduct fundamental studies on electrode fouling with a much greater information density that procedures such as electrochemical impedance spectroscopy, especially when combined with simultaneous measurement of the faradaic processes. In addition to this in low conductivity environments (such as drinking water) the RC decay can impinge on the nominally faradaic only portion of a SWV. If these non-faradaic processes are well defined and understood (such as from this procedure) then the non-faradaic currents can be treated as backgrounds, and subtracted on a pulse by pulse basis, to provide a truly faradaic only voltammogram, with possible increases in sensitivity. In addition to this the non-faradaic processes have only been studied in potential regions where no faradaic reactions are occurring. If the solution conductivity and length of the pulse is sufficient it can be assumed that the non-faradaic components decay to zero, and for all subsequent times the currents are purely faradaic. This information can then be fitted, and subtracted as a background in the non-faradaic region (at the start of the pulse) to leave only non-faradaic currents that can be used to calculate the resistance and capacitance. This can provide information on processes at the interface, with changes in the resistance and capacitance providing additional information on reactions at the surface.

Currently, our development of this approach has been limited by the capabilities of the potentiostat employed (Ivium Compactstat). The acquisition of a potentiostat capable of capturing more data points at an increased frequency (higher bandwidth) will allow for many of the proposed experiments above to be realised.

7.2.3 pH measurement with other potential analytes of interest

The pH at an electrode surface has a significant bearing on the speciation and reaction of other analytes at an electrode surface. For instance work has been carried out on the detection of HOCl and OCl^-, the speciation of which depends on the pH- in particular at the electrode surface where the reaction occurs. As such to understand the reaction of these analytes under changing pH conditions, a measurement of the pH at the electrode surface is required. Laser micro-machined BDD electrodes of a similar nature to those used in Chapters 3-6 of this thesis have been shown to be effective for detecting OCl^-,[2] and as such should also be capable of measuring solution pH. By performing this measurement simultaneously with HOCl/OCl^- detection should allow the full speciation curve to be resolved, relative to the local pH.

7.2.4 Towards commercialisation

The measurement of pH is of great importance for a large number of commercial applications. With the known limitations of the glass pH sensor there is a motivation for the development of a commercial voltammetric pH sensor. To be commercially viable the sensor must operate correctly in all environments and under all conditions under which it may feasibly be applied. As the buffer capacity of a solution is often an unknown the sensor must operate independently of buffer capacity, which chapter 4 has started to address however further work is needed to demonstrate its utility. In addition to this the sensor must function regardless of solution conductivity, a property that has been measured in Chapter 6. To commercialise this device the sensor must be demonstrated to work in unbuffered *and* low conductivity solutions. Implementation of the post processing techniques developed in Chapter 6, with the electrodes developed throughout this thesis may allow for this.

7.3 References

(1) Ayres, Z. J.; Borrill, A. J.; Newland, J. C.; Newton, M. E.; Macpherson, J. V. Controlled Sp2 Functionalization of Boron Doped Diamond as a Route for the Fabrication of Robust and Nernstian PH Electrodes. *Anal. Chem.* **2016**, *88* (1), 974–980. https://doi.org/10.1021/acs.analchem.5b03732.

(2) Meyler, R. E. P.; Edwards, M. A.; Macpherson, J. V. Exploring the Suitability of Different Electrode Materials for Hypochlorite Quantification at High Concentration in Alkaline Solutions. *Electrochem. Commun.* **2018**, *86* (November 2017), 21–25. https://doi.org/10.1016/j.elecom.2017.11.004.